Lehrstuhl E15
Physik - Department

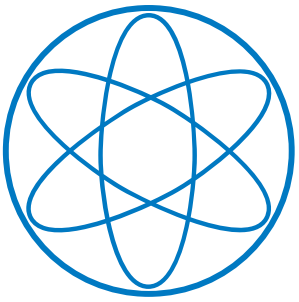

Modulations of the Cosmic Muon Flux & Identification of Atmospheric Neutrino Interactions in Borexino

Dissertation
von

Dominik Jeschke

Technische Universität
München

Technische Universität München

Physik Department
Lehrstuhl für Experimentalphysik und Astroteilchenphysik E15
Prof. Dr. Stefan Schönert

Modulations of the Cosmic Muon Flux & Identification of Atmospheric Neutrino Interactions in Borexino

Dominik Jeschke

Vollständiger Abdruck der von der Fakultät für Physik der Technischen Universität München zur Erlangung des akademischen Grades eines

Doktors der Naturwissenschaften (Dr. rer. nat.)

genehmigten Dissertation.

Vorsitzende/-r:	apl. Prof. Dr. Norbert Kaiser
Prüfende/-r der Dissertation:	1. Prof. Dr. Lothar Oberauer
	2. Prof. Dr. Elisa Resconi
	3. Prof. Dr. Robert Svoboda

Die Dissertation wurde am 09.05.2018 bei der Technischen Universität München eingereicht und durch die Fakultät für Physik am 13.09.2018 angenommen.

Abstract

The liquid scintillator based solar neutrino experiment Borexino has been accumulating data since May 2007. To minimize the background from cosmic muons and cosmogenic radio-isotopes, the detector is located at the Laboratori Nazionali del Gran Sasso (LNGS) with a rock coverage of $3,800$ meter water equivalent. The present work encompasses two analyses of data from the Borexino experiment.
In the first part, a measurement of the residual cosmic muon flux and its modulations using ten years of Borexino data is presented. A mean flux of $(3.432 \pm 0.003) \times 10^{-4}\,\mathrm{m^{-2}s^{-1}}$ was observed and the cosmic muon flux was found to be modulated seasonally in leading order with a period of $(366.3 \pm 0.6)\,\mathrm{d}$ and a relative amplitude of $(1.36 \pm 0.4)\%$. The phase of the seasonal modulation was measured to be $(181.7 \pm 0.4)\,\mathrm{d}$, corresponding to a first maximum of the flux at July 1st, 2007. Using data provided by the European Center for Medium-range Weather Forecast (ECMWF), the cosmic muon flux is shown to be positively correlated with the atmospheric temperature. The effective temperature coefficient that quantifies the correlation was measured to be $\alpha_\mathrm{T} = 0.90 \pm 0.02$. This coefficient can be interpreted as an indirect measurement of the atmospheric kaon to pion production ratio $r_{\mathrm{K}/\pi} = 0.11^{+0.11}_{-0.07}$ for primary cosmic ray energies $E_\mathrm{p} \gtrsim 18\,\mathrm{TeV}$.
Besides the seasonal modulation, evidence for a long-term modulation of the cosmic muon flux with a period of $\sim 3,000\,\mathrm{d}$ and a maximum in June 2012 was found. This modulation is not observed in the atmospheric temperature data, but hints for a correlation to the modulation of the solar activity were noticed.
The production rate of cosmogenic neutrons in spallation processes of cosmic muons was found to show a seasonal modulation in phase with the cosmic muon flux but with an increased relative amplitude of $(2.6 \pm 0.4)\%$.
In the second part of the present work, neutral current (NC) interactions of atmospheric neutrinos in Borexino are investigated. For an exposure of $1.48\,\mathrm{kt} \times \mathrm{yr}$ and a visible energy range from $(7.5 - 30)\,\mathrm{MeV}$, twelve candidate events were observed, matching the expectation of 11.6 ± 4.1 events including backgrounds. With a pulse shape analysis of the candidates, evidence for the observation of atmospheric neutrino NC interactions could be obtained, which marks the second observation of these interactions in liquid scintillator experiments after KamLAND.
For the first time, it could be shown based on data of a running liquid scintillator experiment that the pulses of atmospheric neutrino NC interactions differ from pulses generated by $\overline{\nu}_\mathrm{e}$ in the inverse β decay for the investigated visible energy range. With this proof of principle, pulse shape discrimination techniques are shown to offer promising prospects to suppress the background from atmospheric neutrino NC interactions in future experiments aiming for the first observation of $\overline{\nu}_\mathrm{e}$ from the Diffuse Supernova Neutrino Background.

Zusammenfassung

Das auf der Flüssigszintillator-Technik basierende solare Neutrino Experiment Borexino zeichnet seit Mai 2007 Daten auf. Um den Untergrund von kosmischen Myonen und kosmogenen Radioisotopen zu minimieren, wird der Detektor in den Laboratori Nazionali del Gran Sasso (LNGS) mit einer Abschirmung von 3800 Meter Wasseräquivalent betrieben. Die vorliegende Arbeit umfasst zwei Analysen von Daten des Borexino Experiments.

Im ersten Teil wurde der Fluss kosmischer Myonen in den LNGS und dessen Modulationen mit Borexino Daten, die während zehn Jahren gewonnen wurden, bestimmt. Ein mittlerer Fluss von $(3.432 \pm 0.003) \times 10^{-4}\,\mathrm{m^{-2}s^{-1}}$ wurde gemessen. In führender Ordnung wurde eine saisonale Modulation des Flusses mit einer Periode von $(366.3 \pm 0.6)\,\mathrm{d}$ und einer relativen Amplitude von $(1.36 \pm 0.4)\%$ festgestellt. Die Phase der Modulation wurde zu $(181.7 \pm 0.4)\,\mathrm{d}$ bestimmt, was einem ersten Maximum am 1. Juli 2007 entspricht.

Mit Hilfe von Daten des European Center for Medium-range Weather Forecast (ECMWF) wurde eine positive Korrelation zwischen dem Fluss kosmischer Myonen und der Atmosphärentemperatur aufgezeigt. Der effektive Temperaturkoeffizient, der diese Korrelation quantifiziert, wurde zu $\alpha_\mathrm{T} = 0.90 \pm 0.02$ gemessen. Dieser Koeffizient kann als indirekte Messung des Produktionsverhältnisses von Kaonen zu Pionen in der Atmosphäre $r_{\mathrm{K}/\pi} = 0.11^{+0.11}_{-0.07}$ für primäre kosmische Strahlungsenergien $E_\mathrm{p} \gtrsim 18\,\mathrm{TeV}$ verstanden werden.

Neben der saisonalen Modulation konnte ein Beleg für eine langzeitliche Modulation des kosmischen Myonenflusses mit einer Periode von $\sim 3000\,\mathrm{d}$ und einem Maximum im Juni 2012 gefunden werden. Diese Modulation konnte nicht in der Atmosphärentemperatur beobachtet werden, wohingegen Hinweise für eine Korrelation mit der Modulation der solaren Aktivität festgestellt wurden.

Für die Produktionsrate kosmogener Neutronen in Spallationsprozessen kosmischer Myonen wurde eine saisonale Modulation in Phase mit dem kosmischen Myonenfluss aber einer im Vergleich dazu erhöhten relativen Amplitude von $(2.6 \pm 0.4)\%$ beobachtet.

Im zweiten Teil der Arbeit wurden neutrale Strom(NC)-Wechselwirkungen atmosphärischer Neutrinos in Borexino untersucht. Für eine Exposition von $1.48\,\mathrm{kt} \times \mathrm{yr}$ wurden zwölf Kandidaten mit einer sichtbaren Energie zwischen 7.5 MeV und 30 MeV gefunden, was mit der Erwartung von 11.6 ± 4.1 Ereignissen inklusive Untergrund-Beiträge gut übereinstimmt. Durch eine Pulsformanalyse der Kandidaten konnte der Beleg für die Beobachtung von NC-Wechselwirkungen atmosphärischer Neutrinos erbracht werden. Dies ist die zweite Beobachtung solcher Wechselwirkungen in Flüssigszintillator-Experimenten nach dem KamLAND-Experiment.

Zum ersten Mal konnte basierend auf Daten eines laufenden Flüssigszintillator-Experiments gezeigt werden, dass sich die Pulse von NC-Wechselwirkungen atmosphärischer Neutrinos von Pulsen inverser β-Zerfälle im untersuchten Energiebereich zwischen 7.5 MeV und 30 MeV unterscheiden. Es wurde gezeigt, dass diese Unterscheidungsmöglichkeit in zukünftigen Flüssigszintillator-Experimenten mit dem Ziel der ersten Beobachtung von $\overline{\nu}_{\mathrm{e}}$ des Diffusen Supernova-Neutrino-Untergrundes von entscheidendem Nutzen sein könnte, um den überwältigenden Untergrund durch NC-Wechselwirkungen atmosphärischer Neutrinos zu unterdrücken.

Contents

Chapter 1

Introduction

The neutrino was first introduced by Wolfgang Pauli in 1930 as a possibility to conserve energy and spin in the β decay of radioactive nuclei [1]. With the first observation of the neutrino by Cowan and Reines in 1956 [2], a new field of experimental particle physics was established. In succession to the discovery of neutrinos, many experiments have been built with the goal to detect these particles and investigate their properties.
Various exotic and unanticipated properties of the neutrino were revealed in the following decades. Most prominently, the solar neutrino problem [3] describing the unexpectedly low rate of solar neutrinos observed in terrestrial detectors challenged the understanding of particle physics and solar physics. While this observation could eventually be explained by the mechanism of neutrino flavor oscillations [4] that was also exposed in studies of reactor [5] and atmospheric neutrino data [6], many properties of the neutrino still remain unknown. Especially, the absolute mass scale of the neutrino mass eigenstates, their ordering, and the size of the CP violating phase δ of the mixing matrix are still unresolved [7]. Further, the nature of neutrinos as Dirac or Majorana particles could not be ascertained yet [8], motivating continuing research in the field of neutrino physics.
Since neutrinos only interact weakly and are neither affected by matter surrounding their source nor by electromagnetic fields on their passage towards a detector, neutrinos are well suited as messenger particles pointing back straight to their origin. Thus, they carry valuable information on the environment in which they were created and allow to investigate, e.g., the fusion processes inside the Sun, radiogenic heat production and element abundances in the Earth's crust, or the processes occurring during the core collapse of a massive star and the subsequent supernova explosion. However, due to the low cross sections for neutrino interactions with matter, huge detector target masses are required and a precise understanding of the detector and the relevant backgrounds is vital for the detection of neutrinos.
Since May 2007, the Borexino experiment is accumulating data with the main

goal to perform spectroscopic measurements of neutrinos generated in fusion processes inside the Sun. Based on the unprecedented radio-purity of its liquid scintillator target, outstanding results were obtained. Precision measurements of the neutrino fluxes of all solar pp-chain branches but the least abundant hep neutrinos [9, 10], the currently best limit on the flux of neutrinos generated in the solar CNO-cycle [11], and a spectroscopic measurement of geo-neutrinos [12] could be accomplished. Currently, major efforts are undertaken to realize the first observation of solar CNO neutrinos.

The present work comprises two separate analyses performed in the scope and based on data of the Borexino experiment. First, the cosmic muon flux in the Laboratori Nazionali del Gran Sasso (LNGS), where the experiment is situated, was measured and its modulations were studied using ten years of Borexino data. In a second analysis, neutral current (NC) interactions of atmospheric neutrinos in the Borexino detector were investigated. Techniques to identify these interactions are of special interest also for future experiments aiming for the first observation of the Diffuse Supernova Neutrino Background (DSNB) since atmospheric neutrino NC interactions impose the major background in liquid scintillator based detectors.

After introducing the neutrino and its properties as well as several astrophysical neutrino sources in the present chapter 1, the main techniques applied in real-time neutrino detectors and the most relevant backgrounds for neutrino analyses are described in chapter 2. In chapter 3, the experimental setup of the Borexino detector is illustrated and its physics program is summarized. The subsequent chapters focus on the results of the analysis of the cosmic muon flux and its modulations. In chapter 4, the measurement of the cosmic muon flux and its seasonal modulation is presented. Further, the correlation between this modulation and fluctuations of the atmospheric temperature as well as a long-term modulation of the cosmic muon flux are investigated. In chapter 5, the observed correlation is used to explore the ratio at which kaons and pions are produced in the upper atmosphere. In chapter 6, the seasonal modulation of the cosmogenic neutron production rate in Borexino is investigated. In chapter 7, the analysis of atmospheric neutrino NC interactions in the Borexino detector is presented. In chapter 8, the results of the present work are concluded and an outlook is given.

In the first section 1.1 of the present chapter 1, the description of neutrinos in the Standard Model of Particle Physics is summarized. Section 1.2 describes the mechanism of neutrino oscillations in vacuum, section 1.3 the mechanism of neutrino oscillations in matter. In section 1.4, an overview of several astrophysical sources in which neutrinos are generated and of the involved processes is given.

1.1 Neutrinos in the Standard Model

In the Standard Model of Particle Physics (SM), interactions of particles are described in an $\mathrm{SU}(3) \times \mathrm{SU}(2) \times \mathrm{U}(1)$ quantum field theory. In this model, the strong force is represented by the SU(3), the weak force by the SU(2), and the electromagnetic force by the U(1) component [7]. Electromagnetic and weak interactions can further be combined in an $\mathrm{SU}(2) \times \mathrm{U}(1)$ gauge group, introducing the theory of electroweak interactions [13]. Besides these three fundamental interactions, gravitation is considered to be a fourth fundamental force that, however, so far escapes a quantum field theoretical description and could not be included in the SM yet [14]. Nevertheless, due to the smallness of gravitational effects compared to effects supplied by the other forces, the SM still provides extremely precise predictions of particle interactions.
In the scope of the SM, neutrinos are referred to as the mass- and chargeless counterparts of the charged leptons e, μ, and τ and are only affected by the weak SU(2) interactions. Thus, neutrinos exist in the three flavor states ν_e, ν_μ, and ν_τ. Under SU(2), left-handed fermions transform as doublets while right-handed fermions are understood as singlets [7] and the leptons are grouped as

$$\begin{pmatrix} \nu_\mathrm{e} \\ \mathrm{e}^- \end{pmatrix}_\mathrm{L}, \begin{pmatrix} \nu_\mu \\ \mu^- \end{pmatrix}_\mathrm{L}, \begin{pmatrix} \nu_\tau \\ \tau^- \end{pmatrix}_\mathrm{L}, \mathrm{e}_\mathrm{R}, \mu_\mathrm{R}, \tau_\mathrm{R}. \tag{1.1}$$

The indices L and R denote the left- and right-handed fields, respectively. After parity violation in the weak interactions was discovered, Landau [15], Lee and Young [16], and Salam [17] introduced the two component theory of the neutrino in which only left-handed neutrinos and right-handed antineutrinos exist. This does not allow to generate a neutrino mass via the standard Higgs mechanism since the corresponding Yukawa interactions require both left- and right-handed fields and cannot be built [18]. Hence, neutrinos are assumed to be massless and eigenstates of helicity within the SM.
In contrast to those predictions, oscillations between neutrino flavors, a process that violates lepton family number and is only possible if neutrinos do possess mass, have been observed in atmospheric [6], solar [19], and reactor neutrino experiments [5] marking physics beyond the SM.

1.2 Vacuum Neutrino Oscillations

The mechanism of neutrino oscillations was first proposed by Pontecorvo in 1957 who considered the possibility of oscillations between neutrinos and antineutrinos [20]. After the exclusion of this type of oscillations, oscillations between different neutrino flavors were suggested by Maki, Nakagawa, and Sakata in 1962 [21].

In this model, the weak neutrino eigenstates ν_e, ν_μ, and ν_τ are expressed as linear superpositions of the orthogonal mass eigenstates ν_1, ν_2, and ν_3 with defined masses m_i, where $\mathrm{i}\,\epsilon\,[1,2,3]$ [22]. The translation between mass and flavor eigenstates is carried by a unitary matrix U, the so-called PMNS matrix after the founders of the theory of neutrino oscillations, and

$$\begin{pmatrix} \nu_\mathrm{e} \\ \nu_\mu \\ \nu_\tau \end{pmatrix} = U \begin{pmatrix} \nu_1 \\ \nu_2 \\ \nu_3 \end{pmatrix}. \tag{1.2}$$

Neutrinos are produced and detected in their flavor eigenstates but propagate as mass eigenstates, which allows the oscillation from one flavor into another. Similarly to the CKM matrix of the quark sector [23, 24], the PMNS matrix may be parametrized with three rotation angles θ_ij and a CP violating phase δ [25]:

$$U = \begin{pmatrix} 1 & 0 & 0 \\ 0 & \mathrm{c}_{23} & \mathrm{s}_{23} \\ 0 & -\mathrm{s}_{23} & \mathrm{c}_{23} \end{pmatrix} \begin{pmatrix} \mathrm{c}_{13} & 0 & \mathrm{s}_{13}\mathrm{e}^{-\mathrm{i}\delta} \\ 0 & 1 & 0 \\ -\mathrm{s}_{13}\mathrm{e}^{-\mathrm{i}\delta} & 0 & \mathrm{c}_{13} \end{pmatrix} \begin{pmatrix} \mathrm{c}_{12} & \mathrm{s}_{12} & 0 \\ -\mathrm{s}_{12} & \mathrm{c}_{12} & 0 \\ 0 & 0 & 1 \end{pmatrix}. \tag{1.3}$$

In this parametrization, the abbreviations c_ij and s_ij substitute $\cos\theta_\mathrm{ij}$ and $\sin\theta_\mathrm{ij}$, respectively. If neutrinos are found to be Majorana particles, i.e. if neutrinos are their own antiparticles, two additional CP violating phases have to be included to describe the oscillations [26]. However, since these Majorana phases do not influence the oscillation probabilities, they will be neglected in the following considerations. Further, the number of neutrino states is assumed to be $n = 3$ as in the SM and possible other states like sterile neutrinos are not taken into account. Neutrino mixing with such sterile states, i.e. neutrino states that do not interact via the standard weak force, would require to extend the dimensions of the PMNS matrix in equation 1.3 by the number of assumed additional states and lead to the introduction of corresponding mixing angles [27]. To illustrate the mechanism of vacuum neutrino oscillations, the plane wave approach is used. A more complete theoretical treatment following the wave packet and quantum field theoretical approach can be found in [28].

Since the mass eigenstates have to solve the Schrödinger equation [7], the temporal development of a mass eigenstate $|\nu_\mathrm{i}(t)\rangle$ may be expressed as

$$|\nu_\mathrm{i}(t)\rangle = \mathrm{e}^{-\mathrm{i}\mathrm{E}_\mathrm{i}t}|\nu_\mathrm{i}(0)\rangle \tag{1.4}$$

with E_i being the energy of the mass eigenstate ν_i and $\hbar = c = 1$.

Assuming a finite and small neutrino mass, it follows that $m_\mathrm{i} \ll p_\mathrm{i}$ and $p_\mathrm{i} \sim E_\mathrm{i}$. This allows to approximate the neutrino energy E_i as

$$E_\mathrm{i} = \sqrt{p_\mathrm{i}^2 + m_\mathrm{i}^2} \sim p_\mathrm{i} + \frac{m_\mathrm{i}^2}{2p_\mathrm{i}^2} \sim E + \frac{m_\mathrm{i}^2}{2E}, \tag{1.5}$$

where $E = p$ is the neutrino energy at $m_\mathrm{i} \to 0$. The oscillation probability to detect a neutrino that was produced in the flavor eigenstate α in the flavor eigenstate β at time t after the creation of the neutrino, with $\alpha, \beta \in [\mathrm{e}, \mu, \tau]$, may be derived via

$$P_{\alpha\to\beta} = |\langle\nu_\beta|\nu_\alpha(t)\rangle|^2 \tag{1.6}$$

with $|\nu_\alpha(t)\rangle = \sum_{\mathrm{i}=1}^{3} U_{\alpha\mathrm{i}}|\nu_\mathrm{i}(t)\rangle$ for the mass eigenstates $\mathrm{i} \in [1, 2, 3]$. Thus, the oscillation probability may be expressed as

$$P_{\alpha\to\beta} = \left|\sum_{\mathrm{i}=1}^{3}\langle\nu_\beta|\nu_\mathrm{i}\rangle \mathrm{e}^{-\mathrm{i}E_\mathrm{i}t}\langle\nu_\mathrm{i}|\nu_\alpha\rangle\right|^2 = \left|\sum_{\mathrm{i}=1}^{3} U_{\beta\mathrm{i}}U^*_{\alpha\mathrm{i}}\mathrm{e}^{-\mathrm{i}\frac{m_\mathrm{i}^2 t}{2E}}\right|^2. \tag{1.7}$$

For the contrary situation, the so-called survival probability to observe a neutrino that was produced in the flavor eigenstate α in the same eigenstate α after a time t is given by

$$P_{\alpha\to\alpha} = \left|\sum_{\mathrm{i}=1}^{3} U_{\alpha\mathrm{i}}U^*_{\alpha\mathrm{i}}\mathrm{e}^{-\mathrm{i}\frac{m_\mathrm{i}^2 t}{2E}}\right|^2 = \left|\sum_{\mathrm{i}=1}^{3} |U_{\alpha\mathrm{i}}|^2\mathrm{e}^{-\mathrm{i}\frac{m_\mathrm{i}^2 t}{2E}}\right|^2. \tag{1.8}$$

When oscillations between antineutrinos are considered, U needs to be replaced by its complex conjugate U^* in equations 1.7 and 1.8 [29]. Assuming the ultrarelativistic case, the distance L that has been traveled by the neutrino from its origin is approximately $L \sim t$ and equations 1.7 and 1.8 may be rewritten as [25]

$$P_{\alpha\to\beta} = \left|\sum_{\mathrm{i}=1}^{3} U_{\beta\mathrm{i}}U^*_{\alpha\mathrm{i}}\mathrm{e}^{-2\mathrm{i}\Delta_\mathrm{pi}}\right|^2 \tag{1.9}$$

and

$$P_{\alpha\to\alpha} = \left|\sum_{\mathrm{i}=1}^{3} |U_{\alpha\mathrm{i}}|^2\mathrm{e}^{2\mathrm{i}\Delta_\mathrm{pi}}\right|^2 \tag{1.10}$$

with an arbitrary fixed index p and

$$\begin{aligned} \Delta_\mathrm{pi} &= (E_\mathrm{i} - E_\mathrm{p})t \sim \frac{\Delta m^2_\mathrm{pi} L}{4E}, \\ \Delta m^2_\mathrm{pi} &= m^2_\mathrm{i} - m^2_\mathrm{p}. \end{aligned} \tag{1.11}$$

Following these equations, the probability to find a neutrino in its original flavor α as well as the probability to find the neutrino in a different flavor β oscillate with a period $\tau \propto L/E$ scaled by the mass difference between certain mass eigenstates. Thus, neutrino oscillations are possible if:

Parameter	Value
Δm^2_{12}	$(7.37^{+0.6}_{-0.44}) \times 10^{-5}\,\mathrm{eV}^2$
$\lvert\Delta m^2\rvert$	$(2.50 \pm 0.13) \times 10^{-3}\,\mathrm{eV}^2$ (NH)
$\lvert\Delta m^2\rvert$	$(2.46^{+0.14}_{-0.13}) \times 10^{-3}\,\mathrm{eV}^2$ (IH)
$\sin^2(\theta_{12})$	$0.297^{+0.57}_{-0.47}$
$\sin^2(\theta_{23})$	$0.437^{+0.179}_{-0.058}$ (NH)
$\sin^2(\theta_{23})$	$0.569^{+0.068}_{-0.186}$ (IH)
$\sin^2(\theta_{13})$	$0.0214^{+0.0032}_{-0.0029}$ (NH)
$\sin^2(\theta_{13})$	$0.0218^{+0.0030}_{-0.0032}$ (IH)
δ/π	$1.35^{+0.64}_{-0.43}$ (NH)
δ/π	$1.32^{+0.67}_{-0.49}$ (IH)

Table 1.1: Neutrino mixing parameters [31].

1. At least one mass difference between two neutrino mass eigenstates does not equal zero.

2. U is not diagonal, i.e. the mixing angles $\theta_{\mathrm{ij}} \neq 0$.

Since θ_{13} is much smaller than the other two mixing angles and since $\Delta m^2_{13} \gg \Delta m^2_{12}$ [7], equation 1.3 is effectively decoupled and it is often sufficient to consider oscillations between only two neutrino flavors. Thus, θ_{12} describes the mixing of solar and θ_{23} the mixing of atmospheric neutrinos [30]. For this two flavor approximation, equation 1.7 simplifies to

$$P_{\alpha\to\beta} = \sin^2(2\theta)\sin^2\left(\frac{m_2^2 - m_1^2}{4E}L\right). \tag{1.12}$$

The three mixing angles θ_{ij} and the mass differences Δm^2_{12} and $|\Delta m_{23}|^2$ have been measured in several experiments. The best fit values and the 3σ ranges of these parameters as obtained from a global fit of the current oscillation data [31] are summarized in table 1.1. The CP violating phase δ is given with its 2σ allowed region since no physical values of δ are disfavored at 3σ at the moment of writing. While the sign of Δm^2_{12} has been inferred from solar neutrino experiments [19, 32], the sign of Δm^2_{23} is still unknown. This allows two possible mass orderings of the neutrino mass eigenstates. In the so-called normal hierarchy (NH), $m_3 > m_2 > m_1$, while in the inverted hierarchy (IH), $m_2 > m_1 > m_3$. Due to this, the definition of

$$\Delta m^2 = m_3^2 - (m_2^2 + m_1^2)/2 \tag{1.13}$$

is used in table 1.1. This quantity is $\Delta m^2 > 0$ for the NH and $\Delta m^2 < 0$ for the IH [7].

Since the unknown CP violating phase δ does not affect the survival probability as can be seen in equation 1.8, it cannot be measured in disappearence experiments. Such experiments search for a lower neutrino flux than expected under the non-oscillation hypothesis, exemplarily in the reactor neutrino flux with experiments built close to reactor cores. Instead, appearance experiments must be performed to infer the value of δ.

1.3 Neutrino Oscillations in Matter

In ordinary matter, neutrinos may scatter coherently off the weak potential created by nucleons and electrons. While neutrinos of all flavors can interact with the electrons via neutral current (NC) interactions, only ν_e may additionally interact via charged current (CC) interactions. This leads to an enhanced overall cross section for ν_e interactions compared to neutrinos of the other flavors and the oscillation mechanism is altered compared to the vacuum case. The following considerations on the oscillations of neutrinos in matter mainly follow the explanations in [30]. The enhanced cross section for the interactions of ν_e leads to an additional potential for these particles given by

$$V = \sqrt{2}\mathrm{G_F} N_\mathrm{e}(\overrightarrow{x}) \tag{1.14}$$

with $\mathrm{G_F}$ being the Fermi coupling constant and $N_\mathrm{e}(\overrightarrow{x})$ the electron density. Due to this additional potential, a new mass term that modifies the mixing angles and mass differences compared to the vacuum situation is introduced in the Hamiltonian describing the propagation of the mass eigenstates. Since the mass eigenstate ν_3 is effectively decoupled from the first two mass eigenstates and since it is not affected by terrestrial or solar matter, the ν_e survival probability may be approximated as [33]

$$P_\mathrm{ee} = \mathrm{c}_{13}^4 P_\mathrm{2f}(\theta_{12}, \Delta m_{12}^2, \mathrm{c}_{13}^2 V) + \mathrm{s}_{13}^4 \tag{1.15}$$

with P_2f being the ν_e survival probability in the two flavor approximation considering the mixing parameters of the mass eigenstates 1 and 2 and an effective potential $\mathrm{c}_{13}^2 V$. The mixing angle in matter $\theta_{12,\mathrm{m}}$ can be defined via

$$\cos(2\theta_{12,\mathrm{m}})(V) = \frac{\cos(2\theta_{12}) - 2EV/\Delta m_{12}^2}{\sqrt{(\cos(2\theta_{12}) - 2EV/\Delta m_{12}^2)^2 + \sin(2\theta_{12})}} \tag{1.16}$$

with E being the neutrino energy, θ_{12} the vacuum mixing angle, and Δm_{12}^2 the squared vacuum mass difference between the mass eigenstates. This equation leads to three special scenarios:

- $2EV/\Delta m_{12} \ll \cos(2\theta_{12}) \Rightarrow \cos(2\theta_{12,\mathrm{m}}) \sim \cos(2\theta_{12})$:
  For low electron densities, the mixing angle is almost not affected (vacuum region).

- $2EV/\Delta m_{12} \sim \cos(2\theta_{12}) \Rightarrow \theta_{12,\mathrm{m}} \sim 45°$:
  Maximum mixing between the two neutrino mass eigenstates, independent of θ_{12} (transition region).

- $2EV/\Delta m_{12} \gg \cos(2\theta_{12}) \Rightarrow \theta_{12,\mathrm{m}} \sim 90°$:
  Almost no mixing and $\nu_\mathrm{e} \sim \nu_{2,\mathrm{m}}$ (matter dominated region).

The last case applies to a neutrino generated in fusion processes in the core of the Sun. As detailed in section 1.4.1, these neutrinos are produced as electron neutrinos. Thus, they consist mainly of the mass eigenstate $\nu_{2,\mathrm{m}}$ for the given electron density. The implications of the matter effect during the propagation of an ν_e from the core to the surface of the Sun are depicted in figure 1.1.
As the neutrino propagates towards the surface of the Sun, the electron density decreases, which alters the mixing angle $\theta_{12,\mathrm{m}}$. Due to the small gradient of the electron density inside the Sun compared to the oscillation length of the neutrino in matter $L_\mathrm{m} = L\frac{\sin(2\theta_{12})}{\sin(2\theta_{12,\mathrm{m}})}$, an adiabatic conversion may occur at a resonance point leaving the neutrino in the mass eigenstate $\nu_{2,\mathrm{m}}$. This resonant conversion is known as the Mikheev-Smirnov-Wolfenstein (MSW) effect after its discoverers [22]. Since non-adiabatic corrections to that mechanism are very small [34], they are neglected in the evaluations given here. When the neutrino reaches the vacuum, the vacuum PMNS matrix applies and mostly ν_μ, which dominantly consist of ν_2 in the vacuum, remain.
Since the neutrinos are in the mass eigenstate $\nu_{2,\mathrm{m}}$ when leaving the Sun, they do not oscillate on their way to the Earth. Neglecting the so-called Earth-matter effect, which describes the transition $\nu_{2,\mathrm{m}} \to \nu_{1,\mathrm{m}}$ for neutrinos passing through the Earth that changes the survival probability of ν_e produced in the Sun by about $(1-2)\%$ [33], the ν_e survival probability is given by

$$P_\mathrm{ee} = |\langle\nu_{2,\mathrm{m}}|\nu_\mathrm{e}\rangle|^2 \sim \sin^2(2\theta_{12}) \sim 30\%. \tag{1.17}$$

Considering all possible production points of neutrinos in the Sun and averaging, the two flavor ν_e survival probability in the Sun may be expressed as

$$P_\mathrm{2f} = \frac{1}{2}\left[1 + \cos 2\theta_{12}\langle\cos 2\theta_{12,\mathrm{m}}\rangle\right]. \tag{1.18}$$

Here, $\langle\cos 2\theta_{12,\mathrm{m}}\rangle$ denotes the average value of $\cos 2\theta_{12,\mathrm{m}}$ over all production points that is given by

$$\langle\cos 2\theta_{12,\mathrm{m}}\rangle = \int_0^{R_\odot} \mathrm{d}r\, f(r)\, \cos 2\theta_{12,\mathrm{m}}(r) \tag{1.19}$$

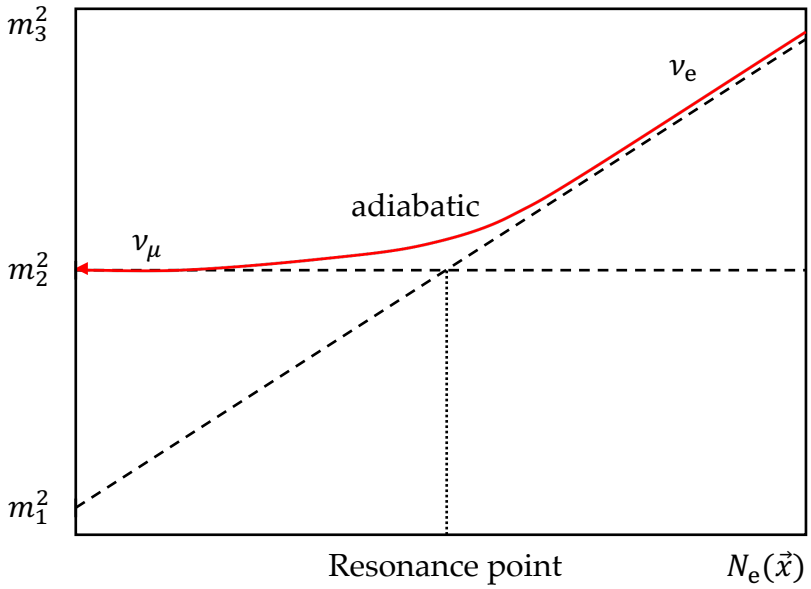

Figure 1.1: Illustration of the MSW effect. An ν_e created in the core of the Sun (right) propagates through the solar matter with a decreasing electron density towards the vacuum. If the adiabatic conversion takes place, the ν_e leaves the Sun in the mass eigenstate ν_2 that in vacuum basically forms ν_μ. The drawing is based on the illustration of the MSW effect in [30].

with $R_\odot$ being the radius of the Sun and $f(r)$ the normalized radial distribution function of the neutrino sources [35]. As can be seen in equation 1.16, $\langle \cos 2\theta_{12,m} \rangle$ depends on the energy and, hence, also the ν_e survival probability is energy dependent.

Figure 1.2 shows the 1σ range of the survival probability of solar neutrinos as predicted in the MSW-LMA (large mixing angle) solution of neutrino oscillations as a magenta band together with results from measurements of the Borexino experiment for different solar neutrino branches [36]. The LMA solution yields the only combination of Δm^2_{12} and θ_{12} consistent with measurements from KamLAND [37] and Borexino [11]. Thus, it constitutes the favored description of solar neutrino oscillations.

Two oscillation regimes can be distinguished. While the oscillations of the low-energetic pp, ^{7}Be, and pep neutrinos are vacuum dominated, the oscillations of the high-energetic ^{8}B neutrinos are matter dominated. The difference in the survival

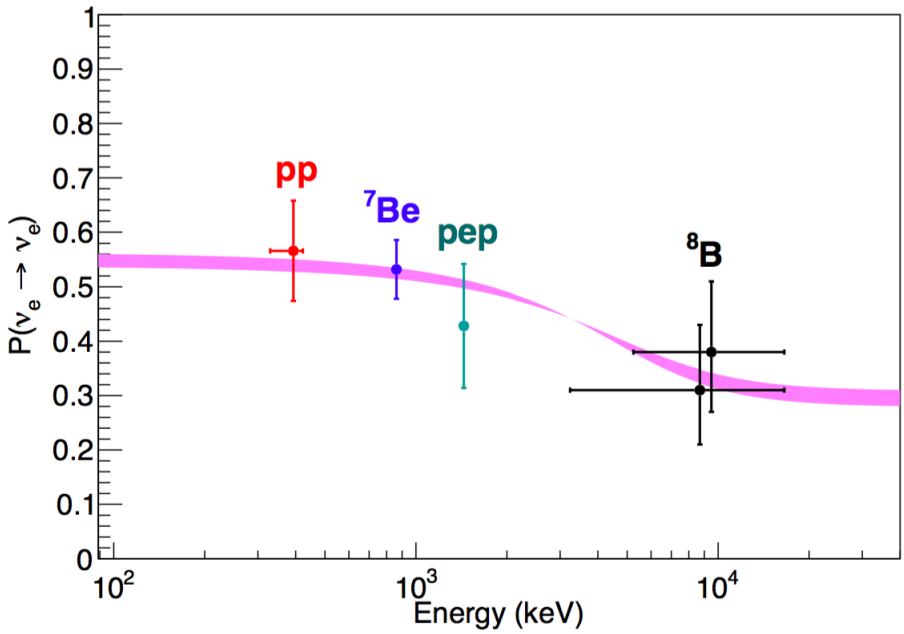

Figure 1.2: The energy dependent survival probability for ν_e produced in the Sun [36]. The magenta band shows the 1σ range of the survival probability as theoretically predicted by the MSW-LMA solution. The latest measurements from Borexino for solar ^{7}Be, pep, and pp neutrinos [36] together with the Borexino result for ^{8}B neutrinos from [38] are shown, all in agreement with the predictions.

probability of ν_e generated in the two regimes and the agreement of all measurements with the MSW-LMA solution clearly proves the existence of the MSW effect and, since this effect is only possible for $m_2^2 > m_1^2$ [22], determines the sign of Δm_{12}^2 to be positive.

Until today, all measurements of the solar ν_e survival probability have been performed in either the vacuum or the matter dominated region while the transition region between those two regimes from $\sim 2\,\text{MeV}$ to $\sim 5\,\text{MeV}$ remains mostly unexplored so far. However, a measurement in this region might yield important implications since new physics could influence the survival probability at these energies.

As an example, non-standard neutrino interactions could affect the survival probability in the transition region. Assuming such interactions, the Fermi coupling constant can be replaced by $A_{\text{MSW}} G_{\text{F}}$ in a simple general model of non-standard neutrino interactions [39]. $A_{\text{MSW}} = 1$ describes the SM model case. While for $A_{\text{MSW}} < 1$, the matter effect is weakened, it is enhanced for $A_{\text{MSW}} > 1$. Thus,

the survival probability in the transition region is either increased or reduced, respectively. For current solar neutrino data, A_{MSW} can be constrained to

$$A_{\mathrm{MSW}} = 1.47^{-0.42}_{+0.54} \tag{1.20}$$

with a detection of the upturn of the ^{8}B neutrino spectrum at low energies being a favored choice to improve the given 1σ bounds of this quantity [39]. Besides non-standard interactions of neutrinos, also the existence of sterile neutrinos could alter the survival probability of solar ν_{e} in the transition region. For a light sterile neutrino state ν_{s} mainly consisting of the mass eigenstate m_4 with $m_1 < m_4 < m_2$ and for a small mixing angle θ_{14}, the ν_{e} survival probability remains almost unchanged in the vacuum and matter dominated regions. However, it is strongly affected in the transition region. In this region, the mixing angle $\theta_{14,\mathrm{m}}$ is enhanced and a resonant conversion of ν_{e} into ν_{s} becomes possible [40]. Hence, even very small mixing angles θ_{14} may lead to significant reductions of the solar ν_{e} survival probability in the transition region compared to the MSW-LMA prediction, potentially even dispelling the upturn of the ^{8}B spectrum [40].

1.4 Astrophysical Neutrino Sources

Since neutrinos only interact weakly, matter is largely transparent to these particles. Hence, they may be used as messenger particles pointing back straight to their production point, which allows to investigate the processes of their generation as well as the physical conditions of the source from which they have been emitted. Further, the investigation of neutrinos coming from astrophysical sources facilitates to infer intrinsic properties of the neutrino like limits on the absolute neutrino mass scale [41] or information on the mass ordering [42]. In the following, the main astrophysical neutrino sources are discussed.

1.4.1 Solar Neutrinos

The Borexino experiment has been built with the main goal to measure and understand the fluxes of neutrinos generated inside the Sun. In the solar core, energy is released via the fusion of hydrogen to helium with the net reaction [43]

$$4\mathrm{p} \rightarrow^4 \mathrm{He} + 2\mathrm{e}^+ + 2\nu_{\mathrm{e}}. \tag{1.21}$$

In this reaction, the energy of $Q = 26.73\,\mathrm{MeV}$ is released. The fusion of four hydrogen cores to one helium core is realized in two separate reaction chains. Dominant in the Sun is the pp-chain [43], for which the respective reaction steps are shown in figure 1.3. Commonly, the neutrinos are labeled by the reaction in which they are

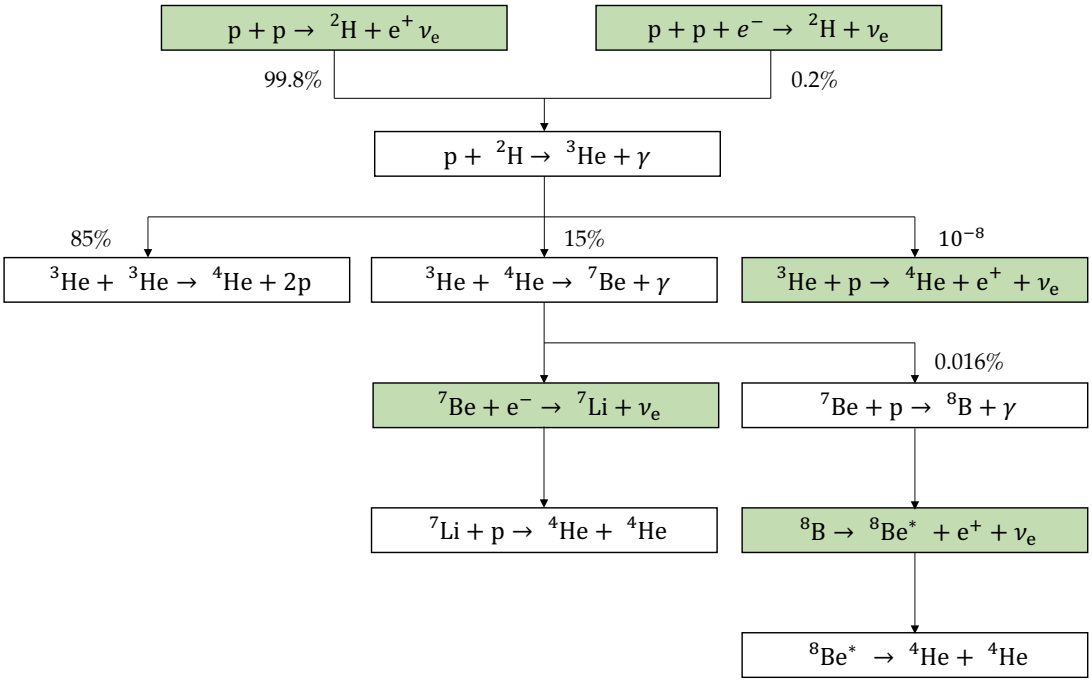

Figure 1.3: The pp-chain. The five reactions in which neutrinos are produced are marked in green. The energy spectra of the pp, ^{8}B, and hep neutrinos are continuous, the ^{7}Be and pep neutrinos are monoenergetic due to the kinematics of the reactions. The reactions and corresponding branching ratios are taken from [44].

produced. In the pp-chain, neutrinos are produced in five reactions generating the pp, the pep, the ^{7}Be, the ^{8}B, and the hep neutrinos. The corresponding reactions are marked in green in figure 1.3. Due to the kinematics of the associated fusion processes, the pp, ^{8}B, and hep neutrinos have continuous energy spectra, while the ^{7}Be and pep neutrinos are monoenergetic.
The second, subdominant chain is the so-called CNO-cycle [45]. This cycle is more sensitive to the core temperature of a star due to the higher Coulomb barrier of its reactions compared to the reactions of the pp-chain and depends on the metallicity of the star, i.e. on the abundance of elements heavier than He. It, thus, constitutes the primary energy source of heavy stars with high core temperatures. In the Sun, this fusion cycle, which is depicted in figure 1.4 and in which carbon, nitrogen, and oxygen act as catalysers, is expected to account for approximately 1.5% of the energy production [46]. The ^{13}N, ^{15}O, and ^{17}F neutrinos generated in the CNO-cycle all feature continuous energy spectra.
Figure 1.5 taken from [35] depicts the fluxes of the neutrinos produced in the Sun

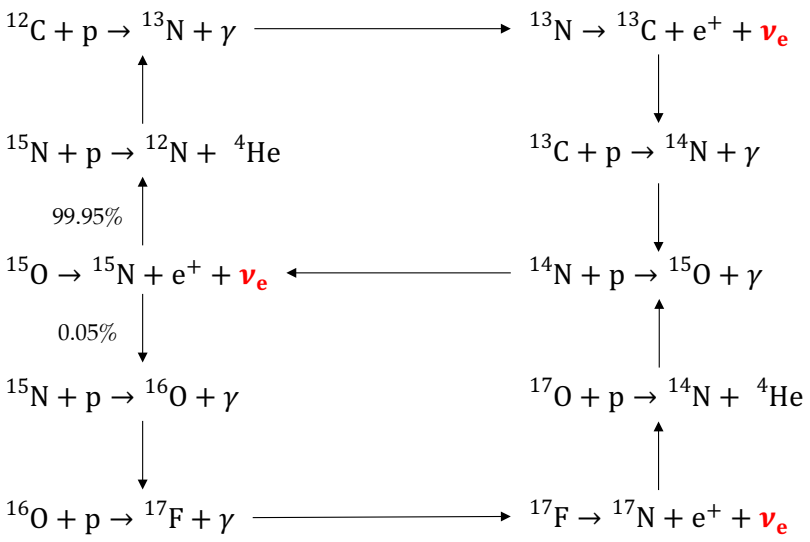

Figure 1.4: The CNO-cycle. Each of the ^{13}N, ^{15}O, and ^{17}F neutrinos have continuous energy spectra. The reactions and the branching ratio of the two subcycles are taken from [44].

as predicted by the Standard Solar Model (SSM) with the theoretical 1σ uncertainties of the fluxes. Since most of the energy of the Sun is generated via the pp-chain, its starting reactions are closely related to the solar luminosity. Since, further, the branching ratio of the pp and the pep reaction is very well known, the fluxes of neutrinos produced in these reactions may be predicted very accurately with low uncertainties. Due to the incomplete knowledge of cross sections and element abundances in the Sun, the other fluxes may only be predicted with less accuracy [47]. The ^{7}Be neutrinos are generated at two separate mono-energetic lines since in the production reaction, ^{7}Li is formed in an excited state in $\sim 10\%$ of the cases leaving less energy to the neutrino than in the remaining $\sim 90\%$, in which ^{7}Li is formed in its ground state.
Solar neutrinos were first measured with the Homestake experiment. This radiochemical experiment used the reaction [3]

$$\nu_e + {}^{37}\mathrm{Cl} \rightarrow e^- + {}^{37}\mathrm{Ar} \tag{1.22}$$

to determine the solar neutrino flux. A deficit of $\sim 2/3$ of the predicted ν_e flux from the Sun was observed by this experiment giving rise to the so-called solar neutrino problem. Besides an inaccurate knowledge of the fusion processes inside the Sun, the mechanism of neutrino oscillations was discussed as a possible ex-

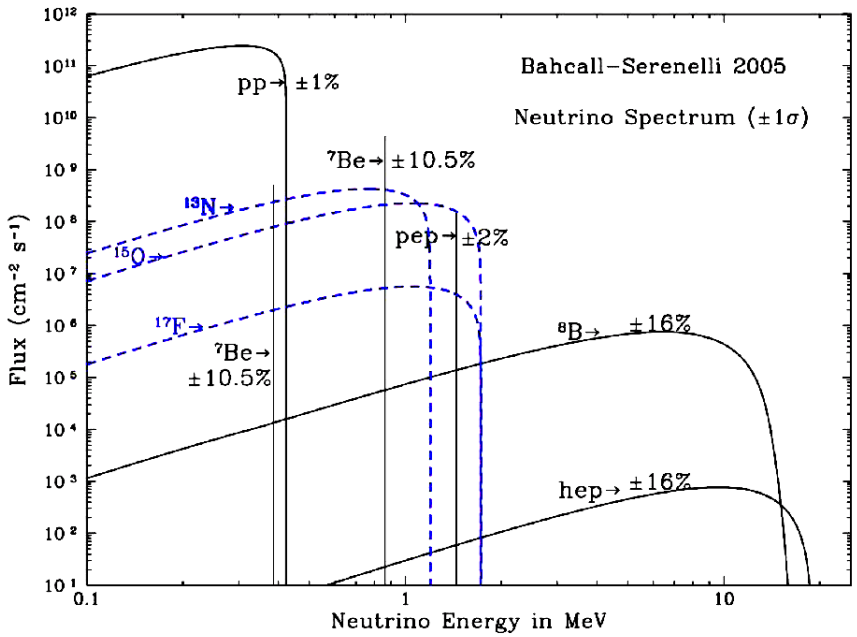

Figure 1.5: The solar neutrino spectrum as predicted by the SSM [35]. The fluxes of neutrinos originating from the pp-chain are shown in solid black, the fluxes of CNO-neutrinos in dashed blue lines. The theoretical uncertainties mainly arise due to uncertainties of the reaction cross sections and element abundances in the Sun [47].

planation of the deficit. With the measurement of the real-time Water Čerenkov experiment SNO that could show that the integral neutrino flux of all flavors from the Sun matches the expectations from the SSM [48], an unambiguous observation of neutrino oscillations was accomplished solving the solar neutrino problem. In succession, several experiments performed precision measurements of the solar neutrino fluxes. This strongly broadened the understanding of the mechanisms of energy production in the Sun as well as neutrino oscillation properties with the Borexino experiment leading the way as described in detail in section 3.2.1.

1.4.2 Supernova Neutrinos

While the Sun does not possess a sufficiently high mass to ignite the subsequent steps of energy production after the helium burning, heavier stars may continue to release energy through the fusion of heavier elements. These processes continue until, ultimately, Fe is formed from Si in stars with masses higher than $\sim 8 M_{\odot}$ [49],

where $M_\odot$ is the solar mass. Since the binding energy reaches its maximum at Fe, no further energy can be released through fusion and the star becomes unstable against its own gravitation due to the drop of the radiation pressure. With the missing radiation pressure and the Fermi pressure of the electrons in the innermost Fe core not lasting to balance the gravitational pressure, the core collapses to a proto-neutron star. When the density of the core reaches nuclear dimensions of about $3 \times 10^{14}\,\mathrm{g\,cm^{-3}}$, repulsive nuclear forces stop the collapse and further infalling material bounces off the core. After the bounce, the material propagates as a shock wave into the outer core. These optically very bright events are described as Supernovae (SNe) type II [50].
While the shock propagates through the outer core, nuclei are dissociated into nucleons and a huge number of ν_e is generated behind the shock front via the electron capture process $\mathrm{e^-} + \mathrm{p} \rightarrow \mathrm{n} + \nu_\mathrm{e}$. Due to the high densities at the core, the ν_e are effectively trapped since their diffusion time is much longer than the one of the shock propagation. When the shock approaches the so-called neutrinosphere that is defined by the radius at which neutrinos decouple from matter, the neutrinos start propagating ahead of the shock in a so-called neutronization burst. Even though the peak luminosity of the neutronization burst exceeds $10^{53}\,\mathrm{erg\,s^{-1}}$, the total energy released through this effect is only of the order $10^{51}\,\mathrm{erg}$ due to the short duration timescale that is related to the shock propagation and, thus, less than $\sim 20\,\mathrm{ms}$ as can be seen in figure 1.6 [50].
Some part of the outer core accretes to the proto-neutron star and the gravitational energy is converted into thermal energy. Through thermal processes, neutrinos of all flavors are produced for a timescale of $\sim 1\,\mathrm{s}$. Finally, the proto-neutron star deleptonizes and a neutron star is built. In this phase, it mainly cools through the emission of thermally produced neutrinos of all flavors since the ultra-dense core is opaque to all other kinds of radiation. The total energy of the neutrinos emitted in the cooling phase approximately equals the binding energy of the produced neutron star of $\sim 3 \times 10^{53}\,\mathrm{erg} \left(\frac{M_\mathrm{NS}}{M_\odot}\right)^2 \left(\frac{10\,\mathrm{km}}{R_\mathrm{NS}}\right)$ and the neutrinos are emitted for a duration of $\sim 10\,\mathrm{s}$ [50], the timescale of the neutrino diffusion.
Besides this neutrino cooling of the star, neutrinos are assumed to be essential for the eventual explosion of a SN [51]. Several SN models predict a neutrino heating process that can enforce explosions that would otherwise stall. In principle, the shock stalls due to iron peak nuclei dissociation and ν_e production via electron capture on the recently liberated protons after the nucleon dissociation. Only milliseconds after the shock stalled, a quasi-hydrostatic equilibrium between the proto-neutron star and the stalled accretion shock is established. However, in the hot and dense core of the proto-neutron star, high-energetic neutrinos of all flavors are produced and the energy transfer of these neutrinos to matter near the stalled shock can be large enough to realize the explosion.

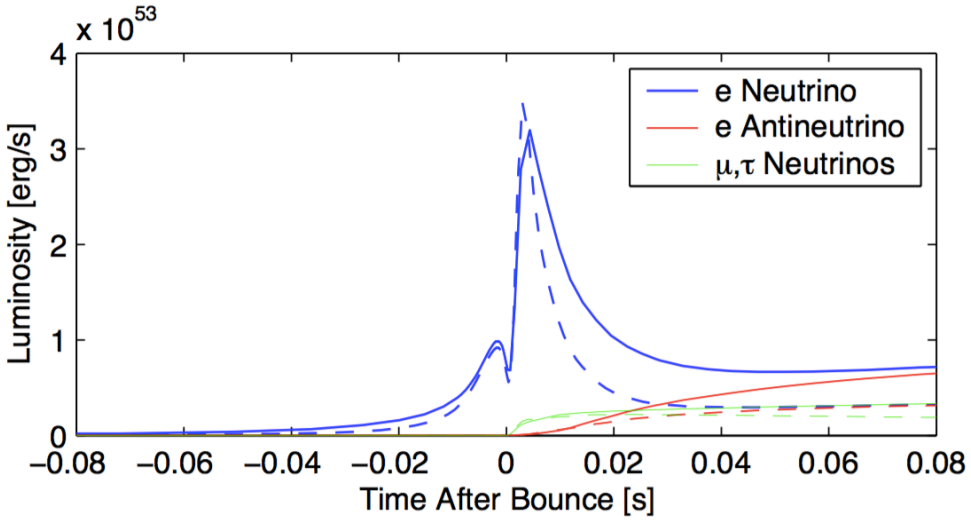

Figure 1.6: SN neutrino luminosities as a function of time [50]. The peak in the ν_e luminosity related to the neutronization burst is clearly visible. Afterwards, the cooling of the neutron star via $\nu\bar{\nu}$ emission that lasts for about 10 s leads to increased fluxes of all neutrino flavors.

The neutrinos emerge out of the neutrinosphere when they decouple from matter and their energy distribution is determined by the temperature at which they decouple. While the thermalized ν_μ and ν_τ as well as the respective antineutrinos only interact via NC reactions with ordinary matter, ν_e and $\bar{\nu}_e$ are also affected by CC reactions. Due to the high neutron density in and around the proto-neutron star, the surrounding matter is, further, more opaque to ν_e than to $\bar{\nu}_e$. Thus, a temperature hierarchy of the decoupling of $T_{\nu_e} < T_{\bar{\nu}_e} < T_{\nu_x}$, where ν_x denotes $\nu_{\tau,\mu}$ and $\bar{\nu}_{\tau,\mu}$, evolves [52].
In a first approximation, the neutrinos of each species may be expected to follow a Fermi-Dirac distribution with zero chemical potential [53]. However, since the cross sections of the interactions of neutrinos with matter rise with energy, lower-energetic neutrinos may be emitted at higher densities and the corresponding neutrinospheres have smaller radii than for high-energetic neutrinos of the same flavor. This effect leads to a pinched shape of the energy distribution compared to the Fermi-Dirac assumption [50]. Monte Carlo simulations taking this into account as the ones performed by Thompson, Burrows, and Pinto (TBP) [54] and by Keil, Raffelt, and Janka (KRJ) [55] yield energy distributions for each individual flavor that can be parametrized as [56]

$$\frac{\mathrm{d}N_\nu}{\mathrm{d}E_\nu} = \frac{(1+\beta_\nu)^{1+\beta_\nu} L_\nu}{\Gamma(1+\beta_\nu)\langle E_\nu\rangle^2} \left(\frac{E_\nu}{\langle E_\nu\rangle}\right)^{\beta_\nu} e^{-(1+\beta_\nu)E_\nu/\langle E_\nu\rangle} \tag{1.23}$$

Model	Mass $[M_\odot]$	$\langle E_{\nu_e} \rangle$ [MeV]	$\langle E_{\nu_e} \rangle$ [MeV]	$\beta_{\bar{\nu}_e}$	β_{ν_x}
LL [57]	20	15.4	21.6	3.8	1.8
TBP [54]	11	11.4	14.1	3.7	2.2
	15	11.4	14.1	3.7	2.2
	20	11.9	14.4	3.6	2.2
KRJ [55]	—	15.4	15.7	4.2	2.5

Table 1.2: Parameters of SN neutrino energy spectra obtained by models from three different groups as summarized in [56]. The mean energies $\langle E_\nu \rangle$ for $\bar{\nu}_e$ and ν_x with x representing μ and τ type neutrinos and antineutrinos as well as the pinching factors at varying progenitor masses are listed. The pinching factor accounts for a different shape of the neutrino energy spectra compared to the Fermi-Dirac assumption due to the finite width of the neutrinosphere of a certain flavor.

with N_ν being the number of neutrinos, E_ν the neutrino energy, $\langle E_\nu \rangle$ the average neutrino energy, and L_ν the expected luminosity of the respective flavor. β_ν is a so-called pinching factor that accounts for the effect of the spatial extension of the neutrinospheres. Due to the origin of the neutrinos in thermal pair production, the totally released binding energy of the star is expected to be equally distributed to the luminosities of the three neutrino flavors. Table 1.2 lists $\langle E_\nu \rangle$ and β_ν as the parameters defining the shape of the energy distributions for $\bar{\nu}_e$ and ν_x, where x represents all μ and τ type neutrinos and antineutrinos for the two mentioned SN simulations. Further, results from a third simulation performed by the Lawrence-Livermore National Laboratory group (LL) [57] that does not consider the effects of an extended neutrinosphere but, in contrast to the other two simulations mentioned, could be continued long enough to produce an explosion is included.
For terrestrial detectors like Water Čerenkov and liquid scintillator detectors as Borexino, most of the neutrino signal from SNe is obtained from $\bar{\nu}_e$ via the inverse β decay (IBD) [56] that is described in section 2.2.2. To obtain the SN $\bar{\nu}_e$ spectrum at Earth, the general mixing of $\bar{\nu}_e$ and $\bar{\nu}_x$ as well as the impact of the matter potential caused by the proto-neutron star and the surroundings need to be considered. Due to the mixing of $\bar{\nu}_e$ and $\bar{\nu}_x$, about 30% of the neutrinos arriving as $\bar{\nu}_e$ were originally produced as $\bar{\nu}_x$. As can be seen in table 1.2, the ν_x spectra are usually harder than the $\bar{\nu}_e$ spectra due to their higher mean energy. Thus, the $\bar{\nu}_e$ spectra observed at Earth will be hardened compared to the $\bar{\nu}_e$ production spectra.
In case of the inverted mass hierarchy being realized in nature, an adiabatic conversion of $\bar{\nu}_e$ into $\bar{\nu}_x$ via the mixing angle θ_{13} is possible for SN neutrinos [58]. Because of the large matter potential at the production site, $\bar{\nu}_e$ are created in the, for inverted hierarchy, lightest mass eigenstate $\bar{\nu}_3$. Analogously to the MSW effect

for solar neutrinos as described in section 1.3, a resonance point exists due to the decreasing density on the neutrino's way to the surface of the stellar envelope. For the current best fit value of $\sin^2(\theta_{13}) = 0.0218^{+0.0030}_{-0.0032}$ [31], the resonance would be completely adiabatic [59], such that $\bar{\nu}_\mathrm{e}$ are bound to enter the vacuum as $\bar{\nu}_3$. This would lead to the observed $\bar{\nu}_\mathrm{e}$ spectrum corresponding approximately to the ν_x production spectrum [56].
Neutrinos emitted by a SN explosion were first observed at terrestrial detectors in 1987 with a neutrino signal from SN1987A, a SN that occurred in the Large Magellanic Cloud at a distance of $\sim 50\,\mathrm{kpc}$. The two Water Čerenkov experiments IMB [60] and Kamiokande [61] observed a total of 19 $\bar{\nu}_\mathrm{e}$ events. While this number is in rough agreement with theoretical predictions, the mean energy of the observed neutrinos was rather low. Nowadays, many experiments are running that would be able to observe a neutrino signal from a SN. For instance, a core collapse SN at the galactic center at about 10 kpc distance would generate 180-190 registered neutrino events in the Borexino detector [62]. In 2009, Borexino joined the SuperNova Early Warning System (SNEWS), a collaboration that further consists of, e.g., Super-Kamiokande [63], LVD [64], and IceCube [65]. In case of a SN, astronomers can be prepared for and pointed towards the imminent optical event through the coincident neutrino burst signals in several of those detectors. The position of the SN may be determined by the track reconstruction capabilities as well as the relative timing of the detectors. Further, the extensive neutrino signal of a galactic SN would provide a strong test of SN models, allow to infer neutrino mass limits, and, possibly, the neutrino mass hierarchy. With the predicted SN rate in our galaxy being between zero and three per century [50], it is very probable that such an event will be observed in the nearer future, thus, widely extending our understanding of the physics of core collapse SNe and the nature of neutrinos.

1.4.3 The Diffuse Supernova Neutrino Background

The cumulative neutrino emission of all SNe throughout the Universe forms a cosmic background of neutrinos that is predicted to be of the order of $10^2\,\mathrm{cm}^{-2}\,\mathrm{s}^{-1}$ [56, 66]. The weakness of this Diffuse Supernova Neutrino Background (DSNB) together with the fact that the energy of neutrinos coming from far away SNe is redshifted inhibited its detection up to the moment of writing. The best limit has been achieved by the Super-Kamiokande experiment with an upper bound on the $\bar{\nu}_\mathrm{e}$ flux of $1.2\,\mathrm{cm}^{-2}\,\mathrm{s}^{-1}$ above 19.3 MeV [67], which is about a factor of ~ 3 above theoretical expectations. However, future experiments like the Jiangmen Underground Neutrino Observatory (JUNO) [68] and the gadolinium enhaced Super-Kamiokande [69] experiment will offer sufficiently large target masses to possibly achieve the first observation of neutrinos from the DSNB.
The flux of the DSNB can be derived by combining the SN neutrino spectrum

$\frac{\mathrm{d}N_\nu}{\mathrm{d}E_\nu}(E_\nu)$ with the redshift dependent SN rate $R_{\mathrm{SN}}(z)$ as [56]

$$\frac{\mathrm{d}F_\nu}{\mathrm{d}E_\nu} = \frac{c}{H_0}\int_0^{z_{\max}} R_{\mathrm{SN}}(z)\frac{\mathrm{d}N_\nu(E'_\nu)}{\mathrm{d}E'_\nu}\frac{\mathrm{d}z}{\sqrt{\Omega_{\mathrm{m}}(1+z)^3+\Omega_\Lambda}} \tag{1.24}$$

with $H_0 = 70\,\mathrm{km\,s^{-1}\,Mpc^{-1}}$ being the Hubble constant, $\Omega_{\mathrm{m}} \sim 0.3$ and $\Omega_\Lambda \sim 0.7$ the contribution of matter to the total density of the Universe and the cosmic constant, respectively, c the speed of light, $E'_\nu = E_\nu(1+z)$ the redshift corrected neutrino energy, and $\frac{\mathrm{d}N_\nu}{\mathrm{d}E_\nu}(E_\nu)$ the average SN neutrino energy spectrum as derived in section 1.4.2. The first SNe are expected to occur at redshift $z_{\max} \simeq 5$ and the factor $1/H_0\sqrt{\Omega_{\mathrm{m}}(1+z)^3+\Omega_\Lambda}$ accounts for the expansion of the Universe. Since most of the signal in Water Čerenkov and liquid scintillator experiments will be observed via the inverse β decay (IBD) described in section 2.2.2, the implications of neutrino oscillations need to be considered also for the DSNB spectrum.
Under the assumption that every star with a mass $m \geq 8M_\odot$ ends in a core collapse SN, the SN rate $R_{\mathrm{SN}}(z)$ can be derived from optical information on the star formation rate $R_*(z)$ and the initial mass function (IMF) of stars in the Universe. Using the standard Salpeter IMF of $\Psi(M) \propto M^{-2.35}$ [70], the relation between $R_{\mathrm{SN}}(z)$ and $R_*(z)$ can be expressed as [56]

$$R_{\mathrm{SN}}(z) = \frac{\int_{8M_\odot}^{125M_\odot}\Psi(M)\mathrm{d}M}{\int_{0M_\odot}^{125M_\odot}\Psi(M)\mathrm{d}M}R_*(z) = 0.0122M_\odot^{-1}R_*(z). \tag{1.25}$$

However, this result strongly depends on the applied IMF and calculations with modified IMFs yield values of -25% to $+8\%$ difference [71, 72]. With the parametrization of the star formation rate as in [56, 73], the SN rate is given by

$$R_{\mathrm{SN}}(z) = 3.9\times10^{-3}f_{\mathrm{SN}}h_{70}\frac{e^{3.4z}}{e^{3.8z}+45}\frac{\sqrt{\Omega_{\mathrm{m}}(1+z)^3+\Omega_\Lambda}}{(1+z)^{3/2}}\,\mathrm{yr^{-1}\,Mpc^{-3}}, \tag{1.26}$$

where $h_{70} = 1$ for a Hubble constant $H_0 = 70\,\mathrm{km\,s^{-1}\,Mpc^{-1}}$ and where f_{SN} is a factor of order unity accounting for the uncertainty of the star formation rate.
Using the three SN Monte Carlo models mentioned in section 1.4.2 and combining them with the SN rate described by equation 1.26, the resulting DSNB neutrino flux was calculated for each model in [74]. Figure 1.7 displays the obtained total fluxes on the left side and the flux as obtained for the LL model divided into the contributions from different redshift regions. In addition, the indistinguishable background from atmospheric $\bar{\nu}_{\mathrm{e}}$ [75, 76] is also shown on the left side. The DSNB flux peaks at $\sim 5\,\mathrm{MeV}$, where the TBP model yields the largest fluxes. However, this model predicts lower fluxes at higher energies compared to the other two models. The spectrum obtained from the LL model shows a much higher flux towards

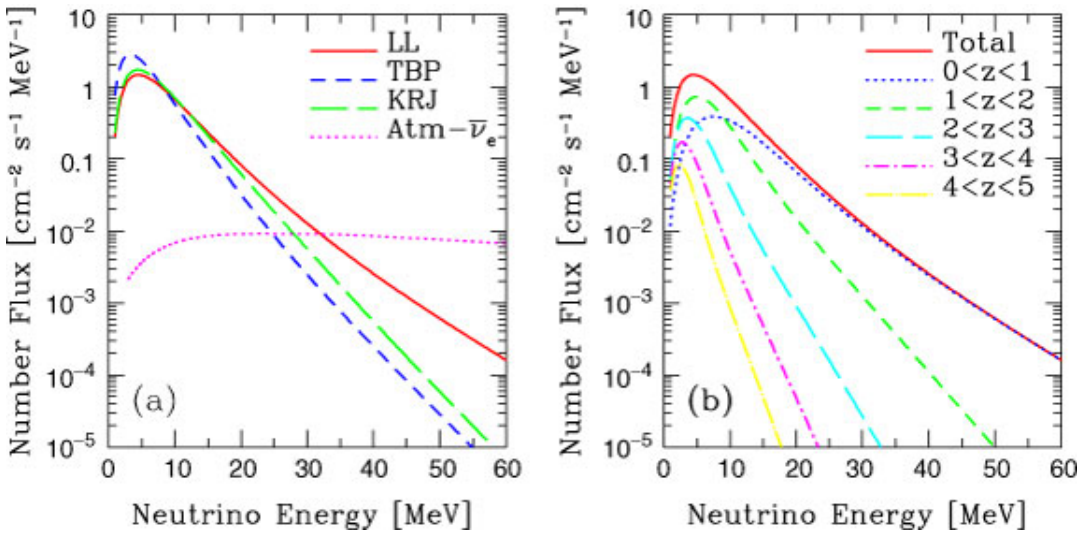

Figure 1.7: DSNB spectra as predicted assuming different SN models. *Left:* The DSNB neutrino spectra for different SN models as calculated in [74] are shown. Due to a higher average $\bar{\nu}_x$ energy in the LL model, the DSNB neutrino flux is enhanced at high energies for this model. *Right:* The contributions of different redshift regions to the DSNB neutrino flux using the LL model are shown. The figure is taken from [56].

the high energy tail that is mainly contributed by the harder $\bar{\nu}_x$ component. As can be seen in table 1.2, the average energy of the $\bar{\nu}_x$ is much higher in this model resulting in an enhanced flux at high energies. Further, the high-energetic part of the DSNB spectrum is found to be populated mainly by SNe occurring at redshifts of $z \lesssim 2$.

With the expected DSNB neutrino rate in the currently constructed JUNO and gadolinium enhanced Super-Kamiokande detectors of a few events per year, a detection of neutrinos from the DSNB in the following $\sim 10 - 15$ years seems achievable. However, both experiments will have to overcome major experimental challenges as described in section 2.4.2 for the case of the JUNO experiment. While the absence of a DSNB signal if sensitivities corresponding to current theoretical estimations of this neutrino flux can be reached in future experiments would require the description of new physics and strongly provoke our understanding of the mechanism of core collapse SNe, a measurement would carry huge astrophysical implications.

Besides a general understanding of the mechanism of SNe and the physical conditions in which the neutrinos are produced, several uncertainties affect the expected DSNB spectrum at the Earth [66]. The expected SN rate and, thus, also the flux of DSNB neutrinos are calculated via the star formation rate and the IMF. The

detectable DSNB neutrino flux mainly originates from SNe occurring at redshifts $z \lesssim 1-2$ since the energies of neutrinos produced in farther SNe are too far red-shifted to significantly contribute to the signal. Even though optical measurements of the SN rate are relatively robust in this redshift region and agree well with the predictions [66], the expected SN rate based on these measurements is still uncertain and might especially be underestimated due to dark or extremely faint SNe not being registered by experiments. Due to this, the measured SN rates partly rather constitute a lower limit and the DSNB neutrino flux could be higher than currently expected [69]. Further, also the minimum mass required for a SN to happen that has been assumed to be $m \geq 8M_{\odot}$ is quite uncertain. With an experimental determination of the DSNB neutrino flux, thus, conclusions on the SN and overall star formation rate as well as the IMF could be drawn.
The spectrum of the DSNB neutrinos describes the average, red-shifted SN neutrino emission spectrum. It carries imprints of the neutrino production processes and the equation of state of nuclear matter as well as the matter accretion rate of the proto-neutron star [77]. Further, not all SNe terminate in the formation of a neutron star as described in section 1.4.2 but a fraction of $\mathcal{O}(10\%)$ is thought to collapse into a black hole, especially for extremely massive progenitors [78]. These so-called failed SNe are optically not visible since no explosion occurs and, thus, contribute to the uncertainty of the measured SN rate. Additionally, it has been shown that in case of a collapse into a black hole, the more rapid contraction of the proto-neutron star leads to a slightly larger neutrino emission at significantly higher energies compared to the neutron star termination [77]. However, since the fraction of black hole formation and the progenitor masses for which this scenario is possible are quite uncertain [78], the impact on the DSNB spectrum is difficult to predict. Since especially the high-energetic part of the DSNB spectrum is of interest for the experiments aiming for a detection due to overwhelming backgrounds at low energies [68], upcoming experiments would clearly benefit from the harder DSNB spectrum and the increased flux for a significant fraction of SNe terminating as black holes. However, due to the limited statistics that can be acquired by the currently constructed experiments, only farer future experiments offering even larger target masses might be able to perform clear spectroscopic measurements of the DSNB neutrinos and, thus, probe the fraction of SNe terminating as black holes or even black hole properties.

1.4.4 Atmospheric Neutrinos

Primary cosmic radiation, which is composed to 90% of protons, 9% of α particles, and 1% of heavier nuclei, hits the Earth's atmosphere at a rate of $\sim 1,000\,\mathrm{m}^{-2}\,\mathrm{s}^{-1}$. Most of this radiation is of galactic origin and the lower-energetic part even originates in solar processes, while the high energy tail of the distribution is generated

in processes outside the galaxy [79]. The energy spectrum of primary cosmic rays can be described by a power law as

$$\frac{\mathrm{d}N}{\mathrm{d}E} \propto E^{-(\gamma+1)} \tag{1.27}$$

with the spectral index γ changing its value depending on the energy region. For low energies, $\gamma \sim 1.7$ is found [80]. At $\sim (10^{12} - 10^{13})\,\mathrm{eV}$, a so-called knee is registered in the spectrum where it steepens with $\gamma \gtrsim 2$ [81] before γ decreases again at $\sim 3 \times 10^{18}\,\mathrm{eV}$ [82], the so-called ankle. A strong cut in the spectrum is observed at $\sim 4 \times 10^{19}\,\mathrm{eV}$, which is consistent with the expectations based on the Greisen-Zatsepin-Kuz'min effect [83, 84].
When the primary cosmic radiation impinges on the atoms of the atmosphere, hadronic showers that consist to a large extend of unstable mesons are produced. At a typical height of 15 km, the generated charged pions and kaons decay into muons and the corresponding neutrinos via

$$\pi^{+/(-)} \rightarrow \mu^{+/(-)} + {}^{(}\overline{\nu}^{)}_{\mu} \tag{1.28}$$

and

$$\mathrm{K}^{+/(-)} \rightarrow \mu^{+/(-)} + {}^{(}\overline{\nu}^{)}_{\mu}. \tag{1.29}$$

Up to an energy of $\sim 1\,\mathrm{GeV}$, these muons are expected to further decay on their way to the Earth into electrons via

$$\mu^{+/(-)} \rightarrow \mathrm{e}^{+/(-)} + {}^{(}\overline{\nu}^{)}_{\mu} + {}^{(}\overline{\nu}^{)}_{\mathrm{e}}. \tag{1.30}$$

Thus, a ratio of muon type neutrinos to electron type neutrinos of $R \sim 2$ is expected at low energies. For higher energies, this ratio quickly decreases since the decay length of the muons becomes larger than the distance between their production point at typically 15 km height and the Earth's surface due to the time dilation [79].
Atmospheric neutrinos range up to energies of $\sim 100\,\mathrm{TeV}$ and their spectral shape closely resembles the one of the primary cosmic radiation [85]. However, the propagation of a primary cosmic ray nucleus is affected by the geomagnetic field. Thus, low-energetic primary particles at low geomagnetic latitudes cannot reach the atmosphere to produce the secondary mesons that decay into neutrinos due to their magnetic rigidity. This results in a latitude dependence of the atmospheric neutrino flux and the mean atmospheric neutrino energy at the Earth's surface [86]. For a more detailed derivation of the atmospheric neutrino spectrum, refer to section 7.1.
Theoretical estimations of the ratio R of atmospheric muon type neutrinos and atmospheric electron type neutrinos agree within 5% since they mainly depend on the

well calculable energy dependent in-flight decay probability of cosmic muons [87]. Thus, the estimation of this ratio is decoupled from the major sources of uncertainties of the cosmic ray fluxes and spectra.
Through CC interactions, the Water Čerenkov experiment Kamiokande was able to compare the observed ratio of atmospheric muon type neutrinos and atmospheric electron type neutrinos to a Monte Carlo prediction and obtained a result of [87]

$$R(\mu/\mathrm{e}) = \frac{R_{\mathrm{Data}}}{R_{\mathrm{MC}}} 0.60^{+0.07}_{-0.06}(\mathrm{stat.}) \pm 0.05(\mathrm{syst.}), \tag{1.31}$$

formulating the atmospheric neutrino problem. Several experiments like IMB [88] or Soudan 2 [89] found similar values for this quantity. In 1998, the Super-Kamiokande experiment measured this ratio with much higher statistics finding [6]

$$R(\mu/\mathrm{e}) = 0.65 \pm 0.05_{\mathrm{stat}} \pm 0.08_{\mathrm{syst}}. \tag{1.32}$$

As an explanation of the observed ν_μ deficit, evidence for neutrino oscillations could be found in the data. While for downward traveling neutrinos, the covered distance between the production point and the detection is only $\sim 15\,\mathrm{km}$, it is significantly enhanced to $\sim 13,000\,\mathrm{km}$ for neutrinos that cross through the Earth before being detected. Thus, the zenith angle distribution of muon and electron type events in the detector can be used to investigate neutrino oscillations.
While the zenith angles of electron like events observed by the Super-Kamiokande experiment were symmetrically distributed, the distribution for muon type events clearly showed that the deficit in the ratio was caused by events coming from below the horizon. With this observation, the deficit could be unambiguously explained to be caused by neutrino oscillations with the two flavor oscillation hypothesis of $\nu_\mu \to \nu_\tau$ transitions mediated by the mixing angle θ_{23} perfectly fitting the data. Oscillations between ν_μ and ν_e could be rejected at 3.4σ [6] since such a transition would generate an asymmetry also in the electron type events with more ν_e registered as traveling upwards due to a CC matter effect in the Earth. The hypothesis of oscillations of ν_μ into sterile neutrinos was rejected at 99% confidence level [90] due to the absence of any matter effect during the passage of the neutrinos through the Earth.
Further, these results allow to infer the mixing angle θ_{23} and the squared mass difference Δm^2_{23}. An analysis of $328\,\mathrm{kton} \times \mathrm{yr}$ of Super-Kamiokande data yields for the NH [91]

$$\Delta m^2_{23} = 2.47^{+0.17}_{-0.28} \times 10^{-3}\,\mathrm{eV}^2 \tag{1.33}$$

and

$$\sin^2\theta_{23} = 0.584^{+0.039}_{-0.069}. \tag{1.34}$$

With these results revealing the existence of neutrino oscillations in the atmospheric sector and determining the applying oscillation parameters, a major contribution to the understanding of the neutrino and its properties could be accomplished.

Chapter 2

Real-Time Neutrino Experiments

The first solar neutrino experiment Homestake Chlorine [92] as well as the subsequent GALLEX [93], SAGE [94], and GNO [95] experiments were radiochemical detectors. These detectors discovered the deficit of solar ν_e and formulated the solar neutrino problem. Due to the low energy threshold, the experiments were able to measure the entire spectrum of solar neutrinos, including the low-energetic pp neutrinos. However, only the integral neutrino flux arriving from the Sun could be measured by these experiments. To perform spectroscopic measurements of solar neutrinos as well as neutrinos from other sources and to provide flavor identification, real-time neutrino detectors had to be developed.
Real-time neutrino detectors first emerged as Water Čerenkov detectors. In these detectors, neutrino interactions can be registered by utilizing the Čerenkov light emitted in the water by secondary charged particles that are generated in the interactions. The energy and direction dependent Čerenkov light emission allows to identify neutrinos from different production mechanisms and locate the source from which they originate [80].
Besides Water Čerenkov detectors, liquid scintillator based experiments with high energy resolutions and low energy thresholds were built. At first, these were mainly constructed next to nuclear power plants and used to analyze the disappearance of nuclear reactor $\bar{\nu}_e$ [80].
The operation of real-time experiments eventually led to immensely important results with the discoveries of neutrino oscillations in the atmospheric sector by Super-Kamiokande [6], in the solar sector by SNO [4], and in the reactor neutrino sector by KamLAND [5].
In succession to these observations, the fluxes of neutrinos from various sources were investigated in precision measurements. In the reactor neutrino sector, especially the Daya Bay [96], Double Chooz [97], and RENO [98] experiments that are based on the liquid scintillator technique deeply explored the neutrino mixing angle θ_{13}. Besides the mentioned Super-Kamiokande experiment [6], the IceCube

detector [99] obtained major results on atmospheric neutrinos and accomplished the observation of high-energetic astrophysical neutrino sources. This detector uses chains of PMTs deployed in the ice at the South Pole and detects the Čerenkov light emitted by charged particles after a neutrino interaction in this naturally abundant target material. Thus, a cubic-kilometer-scale detector can be operated. Similarly, the ANTARES detector [100] uses the Čerenkov light generated by charged particles in the Mediterranean Sea to detect high-energetic astrophysical neutrinos.
With respect to the spectroscopy of solar neutrinos, the liquid scintillator experiment Borexino led the way and performed highly precise measurements of the solar neutrino fluxes that culminated in the first real-time measurements of the solar pp neutrinos [9, 10]. A distinct chapter 3 will be devoted to the Borexino detector and its physics program since the work presented in this thesis was performed in the scope of this experiment.
Carrying the technique of liquid scintillators further, the Jiangmen Underground Neutrino Observatory (JUNO) [68] is currently under construction. This liquid scintillator experiment with a planned target mass of 20 kt is designed mainly to explore and clarify the neutrino mass hierarchy from reactor neutrino data. It will strongly benefit from and be built on the experiences obtained in former liquid scintillator experiments with collaboration overlaps to, e.g., the Daya Bay [96], Double Chooz [97], LENA [101], and Borexino [9] collaborations. With respect to Borexino, especially the developments on scintillator purity and detector construction that led to the unprecedentedly high radio-purity of its liquid scintillator target may be of great value to achieve the ambitious physics goals in JUNO. With its large target volume and the anticipated resolution capabilities, this detector is expected to constitute a new benchmark liquid scintillator experiment allowing the investigation of many neutrino sources and their properties like supernova (SN) neutrinos or the observation of the Diffuse Supernova Neutrino Background (DSNB).
In this chapter, an overview on the technique and experimental challenges of real-time neutrino detectors is given. In section 2.1, the detection principle of real-time neutrino detectors is described. The focus is set on liquid scintillators since this is the main neutrino target of the Borexino detector in the scope of which the present work was performed. Nevertheless, also the detection principle of Water Čerenkov detectors is presented due to the huge impact on neutrino physics and the usage of an active Water Čerenkov muon veto in Borexino. In section 2.2, the reactions via which neutrinos may deposit energy in the liquid scintillator and, thus, can be detected are summarized. In section 2.3, possible background sources for a neutrino detection in liquid scintillators are described. The chapter closes with a description of the JUNO project as a future state of the art liquid scintillator experiment in section 2.4.

2.1 Detection Principle

Water Čerenkov and liquid scintillator detectors both allow to explore neutrinos and their energy spectra in real-time. This facilitates, for instance, to disentangle neutrinos originating in the different reactions of the solar pp-chain as described in section 1.4.1. For both detector principles, the neutrinos are detected via energy depositions of secondary charged particles that are produced in interactions of neutrinos in the target material. In turn, the scintillation or Čerenkov light produced by these secondary particles is collected by photomultiplier tubes (PMTs) distributed on the embedding of the detector. Based on the amount of photons registered by the PMTs and their respective arrival time, energy and position of the interaction can be reconstructed.
Since neutrinos only interact weakly and the interaction cross sections are very small, real-time neutrino detectors must compensate this by offering a huge target mass of the order of several tons to even kilotons with a huge amount of potential interaction partners. Further, long exposure times are usually necessary to acquire significant signals in these rare event searches. This requires a stable and reliable detector behavior over the time scale of several years. Especially for weak neutrino sources like the DSNB, long exposure times are indispensable.
Both detector materials, water and liquid scintillators, are well suited for these requirements since both materials are relatively cheap and allow the construction of even kiloton scale detectors. Water Čerenkov detectors clearly benefit from the possibility to most cheaply build extremely large detectors like the proposed Hyper-Kamiokande experiment [102] and the possibility to reconstruct the direction of the incoming neutrino. The usage of liquid scintillators, however, allows to achieve unprecedentedly low energy thresholds for real-time experiments and low background levels, enabling the precise spectroscopy of neutrinos at even lowest energies [9].

2.1.1 Water Čerenkov Detectors

When a charged particle travels with superluminous velocity through a medium, it emits light known as Čerenkov radiation [103]. This radiation manifests as a light front with the shape of a spherical cone through the interference of spherical waves emitted along the charged particle's track. Figure 2.1 shows an illustration of the Čerenkov effect. The opening angle α of the light cone depends on the refractive index n of the material through which the particle is passing and its velocity $\beta = v/c$. Usually, Čerenkov radiation is characterized by the angle at which the radiation impinges on a surface perpendicular to the particle track. This angle is given by $\alpha_C = 90° - \alpha$, where α is the opening angle of the light cone, and may

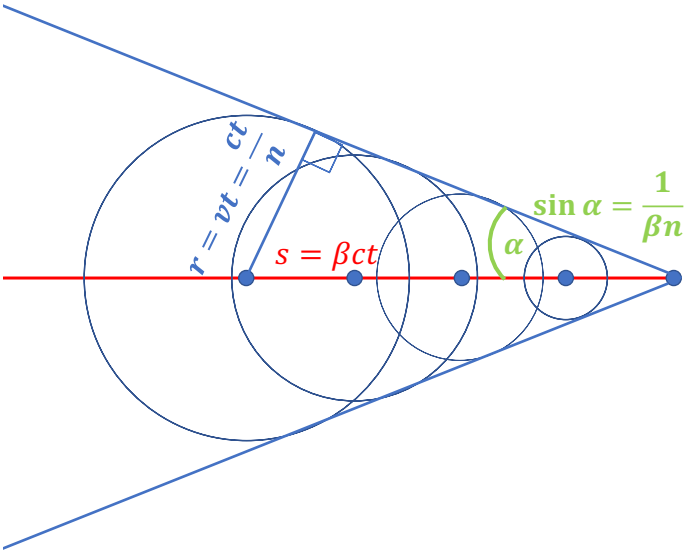

Figure 2.1: Illustration of the Čerenkov radiation created by an ultrarelativistic charged particle with $\beta = v/c \simeq 1$ passing through a medium with a refractive index $n > 1$ [103]. The interference of the spherical light waves emitted along the particle's track causes the conical shape of the radiation. The opening angle α depends on the refractive index of the material and the actual velocity of the particle.

be derived via [103]

$$\cos\alpha_{\mathrm{C}} = \frac{1}{\beta n}. \tag{2.1}$$

In the ultrarelativistic case of $\beta \sim 1$, α_{C} reaches a maximum defined by $\alpha_{\mathrm{C,max}} = \mathrm{acos}(\frac{1}{n})$. Further, a minimum energy of the charged particle is required to produce Čerenkov radiation since its velocity must be at least $\beta \geq \frac{1}{n}$. This implies a threshold energy of

$$E_{\mathrm{thr}} = \gamma m_0 = \frac{1}{\sqrt{1-\frac{1}{n^2}}} m_0, \tag{2.2}$$

with $\gamma = 1/\sqrt{1-\beta^2}$ and m_0 the rest mass of the charged particle.
For the refractive index of water $n_{\mathrm{W}} \simeq 1.33$ [104], the corresponding values are $\alpha_{\mathrm{C,max}} = 41.4°$ and $E_{\mathrm{thr}} = 1.52\, m_0$. Thus, a particle needs to possess at least a kinetic energy of half its rest mass to generate Čerenkov radiation in water. In this medium, Čerenkov radiation is mostly emitted in the ultraviolet (UV) region and in the blue part of the visible spectrum. The usual light yield is approximately 200 photons per MeV [80].

Water Čerenkov detectors captivate especially to produce immensely large target volumes at low costs. Through purification processes, attenuation lengths as high as $\gtrsim 100\,\mathrm{m}$ at 400 nm wavelength for the proposed Hyper-Kamiokande experiment [105] may be achievable and guaranty a huge detection efficiency. While hydrogen and oxygen already offer a huge variety of interaction channels for neutrinos, the detection efficiency for $\bar{\nu}_\mathrm{e}$ can be significantly improved by adding elements that feature large neutron capture cross sections like gadolinium to the detector target [106]. The addition of such elements strongly enhances the signature of the inverse β decay (IBD) described in section 2.2.2, which is the main interaction channel for $\bar{\nu}_\mathrm{e}$ and supernova (SN) neutrinos or neutrinos from the Diffuse Supernova Neutrino Background (DSNB) in terrestrial detectors [56].
A strong benefit of Water Čerenkov detectors is the possibility to use the orientation of the Čerenkov cone to determine the direction of the charged particle emitting the radiation. For neutrino-electron scattering, the accordance between the direction of the electron and the direction of the neutrino increases with the neutrino's energy since forward scattering becomes more probable for higher energies. As shown by the Super-Kamiokande experiment, the correlation between the directions of the neutrinos and the electrons can be already used at energies of the solar ^{8}B neutrinos to strongly reduce the background [107].
Further, due to a differing distortion of the ring as which the Čerenkov cone arrives at the PMTs, a discrimination between muon and electron like events is possible. This feature was used for the determination of the atmospheric ν_μ to ν_e ratio and the observation of neutrino oscillations in the atmospheric neutrino sector by the Super-Kamiokande experiment [6] as detailed in section 1.4.4.
In the Borexino detector, an outer Water Čerenkov detector is used as an active muon veto. Besides guarantying a highly efficient identification of cosmic muons, the arrival time and distribution of the Čerenkov radiation is used to obtain an information on the muon's track if it also crosses the inner liquid scintillator target volume [108].

2.1.2 Liquid Scintillator Detectors

In liquid scintillator based neutrino detectors like Borexino [109], KamLAND [5], Double Chooz [97], Daya Bay [96], or the currently constructed JUNO [68] experiment, organic solvents are used both as the target and the active detector material emitting the light that can be detected. These solvents are based on conjugated aromatic molecules usually featuring one or two benzene rings that consist of six carbon atoms. Due to the altered configuration of the electronic structure of carbon atoms in chemical bonds, six fully delocalized, so-called π-orbitals with weakly bound electrons and three additional bonds are formed [110].
Charged particles passing through the scintillator excite or ionize these weakly

bound electrons. Upon their deexcitation, photons in the near UV region are emitted isotropically. The electrons are excited from the ground state to excited states. These exist as singlet states, for which the spins of the two electrons in a π-bond are antiparallel, and as triplet states, for which the spins are parallel. Additionally, vibrational modes exist for each of the excited states and the ground state that broaden the energy range of the emitted photons [111].
For the singlet states, states above the first excited state have a lifetime of $\sim 10^{-11}$ s and they rapidly deexcite to the first excited state through radiationless internal conversion of adjacent electronic states [110]. After the thermalization of the vibrational substates that have a lifetime of $\sim 10^{-12}$ s, the molecule deexcites into its ground state with a lifetime of 10^{-9} s to 10^{-8} s. The relative intensities for the deexcitation into the respective vibrational modes of the ground state are related to the overlap of the vibrational wavefunctions and can be described by the Franck-Condon factors [112, 113]. This radiation emission from the singlet states constitutes the fast component of the luminescence of liquid scintillators and is referred to as fluorescence [111].
Due to the necessary spin flip of one of the electrons in the π-bond, the first excited triplet state cannot be populated directly from the ground state. However, through the process of the so-called inter-system crossing, which causes a spin flip via the spin orbit coupling, a population of this state from the first excited singlet state is possible [110]. More efficiently, triplet states are populated if the organic molecule has been ionized before. Ionized molecules mainly recombine with an electron in one of the excited states and since $\sim 75\%$ of the available excited states are triplet states, the population of a triplet state is favored in such a scenario [110]. Similarly to the singlet case, higher excited triplet states quickly deexcite via internal conversion and quick thermalization of the vibrational states into the first excited triplet state. Since the radiative transition from this state into the ground state is strongly forbidden, the lifetime of the first excited triplet state is comparably long with $\sim 10^{-4}$ s and the longer phosphorescence component of the light emission arises [111]. Besides this deexcitation via phosphorescence, the triplet state may, under certain conditions, gather sufficient thermal energy to return to the first excited singlet state and decay into the ground state. Also an interaction of two excited triplet states into one excited singlet state and one ground state is possible. Both processes result in the emission of a delayed fluorescence light with a lifetime of $\sim 10^{-7}$ s to 10^{-6} s [111].
Commonly, organic liquid scintillators are composed of a solvent that constitutes the major target for neutrino interactions and one or two solutes added at small concentrations. Since the emission and absorption spectra of the molecules of the solvent strongly overlap [111], the detectable amount of photons would be strongly reduced due to self absorption if only the solvent was used. Through the insertion

of small amounts of a second organic substance with an absorption band close to the emission band of the solvent but with a lower energy gap for radiative deexcitation from the first excited state to the ground state, the scintillation photons can be shifted to larger wavelengths. Due to the small abundances of these so-called wavelength shifters in the scintillator of typically $\sim (1-10)\,\mathrm{g/l}$ or $\leq 1\%$ of mass fraction, self absorption of the solute can usually be neglected except for immensely large detectors. In principle, a second wavelength shifter can be added at even lower concentrations to further reduce the effect of self absorption.
In some cases, also diluters that do not scintillate and lower the light output are added to the scintillator. For example, diluters may be used to increase the transparency and to prevent background from the surroundings of the detector to overpower the signal in a shielded central scintillator target [111].
Neutrinos are detected via the scintillation light generated by the secondary charged particles that are emitted in the interactions of the neutrinos with the scintillator target. Minimum ionizing particles that cross the scintillator lose only about $2\,\mathrm{MeV/cm}$ [7] and create primary excitations and ionizations several molecule distances apart. Since the probability of interactions between the excited or ionized molecules and non-radiative energy loss is, thus, rather small, the light output L per distance x traveled by such a particle in the scintillator depends linearly on the energy loss $\frac{\mathrm{d}E}{\mathrm{d}x}$ of the particle. Hence [110],

$$\frac{\mathrm{d}L}{\mathrm{d}x} = S\frac{\mathrm{d}E}{\mathrm{d}x} \tag{2.3}$$

with S being the absolute scintillation light yield. For a scintillator composed of a solvent doped with one solute, the absolute scintillation light yield depends mainly on the primary excitation efficiency, the quantum efficiency of the transfer of the excitation energy from the solvent to the solute, and the fraction of the mean excitation energy contributing to fluorescence transitions [111]. For organic liquid scintillators, huge light outputs of the order of 10^4 photons per MeV of deposited energy can be achieved. Thus, even considering the limited optical coverage provided by the PMTs in large detectors, yields of hundreds of photoelectrons per MeV can be realized allowing to reconstruct energy depositions with significantly better resolution compared to Water Čerenkov detectors [80]. Also, a low energy threshold of a few hundreds of keV for the neutrino detection can be achieved in liquid scintillators if the intrinsic background contamination can be kept at a sufficiently small level. Due to the isotropic light emission, the arrival times of the photon hits can be used to infer the interaction point via a time of flight calculation. However, no information on the direction of the interacting particle is obtained, which marks the major technical disadvantage of liquid scintillator detectors compared to Water Čerenkov detectors. Only for very high-energetic events like muons, a track may be reconstructed due to the deformation of the sphericity

of the light output. Additionally, the organic liquids used as scintillators are often toxic and easily flammable, which requires more extensive care in the dealing with those substances than for water [80].
For particles with stronger ionization capabilities like protons or α particles at energies usually relevant for liquid scintillator based neutrino experiments, the energy loss $\frac{\mathrm{d}E}{\mathrm{d}x}$ in the scintillator is larger than for minimum ionizing particles. Thus, higher densities of excited and especially ionized molecules result and non-radiative deexcitation in reactions between these molecules becomes relevant. Further, the ionized molecules preferably recombine with electrons to an excited triplet state, which lowers the quantum efficiency for the excitation energy transfer from the solvent to the solute. Due to this, the fluorescence light yield is reduced for interactions of these particles, an effect called ionization quenching that causes a non-linear dependence of the light output on the particle's energy loss [111]. This non-linear behavior is described by a semi-empirical model, the so-called Birk's formula [110], that is given by

$$\frac{\mathrm{d}L}{\mathrm{d}x} = \frac{S\frac{\mathrm{d}E}{\mathrm{d}x}}{1 + kB\frac{\mathrm{d}E}{\mathrm{d}x}} \tag{2.4}$$

with $B\frac{\mathrm{d}E}{\mathrm{d}x}$ the specific density of excited and ionized molecules along the track and k a factor accounting for the strength of the quenching effect. The factors k and B are nowadays often combined to the so-called kB- or Birk's factor. Typical values of the kB-factor for liquid scintillators are of the order of $\sim 0.01\,\mathrm{cm/MeV}$. Thus, the light emission for heavy particles like protons is reduced by a factor $2-3$ compared to electrons of the same energy [111].
To accomplish the necessary low background rates for rare event neutrino searches, liquid scintillators may be purified from internal radioactive contaminations by techniques like distillation, water extraction, gas stripping, and filtration [114]. By removing organic impurities, a high light transparency of the order of $\gtrsim 20\,\mathrm{m}$ attenuation length [68] may be achievable in liquid scintillators. Further, neutrino detectors are usually built in laboratories deep underground to shield them against cosmic radiation and the cosmogenic radioactive isotopes produced by cosmic muons in spallation processes. The introduction of diluters to the scintillator allows to define a fiducial volume and to use the self-shielding of outer layers to suppress background contaminations.
In liquid scintillators, spatial and temporal coincidences of events may be used to distinguish background events from the signal. For example, the IBD as described in section 2.2.2 results in a clear signature that allows to identify CC interactions of $\bar{\nu}_\mathrm{e}$. The fast coincidence of a ^{214}Bi β decay and the subsequent ^{214}Po α decay may be used to identify those isotopes. The combination of temporal and spatial information has further been used to identify decays of ^{11}C via the coincidence of

the incoming muon, a produced neutron, and the actual ^{11}C decay [9].
To discriminate between energy depositions of different particle types in a liquid scintillator, the temporal shape of the pulse of the photon hits registered at the PMTs may be utilized. The scintillation time decay may be approximated by a sum of several exponential decays accounting for the population of different excited states that lead to different decay times as [115, 116]

$$N(t) = \sum_{\mathrm{i}=0}^{N_{\max}} N_{\mathrm{i}} \cdot e^{-\frac{1}{\tau_{\mathrm{i}}}}. \tag{2.5}$$

Here, $N(t)$ describes the number of excited states at a time t after the interaction, N_{i} the number of excited molecules in the state i at time $t = 0$, and τ_{i} the scintillation decay time of the respective state. While the shape of the fast and slow component of the scintillation light is found to be almost independent of $\frac{\mathrm{d}E}{\mathrm{d}x}$, the amplitudes of the respective components strongly depend on the particle type since energy depositions of heavier ionizing particles result in a stronger population of the slowly decaying triplet states [110]. These effects allow to identify particles based on their normalized pulse shape with an enhanced slow component hinting the scintillation light emission being caused by heavier particles. Using the differences of the pulses for distinct particle interactions, several pulse shape parameters may be constructed. Common examples are the tail-to-total parameter [111], which compares the ratio of hits registered in the tail of the pulse to all registered hits, or the Gatti parameter [117], which compares the pulse of an event to reference pulses and estimates the agreement.
In Borexino, pulse shape discrimination techniques have been successfully applied to suppress the background from α decaying isotopes in the solar neutrino analyses [9]. Besides the identification of heavier ionizing particles via the slower decay of the scintillation light emission, pulse shape discrimination can also be utilized to suppress backgrounds from β^+ emitters in liquid scintillators. Positrons may form the bound state of positronium in the scintillator. Since positronium is potentially produced in the spin state of orthopositronium with a lifetime of $\sim 3\,\mathrm{ns}$, the scintillation light emission of positron interactions may slightly differ from the signal for electron interactions [118]. Harnessing these differences in the reconstructed pulses, a suppression of the cosmogenically produced β^+ emitter ^{11}C as a background for solar neutrino measurements could be achieved in Borexino [9]. However, the usage of pulse shape discrimination techniques has been limited to the low visible energy region relevant for solar neutrino analyses so far except for their application in the identification of cosmic muons. In the scope of this thesis, these techniques were applied for the first time at comparably high visible energies to identify interactions of atmospheric neutrinos in the Borexino detector as described in chapter 7.

2.2 Energy Deposition

Neutrinos transfer energy to the solvent of a liquid scintillator or the water of a Water Čerenkov detector via CC or NC weak interactions. Since liquid scintillators are based on hydrocarbons, the electrons, the free and the bound protons, and the neutrons of the carbon nuclei constitute the possible interaction partners of the neutrinos. Water Čerenkov detectors feature the same detection reactions except for reactions on carbon. However, very similar reactions on oxygen are provided [80].

2.2.1 Elastic Scattering

For several solar neutrino experiments including Borexino, the elastic scattering of ν_{e} off electrons in the target constitutes the major detection channel. While all neutrino species may interact with the electrons via NC reactions, ν_{e} may further interact via CC reactions to the same final state. This enhances the cross section for this neutrino species as summarized in table 2.1. Table 2.1 lists the reactions through which neutrinos may be detected in liquid scintillator based experiments with the applying weak current, the energy threshold of the reaction, and the respective cross section. Additionally, eventual follow-up reactions are given with the corresponding decay or capture times. Since the elastic scattering process closely resembles the Compton effect of γ rays, the maximum energy $E_{\mathrm{e,max}}$ that can be transferred by a neutrino of the energy E_ν to an electron is given by

$$E_{\mathrm{e,max}} = \frac{2E_\nu^2}{m_{\mathrm{e}}c^2 + 2E_\nu} \tag{2.6}$$

with the electron rest mass m_{e} and c the speed of light. Since the elastic neutrino-electron scattering has no intrinsic energy threshold, the detection of low-energetic neutrinos via this detection channel solely depends on the experimental energy threshold and the background level. Due to the energy depositing particle being an electron as in β^- decays, a discrimination of neutrino interactions from radioactive β^- decays on an event-by-event basis cannot be provided for this detection channel. Besides the scattering off electrons, also the scattering of neutrinos off protons is possible. However, due to the larger mass of the proton and the quenching effect, these neutrino interactions result in a strongly reduced visible energy output in the detector and a signal just above the possibly low experimental threshold of a few hundreds of keV translates to several MeV of energy transferred to a proton. Thus, this reaction contributes only very little to the detection of solar neutrinos [80]. However, it would be very helpful to investigate SN neutrinos. The event number resulting from the higher-energetic ν_{x}-proton scattering is expected to be similar to the event number from the inverse β decay, the main detection channel for

Reaction	Current	Threshold [MeV]	Cross section $[10^{-44}\,\mathrm{cm}^2]$
$\nu_\mathrm{e} + \mathrm{e}^- \to \nu_\mathrm{e} + \mathrm{e}^-$	NC/CC	–	$0.92 \cdot E_\nu/\mathrm{MeV}$
$\bar{\nu}_\mathrm{e} + \mathrm{e}^- \to \bar{\nu}_\mathrm{e} + \mathrm{e}^-$	NC	–	$0.38 \cdot E_\nu/\mathrm{MeV}$
$\nu_\mathrm{x} + \mathrm{e}^- \to \nu_\mathrm{x} + \mathrm{e}^-$	NC	–	$0.16 \cdot E_\nu/\mathrm{MeV}$
$\bar{\nu}_\mathrm{x} + \mathrm{e}^- \to \bar{\nu}_\mathrm{x} + \mathrm{e}^-$	NC	–	$0.13 \cdot E_\nu/\mathrm{MeV}$
$\nu_\mu + \mathrm{p} \to \nu_\mu + \mathrm{p}$	NC	–	$0.32 \cdot (E_\nu/\mathrm{MeV})^2$
$\bar{\nu}_\mathrm{e} + \mathrm{p} \to \mathrm{n} + \mathrm{e}^+$ $\mathrm{n} + \mathrm{p} \to \mathrm{d} + \gamma\,(2.2\,\mathrm{MeV})$, $\tau \simeq 250\,\mu\mathrm{s}$	CC	1.8	$9.5(E_\nu - 1.29\,\mathrm{MeV})^2$
$\nu_\mathrm{e} + {}^{12}\mathrm{C} \to \mathrm{e}^- + {}^{12}\mathrm{N}$ ${}^{12}\mathrm{N}$: β^+, $\tau = 11.0\,\mathrm{ms}$	CC	17.34	28.7 at 20 MeV
$\bar{\nu}_\mathrm{e} + {}^{12}\mathrm{C} \to \mathrm{e}^+ + {}^{12}\mathrm{B}$ ${}^{12}\mathrm{B}$: β^-, $\tau = 20.2\,\mathrm{ms}$	CC	13.37	71.1 at 20 MeV
$\nu + {}^{12}\mathrm{C} \to \nu + {}^{12}\mathrm{C}^*$ $\bar{\nu} + {}^{12}\mathrm{C} \to \bar{\nu} + {}^{12}\mathrm{C}^*$ ${}^{12}\mathrm{C}^* : \gamma$	NC NC	15.11 15.11	30.2 at 20 MeV 27.9 at 20 MeV
$\nu_\mathrm{e} + {}^{13}\mathrm{C} \to \mathrm{e}^- + {}^{13}\mathrm{N}$ ${}^{13}\mathrm{N}$: β^+, $\tau = 862\,\mathrm{s}$	CC	2.22	85.7 at $\langle E_{{}^8\mathrm{B}} \rangle$
$\nu + {}^{13}\mathrm{C} \to \nu + {}^{13}\mathrm{C}^*$ ${}^{13}\mathrm{C}^* : \gamma$	NC	3.68	11.5 at $\langle E_{{}^8\mathrm{B}} \rangle$

Table 2.1: Cross sections of neutrino detection channels in liquid scintillators with applying weak current, energy threshold, and possible follow-up reactions. All energies are given in MeV. The index x represents both μ and τ type neutrinos. In the reaction column, τ denotes the decay time of a follow-up reaction and the neutron capture time in case of the inverse β decay. $\langle E_{{}^8\mathrm{B}} \rangle$ refers to the respective cross section averaged over the ^{8}B neutrino spectrum. Values are taken from [80, 119, 120, 121, 122].

SN neutrinos. Thus, the elastic scattering off protons offers a possibility to deeply explore the SN ν_x spectra [121].

2.2.2 Inverse β Decay

The inverse β decay (IBD)

$$\bar{\nu}_\mathrm{e} + \mathrm{p} \to \mathrm{e}^+ + \mathrm{n} \tag{2.7}$$

is the main detection channel for $\bar{\nu}_\mathrm{e}$ in liquid scintillators due to its comparably large cross section at low energies as listed in table 2.1. It further provides a distinct signature allowing an unambiguous identification of $\bar{\nu}_\mathrm{e}$ signals.

Due to the kinematics of the IBD, the positron receives almost the entire energy of the $\overline{\nu}_{\mathrm{e}}$ and the neutron's kinetic energy is negligible in most of the cases [123]. Thus, the kinetic energy of the positron is closely linked to the energy of the initial $\overline{\nu}_{\mathrm{e}}$ and may be approximated as

$$E_{\mathrm{kin}}(\mathrm{e}^{+}) = E_{\nu} - Q_{\mathrm{IBD}} \tag{2.8}$$

with $Q_{\mathrm{IBD}} = 1.8\,\mathrm{MeV}$ the energy threshold of the IBD. After depositing its kinetic energy, the positron is stopped and annihilates with an electron under the emission of two 511 keV γ rays. Since these two γ rays add to the scintillation light output of the positron thermalization, the eventually visible energy of the positron and the $\overline{\nu}_{\mathrm{e}}$ energy are connected as [124]

$$E_{\nu} = E_{\mathrm{vis}} + 0.782\,\mathrm{MeV}. \tag{2.9}$$

While the positron deposits its energy promptly, the neutron is thermalized in scattering interactions off protons and carbon nuclei. However, due to the, usually, low energy of the neutron and the quenching of the proton signals, the thermalization of the neutron is mostly not recognizable in the detector. After a scintillator dependent capture time of $\sim 250\,\mu\mathrm{s}$, the neutron is captured in $\sim 99\%$ of the cases on a free proton for a typical scintillator mixture [62]. The capture is followed by the release of the deuteron binding energy in form of a 2.2 MeV γ ray. In $\sim 1\%$ of the cases, the neutron is captured on ^{12}C and in the deexcitation of the ^{13}C nucleus, a total γ ray energy of 4.95 MeV is released [62]. This temporal and spatial coincidence between the prompt signal and the delayed 2.2 MeV or 4.95 MeV γ ray signal offers a clear signature and a strong facility of background suppression. Due to the relatively low energy of the γ ray released after a neutron capture on hydrogen that is below the experimental threshold of the currently running Water Čerenkov detectors, this signature cannot be used at this type of detectors up to now. Lowering the experimental threshold with an increased optical coverage or adding atoms with a high neutron capture cross section followed by a higher energy emission in the deexcitation process may be possibilities to harness this interaction channel also in Water Čerenkov detectors. A proclaimed candidate for such a neutron catcher is gadolinium in the deexcitation of which a γ ray cascade with a total energy of 8 MeV may be observed [125, 126]. These neutron catchers and especially gadolinium can also be used in liquid scintillator detectors to enhance the IBD detection efficiency [127].
Since the positron is usually emitted in the forward direction, the IBD provides an information on the direction of the neutrino that can be extracted by the deformation of the Čerenkov cone in Water Čerenkov detectors. For liquid scintillators, the direction cannot be analyzed on an event-by-event basis. However, the relative positions of the promptly annihilating positrons and the captured neutrons still

offer the possibility to obtain an information on the position of a source causing a sufficient amount of $\bar{\nu}_e$ events in the detector.
As the main channel of $\bar{\nu}_e$ detection, the IBD is especially used to explore reactor neutrinos [128], SN neutrinos [56], and geo-neutrinos [124].

2.2.3 Reactions on Carbon

As shown in table 2.1, ^{12}C offers two CC and one NC channel for neutrino interactions that provide accessible signatures. Since the thresholds of the reactions are mostly around 15 MeV, these channels only play a minor role for the detection of low-energetic neutrinos but may be used for the observation of higher-energetic neutrinos like SN or atmospheric neutrinos.
Especially the two CC reactions, via which only ν_e and $\bar{\nu}_e$ can interact, provide clear coincidences after the neutrino capture that initiates a prompt $e^{+/-}$ signal. This is followed by a delayed β decay of the produced unstable daughter nuclei. However, due to the endpoints of the ^{12}N β^+ decay and the ^{12}B β^- decay and their respective decay times of 11.0 ms and 20.2 ms being very close to each other, it is experimentally very challenging to disentangle both contributions and obtain an information on the initial neutrino type. The NC reaction that is possible for all neutrino flavors, inelastic scattering of a neutrino off a ^{12}C nucleus, leads to an excited ^{12}C nucleus that deexcites via the emission of a 15.11 MeV γ ray. Besides this signature of the reaction having occurred, no spectroscopic or flavor information may be obtained.
Also ^{13}C offers a CC and a NC neutrino interaction channel. With a natural abundance of 1.1% of ^{13}C, the interaction rate in liquid scintillators is very small, though [80]. However, due to the small energy thresholds of 2.2 MeV for the ν_e CC reaction and 3.7 MeV for the inelastic NC neutrino scattering as well as the delayed coincidence with the subsequent ^{13}N β^+ decay for the CC reaction, these reactions still offer possibilities for the solar ^{8}B and SN ν_e detection, especially in extremely large detectors [122].
Besides these reactions, several elastic scattering NC reactions of high-energetic neutrinos on ^{12}C exist in which one or more neutrons are liberated from the nucleus. Since these neutrons may fake an IBD signal, such NC reactions of atmospheric neutrinos impose a major background for the DSNB detection in liquid scintillators as detailed in chapter 7.

2.3 Background Sources

Due to the small cross sections of neutrino interactions, the expected signal in searches for these particles is very weak. Hence, a low background level is essential

for a successful observation. This requires to suppress the residual radioactivity in the surroundings of the detector, in the supporting structure in which the detector is built, in the PMTs, and in the target material itself to a minimum level. As has been mentioned, techniques like distillation, water extraction, gas stripping, and filtration allow to purify liquid scintillators and remove contaminations [114].
To minimize backgrounds caused by cosmic radiation, neutrino detectors are usually built deep underground. While the electromagnetic component of cosmic showers is already absorbed in the rock coverage for the relevant depths at which neutrino detectors are usually constructed, high-energetic muons may still reach the detectors. These cosmic muons may either cause a background signal themselves or, which is even more challenging to suppress, produce potentially long-lived radioactive isotopes in spallation processes inside the liquid scintillator. Further, muons passing through the surroundings of a detector may produce fast neutrons that can enter the detector and mimic an IBD interaction without the possibility to correlate them to the undetected muon.

2.3.1 Intrinsic Background

With the composition of liquid scintillators as hydrocarbons, long-lived radioactive carbon or hydrogen isotopes constitute a source of background intrinsic to even extremely pure scintillators without any ulterior contamination. The only isotope to consider is the atmospherically produced ^{14}C with an endpoint of 156 keV and a half-life of $5,730$ yr [129]. Due to its production in the atmosphere, it is only integrated in living materials and the abundance of this isotope is significantly lower in petroleum, which is developed naturally in processes taking much longer than the ^{14}C decay time. With the usage of petroleum derivates as the solvents of liquid scintillators, this background can be kept at a minimum. However, due to the large target masses necessary for neutrino detectors, the ^{14}C β^- decay will still dominate the event rate and preclude the detection of neutrinos with energies below the endpoint of the decay [9].
Besides this background intrinsic even to a perfectly produced scintillator, radioactive contaminations may enter the scintillator during its production, transport, or storage. While the production processes can usually be kept very clean, surface contaminations of the transport, filling, or storage utilities that are very hard to avoid completely can enter the scintillator via diffusion and, mainly, convection. These surface contaminants may be the initial ^{238}U and ^{232}Th nuclides of the uranium and thorium chains with extremely long half-lifes of 4.468×10^9 yr and 1.405×10^{10} yr [129], respectively, or long-lived radio-isotopes being produced later in the decay chains like ^{210}Pb or ^{210}Po. The major intrinsic background components with their respective half-lifes, decay modes, and endpoint energies as given in [129] are listed in table 2.2.

Isotope	$T_{1/2}$	Decay Mode	$E_{\max}$ [keV]
^{14}C	5,730 yr	β^-	157
^{40}K	1.3 Gyr	β^-(89%)	1,311
		β^+(11%)	1,505
^{85}Kr	10.8 yr	β^-	687
^{222}Rn	3.8 d	α	5,590
^{210}Pb	22.3 yr	β^-	64
^{210}Bi	5.0 d	β^-	1,162
^{210}Po	138.4 d	α	5,408
^{208}Tl	3.1 min	β^-	5,001
^{212}Bi	60.6 min	β^-(64%)	2,254
		α (36%)	6,207
^{212}Po	0.3 μs	α	8,954
^{214}Pb	26.8 min	β^-	1,024
^{214}Bi	19.9 min	β^-	3,272
^{214}Po	164.3 μs	α	7,833

Table 2.2: Intrinsic radioactive background components in liquid scintillators together with their half-lifes, decay modes, and endpoint energies. The α particles are emitted at fixed energies. Values are taken from [129].

Even while great care is taken during the transport and filling of the scintillator and the storage structure is kept extremely clean, small amounts of radioactivity cannot be prevented from entering the scintillator liquid. However, fast coincidences of subsequent decays and the pulse shape discrimination method still offer possibilities to suppress a part of this background. Since α particles are emitted at a distinct energy for a given α decaying nucleus, they are clearly visible as prominent lines in the energy spectrum. Even though these particles are emitted at energies of several MeV, they are detected at visible energies corresponding to low energy neutrino interactions due to the quenching effect. Thus, α decays constitute a major background for analyses of low-energetic neutrinos. However, since α particles are heavier ionizing than electrons at the relevant energies, the population of triplet states in the excited molecules is preferred as described in section 2.1.2. This leads to a stronger contribution of the slow component of the luminescence allowing to distinguish the α pulses from electron pulses. Additionally, the α decays allow to suppress some of the β emitters if they occur in a decay chain as in the case of the fast ^{214}Bi-^{214}Po coincidence. The temporal and spatial coincidence of an energy deposition and a following deposition at the quenched α energy together with the pulse shape information allow to suppress both back-

ground contributions. However, the half-life of the α emitter needs to be small to make the coincidence unambiguous.
Besides the contaminations from surfaces in contact with the scintillator, radioactive noble gases like radon or krypton may diffuse into the scintillator. To prevent this, liquid scintillators are usually kept in airtight closures and tanks are prefilled with nitrogen before the scintillator enters. However, air leaks or impurities of the utilized nitrogen may cause contaminations. While radon quickly decays into longer-living nuclei of the U/Th decay chains like Po, Bi, and Pb that partly can be discriminated, the only possibility to identify krypton decays is via fast $\beta - \gamma$ coincidences at low energies. However, due to the small branching ratio for this coincidence of $B = 0.43\%$, the suppression of this background is extremely challenging [9].
Apart from the radioactive nuclei integrated in the scintillator liquid, also radioactive contaminations of the surroundings may enter the scintillator and cause a signal. Especially γ rays as uncharged particles may penetrate several meters of the scintillator liquid before being absorbed and can induce multiple energy depositions via Compton scatterings on their path. ^{40}K that is contained in the glass of PMTs constitutes a major source of this external background, which may be suppressed by shielding layers of Z rich materials, water, or scintillators doped with diluters around a fiducial volume.

2.3.2 Cosmic Muons

As has been mentioned in section 1.4.4, charged pions and kaons that are part of the hadronic showers produced in interactions between the primary cosmic radiation and nuclei of the atmosphere decay into muons via

$$\pi^{+/(-)} \rightarrow \mu^{+/(-)} + {}^{(}\overline{\nu}_{\mu}^{)} \tag{2.10}$$

and

$$\mathrm{K}^{+/(-)} \rightarrow \mu^{+/(-)} + {}^{(}\overline{\nu}_{\mu}^{)}. \tag{2.11}$$

Due to the relatively long lifetime of these muons of $\tau = 2.2\,\mu$s, the time dilation, and the small cross sections for interactions with matter, cosmic muons reach the Earth at a rate of $(180 \pm 20)\,\mathrm{m}^{-2}\mathrm{s}^{-1}$ [130]. The energy spectrum resembles the power law spectrum of the primary cosmic rays described by equation 1.27 since the energy of the produced muon is closely related to the energy of the initial primary cosmic ray particle. The spectral index of the muon energy spectrum has been measured by the LVD experiment to be $\gamma_{\mu} = 1.78 \pm 0.05$ [131].
For neutrino detectors located deep underground, the hadronic and electromagnetic components of the cosmic radiation are absorbed in the rock overburden.

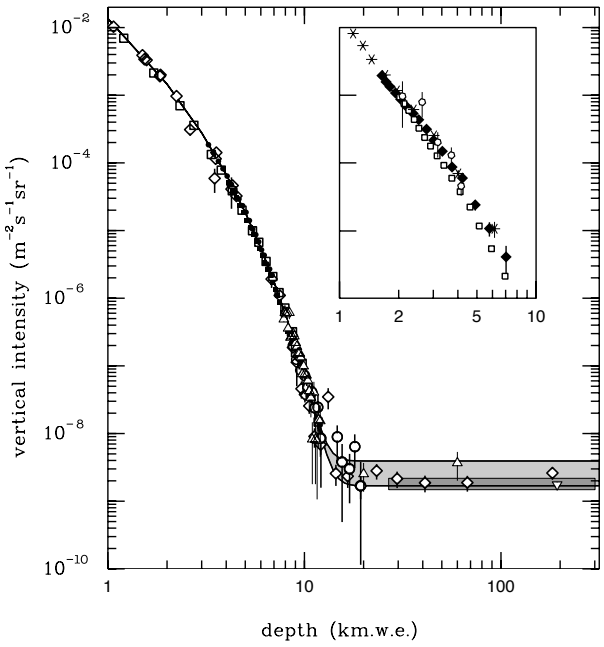

Figure 2.2: Depth dependent residual cosmic muon flux. Due to the higher rock coverage, more muons get absorbed and the intensity decreases with depth. The inlet shows measurements in ice. The figure is taken from [7], data points from references therein.

However, muons possessing sufficient energy may penetrate the rock and eventually reach the detectors due to the small ionization loss of $\sim (2\rho)\,\mathrm{MeV/cm}$ in a material of the density ρ in g/cm^3 [132] and a residual muon flux may be observed. For muons above a threshold energy of $\epsilon = 500\,\mathrm{GeV}$, the constant ionization loss becomes subdominant to losses via fluctuating radiation processes like pair production, bremsstrahlung, and nuclear interactions [79]. As has been shown by Monte Carlo simulations, a cosmic muon flux may still be observed at 10^4 meters water equivalent (m we) [133]. Figure 2.2, taken from [7], shows the depth dependent muon intensity in $\mathrm{m^{-2}s^{-1}sr^{-1}}$. With increasing depth, more muons are absorbed in the overburden of a detector and the flux of cosmic muons decreases. Eventually, for depths $\gtrsim 10\,\mathrm{km\,we}$, the muon intensity reaches a plateau and only muons produced in CC interactions of atmospheric ν_μ may be observed while all cosmic muons are absorbed. The inlet of figure 2.2 shows data from measurements in ice. For a more detailed derivation of the muon spectrum and the intensity underground, refer to section 4.1.1.
Besides the flux, also the energy spectrum of cosmic muons changes with depth. Due to the linear energy loss caused by ionization, the low-energetic part of the

muons is absorbed already at smaller depths. Thus, the mean muon energy rises continuously with the depth as long as it remains smaller than the critical energy ϵ. Muons with higher energies than ϵ lose high amounts of energy via radiative processes and the high-energetic part of the initial muon spectrum is depopulated during the passage through matter. Thus, the mean energy of the muons will rise with increasing depth and converge towards the critical energy ϵ [79].
A cosmic muon passing through a liquid scintillator deep underground deposits a huge amount of energy due to the ionization loss. Thus, the background arising directly from prompt muon signals does usually not influence analyses of neutrinos at low energies. However, in case the muon only grazes the scintillator or only crosses a part of the scintillator that is doped with a diluter such that the scintillation light output is reduced, visible energies similar to neutrino interactions might result. Further, muons may create radioactive isotopes with decay products in the energy range of usual neutrino searches via spallation processes in the scintillator. Since the identification of these background events often requires their correlation to the parent muon, many neutrino detectors use active muon vetos to enhance the muon identification efficiency.
Also the angular distribution of cosmic muons arriving at an underground detector depends on the depth and the shape of the rock coverage. While the zenith angle distribution of muons at the surface follows a $\cos^2(\theta)$ dependence, muons arriving from angles that correspond to increased rock coverages are stronger suppressed at underground sites. Thus, for a flat overburden, most of the muons arrive from vertically above following the shortest path through the rock. Since the Borexino detector is located at the Laboratori Nazionali del Gran Sasso (LNGS) under a mountain ridge, the coverage of $3,800\,\mathrm{m}$ we for muons arriving from straight above is reduced for higher zenith angles due to the steep mountain flanks and significant contributions to the muon flux from non-vertical directions result. This leads to an increased flux compared to an experimental site of the same vertical depth but with a flat coverage. As presented in section 4.2, the cosmic muon flux at the LNGS was measured to be $(3.432 \pm 0.001) \times 10^{-4}\,\mathrm{m^{-2}s^{-1}}$ using ten years of Borexino data. The mean muon energy at the LNGS was measured as $(270 \pm 3_{\mathrm{stat}} \pm 18_{\mathrm{syst}})\,\mathrm{GeV}$ by the MACRO experiment [134]. Further, the topology of the mountain ridge is mirrored in the azimuth angle distribution of cosmic muons [80].

2.3.3 Cosmogenic Radio-Isotopes

Besides the direct signal muons create in the scintillator, radioactive isotopes may be produced in spallation processes of cosmic muons. In these processes, one or several nucleons are liberated from a nucleus of the scintillator material and unstable isotopes may be generated. Additionally, particle showers may emerge that can produce further radioactive isotopes. Due to their production by cosmic muons,

these radio-isotopes are referred to as cosmogenic.
The production rate R of a certain cosmogenic radio-isotope is determined by the energy dependent cross section for its production $\sigma(E)$, the energy and depth dependent flux of cosmic muons $\Phi_\mu(E, D)$, and the number of target nuclei N_t. Since liquid scintillators are composed of hydrocarbons, the target basically consists of carbon nuclei with the most abundant isotope being ^{12}C. N_t, thus, refers to the number of ^{12}C nuclei in the target. Since the energy of the muons may be approximated by their depth dependent mean energy $\langle E_\mu \rangle(D)$ [135], the dependence of the muon flux reduces to the depth and the cross section may be evaluated at the corresponding mean muon energy. Thus, also the production rate reduces to the solely depth dependent expression

$$R(D) = \Phi_\mu(D) N_\mathrm{t} \sigma(\langle E_\mu \rangle(D)) = \Phi_\mu(D) N_\mathrm{t} \sigma_0 \left[\langle E_\mu \rangle(D)\right]^\alpha . \tag{2.12}$$

On the right side of this equation, the depth dependence of the production cross section is expressed as an exponential of the mean muon energy with an exponent α multiplied with a constant cross section σ_0. The values of α have been determined for different radio-isotopes at the NA54 experiment at CERN [136]. In this experiment, a liquid scintillator sample has been placed in a muon beam and the cross section for the production of different nuclei was measured. To explore the depth dependence of the production rate, the energy of the muon beam was altered. Table 2.3 lists the isotopes that were analyzed in [136] together with their half-lifes, decay modes, maximum decay energies, the rate calculated in [136] for the depth of the LNGS, and the measured value of α. This value also allows to extrapolate the rate to different depths and other underground laboratories.
The most dangerous cosmogenic isotopes for neutrino searches are the β^+ emitters ^{10}C and ^{11}C due to their relatively long lifetimes and high production rates. Further, the $\beta -$ n emitters ^{9}Li and ^{8}He can mimic an IBD signal and impose an important background for $\bar{\nu}_\mathrm{e}$ spectroscopy. Besides the isotopes listed in table 2.3, several short-lived radio-isotopes may be produced cosmogenically [137]. However, due to their short lifetimes, they may easily be vetoed by blinding the detector for several half-lifes after the passage of a muon without introducing an inacceptable deadtime. To rely on this technique, a highly efficient identification of cosmic muons is mandatory to any neutrino experiment.
Since ^{10}C and ^{11}C are both β^+ emitters, the energy of the positron annihilation adds to the visible energy deposition. Thus, the ^{11}C decay results in an energy deposition equivalent to neutrino interactions of $(1 - 2)\,$MeV and it becomes the main background for solar pep and CNO neutrino measurements. In the case of ^{10}C, also a $0.72\,$MeV deexcitation γ ray needs to be considered and the visible energy ranges from $1.7\,$MeV up to $3.6\,$MeV, interfering with a part of the solar ^{8}B neutrino spectrum [80].
Since most of these cosmogenic carbon isotopes are produced by muons knocking

Isotope	$T_{1/2}$	Decay Mode	$E_{\max}$ [MeV]	Rate [$\mathrm{d}^{-1}\,100\mathrm{t}^{-1}$]	α
^{7}Be	53.3 d	β^+	0.48	0.34 ± 0.04	0.93 ± 0.23
^{10}C	19.3 s	$\beta^+\gamma$	2.9 + 0.72	2.0 ± 0.2	0.62 ± 0.22
^{11}Be	13.8 s	β^-	11.5	< 0.034	
^{11}C	20.4 min	β^+	1.98	14.5 ± 1.5	0.70 ± 0.16
^{8}He	0.12 s	β^-n	10.7	0.034 ± 0.007	
^{9}Li	0.18 s	β^-n	13.6		

Table 2.3: Production rates of cosmogenic radio-isotopes in interactions between cosmic muons and nuclei of the liquid scintillator target. The respective half-lifes, decay modes, maximum energies of the decays, and the measured exponent α of the energy dependent production cross section as defined by equation 2.12 are listed additionally [136]. While the given values of the production rates refer to the depth of the LNGS where the Borexino experiment is situated, the exponent α allows to extrapolate the result to different depths and underground laboratories.

out one or two neutrons of a ^{12}C nucleus, the coincidence between the actual decay, the passage of a cosmic muon, and the neutron capture on hydrogen accompanied by the release of the deuteron binding energy of 2.2 MeV may be used to partially suppress this background. Due to the cosmic muon rate at typical depths of neutrino detectors being small compared to the neutron capture time of $\sim 250\,\mu$s in liquid scintillators [62], the association of the neutron capture to a muon is mostly unambiguous. Besides the temporal correlation, also the spatial correlation between the muon, the carbon decay, and the neutron capture may be used. The carbon isotopes are produced on the muon track and the neutron travels only a short distance before being captured. The background arising from those isotopes may be reduced significantly by vetoing the intersection of a sphere around the neutron capture point and a cylinder around the muon track for several half-lifes of the relevant isotopes. The radius of the sphere around the neutron capture point needs to be defined considering the neutron's mean free path. This so-called Threefold Coincidence technique [138], thus, also relies on the muon identification efficiency and tracking capabilities of the detector as well as a sufficiently good position reconstruction of the neutron capture events. The deadtime induced by this veto can be kept at a minimum by applying appropriate radii to the cylinder around the muon track and the sphere around the neutron capture point and only vetoing the relevant intersection region [80].
Besides the knock-out of neutrons, also protons may be knocked out of the ^{12}C nucleus producing neutron rich radio-isotopes that decay via β^- decays. For ^{9}Li and ^{8}He, the decay may lead to an excited state of the daughter nucleus that deexcites

via neutron emission. Since the deexcitation is mediated by strong interactions, the neutron is emitted instantaneously but thermalizes without leaving a visible signal due to its low energy. Only the γ ray emitted after the neutron capture may be registered. The coincidence of the first β^- decay and the neutron capture may mistakenly be considered as an IBD event caused by the interaction of an $\bar{\nu}_e$ [124]. In case of the population of an excited state, the endpoints of the β decays of the cosmogenic radio-isotopes are reduced to 7.4 MeV and 11.2 MeV for ^{8}He and ^{9}Li, respectively. In principle, this background may be strongly suppressed by applying a ~ 1 s veto to the detector after the passage of a muon in $\bar{\nu}_e$ analyses. However, depending on the rate of cosmic muons, this approach potentially introduces a large deadtime, such that it is advisable to only veto a certain part of the detector around a muon track if a muon tracking can be provided [80].

2.3.4 Fast Neutrons

A significant amount of the energy of cosmic muons may be transferred to neutrons that are knocked out of nuclei. Due to the high kinetic energy up to ~GeV and the lack of electromagnetic charge, these neutrons may travel several meters before interacting or being stopped [135]. Thus, such so-called fast neutrons may even reach the detector when they are produced in the surrounding rock where the detection of the parent muon is not possible. Even though the production of fast neutrons is often accompanied by the evolution of hadronic showers and the neutron itself can produce charged particles that can be detected in an active muon veto, it is still possible that fast neutrons enter the scintillator liquid without being recognized before. Through the transfer of its kinetic energy to recoil protons, the fast neutron may produce a prompt signal and with the release of the delayed 2.2 MeV γ ray following the eventual capture of the neutron on hydrogen, the IBD signature is mimicked. Thus, fast neutrons may constitute a background for $\bar{\nu}_e$ analyses at various energies.

2.4 The Jiangmen Underground Neutrino Observatory

The Jiangmen Underground Neutrino Observatory (JUNO) is a multipurpose neutrino oscillation experiment currently under construction. With a large target mass of 20 kt, it is mainly designed to perform a high statistics measurement of reactor $\bar{\nu}_e$ generated at the near by nuclear power plants Yangjiang and Taishan to reveal the neutrino mass hierarchy. The large target mass and the aimed at unprecedented energy resolution of 3% at a visible energy of 1 MeV are expected to seek this experiment as a new state of the art liquid scintillator neutrino experiment.

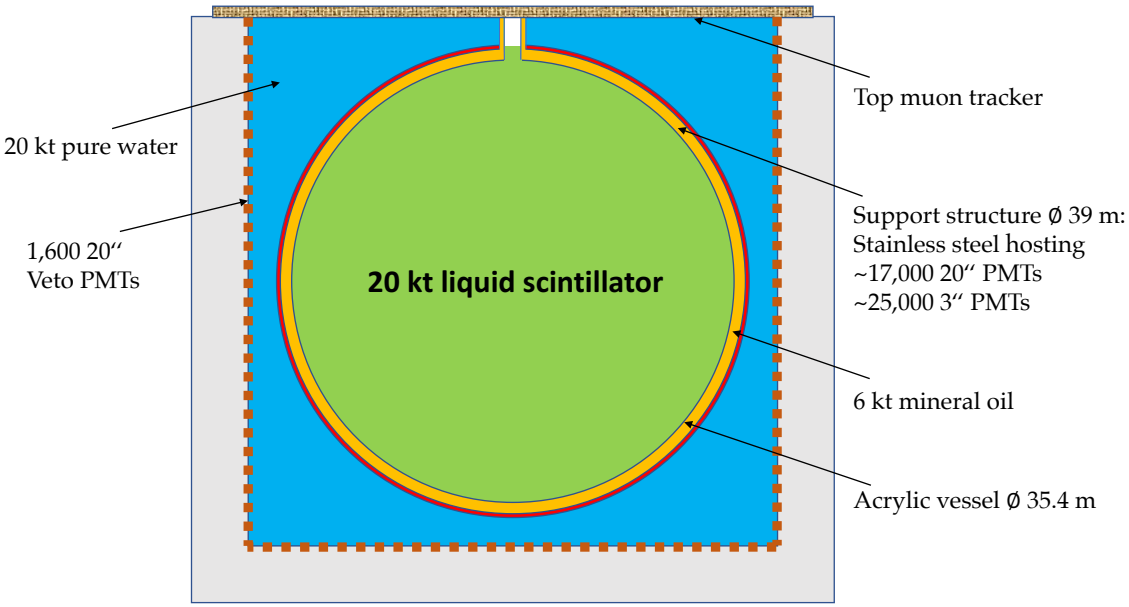

Figure 2.3: Conceptional drawing of the JUNO detector based on [68].

In the construction and operation of the experiment, the experiences and technical developments obtained at the Borexino detector and further currently running liquid scintillator experiments may be bundled to enable a rich physics program. Besides revealing the mass hierarchy, precision measurements of solar neutrinos and the detection of the DSNB are planned to be accomplished with this detector.

2.4.1 Detector Concept

The JUNO experiment will be constructed in Jiangmin, Kaiping, in southern China with a baseline of $\sim 52\,\mathrm{km}$ to the two nuclear power plants Yangjiang and Taishan that generate $\bar{\nu}_\mathrm{e}$ in ten nuclear cores with a total thermal power of $\sim 36\,\mathrm{GW}$ [139]. Futher, a non-negligible contribution of $\bar{\nu}_\mathrm{e}$ from the Daya Bay and Huizhou reactor cores at a distance of about $200\,\mathrm{km}$ needs to be considered [140]. To reduce the backgrounds arising from cosmic muons, the JUNO detector is constructed in a newly built underground laboratory with a total rock overburden of $\sim 700\,\mathrm{m}$ corresponding to $\sim 1,900\,\mathrm{m\,we}$. This leaves an expected muon rate of $0.003\,\mathrm{Hz\,m^{-2}}$ with a mean energy of $215\,\mathrm{GeV}$ at the experimental site [68].
Figure 2.3 shows a conceptional drawing of the JUNO detector based on [68]. The $20\,\mathrm{kt}$ of liquid scintillator will be contained in an acrylic sphere with a diameter of $35.4\,\mathrm{m}$ and a thickness of $120\,\mathrm{mm}$. As the scintillator solvent, linear alkylbenzene

Experiment	Daya Bay	Borexino	KamLAND	JUNO
Liquid scintillator mass	20 t	~ 300 t	~ 1 kt	20 kt
Optical coverage	$\sim 12\%$	$\sim 34\%$	$\sim 34\%$	$\sim 80\%$
Energy resolution	$\frac{7.5\%}{\sqrt{E\,[\mathrm{MeV}]}}$	$\frac{\sim 5\%}{\sqrt{E\,[\mathrm{MeV}]}}$	$\frac{\sim 6\%}{\sqrt{E\,[\mathrm{MeV}]}}$	$\frac{\sim 3\%}{\sqrt{E\,[\mathrm{MeV}]}}$
Light yield	$\sim 160 \frac{\mathrm{p.e.}}{\mathrm{MeV}}$	$\sim 500 \frac{\mathrm{p.e.}}{\mathrm{MeV}}$	$\sim 250 \frac{\mathrm{p.e.}}{\mathrm{MeV}}$	$\sim 1200 \frac{\mathrm{p.e.}}{\mathrm{MeV}}$

Table 2.4: Comparison of technical parameters of JUNO to current liquid scintillator experiments [140].

(LAB) is chosen due to its good transparency, high flash point, low chemical reactivity, and excellent light yield. Two solutes will be added to the scintillator as wavelength shifters, 2,5-Dyphenyloxazole (PPO) at a concentration of 3 g/l and p-bis(O-methylstyril)-benzene (bis-MSB) at a concentration of 15 mg/l. The acrylic sphere will be surrounded by a spherical stainless steel supporting structure with a diameter of 39 m. On this structure, 17,000 20″ PMTs and 25,000 additional 3″ PMTs are planned to be mounted. This double calorimetry structure guarantees an excellent event reconstruction due to an optical coverage of $\sim 80\%$. The PMTs are aimed to provide a high quantum efficiency of $\sim 30\%$. With the design goal of $\sim$ 1,200 photoelectrons per MeV, the unprecedented energy resolution of $\sim 3\%/\sqrt{E\,[\mathrm{MeV}]}$ is feasible [140]. To achieve the necessary light attenuation length of ≥ 20 m and to avoid radioactive contaminations in the target volume, the scintillator will have to be cleaned in several steps. Table 2.4 lists the main technical parameters of the JUNO design compared to current state of the art liquid scintillator neutrino detectors [140]. As can be seen, huge advancements concerning the detector performance are planned to be achieved in JUNO.
The central JUNO detector will be encompassed by a cylindrical water tank such that at least 2 m of water protect the scintillator target from radioactivity of the surrounding rock. Instrumented with $\sim$ 1,600 20″ PMTs, the water tank will be used as an active Water Čerenkov muon veto with an expected efficiency similar to the Daya Bay Water Čerenkov detector of 99.8% [68]. Further, a muon tracker composed of plastic scintillator strips decommisioned from the OPERA experiment [141] will be placed on top of the water tank to increase the muon identification efficiency and provide a precise tracking of penetrating muons. The start of data taking is scheduled for 2021.

2.4.2 Physics Program

With the huge technical advancements planned for the JUNO experiment, a broad physics program is feasible. Besides the main goal of the determination of the neutrino mass hierarchy, results on solar neutrinos, SN neutrinos, the first observation

of DSNB neutrinos, and a measurement of geo-neutrinos are planned.

Determination of the Neutrino Mass Hierarchy and Oscillation Parameters

To determine the neutrino mass hierarchy, oscillations of the reactor $\bar{\nu}_e$ arriving from the two nuclear power plants Yangjiang and Taishan will be analyzed. The $\bar{\nu}_e$ will be detected via the IBD as described in section 2.2.2 with the neutron capture mainly occurring on hydrogen after a mean capture time of $\sim 200\,\mu$s [68].
The $\bar{\nu}_e$ survival probability can be expressed as [140]

$$\begin{aligned} P_{ee} &= 1 - \cos^4(\theta_{13})\sin^2(2\theta_{12})\sin^2\left(\frac{\Delta m^2_{21}L}{4E}\right) \\ &\quad - \sin^2(2\theta_{13})\left(\cos^2(\theta_{12})\sin^2\left(\frac{\Delta m^2_{31}L}{4E}\right) + \sin^2(\theta_{12})\sin^2\left(\frac{\Delta m^2_{32}L}{4E}\right)\right) \\ &= 1 - \cos^4(\theta_{13})\sin^2(2\theta_{12})\sin^2\left(\frac{\Delta m^2_{21}L}{4E}\right) - P_{\mathrm{MH}}. \end{aligned} \tag{2.13}$$

Here, P_{MH} denotes a mass hierarchy dependent term contributing to the survival probability that can be expanded as

$$P_{\mathrm{MH}} = \frac{1}{2}\sin^2(2\theta_{13})\left(1 - \sqrt{1 - \sin^2(2\theta_{12})\sin^2\left(\frac{\Delta m^2_{21}L}{4E}\right)}\cos\left(2\left|\frac{\Delta m^2_{ee}L}{4E}\right| \pm \phi\right)\right) \tag{2.14}$$

with $\Delta m^2_{ee} = \cos^2(\theta_{12})\Delta m^2_{31} + \sin^2(\theta_{12})\Delta m^2_{32}$. The phase ϕ depends on the mass and mixing parameters of the first two mass eigenstates with details on the calculation given in [68]. Since this phase has a positive sign for normal hierarchy (NH) and a negative sign for inverted hierarchy (IH), the actual neutrino mass hierarchy influences the phase of the measured neutrino survival probability. Figure 2.4 shows the expected $\bar{\nu}_e$ spectrum without oscillations at the JUNO detector in red and the oscillated spectra for NH in blue and IH in green taken from [142]. The unoscillated $\bar{\nu}_e$ spectrum gets firstly suppressed due to the mixing of the first two neutrino mass eigenstates. Further, the spectrum is overlaid by smaller oscillations due to the mixing angle θ_{13} and the effect of the phase difference depending on the mass hierarchy is visible.
Backgrounds to the determination of the mass hierarchy arise due to events mimicking the IBD coincidence signature. These are mainly accidental coincidences, cosmogenically produced ^{8}He and ^{9}Li as described in section 2.3.3, fast neutrons as described in section 2.3.4, $^{13}\mathrm{C}(\alpha, \mathrm{n})^{16}\mathrm{O}$ reactions, and geo-neutrino IBD interactions. In order to suppress these backgrounds, the temporal and spatial cuts between a prompt and a delayed signal must be tuned and the detector should

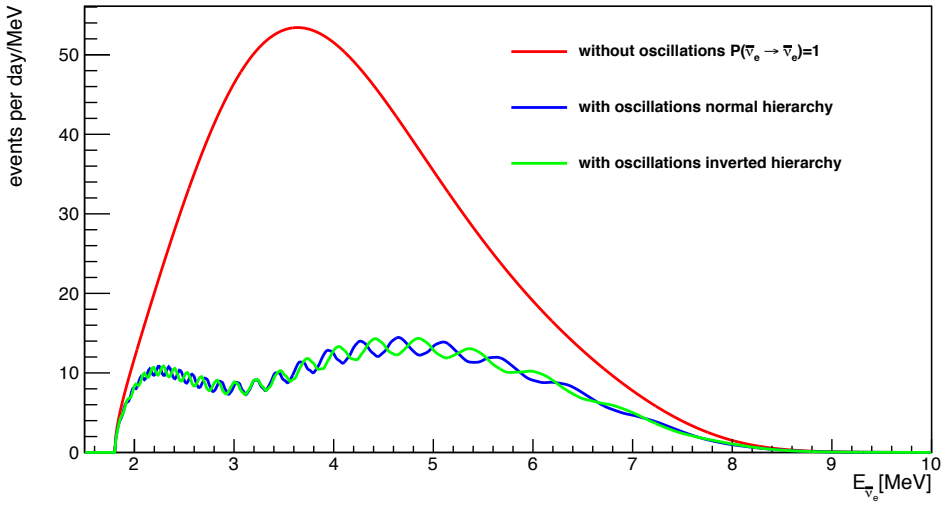

Figure 2.4: Expected $\bar{\nu}_e$ spectrum at JUNO. The spectrum without oscillations is depicted in red, the oscillated spectrum for NH in blue, and the oscillated spectrum for IH in green.

be vetoed for several lifetimes of the neutron unstable cosmogenic radio-isotopes around a muon track. After the application of such cuts, 60 IBD events per day of which 3.8 are caused by backgrounds are expected in JUNO [68]. Performing a Fourier analysis of the reactor $\bar{\nu}_e$ spectrum, the neutrino mass hierarchy is expected be measured with a $\sim 3\sigma$ accuracy after acquiring data for six years [68]. Thus, especially through the combination of the JUNO results with complementary measurements of, e.g., the PINGU experiment [143] that may investigate the neutrino mass hierarchy using atmospheric neutrino data, this fundamental parameter of neutrino physics will be precisely determined in the near future.
Besides this, the excellent energy resolution of the JUNO detector will allow to significantly improve the precision of Δm^2_{12}, Δm^2_{32}, and $\sin^2\theta_{12}$ to the sub-percent level, which requires knowledge of the mass hierarchy in the case of Δm^2_{32}. Together with the expected improved measurement of $\sin^2\theta_{13}$ to 4% accuracy by the Daya Bay experiment, the unitarity of the neutrino mixing matrix can be tested at the 1% level [144]. Any deviation from unitarity is considered to be a hint towards new physics, such as the existence of more than three light neutrinos [145]. Further, combining the JUNO results with results from long baseline accelerator neutrino experiments will allow to evaluate all neutrino mixing parameters including the CP-violating phase δ [146].

Solar Neutrinos

With its large target mass and the unprecedented energy resolution, JUNO may also study neutrinos originating from the Sun via the elastic neutrino-electron scattering as described in section 2.2.1. Of major interest, JUNO could provide a high statistics measurement of the solar ^{8}B neutrinos. However, a successful measurement especially of lower-energetic solar neutrinos deeply depends on the actual intrinsic background level [68]. Also the relatively high rate of cosmic muons of $\sim 3\,\mathrm{Hz}$ exacerbates the solar neutrino measurements.
For the minimum requirement of purity that corresponds to a signal to background ratio of approximately 3:1 as in the solar phase of the KamLAND experiment [147], only the ^{7}Be neutrinos can be observed in the JUNO experiment with respect to the low-energetic part of the solar neutrino spectrum [68]. However, the measurement is still challenging since especially the ^{210}Bi background needs to be determined precisely and also the decays of ^{85}Kr, ^{238}U, and ^{40}K contribute non-negligibly in the solar ^{7}Be neutrino range. Despite the comparably high rate of cosmic muons, cosmogenic ^{11}C does not affect the measurement since its β^{+} decay at the minimum produces a 1.022 MeV energy deposition in the detector that can be separated well from the ^{7}Be neutrinos with a maximum visible energy of $E_{\mathrm{max}} = 665\,\mathrm{keV}$.
For a purity level similar to that of Borexino phase I [9], also the pp neutrinos could potentially be observed [68]. In this case, the ^{210}Bi background would be small enough that the pp neutrino flux dominates the energy spectrum between approximately 160 keV and 230 keV. Only the excellent resolution of the JUNO detector would allow to discriminate this signal from the overwhelming ^{14}C background that reaches up to 156 keV. Nevertheless, a good pulse shape discrimination of highly quenched α particles, a clean removal of pile-up events, and a good understanding of low-energetic noise are still mandatory but very challenging. The observation of solar pep and CNO neutrinos is supposed to be extremely difficult with the JUNO detector since the ^{210}Bi decays at low energies and the cosmogenic ^{11}C decays at high energies are expected to strongly overwhelm the neutrino signals [68].
Besides the mentioned prospects for low-energetic solar neutrinos, JUNO will be able to measure the ^{8}B neutrino flux with unprecedented statistics and even with a lowered energy threshold compared to former measurements due to the enlarged photoelectron yield [68]. The main component of intrinsic background for this measurement is caused by the decay of ^{208}Tl with a Q-value of 5 MeV. While this background can in principle be estimated via the coincidence of ^{212}Bi $-^{212}$ Po decays, it is still mandatory to keep the internal ^{232}Th contamination at a level below 10^{-17} g/g to enable an analysis threshold significantly smaller than 5 MeV. The external background will be dominated by 2.6 MeV γ rays of ^{208}Tl decays in the PMTs. However, this background may be easily reduced by applying a fidu-

cial volume cut. Since at least a 5 m cut will be necessary [148], this will demand a reduction of the fiducial mass by more than 50%, though. Above 5 MeV, the most relevant background sources are cosmogenic radio-isotopes such as ^{8}Li, ^{16}N, ^{11}C, ^{10}C, and, most importantly, ^{11}Be [68, 140]. While the shorter-lived isotopes may be suppressed by vetoing a certain volume around a muon track as long as excellent muon identification and tracking are guaranteed, the spectra and rates of the longer-lived isotopes must be measured accurately and subtracted from the accumulated data. Besides the neutrino-electron elastic scattering, also the $\nu_e + {}^{13}C \rightarrow e^- + {}^{13}N$ reaction with a threshold of 2.2 MeV may be used to study the solar ^{8}B neutrino flux [140].
With a high statistics measurement, the JUNO experiment could possibly explore the transition region between the vacuum and matter dominated oscillation regimes and probe the stability of the MSW-LMA solution. As mentioned in section 1.3, probing the survival probability in this energy region allows to investigate many potential hints of new physics. Besides, a precise determination of the solar ^{8}B neutrino flux facilitates to further disentangle the low and high Z Standard Solar Models [140].

Supernova Burst Neutrinos

As described in section 1.4.2, an immense neutrino burst accompanies the core collapse of massive stars. These neutrinos carry valuable information on the environment in which they have been produced and allow to approach many characteristic properties of these particles themselves.
With its large target mass and excellent energy resolution, the JUNO experiment may acquire a high statistics measurement of neutrinos originating from a SN. Table 2.5 lists the expected number of SN neutrino interactions for different detection channels and mean SN neutrino energies for a hypothetical core collapse SN at a distance of 10 kpc [68]. Approximately 5,000 events in the IBD channel, 2,000 events of elastic neutrino-proton scattering, and 300 events of elastic neutrino-electron scattering can be expected within 10 s.
With the exploration of the time evolution of the neutrino signal, the energy spectrum, and the flavor composition, the neutrino-driven explosion mechanism described in section 1.4.2 may be probed. Further, the separation between the prompt and the delayed signal of the IBD reaction allows to statistically determine the direction of the incoming neutrinos. For the estimated number of 5,000 neutrino signals in this channel, an accuracy of 9° may be achieved and astronomers may be pointed to the imminent optical event. This accuracy may be increased by adding the information of additional neutrino detectors [68]. Also a possible correlation between the SN neutrino signal and a gravitational wave may be investigated and used to combine the complementary information of both signals.

Channel	Type	$\langle E_\nu \rangle = 12\,\mathrm{MeV}$	$\langle E_\nu \rangle = 14\,\mathrm{MeV}$	$\langle E_\nu \rangle = 16\,\mathrm{MeV}$
$\bar{\nu}_\mathrm{e} + \mathrm{p} \rightarrow \mathrm{e}^+ + \mathrm{n}$	CC	4.3×10^3	5.0×10^3	5.7×10^3
$\nu + \mathrm{p} \rightarrow \nu + \mathrm{p}$	NC	0.6×10^3	1.2×10^3	2.0×10^3
$\nu + \mathrm{e} \rightarrow \nu + \mathrm{e}$	ES	3.6×10^2	3.6×10^2	3.6×10^2
$\nu + {}^{12}\mathrm{C} \rightarrow \nu + {}^{12}\mathrm{C}^*$	NC	1.7×10^2	3.2×10^2	5.2×10^2
$\nu_\mathrm{e} + {}^{12}\mathrm{C} \rightarrow \mathrm{e}^- + {}^{12}\mathrm{N}$	CC	0.5×10^2	0.9×10^2	1.6×10^2
$\bar{\nu}_\mathrm{e} + {}^{12}\mathrm{C} \rightarrow \mathrm{e}^+ + {}^{12}\mathrm{B}$	CC	0.6×10^2	1.1×10^2	1.6×10^2

Table 2.5: Expected neutrino signal in JUNO for a core collapse SN at 10 kpc distance for different detection channels and mean SN neutrino energies [68]. The applying current of the interaction is also listed. ν collectively denotes neutrinos and antineutrinos of all flavors, the same mean energy for all flavors is assumed, and neutrino flavor conversions are neglected. A threshold of 0.2 MeV for the proton recoil is chosen in the elastic neutrino-proton scattering.

Further, information on the SN nucleosynthesis may be gained by extracting time averaged spectra of different neutrino emission channels through the detection and identification of significant numbers of neutrinos of different flavors.
Besides these astrophysical implications, the detection of SN neutrinos would give significant insights on the properties of the neutrino as a particle itself. Thus, the time delay between arriving neutrinos may be used to extract a bound on the absolute neutrino mass scale and the estimated statistics are in principle sufficient to investigate the neutrino mass ordering through the shape of the $\bar{\nu}_\mathrm{e}$ spectrum as described in section 1.4.2. Further, the rate of neutrino-electron scattering is affected by the mass ordering, which may also be determined via a comparison of the IBD and elastic neutrino-proton scattering rates. Finally, new physics like the production of exotic weakly interacting particles during a core collapse SN can be significantly constrained by a measurement of SN neutrinos in JUNO [68].

The Diffuse Supernova Neutrino Background

The DSNB neutrino flux is known to be the dominating source of $\bar{\nu}_\mathrm{e}$ for energies of $E_\nu \gtrsim 10\,\mathrm{MeV}$. Further, the main IBD detection channel is not affected by solar neutrinos and with 1.2×10^{33} protons in a fiducial volume of 17 kt, a detectable signal of 1.5 to 2.9 events per year is expected in the JUNO detector, depending on the assumed mean SN neutrino spectrum [68].
The major background for a DSNB neutrino measurement at low energies arises due to the vicinity to the reactor cores and the resulting $\bar{\nu}_\mathrm{e}$ flux effectively impedes a detection of the DSNB below an energy of 10 MeV. Since, potentially, the high energy tail of the reactor $\bar{\nu}_\mathrm{e}$ spectrum might reach up to 13 MeV [149], the low visible energy threshold for a DSNB analysis will have to be set to 11 MeV [68].

Further backgrounds arise due to the cosmogenic $\beta-$n emitters ^{8}He and ^{9}Li as well as CC interactions of atmospheric neutrinos. While the contribution of the cosmogenic isotopes may savely be neglected due to their endpoints being effectively below the required energy threshold, indistinguishable CC interactions of atmospheric $\bar{\nu}_{\mathrm{e}}$ start to dominate the DSNB flux above $\sim 30\,\mathrm{MeV}$. Up to this energy, the atmospheric $\overline{\nu}_{\mathrm{e}}$ CC background is relatively low and a DSNB measurement is feasible. The background rate of CC interactions from atmospheric ν_{μ} and $\bar{\nu}_{\mu}$ may be strongly suppressed by the identification of the final state muon via the coincidence of the Michel electron and the characteristic muon pulse shape [68].
Also fast neutrons produced by cosmic muons impose an important background. Due to the relatively low depth, 20 fast neutron background events per year are expected in the target volume. However, because of the low mean free path of neutrons and the possibilities of pulse shape discrimination, this background is expected to be suppressable to a negligible rate by the application of a fiducial volume cut [68].
The most challenging background is caused by NC reactions of high-energetic atmospheric neutrinos in which one or more neutrons are knocked out of a carbon nucleus. These neutrons produce a prompt signal due to proton recoils and a delayed signal is generated by the γ ray emitted after the neutron has been captured on hydrogen. The event rate of these interactions is assumed to be more than one order of magnitude above the DSNB rate, thus, making the DSNB detection extremely challenging and a suppression of this background vital. Simulations have shown that this background could be reduced to a rate comparable to the DSNB signal via the coincidence of a delayed ^{11}C decay and, especially, pulse shape discrimination techniques [148]. Figure 2.5 taken from [68] shows the expected DSNB signal and background rates in JUNO. On the left side, the expected rates before the application of pulse shape discrimination, on the right side, the expected rates after the application of the cuts are shown. These estimations are based on a simulation of the proposed LENA detector [148] assuming a similar pulse shape discrimination performance for JUNO. The application of the cuts evaluated for LENA would open a window between $\sim 11\,\mathrm{MeV}$ and $\sim 20\,\mathrm{MeV}$ in which the DSNB dominates the signal, eventually enabling a detection. However, the required background reduction by a factor ~ 50 clearly marks the challenging character of a DSNB measurement. For a detailed study of atmospheric neutrino NC interactions and the discriminability of these events based on Borexino data, refer to chapter 7.

Geo-Neutrinos

Geo-neutrinos are emitted in the decays of radioactive isotopes of the ^{238}U and ^{232}Th chains naturally abundant in the Earth. The observation of these $\overline{\nu}_{\mathrm{e}}$ and the

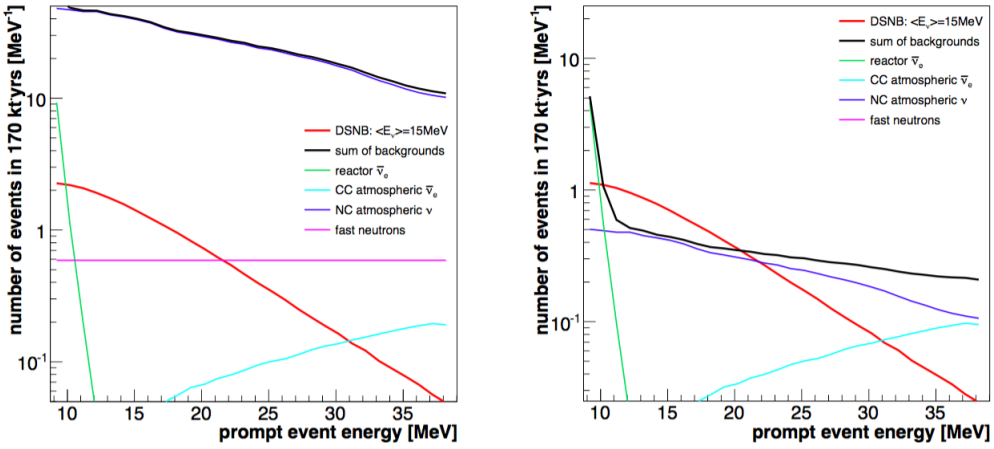

Figure 2.5: Expected DSNB signal and background rates on the *left* side before and on the *right* side after the application of pulse shape discrimination in JUNO.

determination of the contribution of radioactive heat to the total thermal power of the Earth allows to infer information on the Earth's composition, discriminate between different geodynamical models, and give an insight into the structure of the mantle and the nature of mantle convection [140]. So far, geo-neutrinos have been observed by the KamLAND [150, 151] and the Borexino [12, 124, 152] experiment.
The reaction channel for the detection of geo-neutrinos is the IBD. Due to the anticipated radiopurity and the huge target mass, the JUNO detector should detect between 300 and 500 events caused by geo-neutrinos in the first year of data taking. Thus, already higher statistics than the other experiments that observed geo-neutrinos so far would be acquired. Even though the geo-neutrino signal in JUNO is immensely overpowered by the reactor $\bar{\nu}_e$ flux, an observation of geo-neutrinos is expected to be feasible allowing to perform neutrino geoscience with JUNO [68].

Chapter 3

The Borexino Experiment

The Borexino experiment is built mainly with the purpose to perform real-time spectroscopy of solar neutrinos. After having been proposed in 1986 [153], the following 20 years were used to accomplish the world record level of radio purity required to reach the necessary low energy threshold. Since May 2007, the detector is accumulating solar neutrino data.
Already a few months after the start of data taking, the primary goal of the first real-time measurement of the solar ^{7}Be neutrinos could be achieved [154]. In the following years, Borexino published a precision measurement of the solar ^{7}Be neutrino flux [155], a measurement of the solar ^{8}B neutrinos above a record low energy threshold of 3 MeV [38], and obtained the first evidence of the solar pep neutrinos accompanied by the currently best limit on the CNO neutrino flux [11]. Further, the absence of a day-night asymmetry in the solar ^{7}Be neutrino flux could be revealed [156] and the observation as well as a spectroscopic measurement of geo-neutrinos could be fulfilled [12, 124, 152].
After a huge purification campaign in 2010 and 2011, the yet further reduction of the intrinsic background level allowed to accomplish the first real-time measurement of neutrinos generated in the low-energetic main pp branch of the solar pp-chain [10], the first simultaneous spectroscopic measurement of the solar pp, pep, and ^{7}Be neutrinos [36], and an improved measurement of the solar ^{8}B neutrino flux [157]. In the future, the main effort will be centered around the CNO neutrino flux with the goal of a more stringent limit or even the first observation, which would constitute the final capstone of Borexino's rich solar neutrino program.
In the first section 3.1 of this chapter, the design of the Borexino detector is presented while in section 3.2, the major physics results are summarized.

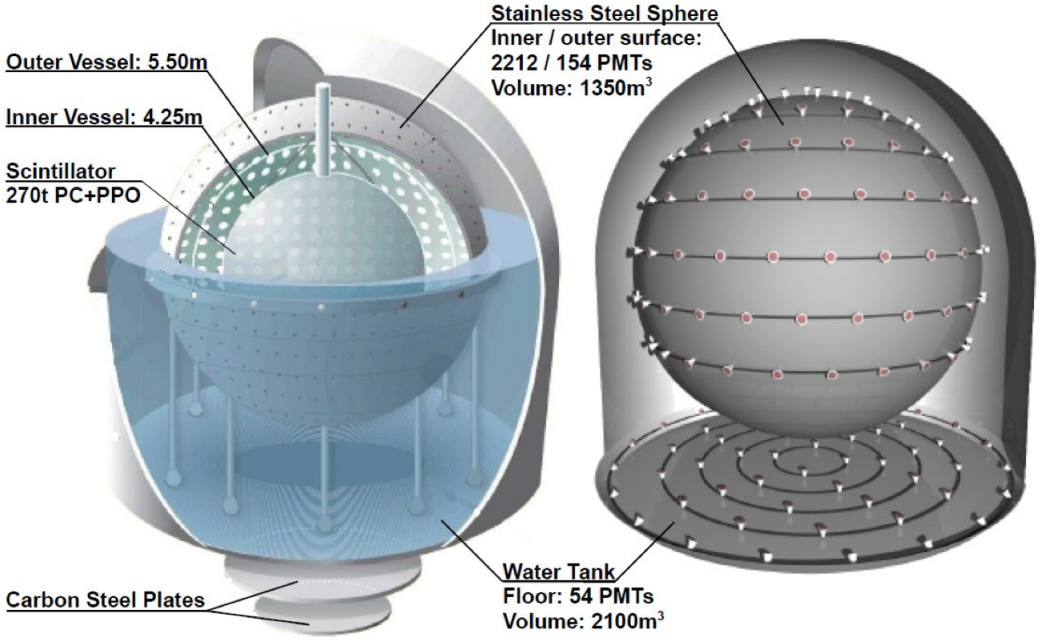

Figure 3.1: Design of the Borexino detector. On the *left* side, sections and dimensions of the detector are depicted. The white dots on the inner surface of the Stainless Steel Sphere (SSS) represent 2,212 PMTs that detect the light emitted in neutrino interactions in the liquid scintillator filled Inner Detector. On the *right* side, the positions of the PMTs registering events in the water tank, which acts as the Outer Detector and active muon veto, are shown. Of these 208 PMTs, 154 are mounted in eight circles on the outer surface of the SSS that separates the two subdetectors. Additional 54 PMTs are mounted in five concentric rings on the floor of the water tank [109].

3.1 Detector Design

The Borexino detector is situated in Hall C of the Laboratori Nazionali del Gran Sasso (LNGS), an underground laboratory that is reachable via a 10 km highway tunnel through the Gran Sasso mountain massif, which shields the laboratory from cosmic radiation. Due to the shape of the mountain site, the depth of the laboratory reaches from $\sim 3,200$ m we to $\sim 3,800$ m we depending on the direction of incoming radiation.
The design of the Borexino detector is depicted in figure 3.1. The detector is divided into two subdetectors that are independent in terms of light propagation by a Stainless Steel Sphere (SSS) with a radius of 6.82 m. The Inner Detector

(ID) containing the liquid scintillator target is encompassed by a steel dome of 18 m diameter and 16.9 m height filled with ultra pure water that acts as an active Water Čerenkov muon veto, the Outer Detector (OD). 2,212 PMTs are mounted on the inner surface of the SSS to detect the light emitted by neutrino interactions in the liquid scintillator target. To identify cosmic muons passing through the detector, 154 PMTs are mounted on the outer surface of the SSS to detect the emitted Čerenkov light. Additionally, 54 PMTs are placed at the floor of the water tank.
To achieve the necessary low radioactivity level of the innermost liquid scintillator target, the principle of gradual shielding is applied. Thus, an onion-like structure evolves in which the radio-purity of the materials increases towards the center and the central target region is shielded from external backgrounds. In the following, the very detailed descriptions of the design of the Borexino detector given in [109] are summarized.

3.1.1 Inner Detector

The ID contains the central liquid scintillator target of $\sim 280\,\mathrm{t}$ with a density of $\rho = 0.88\,\mathrm{t/m^3}$. The organic solvent pseudocumene (PC, 1,2,4-trimethylbenzene, $C_6H_3(CH_3)_3$) is used as the base of the scintillator mixture and doped with the solute PPO (2,5-diphenyloxazole, $C_{15}H_{11}NO$) at a concentration of 1.5 g/l. This solute acts as a wavelength shifter as described in section 2.1.2. After the excitation energy has been transferred to the PPO molecules, photons with a peak wavelength of $\sim 360\,\mathrm{nm}$ are radiated with a fluorescence decay time of $\sim 3\,\mathrm{ns}$. The chosen mixture provides a high light yield of $\sim 10^4$ photons per MeV of deposited energy and the attenuation length of $\sim 8\,\mathrm{m}$ guarantees that a huge number of the photons reaches the PMTs on the SSS.
To ensure the necessary high radio purity of the scintillator, it was purified on-site before the filling. The contaminations from dust (^{238}U, ^{232}Th, ^{40}K), air (^{39}Ar, ^{85}Kr), and cosmogenically produced ^{7}Be were reduced and extremely low uranium and thorium concentrations of $(5.3 \pm 0.5) \times 10^{-18}\,\mathrm{g/g}$ and $(3.8 \pm 0.8) \times 10^{-18}\,\mathrm{g/g}$, respectively, could be accomplished. These values even exceed the design goal of a contamination of $< 10^{-16}\,\mathrm{g/g}$ and could further be reduced to $< 9.4 \times 10^{-20}\,\mathrm{g/g}$ for ^{238}U and $< 5.7 \times 10^{-19}\,\mathrm{g/g}$ for ^{232}Th at 95% confidence level each after the purification campaign in 2010 and 2011 [36].
The innermost target is contained in a 125 μm thick nylon membrane with a radius of 4.25 m. This so-called Inner Vessel (IV) was constructed off-site under clean room conditions to minimize radioactive contaminations. Being attached to the lower part of the SSS with nylon strings, it centers the target volume by balancing small buoyant forces caused by density variations. Since nylon features approximately the same refractive index as PPO and is optically very clear, the optical

properties of the system are not affected in a relevant way by the insertion of the vessel. Further, the IV constitutes a barrier against radon (^{222}Rn).
The spherical shell of 2.4 m thickness between the IV and the SSS is filled with a mixture of PC and DMP (dimethylphthalate) at an initial concentration of 5 g/l. To minimize small density differences between this so-called buffer region and the innermost scintillator target after a small leak in the IV was discovered in 2009, the DMP concentration was reduced to 2 g/l to prevent scintillator liquid leaving the IV [9]. This mixture adds 1,024 t of buffer liquid as a shielding against external γ radiation from the construction materials. Due to the DMP, the light output in this region is quenched by a factor of ~ 20 and signals from the buffer region are strongly suppressed. The liquid closely matches the density and refractive index of the target scintillator such that buoyant forces and optical distortions are prevented. The buffer region is further divided by a second nylon membrane, the so-called Outer Vessel (OV), at a radius of 5.50 m. This vessel has the same thickness as the IV and acts as an additional shielding against radon emanating from the glass of the PMTs mounted on the SSS.
The SSS has a radius of 6.82 m and separates the ID from the OD, thus, creating two independent detectors in terms of light propagation. On the inner surface, 2,212 inward facing 8" ETL 9351 PMTs are mounted to detect the light emitted due to neutrino interactions in the scintillator target. To increase the effective optical coverage of the IV to 30%, 1,828 of these PMTs have been equipped with aluminium light concentrators around the photocathodes. Since these Winston cones limit the light collection to the IV, the remaining 384 PMTs are kept with a larger field of view to enable background studies in the buffer liquid. The chosen PMTs provide a quantum efficiency of 21% and a photoelectron yield of ~ 500 p.e./MeV is achieved [38]. Via optical fibers, laser pulses may be fed to the PMTs in order to check their status and properties. At the moment of writing, 1,315 PMTs are still operational [158].

3.1.2 Outer Detector

The OD contains 2.4 kt of deionized water encompassed by a steel dome of 18 m diameter and 16.9 m height. It acts as an active Water Čerenkov muon veto and shields the ID from external γ radiation as well as fast neutrons produced by cosmic muons in the surrounding rock. The Čerenkov light emitted by muons passing through the detector is registered by 208 PMTs. While 154 of these PMTs are mounted in 8 circles on the upper 3/4 of the outer surface of the SSS, 54 PMTs are arranged in five concentric rings at the floor of the water tank. This configuration has been shown by Monte Carlo simulations to most efficiently identify penetrating cosmic muons. The PMTs are of the same type as the ones used in the ID but additionally embedded in a cone shaped encapsulation to protect them

against the water and the larger pressure. Also the OD PMTs are connected with optical fibers to enable their calibration with LED pulses. In addition to the mere identification of muon events, the photon arrival times may also be used to obtain an information on the muon track for muons entering the ID [80].
The majority of the OD surfaces is covered with highly reflective Tyvek foil that redirects the Čerenkov light to increase the muon detection efficiency. It is further used to divide the OD into two subregions at the equator of the SSS. However, since only 2/3 of the interspace between the SSS and the surface of the steel dome are blocked, the two regions are not fully optically decoupled. While the aimed for improvement of the muon detection efficiency could be achieved by the application of the Tyvek foil, the resulting distortion of the light cones aggravates the muon tracking [80].
To stabilize the thermal detector conditions and prevent radioactive isotopes, especially ^{210}Po, from entering the fiducial volume via convective motions in the ID, a passive and an active thermal insulation were installed starting in December 2015. Thus, the water tank was envelopped with a double layer of mineral wool material of 20 cm thickness covering the full surface. The exterior layer of this material consists of a reflective aluminized film and additionally, an active gradient stabilization system was installed. This system consists of twelve 18 m long independent water loop cycles to maximize the positive thermal gradient between the top and the bottom of the detector and prevent motions of the scintillator. The temperature development is closely monitored with a latitudinal temperature probe system that consists of 28 internal probes around the SSS, 20 external probes on the outer surface of the water tank, six external probes under the floor of the water tank in a pit, and six probes located in the upper dome of the water tank [159].

3.2 Physics Program and Results

With the main focus set on the detection of low-energetic solar neutrinos, the record high radio-purity and energy resolution allow a rich physics program. After the first real-time measurement of the solar ^{7}Be neutrino flux [154], Borexino surpassed this design goal and led the way in experimental solar neutrino physics by a precision measurement of this flux [155], the measurement of the solar ^{8}B neutrino flux above an unprecedentedly low electron recoil energy threshold of 3 MeV [38], and the first detection of solar pep neutrinos together with the currently strictest limit on the CNO neutrino flux [11]. After an intense purification campaign in 2010 and 2011 during which the intrinsic background contamination could be even further reduced, a second phase of the Borexino experiment started and the first real-time measurement of the low-energetic solar pp-neutrinos could

be achieved [10]. Besides, the first evidence of geo-neutrinos at 3σ confidence level was found and a spectroscopic measurement could be performed [12, 124, 152]. In the following, the main results of the Borexino experiment are presented.

3.2.1 Solar Neutrinos

^{7}Be Neutrinos

^{7}Be neutrinos are emitted mono-energetically at 862 keV and may be observed as a Compton like electron recoil spectrum in the liquid scintillator. While a precise measurement of the solar ^{7}Be neutrino flux firstly constitutes a probe of the Standard Solar Model (SSM), it also gives insights into the vacuum dominated regime of neutrino oscillations since the MSW effect does not alter the ν_{e} survival probability at such low energies. Further, a possible day-night asymmetry of the flux through the regeneration of ν_{e} during the passage through terrestrial matter allows to investigate the neutrino oscillation parameter space without antineutrino data, i.e. without the constraint of CP symmetry.
After the first real-time measurement of solar ^{7}Be neutrinos in 2008 [154], Borexino reported a precision measurement of the solar ^{7}Be neutrino flux based on an exposure of $178\,\mathrm{t} \times \mathrm{yr}$ in September 2011. By averaging a Monte Carlo based fit and a fit based on an analytical description of the detector response that is shown on the left side in figure 3.2, an interaction rate of $(46.0 \pm 1.5\,(\mathrm{stat.})^{+1.5}_{-1.6}\,(\mathrm{syst.}))\,(\mathrm{d100\,t})^{-1}$ could be obtained [155]. In both fitting methods, the weights for the ^{7}Be neutrino rate and the radioactive background components ^{85}Kr, ^{210}Po, ^{210}Bi, and ^{11}C were left as free parameters, while the pp, pep, CNO, and ^{8}B neutrino rates were fixed to the values predicted by the SSM. The impact of the fixing was included as a systematic uncertainty. To reduce the contribution of ^{210}Po α decays, pulse shape discrimination and statistical subtraction were applied. Assuming MSW-LMA solar neutrino oscillations, this measurement corresponds to a solar ^{7}Be neutrino flux of

$$\Phi(^{7}\mathrm{Be}) = (4.48 \pm 0.24) \times 10^{9}\,\mathrm{cm}^{-2}\mathrm{s}^{-1}, \tag{3.1}$$

matching the prediction of the SSM under the assumption of neutrino oscillations. By comparing the measured rate to the expectation from the SSM assuming no oscillations, an ν_{e} survival probability of $P_{\mathrm{ee}} = 0.51 \pm 0.07$ at 862 keV is found.
In November 2011, Borexino could announce the absence of a day-night asymmetry in the solar ^{7}Be neutrino rate [156]. The reported asymmetry was

$$A_{\mathrm{DN}} = 2\,\frac{R_{\mathrm{N}} - R_{\mathrm{D}}}{R_{\mathrm{N}} + R_{\mathrm{D}}} = 0.001 \pm 0.012_{\mathrm{stat}} \pm 0.007_{\mathrm{syst}}, \tag{3.2}$$

where R_{N} is the ^{7}Be neutrino rate at night and R_{D} at day. With this measurement of an asymmetry consistent with zero, the low Δm^2 (LOW) solution of the solar

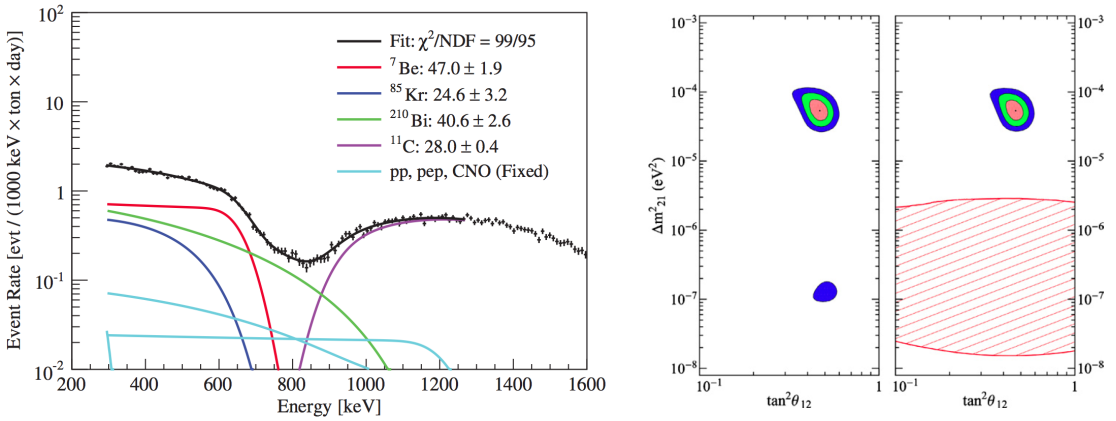

Figure 3.2: Analytical fit in the ^{7}Be neutrino energy region of interest and solar neutrino oscillation parameter space. On the *left* side, an analytical fit of the ^{7}Be neutrino signal and several background components is shown. The mono-energetic ^{7}Be neutrinos manifest as a clear Compton like edge [155]. On the *right* side, the solar neutrino oscillation parameter space is shown. The hatched red region on the right pattern is excluded at 99.73% confidence level by the Borexino measurement of the ^{7}Be day-night asymmetry excluding the LOW neutrino oscillation parameter region at 8.5σ. The LMA parameter region represented with 68.27% (blue), 95.45% (green), and 99.73% (brown) confidence levels is not constrained by the measurement. The left pattern shows the allowed parameter space before the inclusion of the Borexino result with the LOW region still being untouched [156].

neutrino problem could be excluded at 8.5σ as shown in figure 3.2 on the right. For the MSW-LMA solution, no constraints are imposed by this measurement.
Using data taken between December 2011 and December 2015 from the second phase of the solar neutrino program after the purification campaign in 2010 and 2011, Borexino could measure a seasonal modulation of the solar ^{7}Be neutrino rate and exclude the absence of this modulation at 99.99% confidence level [160]. Besides an analytical fit to the event rate, also a Lomb-Scargle analysis and the Empirical Mode Decomposition technique have been applied, all returning results for phase, period, and amplitude consistent with the solar origin. Best fit values of an amplitude of $(7.1 \pm 1.9)\%$, a period of (367 ± 10) d, and a phase of (-18 ± 24) d were observed. This measurement strongly improves the former evidences for an annual modulation reported especially by SNO [161] and Super-Kamiokande [32].

^{8}B Neutrinos

The solar ^{8}B neutrinos allow to probe the MSW-LMA paradigm mainly in the matter dominated region. However, a measurement of the low-energetic part of

the spectrum would be of special interest. In this transition region between the matter and vacuum dominated oscillation regimes, hypothetical non-standard neutrino interactions or additional neutrino states could significantly influence the ν_e survival probability. A very precise measurement of the solar ^{8}B neutrino flux would further give hints on the Sun's metallicity and, thus, test several solar models.

Benefiting from its immense radio-purity and the high light yield, Borexino could measure the ^{8}B neutrino flux in the matter dominated oscillation region above an electron recoil energy of 3 MeV [38]. This threshold energy undercuts the thresholds of the Water Čerenkov detectors SNO and Super-Kamiokande, which had measured the ^{8}B neutrino flux formerly above 3.5 MeV and 5 MeV, respectively [162, 163].

Above the energy of the 2.6 MeV γ rays emitted in decays of ^{208}Tl mainly on the SSS and the PMTs, cosmogenically produced radio-isotopes constitute the major background of the ^{8}B analysis. While the short-lived isotopes with a lifetime below 2 s can be easily rejected by a 6.5 s veto after each muon passing the ID at the cost of 29.2% livetime loss, the long-lived β^+ emitter ^{10}C with a lifetime of 27.8 s and a Q-value of 3.65 MeV could be suppressed at a livetime loss of only 0.16% using the Threefold Coincidence technique. As described in section 2.3.3, the triple coincidence in space and time between the actual ^{10}C decay, the passing muon, and the capture of the neutron that accompanies the production of ^{10}C in $\sim 90\%$ of all cases allows to identify these decays. Due to the lack of additionally produced neutrons, the cosmogenically produced β^- emitter ^{11}Be with a lifetime of 19.9 s and a Q-value of 11.5 MeV had to be considered statistically by scaling the ^{11}Be rate as measured by the KamLAND experiment [164] to the dimensions and depth of Borexino.

Based on 488 live days of data taking, Borexino reported in 2010 an elastic ^{8}B neutrino-electron scattering rate of $(0.22 \pm 0.04_{\text{stat}} \pm 0.01_{\text{sys}})\,(\text{d100 t})^{-1}$ above a threshold of 3 MeV electron recoil energy [38]. This translates to an unoscillated ^{8}B neutrino flux of

$$\Phi_{^8\text{B}} = (2.4 \pm 0.4_{\text{stat}} \pm 0.1_{\text{syst}}) \times 10^6\,\text{cm}^{-2}\text{s}^{-1}. \tag{3.3}$$

Values obtained for the elastic neutrino-electron scattering rate above 5 MeV agree well with the results from SNO and Super-Kamiokande [162, 163]. By conceiving the measured electron recoil rate as a convolution of the detector energy response and the differential neutrino rate considering different cross sections for ν_e and $\nu_{\mu,\tau}$, an ν_e survival probability of $P_{ee} = 0.29 \pm 0.10$ at a mean energy of 8.9 MeV could be derived. This survival probability was found to be 1.9σ off the survival probability reported for ^{7}Be neutrinos in [154], showing the MSW effect to exist.

In September 2017, a more precise result on the solar ^{8}B neutrino flux could be published [157]. Besides the higher statistics of 1.5 kt $\times$ yr exposure recorded between 2008 and 2016, several improvements of the background estimation could be

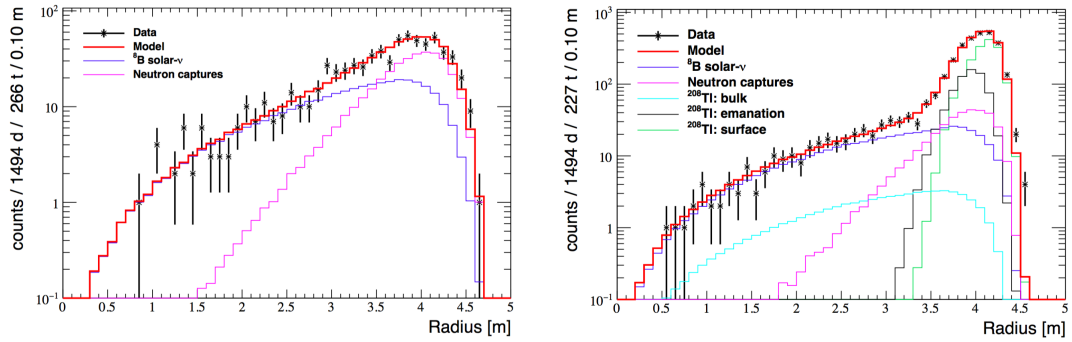

Figure 3.3: Radial fits to the solar ^{8}B neutrino signal and background components in Borexino. On the *left* side, the fit of the high energy region and on the *right* side, the fit of the low energy region are shown. While in the high energy region, only neutron captures need to be considered as a background component, additional backgrounds from ^{208}Tl need to be taken into account in the low energy region [157].

achieved. Thus, a more stringent limit of $R < 9.1 \times 10^{-3}$ cdp/100 t could be set on the cosmogenic ^{11}Be rate via an independent measurement, 3σ lower than the rate extrapolated from KamLAND. Additionally, the ^{208}Tl contamination was lowered in the purification campaign of 2010 and 2011, radiogenic neutron captures on detector components were included to the background model, and the Monte Carlo simulation modeling the data was significantly improved [165]. Further, the data has been separated in a low energy range including events from natural radioactivity and a high energy range that is dominated by the external γ ray background following neutron captures on the detector structure.
The determination of the ^{8}B neutrino rate relies on radial fits in both energy regions as shown in figure 3.3. Due to the presence of PPO in the buffer at high z-values caused by the IV leak, the low-energetic sample was cut at 2.5 m at this coordinate. For the high-energetic sample, the total active volume was used. While the cosmogenic ^{11}Be background is expected to be distributed uniformly in the detector similar to the neutrino signal, several background components feature a different radial behavior. External neutron captures on the detector structure are recognized at larger radii as well as ^{208}Tl decays occurring at the *surface* of the IV and ^{208}Tl *emanated* from the nylon vessel into the outer edge of the scintillator. Only the *bulk* of ^{208}Tl dissolved in the scintillator is expected to show a similar radial distribution as the signal. For the high energy region shown on the left side in figure 3.3, only the contamination from neutron captures needs to be considered as a background source. In the fit of the low energy region shown on the right side, also contributions from bulk, emanated, and surface ^{208}Tl are included.
After subtracting residual backgrounds, the combined rate for both subregions was

found to be

$$R_{\mathrm{LE+HE}} = (0.220^{+0.015}_{-0.016}(\mathrm{stat.})^{+0.006}_{-0.006}(\mathrm{syst.}))\,\mathrm{cpd}/100\,\mathrm{t}. \tag{3.4}$$

The error of $\sim 8\%$ on this rate implies an improvement of more than a factor 2 with respect to the first measurement. The corresponding ^{8}B neutrino flux is

$$\Phi_{^8\mathrm{B}} = (2.55^{+0.17}_{-0.19}(\mathrm{stat.})^{+0.07}_{-0.07}(\mathrm{syst.})) \times 10^6\,\mathrm{cm}^{-2}\mathrm{s}^{-1} \tag{3.5}$$

and an ν_e survival probability of 0.36 ± 0.08 could be determined. Combining this measurement with the ^{7}Be and pp neutrino rates reported in [36], the high-Z solar model is found to be preferred at 3.1σ, while the low-Z model is only compatible at the 0.1σ level.
Due to the huge implications that might be accessed through a measurement of the ν_e survival probability in the transition region, further strong efforts are ongoing in the scope of the Borexino experiment to investigate the ^{8}B neutrino flux for an even lower energy threshold [166].

pep and CNO Neutrinos

The pep branch constitutes a rare alternative to the prevailing pp initial fusion reaction of the pp-chain. Thus, the flux of the mono-energetically at 1.44 MeV emitted pep neutrinos is directly related to the pp branch. Since the ratio between the fluxes is, further, only weakly model dependent and known with 1% accuracy, a measurement of the pep neutrino flux translates to an indirect determination of the pp neutrino flux. With 98% of the solar energy being released via the initial fusion reaction, pep neutrinos additionally allow to explore the solar luminosity.
Besides the dominating pp-chain, the Sun releases a minor part of its energy through the CNO-cycle as described in section 1.4.1. Since the CNO neutrino flux strongly depends on the metallicity of the Sun, a measurement of the flux of neutrinos generated in this fusion cycle provides a strong test of the high metallicity GS98 and the low metallicity AGSS09 SSMs with the CNO neutrino flux being predicted 40% higher in the high metallicity case [167].
Figure 3.4 shows a fit of the pep and CNO neutrino signal components and the contributing backgrounds in the relevant energy region [11]. The main background component arises due to decays of the cosmogenically produced β^+ emitter ^{11}C with a lifetime of 29.4 min and a Q-value of 1.98 MeV. Since its formation is accompanied by at least one free neutron in 95% of the cases, the Threefold Coincidence technique may be applied to lower the contribution of this background by a factor ~ 10 at a livetime loss of 51.5%. Further, pulse shape discrimination techniques revealing small differences of the pulses of electron and positron recoils could be utilized to partly distinguish between background and signal events. The effect of

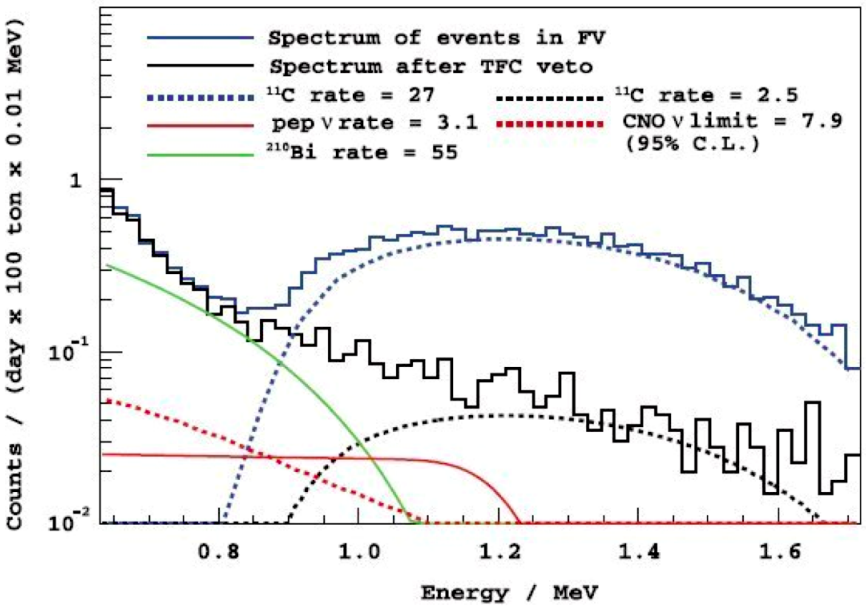

Figure 3.4: Fit to the signal and background components of the Borexino pep neutrino measurement [11].

the application of the Threefold Coincidence cut can be seen in figure 3.4 by comparing the blue spectrum representing the data before the cut was applied to the black spectrum after the application. The Compton like recoil edge at 1.22 MeV caused by the pep neutrinos is represented by the red line.
Based on a multivariate fit in which also the radial distribution of signal and background components was considered, Borexino published the first evidence of solar pep neutrinos in 2012 [11]. Also data rejected by the Threefold Coincidence cut were fitted complementarily requiring the rate of all non-cosmogenic components to be equal in both datasets. Thus, a pep neutrino interaction rate of $(3.1 \pm 0.6_{\text{stat}} \pm 0.3_{\text{syst}})\,(\text{d100 t})^{-1}$ was measured, which translates to a flux of

$$\Phi_{\text{pep}} = (1.6 \pm 0.3) \times 10^8\,\text{cm}^{-2}\text{s}^{-1}. \tag{3.6}$$

Comparing this measurement to the flux expected when neutrino oscillations are neglected, an ν_e survival probability of $P_{ee} = 0.62 \pm 0.17$ at 1.44 MeV results.
Due to the similarity between the spectral shape of the ^{210}Bi β^- decay and the electron recoil spectrum caused by CNO neutrino interactions, the CNO neutrino signal is overwhelmed by the ~ 10 times higher rate of ^{210}Bi decays. Thus, by fixing the pep rate to the value of the SSM, a limit on the CNO neutrino interaction rate of $< 7.9\,(\text{d100 t})^{-1}$ at 95% confidence level could be obtained. This measurement

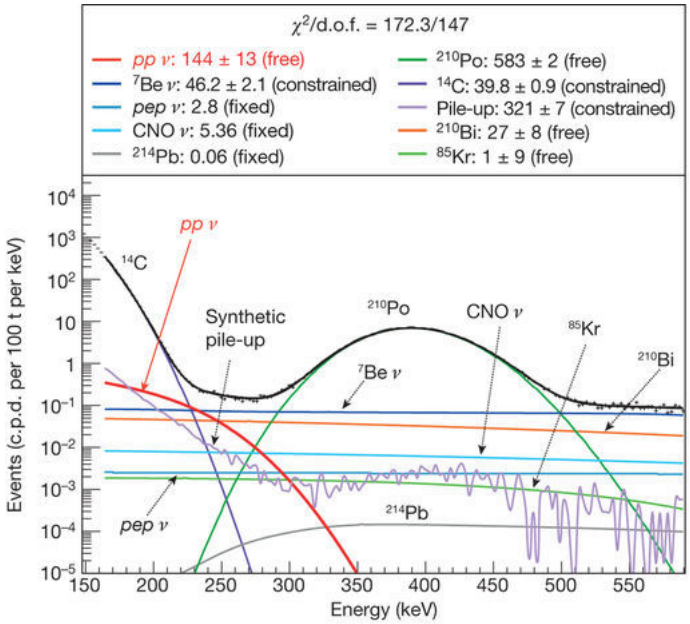

Figure 3.5: Fit of the pp neutrino and relevant background energy spectra in Borexino [10].

allows to extract the currently most stringent limit on the CNO neutrino flux of

$$\Phi_{\mathrm{CNO}} < 7.7 \times 10^{8}\,\mathrm{cm}^{-2}\mathrm{s}^{-1}. \tag{3.7}$$

pp Neutrinos

Being generated in the initial reaction of the solar pp-chain, the pp neutrino flux is directly connected to the Sun's luminosity. Thus, the combination of neutrino and optical observations can provide an experimental confirmation that the Sun has been in thermodynamic equilibrium for a time scale of $\sim 10^5$ yr, the time photons produced in the solar core need to reach the surface of the Sun. Further, a precise measurement of the pp neutrino flux facilitates an accurate test of the MSW-LMA solution and allows precision tests of exotic neutrino properties [168].
After the reduction of especially the ^{210}Bi and ^{85}Kr contaminations intrinsic to the scintillator during the purification campaign in 2010 and 2011, Borexino could provide the first real-time measurement of the solar pp neutrino flux based on data acquired between January 2012 and May 2013. Figure 3.5 shows the fit to the pp neutrino signal and the contributing background components [10].
The main background arises due to the intrinsic ^{14}C contamination, a β^- emitter with an endpoint of 156 keV. Despite its low isotopic fraction of $^{14}\mathrm{C}/^{12}\mathrm{C} \sim 2.7 \times 10^{-18}$ in the Borexino scintillator, it accounts for most of the triggering rate

of $\sim 30\,\mathrm{Hz}$ in the relevant energy region. The ^{14}C decay rate could be determined independently by considering events that are followed by an immediate second event in the data acquisition window of $16\,\mu$s. Thus, the ^{14}C rate could be constrained to the measured value in the pp neutrino analysis. Besides the direct contamination of the analysis region due to ^{14}C decays, pile-up events, i.e. two uncorrelated events occurring too close in time to be separated by the electronic systems such that they are mistakenly interpreted as a single event, constitute a major background component. This background and its energy spectrum were estimated by artificially overlaying real triggered events without any selection cuts with random data samples. This synthetic pile-up construction includes all possible event pile-up combinations present in the dataset and allows to constrain its contribution in the final fit.
Besides the pp neutrino signal, the ^{210}Po contribution and the flat and, thus, clearly distinguishable contributions from ^{85}Kr and ^{210}Bi were left as free parameters in the fit. Also the spectra of the other solar neutrino branches are flat in the relevant energy region. While the rates of the CNO and pep neutrinos were fixed at the level of the SSM, the ^{7}Be neutrino rate was constrained to the value measured in [155]. Considering all background sources, the fit returns a pp neutrino interaction rate of $(144 \pm 13_{\mathrm{stat}} \pm 10_{\mathrm{syst}})\,(\mathrm{d100\,t})^{-1}$, excluding the absence of solar pp neutrinos at 10σ [10]. Applying the latest values of the neutrino oscillation parameters, a solar pp neutrino flux of

$$\Phi_{\mathrm{pp}} = (6.6 \pm 0.7) \times 10^{10}\,\mathrm{cm^{-2}s^{-1}} \tag{3.8}$$

could be measured, in good agreement with the SSM prediction of $(5.98 \times (1 \pm 0.006)) \times 10^{10}\,\mathrm{cm^{-2}s^{-1}}$. By comparing the observed flux with the prediction of the SSM for the unoscillated pp neutrino flux, an ν_{e} survival probability of $P_{\mathrm{ee}} = 0.64 \pm 0.12$ is obtained, providing a constraint on the MSW-LMA solution in the low energy regime.
With this measurement, Borexino became the first experiment to probe the MSW-LMA solution in the matter and vacuum dominated neutrino oscillation regimes as well as in the transition region. Further, the fluxes of all solar neutrino branches from the pp-chain except for the least abundant hep neutrinos could be precisely determined and a huge contribution to the understanding of solar and neutrino physics could be accomplished.
Based on $1,291.51$ days of phase II data collected between December 2011 and May 2016, Borexino could further improve the measurements of solar neutrino fluxes and perform the first simultaneous fit of the solar pp, pep, and ^{7}Be neutrino fluxes [36].
With the application of a fiducial volume cut of $71.3\,\mathrm{t}$, external backgrounds could be significantly reduced and the remaining background is mainly caused by intrinsic contaminations of the scintillator like ^{14}C and ^{210}Bi, by cosmogenic radio-

Solar Neutrino Species	Rate [cpd/100 t]	Flux [$cm^{-2}s^{-1}$]
pp	$134 \pm 10^{+6}_{-10}$	$(6.1 \pm 0.5^{+0.3}_{-0.5}) \times 10^{10}$
^{7}Be	$48.3 \pm 1.1^{+0.4}_{-0.7}$	$(4.99 \pm 0.13^{+0.07}_{-0.10}) \times 10^{9}$
pep (HZ)	$2.43 \pm 0.36^{+0.15}_{-0.22}$	$(1.27 \pm 0.19^{+0.08}_{-0.12}) \times 10^{8}$
pep (LZ)	$2.65 \pm 0.36^{+0.15}_{-0.24}$	$(1.39 \pm 0.19^{+0.08}_{-0.13}) \times 10^{8}$
CNO	< 8.1 (95% C.L.)	$< 7.9 \times 10^{8}$ (95% C.L.)

Table 3.1: Solar pp, pep, and ^{7}Be neutrino rates determined in the first simultaneous fit of these components by Borexino. Since the result of the pep neutrino flux depends on the assumed model, a value for low (LZ) and high metallicity (HZ) is given [36].

isotopes like ^{11}C, and by the residual external γ ray background from the decays of ^{208}Tl, ^{214}Bi, and ^{40}K. Again, the Threefold Coincidence technique was used to reduce the ^{11}C background and the energy spectra of both data rejected by the Threefold Coincidence cut and data surviving this cut were fitted in a Monte Carlo driven as well as an analytical approach. Besides the energy spectra, the radial components of signal and background contributions and the distribution of a pulse shape variable to allow e^+/e^- discrimination were utilized in a binned likelihood function. This function was maximized in a multivariate approach. Besides the pp, pep, and ^{7}Be interaction rates, the decay rates of ^{85}Kr, ^{210}Po, ^{210}Bi, and ^{11}C decays as well as external background rates from ^{208}Tl, ^{214}Bi, and ^{40}K were left as free parameters. Table 3.1 lists the obtained results on the neutrino fluxes. The published solar ^{7}Be neutrino flux corresponds to the sum of both mono-energetic lines at 384 keV and 862 keV. It is in good agreement with the precision measurement from the first phase of the solar neutrino program [155] but determined with an uncertainty of only 2.7%, two times lower than the theoretical uncertainty. Thus, the theoretical estimation clearly becomes the major uncertainty source when probing the SSM based on the ^{7}Be neutrino flux. Also the pp neutrino rate is consistent with the analysis performed in [10] but the uncertainty could be reduced by $\sim 20\%$.

By constraining the CNO interaction rate, the correlation between this contribution and the pep neutrino interaction rate can be broken. Nevertheless, the pep neutrino interaction rate depends on the assumed model from which the CNO flux is predicted. Thus, one value for the low (LZ) and one value for the high metallicity (HZ) case are obtained. The absence of pep neutrinos could be excluded at 5σ for the first time.

Due to the similarity between the ^{210}Bi decay spectrum and the electron recoil

spectrum caused by CNO neutrino interactions, only an upper limit of the CNO neutrino flux could be obtained. While in the former analysis, this was done by fixing the pep neutrino rate to the prediction of the SSM [11], the inclusion of the pp neutrino rate in the extended energy range allows to place a constraint on the pep neutrino rate via the well known pp and pep neutrino flux ratio. The obtained limit cannot improve the former result but confirms it while relying on a weaker hypothesis for the pep neutrino flux.
Figure 1.2 shows the derived survival probabilities from this simultaneous fit together with the phase I result on the ^{8}B neutrino flux. The measured values agree well with the predictions of the MSW-LMA solution. Further, the combination of the measured fluxes of pp and ^{7}Be neutrinos can be used to determine for the first time experimentally the ratio R between the rates of the ^{3}He $-^4$ He and the ^{3}He $-^3$He reactions occurring in the pp-chain. Since this ratio reflects two different modes to terminate the pp-chain, its measurement is a strong probe of solar fusion. Neglecting the pep and ^{8}B neutrino contributions, the ratio is given by

$$R = \frac{2\Phi(^7\mathrm{Be})}{\Phi_{\mathrm{pp}} - \Phi_{^7\mathrm{Be}}} = 0.18 \pm 0.02, \tag{3.9}$$

which is in agreement with the predicted values for both the LZ and the HZ SSMs [169].

3.2.2 Geo-Neutrinos

In the decays of long-lived radioactive isotopes of the ^{238}U and ^{232}Th chains and of ^{40}K that are naturally abundant in terrestrial matter, $\bar{\nu}_{\mathrm{e}}$ are emitted. These so-called geo-neutrinos offer a possibility to probe the abundances and distributions of radioactive isotopes in the Earth's crust and to test various Bulk Silicate Earth (BSE) models that describe the composition of elements in the present day mantle and crust [170]. Further, a measurement allows to infer the contribution of radiogenic power to the total terrestrial heat flow of (47 ± 2) TW [171].
Borexino detects geo-neutrinos via the IBD as described in section 2.2.2. Since the threshold of this interaction of 1.8 MeV is above the endpoint of the ^{40}K β^- spectrum of 1.4 MeV, only geo-neutrinos from the radioactive ^{238}U and ^{232}Th chains contribute to the signal. After the first evidence of geo-neutrinos at 3σ confidence level in 2010 [124] and an update with higher statistics in 2013 [152], Borexino could publish a spectroscopic measurement of geo-neutrinos in 2015 based on 2,056 days of data taking [12].
A major background of the geo-neutrino measurement is caused by the cosmogenic radio-isotopes ^{9}Li and ^{8}He and by fast neutrons. To reduce these contributions, a 2 ms veto was applied after each muon crossing the OD and a 2 s veto after each muon crossing the ID. Further, accidental coincidences mimicking an IBD event

and (α, n) reactions were considered as background sources and their contributions as well as those of cosmogenic backgrounds were estimated independently. Besides geo-neutrinos, $\bar{\nu}_\mathrm{e}$ generated in the energy production of nuclear power plants are a known $\bar{\nu}_\mathrm{e}$ source relevant for the Borexino detector. However, the geo-neutrino analysis benefits from a general reactor shut-down in Italy completed in 1990, such that the mean weighted distance of the LNGS to operational nuclear power plants is rather large with $\sim 1,200\,\mathrm{km}$ [152].
Using an un-binned likelihood fit of the energy spectrum of selected $\bar{\nu}_\mathrm{e}$ candidates that was based on the geo- and reactor neutrino spectra as obtained by Monte Carlo simulations and the estimated backgrounds, a geo-neutrino signal of [12]

$$S_\mathrm{geo} = (43.5^{+11.8}_{-10.4}(\mathrm{stat.})^{+2.7}_{-2.4}(\mathrm{syst.}))\,\mathrm{TNU} \tag{3.10}$$

and a reactor neutrino signal of

$$S_\mathrm{geo} = (96.6^{+15.6}_{-14.2}(\mathrm{stat.})^{+4.9}_{-5.0}(\mathrm{syst.}))\,\mathrm{TNU} \tag{3.11}$$

were measured with 1 Terrestrial Neutrino Unit (TNU) corresponding to 1 event per year and 10^{32} protons. To compute these results, the mass ratio of Th and U of $m(\mathrm{Th})/m(\mathrm{U}) = 3.9$ as suggested by the chondritic model was assumed. With the measured rates, the absence of geo-neutrinos could be excluded at 5.9σ.
Figure 3.6 shows on the left side the values obtained for the separate contributions of decays from the ^{238}U and from the ^{232}Th chain that have been obtained by leaving the respective spectral contributions as free parameters in the fit. The observed $\bar{\nu}_\mathrm{e}$ fluxes from decays of the ^{238}U and the ^{232}Th chain are

$$\Phi(\mathrm{U}) = (2.7 \pm 0.7) \times 10^6\,\mathrm{cm}^{-2}\mathrm{s}^{-1} \tag{3.12}$$

and

$$\Phi(\mathrm{Th}) = (2.3 \pm 0.6) \times 10^6\,\mathrm{cm}^{-2}\mathrm{s}^{-1}, \tag{3.13}$$

respectively.
Further, the total radiogenic power of the Earth adopting the chondritic mass ratio was determined as

$$P_\mathrm{tot}(\mathrm{U} + \mathrm{Th} + \mathrm{K}) = 33^{+28}_{-20}\,\mathrm{TW}. \tag{3.14}$$

This result combined with the measurement of the geo-neutrino flux can be used to constrain several BSE models as shown on the right side of figure 3.6, even though more accurate measurements are required to exclude a model.
With the $\bar{\nu}_\mathrm{e}$ signals from the local crust and the rest of the crust being calculable, the measured geo-neutrino signal by Borexino is composed of these two contributions and a contribution from the mantle. Thus, a mantle contribution of

$$S_\mathrm{geo}(\mathrm{Mantle}) = (20.9^{+15.1}_{-10.3})\,\mathrm{TNU} \tag{3.15}$$

is reported, rejecting the absence of $\bar{\nu}_\mathrm{e}$ generated in the mantle at 98% confidence level.

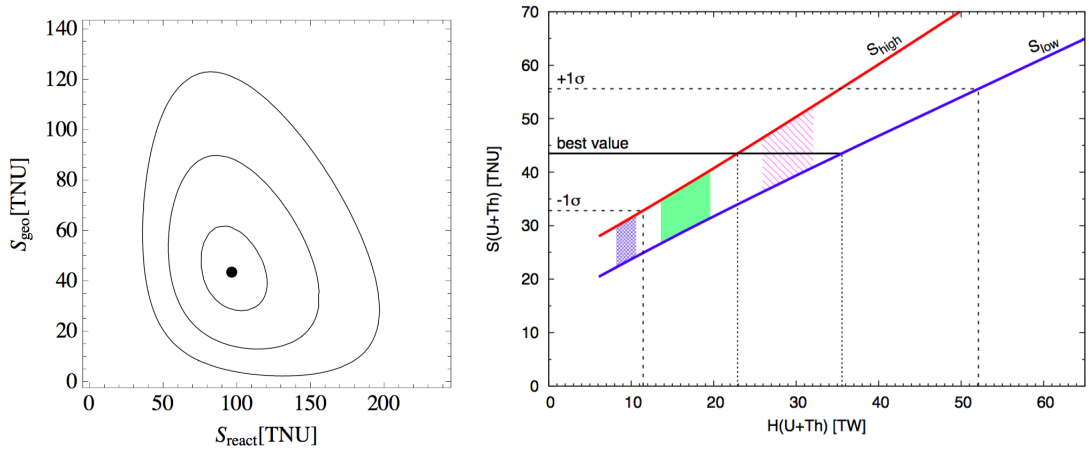

Figure 3.6: On the *left* side, the best fit contours for 1σ, 2σ, and 3σ of the contributions of the ^{238}U and the ^{232}Th chains to the measured geo-neutrino signal are shown. On the *right* side, the expected geo-neutrino signal as a function of the radiogenic heat release is shown [172]. The measurement of Borexino constrains the cosmochemical, geochemical, and the geodynamical BSE models defined in [170] and represented by the filled regions from left to right. The figures are taken from [12].

3.2.3 Supernova Neutrinos

As described in section 1.4.2, heavy stars with masses of more than $\sim 8M_{\odot}$ eventually become unstable against their own gravitation and collapse in a core collapse SN. Since about 99% of the energy of $\sim 3 \times 10^{53}$ erg released in these optically very bright events is carried by neutrinos, $\sim 10^{58}$ neutrinos of all flavors emerge in such an event [50].
Borexino is able to detect SN neutrinos via various detection channels. The expected signal numbers in these channels together with their cross sections averaged over the assumed neutrino energy spectra and the supposed mean energy of the respective neutrino species as given in [52] are listed in table 3.2. In total, a burst of ~ 110 neutrino events within 10 s is expected via the considered channels in case of a core collapse SN at a distance of 10 kpc and a released gravitational energy of $\sim 3 \times 10^{53}$ erg. Besides the channels listed in table 3.2, a signal via elastic neutrino-proton scattering approximately of the order of the signal in the IBD channel is expected [121] and the expected number of SN neutrino interactions increases to ~ 190. Hence, for such an event at the galactic center, a strong test of SN models, neutrino mass limits, and possibly the neutrino mass hierarchy could be provided by the Borexino experiment as detailed in section 1.4.2. Further, Borexino joined the SuperNova Early Warning System (SNEWS) collaboration consisting also of, e.g., Super-Kamiokande [63], LVD [64], and IceCube [65]. Through the coincidence of neutrino burst signals in several of the detectors, the relative timing, and track-

Reaction Channel	$\langle E_\nu \rangle$ [MeV]	$\langle \sigma \rangle$ [cm^2]	N_{events}
$\nu_e + e \rightarrow \nu_e + e$	11	1.02×10^{-43}	2.37
$\bar{\nu}_e + e \rightarrow \bar{\nu}_e + e$	16	6.03×10^{-44}	0.97
$\nu_x + e \rightarrow \nu_x + e$	25	3.96×10^{-44}	0.81
$\bar{\nu}_e + e \rightarrow \bar{\nu}_x + e$	25	3.25×10^{-44}	0.67
$\bar{\nu}_e + p \rightarrow e^+ + n$	16	2.70×10^{-41}	79
$\nu_e + {}^{12}C \rightarrow {}^{12}N + e^-$	11	1.33×10^{-43}	0.65
$\bar{\nu}_e + {}^{12}C \rightarrow {}^{12}B + e^+$	16	1.87×10^{-42}	3.8
$\nu_e + {}^{12}C \rightarrow \nu_e + {}^{12}C^*$	11	1.33×10^{-43}	0.4
$\bar{\nu}_e + {}^{12}C \rightarrow \bar{\nu}_e + {}^{12}C^*$	16	6.88×10^{-43}	1.5
$\nu_x + {}^{12}C \rightarrow \nu_x + {}^{12}C^*$	25	3.73×10^{-42}	20.6
Sum			110.77

Table 3.2: Expected neutrino signal in Borexino for a SN at the galactic center at 10 kpc distance. The number of events in different interaction channels, the respective averaged cross sections, and the assumed mean energy for each neutrino species are listed.

ing capabilities, this collaboration may inform and point astronomers towards the optical event following the SN neutrino signal.

3.2.4 Current Situation and Future Prospects

With all the branches of the solar pp-chain but the extremely faint hep neutrinos measured by the Borexino experiment, the remaining main goal is to most stringently constrain or even measure the flux of neutrinos produced in the solar CNO-cycle. Especially a measurement would constitute the final climax of the long period of solar neutrino physics with Borexino, which then could provide measurements of all the solar neutrino branches and further brighten the knowledge of solar physics, in particular with respect to the solar metallicity.
As has been mentioned and can be seen in figure 3.4, the major complicity of a CNO neutrino measurement arises due to the similarity of the CNO neutrino and the ^{210}Bi β decay spectrum. Thus, spectral fitting algorithms cannot disentangle the contributions of CNO neutrinos and ^{210}Bi decays. Since the ^{210}Bi rate dominates the CNO neutrino rate by a factor of ~ 4 to ~ 10, depending on the assumed solar metallicity, only an upper limit on the CNO neutrino flux could be obtained so far. To break this degeneracy of the two spectra, an independent measurement of the ^{210}Bi decay rate is needed such that its contribution can be constrained to the measured value in the spectral fit. In case sufficient accuracy of the ^{210}Bi rate may be obtained, the CNO neutrino contribution could eventually be extracted

from the data.
As proposed in [173], such a measurement is possible indirectly via measuring the ^{210}Po rate in the detector. Due to the α particles being emitted mono-energetically in the ^{210}Po decay and the possibility to identify these particles via the registered pulse shape, ^{210}Po α decays with a lifetime of $\tau_{\mathrm{Po}} = 199.6\,\mathrm{d}$ may clearly be identified in the Borexino detector.
^{210}Bi is a daughter nucleus of the long-lived ^{210}Pb that is part of the ^{238}U chain and, thus, an intrinsic background component of the scintillator. ^{210}Pb is found to be out of equilibrium due to a certain amount of ^{210}Pb remaining inside the scintillator after the purification campaign and it decays via

$$^{210}\mathrm{Pb} \rightarrow^{210} \mathrm{Bi} \rightarrow^{210} \mathrm{Po} \rightarrow^{206} \mathrm{Pb\,(stable)}. \tag{3.16}$$

Since no evidence for a source supplying the contents of ^{210}Pb and ^{210}Bi in the scintillator is observed, the ^{210}Pb contamination of the scintillator is expected to decay with its lifetime of $\tau_{\mathrm{Pb}} = 32.3\,\mathrm{yr}$ while ^{210}Bi quickly reaches the equilibrium with its parent due to its short lifetime of $\tau_{\mathrm{Bi}} = 7.2\,\mathrm{d}$. Thus, the ^{210}Po abundance is given by [173]

$$\frac{\mathrm{d}N_{\mathrm{Po}}}{\mathrm{d}t} = -\frac{N_{\mathrm{Po}}(t)}{\tau_{\mathrm{Po}}} + \frac{N_{\mathrm{Bi}}(t)}{\tau_{\mathrm{Bi}}} + S_{\mathrm{Po}}(t), \tag{3.17}$$

where the first term describes the decay of ^{210}Po, the second term the supply of ^{210}Po through the decay of ^{210}Bi, and $S_{\mathrm{Po}}(t)$ is a source term indicating contributions from an external source of ^{210}Po that is not in secular equilibrium with ^{210}Pb and ^{210}Bi. In case of the absence of a source term, ^{210}Po would reach the secular equilibrium after $\sim 2\,\mathrm{yr}$ and from this point on, its decay rate would equal the rate of ^{210}Bi decays. While a uniformly distributed amount of ^{210}Po that is not in secular equlibrium with its parent isotopes or a source term solely describing diffusive contributions would not harm a measurement, convective up- and downward motions of the scintillator mostly caused by seasonal temperature changes were observed in the Borexino detector. These motions transport ^{210}Po diffused from the nylon vessel towards the center of the detector precluding the selection of a fiducial volume in which the exponential ^{210}Po decay can be observed. Due to this, the thermal control system described in section 3.1.2 was installed starting from December 2015 to keep the temperature of the detector stable and prevent convective motions of the scintillator. If absolutely stable conditions could be realized, an indirect measurement of the ^{210}Bi decay rate could eventually be feasible. Currently, the thermal conditions of the detector are found to approach the necessary conditions and strong efforts are made to estimate the feasibility of a determination of the ^{210}Bi rate, to analyze the achievable CNO neutrino sensitivity, and to explore the possibilities for such an outstanding measurement in the near future.

Chapter 4

Modulation of the Cosmic Muon Flux

For experiments situated deep underground, the cosmic muon flux is significantly reduced compared to the intensity of $(180 \pm 20)\,\mathrm{m}^{-2}\mathrm{s}^{-1}$ at the surface [130]. Further, the mean energy of the muons is increased since low-energetic muons are absorbed in the rock shielding. High-energetic muons potentially reaching underground detectors are generated when mesons produced in interactions of primary cosmic rays with nuclei of the atmosphere decay in flight without any interaction before the decay. Due to density fluctuations in the upper atmosphere that alter the mean free path of the mesons, the probability for them to decay in flight before interacting variates. Thus, also the intensity of cosmic muons observed in underground laboratories depends on the density of the atmosphere. The magnitude of the intensity variation is regulated by the mean lifetime and the decay properties of the contributing mesons and a measurement of this effect allows to probe the identity of the particles taking part in the muon production.
In the first section 4.1 of this chapter, theoretical derivations of the intensity of muons observed in underground laboratories and of the effect of the seasonally varying atmospheric temperature on the muon flux are outlined. In section 4.2, a measurement of the cosmic muon flux and its seasonal modulation using the Borexino detector is presented. Further, the correlation between the cosmic muon flux and the atmospheric temperature is explored in this section. The chapter closes with an investigation of the presence of long-term, i.e. longer than seasonal, modulations of the cosmic muon flux and an exploration of a correlation of the cosmic muon flux modulation to the solar activity in section 4.3.

4.1 Seasonal Modulation of the Cosmic Muon Flux

Muons arriving at laboratories situated deep underground predominantly originate from decays of mesons high in the atmosphere. Minor contributions arise from atmospheric neutrino CC interactions in which muons in or around the detector are generated. Figure 4.1 gives an overview of the processes and locations relevant for the production of cosmic muons in the upper atmosphere and their passage towards a detector situated deep underground.
The parent mesons, mostly kaons and pions, are produced in hadronic interactions between primary cosmic ray particles and nuclei of the atmosphere depicted by the blue dots. The mesons may either interact with other particles in the upper atmosphere producing electromagnetic cascades of lower-energetic particles or decay in flight into high-energetic muons and the corresponding neutrinos. However, only the muons produced if the mesons decay without interacting before the decay obtain sufficient energy to penetrate through the rock coverage and reach detectors deep underground [174].
The scenario for the production of a high-energetic muon is shown for a kaon decay on the left and for a pion decay in the middle of figure 4.1. The mesons produced in interactions of primary cosmic radiation in the upper atmosphere decay in flight. Thus, the generated muons receive sufficient energy to penetrate the rock coverage and reach a detector situated deep underground represented by the light blue sphere. The production of high-energetic muons is mostly limited to the stratosphere, a part of the atmosphere extending from the tropopause at $\sim 12\,\mathrm{km}$ above the Earth's surface to a height of $\sim 50\,\mathrm{km}$. The lower part of the atmosphere, the so-called troposphere, is only of minor importance for the production of high-energetic cosmic muons [175].
The case for an interaction of the meson before its decay is depicted on the right in figure 4.1, exemplarily for a pion. After its production, the pion interacts and produces an electromagnetic shower of lower-energetic particles. The muon produced in the eventual decay of the pion does not possess the required energy to reach the detector underground and is absorbed in the rock coverage.
Due the required in-flight decay of the mesons to produce muons with sufficient energy to reach underground detectors, the temperature of the upper atmosphere affects the muon flux observed underground. Since a rise in the temperature of the atmosphere lowers its density, the probability that the mesons decay before interacting with other particles increases and also the production of muons with energies high enough to reach underground detectors rises for higher temperatures [175]. Besides this change of the density and the increased production of high-energetic muons, an increase in temperature implies an expansion of the atmosphere re-

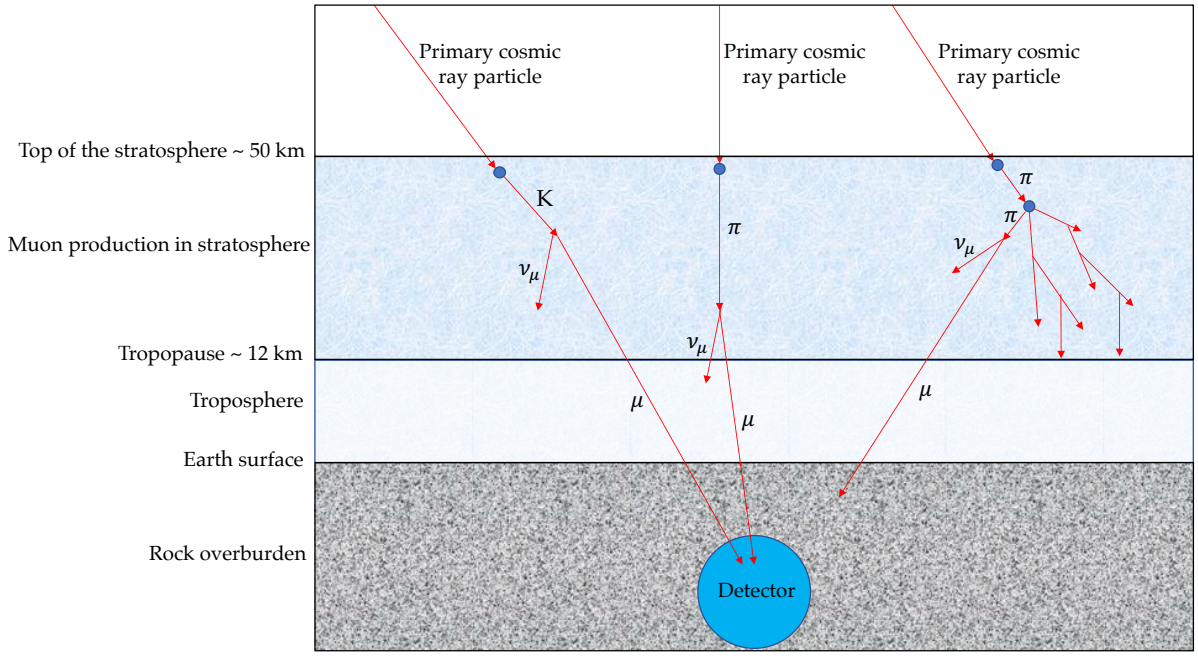

Figure 4.1: Processes and locations relevant for cosmic muon production. Primary cosmic radiation hits the upper atmosphere and produces mesons in interactions with nuclei depicted by the blue dots. These unstable mesons, mostly kaons and pions, decay into muons and the corresponding neutrinos. Most of the cosmic muons are produced in the stratosphere that extends from $\sim$ 12 km to $\sim$ 50 km above the Earth's surface. To penetrate the rock coverage and reach a detector situated deep underground, the muons are bound to be produced by meson decays in flight without any interaction before the decay. This is depicted for a kaon decay in flight on the left and for a pion decay in flight in the middle. In case the meson interacts before decaying, electromagnetic cascades of lower-energetic particles are generated. The muon eventually produced in the final decay of the meson does not receive sufficient energy to penetrate the rock coverage and is absorbed. Such a scenario is depicted on the right for a pion produced in the upper atmosphere.

sulting in a higher altitude at which primary cosmic ray particles interact with atmospheric nuclei and produce mesons [175].
The positive correlation between the temperature and the observed muon flux gets more pronounced the higher the required muon energy is. Higher-energetic mesons travel a longer distance before decaying and are, thus, more sensitive to density variations. For very low-energetic muons, the effect is reversed and the flux decreases for higher atmospheric temperatures. This is caused by the increased probability that the muons decay into electrons and the corresponding neutrinos

before arriving at the Earth due to the higher production altitudes. For underground experiments with a coverage of more than 44 m we, the arriving muons are, however, too high-energetic to observe this effect [175].
The decays of the mesons in which high-energetic muons are produced occur mostly at the top part of the atmosphere and the temperature of the stratosphere varies only slowly on the scale of seasons. Short-term weather phenomena are usually limited to the troposphere [176]. An exception are stratospheric warmings that can rapidly increase the temperature of the polar stratosphere in winter [177]. Hence, the flux of high-energetic cosmic muons is expected to show a seasonal modulation with maxima of the flux in summer when the temperature of the atmosphere is high and the density low and minima of the flux correlated to the low atmospheric temperatures and high densities in winter. The cosmic muon flux is, thus, expected to feature a sinusoidal behavior at leading order. However, short term temperature fluctuations and the fact that the temperature maxima do not necessarily occur at the same date in successive years perturb this approximation [174].
In the following two sections, a theoretical description of the expected intensity of cosmic muons underground and the effect of variations of the atmospheric temperature is displayed.

4.1.1 Muon Intensity Underground

Since most of the cosmic muons reaching the Borexino detector originate in the decays of pions and kaons in the upper atmosphere, the muon intensity is directly coupled to the production of these mesons in hadronic interactions of primary cosmic ray particles with the nuclei of the air molecules in the atmosphere.
Primary cosmic radiation arrives isotropically at the top of the atmosphere at a rate of $\sim 1,000\,\mathrm{m}^{-2}\,\mathrm{s}^{-1}$ [79]. To derive a prediction for the meson intensities in the atmosphere, it is anticipated that the production of mesons and other particles falls exponentially with the amount of atmospheric slant depth X traversed by the primary cosmic ray particle according to $e^{-X/\Lambda_\mathrm{N}}$. The slant depth is measured in the unit $\mathrm{g/cm}^2$ and allows to compare the penetration of particles in environments or materials of different densities. Λ_N is the absorption mean free path of the meson-producing cosmic ray particle expressed in the same units. Further, the mesons are assumed to maintain the direction of the initial primary cosmic ray particle, which is valid especially for the high-energetic mesons producing muons that can be observed underground. Ionization losses in the atmosphere are neglected in the following evaluations and Λ_N is treated as a constant. Also these assumptions are expected to be good approximations with respect to the production and propagation of mesons relevant for the generation of muons observed in Borexino.
Two absorption processes of the mesons are considered. First, nuclear interaction

for which the fractional loss in a thickness $\mathrm{d}X$ is $\mathrm{d}X/\Lambda_\mathrm{M}$ with Λ_M the absorption mean free path of the meson. The second relevant process is the decay of the meson into a muon for which the fractional loss is given by [175]

$$\mathrm{d}N_\mathrm{M}(\mathrm{M} \to \mu + \nu_\mu) = \frac{m_\mathrm{M} c}{p'} \frac{\mathrm{d}X}{\rho c \tau_\mathrm{M}}, \tag{4.1}$$

where ρ is the air density, τ_M the meson lifetime, m_M the meson's mass, p' its momentum, and c the speed of light.
For the meson species M, a critical energy ϵ_M that separates the regime in which nuclear interaction dominates from the regime in which decay dominates can be calculated as

$$\epsilon_\mathrm{M} = \frac{m_\mathrm{M} c^2 H(T)}{c\tau_\mathrm{M}}. \tag{4.2}$$

In this equation, $H(T)$ is the atmospheric scale height in dependence on the temperature T. The atmospheric scale height is defined as the increase in altitude for which the pressure decreases by a factor e and given by $H(T) = R_0 T/Mg$. Here, R_0 is the specific gas constant, M the mean molecular mass of an atmospheric particle, and g the acceleration of gravity. The density ρ and the depth X are related via $\rho = X \cos\theta / H(T)$.
Within the first $250\,\mathrm{g/cm^2}$ of the atmosphere, T and H are practically independent of X [175]. Since most of the interactions of the primary radiation occur in the first interaction lengths [79], $H(T)$ can be treated as a constant with respect to the meson production and $H(T) \approx H_0 = 6.5\,\mathrm{km}$. Thus, a critical pion energy $\epsilon_\pi = 115\,\mathrm{GeV}$ and a critical kaon energy $\epsilon_\mathrm{K} = 850\,\mathrm{GeV}$ result [176].
The assumptions concerning the meson production and absorption made in the beginning together with these considerations lead to the differential meson intensity [175]:

$$\frac{\mathrm{d}\mathcal{M}}{\mathrm{d}X} = \frac{Z_\mathrm{NM}}{\lambda_\mathrm{N}} N_0(E) e^{-X/\Lambda_\mathrm{N}} - \mathcal{M}(E, X, \cos\theta) \left[\frac{1}{\Lambda_\mathrm{M}} + \frac{\epsilon_\mathrm{M}}{EX\cos\theta} \right]. \tag{4.3}$$

Here, λ_N denotes the nucleon interaction length, $N_0(E)$ the differential meson production spectrum of the form $E_\mathrm{M}^{-(\gamma+1)}$, and Z_NM the spectrum weighted inclusive cross section. The first term on the right side of equation 4.3 describes the production of mesons by primary cosmic rays, the second term the absorption of mesons due to nuclear interaction and decay.
Using the integrating factor

$$\mu(X) = e^{\int \mathrm{d}X \, \frac{1}{\Lambda_\mathrm{M}} + \frac{\epsilon_\mathrm{M}}{EX\cos\theta}}, \tag{4.4}$$

equation 4.3 may be rewritten as an exact differential equation:

$$\mu(X)\frac{\mathrm{d}\mathcal{M}}{\mathrm{d}X} + \mu(X)\mathcal{M}(E, X, \cos\theta)\left[\frac{1}{\Lambda_\mathrm{M}} + \frac{\epsilon_\mathrm{M}}{EX\cos\theta}\right] = \frac{\mathrm{d}}{\mathrm{d}X}\left(\mu(X)\mathcal{M}(E, X, \cos\theta)\right) = \mu(X)\frac{Z_\mathrm{NM}}{\lambda_\mathrm{N}}N_0(E)e^{-X/\Lambda_\mathrm{N}}. \tag{4.5}$$

The solution of this exact differential equation is found as

$$\mathcal{M}(E, X, \cos\theta) = \frac{1}{\mu(X)}\int \frac{Z_\mathrm{NM}}{\lambda_\mathrm{N}}N_0(E)e^{-X/\Lambda_\mathrm{N}}\mu(X)\mathrm{d}X. \tag{4.6}$$

Solving the integral yields for the differential meson intensity [175]

$$\begin{aligned}\frac{\mathrm{d}\mathcal{M}}{\mathrm{d}X} &= \frac{Z_\mathrm{NM}}{\lambda_\mathrm{N}}N_0(E)e^{-X/\Lambda_\mathrm{M}}X^{-\epsilon_\mathrm{M}/E\cos\theta}\int_0^X X'^{\epsilon_\mathrm{M}/E\cos\theta}e^{X'/\Lambda'}\mathrm{d}X' \\ &= \frac{Z_\mathrm{NM}}{\lambda_\mathrm{N}}N_0(E)e^{-X/\Lambda_\mathrm{M}}X \times \left\{\frac{1}{\epsilon_\mathrm{M}/E\cos\theta + 1} - \frac{X/\Lambda'}{\epsilon_\mathrm{M}/E\cos\theta + 2}\right. \\ &\qquad \left. + \frac{1}{2!}\frac{(X/\Lambda')^2}{\epsilon_\mathrm{M}/E\cos\theta + 3} - \dots\right\},\end{aligned} \tag{4.7}$$

where the definition $1/\Lambda' \equiv 1/\Lambda_\mathrm{N} - 1/\Lambda_\mathrm{M}$ is introduced.
From this differential meson intensity describing the production and propagation of mesons in the atmosphere, the muon production spectrum has to be derived. The cosmic muons possessing sufficient energy to reach a detector as deep as Borexino are mostly produced in the decays of pions and kaons, i.e. via

$$\pi^{+/(-)} \rightarrow \mu^{+/(-)} + {}^{(}\overline{\nu}_\mu^{)} \tag{4.8}$$

and

$$\mathrm{K}^{+/(-)} \rightarrow \mu^{+/(-)} + {}^{(}\overline{\nu}_\mu^{)}, \tag{4.9}$$

respectively. Besides the muon, also an atmospheric muon neutrino or muon antineutrino is produced in these decays depending on the charge of the parent meson to conserve lepton family number. Minor contributions to the cosmic muon flux from decays of particles composed of charm quarks like the Δ_C^+ hyperon are extremely small compared to the number of muons produced in kaon and pion decays [135]. Thus, they are neglected in these considerations. Due to the negligible mass of the neutrino, the rest frame momentum of the two body decays described by equations 4.8 and 4.9 is given by $p_\mathrm{r} = (1 - m_\mu^2/m_\mathrm{M}^2)\cdot m_\mathrm{M}/2$. The differential flux per energy can be expressed as [178]

$$\frac{\mathrm{d}n}{\mathrm{d}E} = \frac{Bm_\mathrm{M}}{2p_\mathrm{r}E_\mathrm{L}} \tag{4.10}$$

with B the branching ratio for the decay into muons and E_{L} the momentum of the decaying meson in the laboratory frame. The branching ratio for the decay of charged pions into muons is $\sim 100\%$, the branching ratio for the decay of charged kaons into muons $\sim 63.5\%$ [79].
Based on these evaluations, the muon production spectrum for muons originating from meson decays may be expressed as [79]

$$\mathcal{P}(E, X, \cos\theta) = \sum_{\mathrm{M}} \int_{E_{\min}}^{E_{\max}} \frac{\mathrm{d}n(E, E')}{\mathrm{d}E} \frac{\epsilon_{\mathrm{M}}}{E' X \cos\theta} \mathcal{M}(E', X, \cos\theta) \mathrm{d}E'. \tag{4.11}$$

Here, $\frac{\mathrm{d}n(E,E')}{\mathrm{d}E}$ is the inclusive spectrum of muons from the decay of a meson M with the energy E', $\frac{\epsilon_{\mathrm{M}}}{E' X \cos\theta}$ describes the decay rate of the meson M as described above, and the sum considers all relevant meson species. The integration limits $E_{\min}$ and $E_{\max}$ are given by the minimum and maximum energies of a parent meson being able to produce a muon of the energy E [79].
With inserting equation 4.10 in equation 4.11, the muon production spectrum for each parent meson becomes

$$\mathcal{P}_{\mu}(E_{\mu}, X, \cos\theta) = \frac{B\epsilon_{\mathrm{M}}}{X \cos\theta (1 - r_{\mathrm{M}})} \int_{E_{\mu}}^{E_{\mu}/r_{\mathrm{M}}} \frac{\mathrm{d}E}{E} \frac{\mathcal{M}(E, X, \cos\theta)}{E} \tag{4.12}$$

with $r_{\mathrm{M}} = m_{\mu}^2 / m_{\mathrm{M}}^2$ the ratio of the squared muon and meson masses. For the decay of a relativistic meson with the energy E into a muon and a corresponding neutrino, the kinematic limits on the energy of the muon in the laboratory frame E_{μ} are given by [79]

$$\frac{m_{\mu}^2}{m_{\mathrm{M}}^2} \cdot E \leq E_{\mu} \leq E. \tag{4.13}$$

Inverting these limits of the muon energy E_{μ} for a given meson energy E gives the integration limits of equation 4.12.
To retrieve the differential muon energy spectrum, this expression must be integrated over the whole atmosphere [79]:

$$\begin{aligned} \frac{\mathrm{d}I_{\mu}}{\mathrm{d}E_{\mu}} &= \int_0^{\infty} \mathcal{P}_{\mu}(E, X) \mathrm{d}X \\ &\simeq A \times E_{\mu}^{-(\gamma+1)} \left(A_{\pi\mu} \frac{1}{1 + 1.1 \cdot E_{\mu} \cos\theta / \epsilon_{\pi}} + A_{\mathrm{K}\mu} \frac{0.635}{1 + 1.1 \cdot E_{\mu} \cos\theta / \epsilon_{\mathrm{K}}} \right), \end{aligned} \tag{4.14}$$

where

$$A_{\mathrm{M}\mu} \equiv Z_{\mathrm{NM}} \frac{1 - r_{\mathrm{M}}^{-(\gamma+1)}}{(1 - r_{\mathrm{M}})(\gamma + 1)}$$

and $\gamma = 1.78 \pm 0.05$ the muon spectral index as measured by the LVD experiment [131]. Inserting numeric values for the constants as given in [79], equation 4.14 becomes

$$\frac{\mathrm{d}I_\mu}{\mathrm{d}E_\mu} \simeq \frac{0.14 \times E^{-(\gamma+1)}}{\mathrm{cm}^2\,\mathrm{sr}\,\mathrm{GeV}} \left(\frac{1}{1 + 1.1 E_\mu \cos\theta/\epsilon_\pi} + \frac{\eta}{1 + 1.1 E_\mu \cos\theta/\epsilon_\mathrm{K}} \right) \tag{4.15}$$

with [179]

$$\eta \equiv 0.635 \cdot \frac{Z_\mathrm{NK}}{Z_{\mathrm{N}\pi}} \frac{1 - r_\pi}{1 - r_\mathrm{K}} \frac{1 - r_\mathrm{K}^{\gamma+1}}{1 - r_\pi^{\gamma+1}} = 0.054. \tag{4.16}$$

To determine the muon intensity in an underground laboratory, this expression needs to be integrated from a certain threshold energy E_thr to infinity. The threshold energy describes the minimum energy a muon has to possess to traverse the rock coverage of the underground laboratory and reach the experimental site. Thus, the intensity of muons observed in an underground laboratory is given by

$$I_\mu(E) = \int_{E_\mathrm{thr}}^{\infty} \mathrm{d}E_\mu \frac{\mathrm{d}I_\mu}{\mathrm{d}E_\mu}. \tag{4.17}$$

E_thr depends on the rock coverage $D(\theta, \phi)$ a muon coming from the direction defined by the zenith angle θ and the azimuth angle ϕ has to pass through in order to reach the detector. The rock coverage is usually presented as the product of the depth of the detector depending on the muon's direction and the average density of the shielding to receive a measure in the normalized unit of meter water equivalent (m we). While traversing the rock, muons lose energy by ionization and the radiative processes bremsstrahlung, $\mathrm{e}^+\mathrm{e}^-$ pair production, and photonuclear interactions. The total energy loss of the muons in dependence on the amount of rock traversed $D(\theta, \phi)$ is given by [7]

$$-\frac{\mathrm{d}E_\mu}{\mathrm{d}D(\theta,\phi)} = a + bE_\mu \tag{4.18}$$

with a describing the ionization loss and b the fractional energy loss by the three radiation processes. $\epsilon = a/b \approx 500\,\mathrm{GeV}$ for standard rock describes a critical energy for muons below which the continuous ionization loss is more relevant than radiative energy losses. The solution of this differential equation 4.18 is derived as

$$E_\mu\left(D(\theta,\phi)\right) = E_0 e^{-bD(\theta,\phi)} - \epsilon. \tag{4.19}$$

Hence, the energy of a muon at the surface E_0 that reaches an underground laboratory under a rock coverage $D(\theta, \pi)$ with energy E_μ is given by

$$E_0 = (E_\mu + \epsilon) e^{bD(\theta,\pi)} - \epsilon. \tag{4.20}$$

The threshold energy corresponding to the energy at the surface that enables a muon to barely reach the detector, i.e. with $E_\mu(D(\theta,\phi)) = 0$, may be calculated as

$$E_{\text{thr}} = \epsilon \cdot (e^{bD(\theta,\phi)} - 1). \tag{4.21}$$

In principle, the energy loss parameters vary slightly with energy. However, since this effect is very small, it is appropriate to assume $a \approx 2\,\text{MeV}/(\text{g}\,\text{cm}^{-2})$ [79] and $b \approx 4.0 \times 10^{-6}\,\text{g}^{-1}\text{cm}^2$ [180]. Using these values, the rock coverage of the Borexino detector of $3,800\,\text{m}$ we as measured from straight above corresponds to a muon threshold energy of $1.79\,\text{TeV}$. Performing the integration of equation 4.14 as described by equation 4.17, an approximation of the intensity of muons in an underground laboratory is obtained in [175] and given by

$$I_\mu \simeq B \times E_{\text{thr}}^{-\gamma} \left(\frac{1}{\gamma + (\gamma+1)1.1E_{\text{thr}}\cos\theta/\epsilon_\pi} + \frac{0.054}{\gamma + (\gamma+1)1.1E_{\text{thr}}\cos\theta/\epsilon_{\text{K}}} \right). \tag{4.22}$$

4.1.2 Temperature Effect on the Muon Intensity Underground

Mesons and consequently also the muons originating from their decays are produced at various heights in the atmosphere and temperature changes of the atmosphere do not occur uniformly but differently at multiple levels. It would, hence, be very difficult to determine the exact point in the temperature distribution where a certain muon was created and study the correlation between the temperature at the creation points and the intensity of muons observed deep underground. To allow the investigation of the effect of fluctuations in the atmospheric temperature on the flux of high-energetic cosmic muons, the atmosphere is modeled as an isothermal meson-producing entity with the effective temperature T_{eff}. T_{eff} must be chosen in a way that in an isothermal atmosphere with this temperature, the same meson intensity is obtained as in the actual atmosphere with the temperature distribution $T(X)$. Hence, properly chosen weights must be included in the calculation of the effective temperature accounting for the physics that determine the meson and muon production at different atmospheric depths.
To describe the effect of fluctuations in the atmospheric temperature on the muon intensity underground, the quantity $\eta \equiv (T(X) - T_{\text{eff}})/T_{\text{eff}}$ is defined [175]. Then, the critical meson energy, i.e. the energy separating the interaction and the decay regime for a particular meson M, becomes $\epsilon_{\text{M}} = \epsilon_{\text{M}}^0(1+\eta)$, where ϵ_{M}^0 is the critical meson energy for $T = T_{\text{eff}}$. Using these definitions, the differential meson intensity described by equation 4.3 can be expanded to account for its dependence on the

atmospheric temperature:

$$\frac{\mathrm{d}\mathcal{M}}{\mathrm{d}X} = \frac{Z_{\mathrm{NM}}}{\Lambda_{\mathrm{N}}} N_0 e^{-X/\lambda_{\mathrm{N}}} - \mathcal{M}(E, X, \cos\theta) \left[\frac{1}{\Lambda_{\mathrm{M}}} + \frac{\epsilon_{\mathrm{M}}^0 (1 + \eta(X))}{EX\cos\theta} \right]. \tag{4.23}$$

Since $\eta(X')$ is an arbitrary function of X', the analytic solution of this differential equation is difficult to find and must be approximated [178]. A solution to first order in $\eta(X')$ can be found by expanding the exponential in a power series and following the steps outlined to solve equation 4.3.
This solution can be expressed as $\mathcal{M}(E, X, \cos\theta) = \mathcal{M}^0 - \mathcal{M}^1$, where $\mathcal{M}^0$ describes the meson production spectrum for $\epsilon_{\mathrm{M}} = \epsilon_{\mathrm{M}}^0$, i.e. in the situation when the temperature $T = T_{\mathrm{eff}}$. $\mathcal{M}^1$ is found as:

$$\begin{aligned}\mathcal{M}^1(E, X, \theta) = \frac{Z_{\mathrm{NM}}}{\lambda_{\mathrm{N}}} N_0(E) e^{-X/\Lambda_{\mathrm{M}}} \left(\frac{X}{\Lambda_{\mathrm{M}}} \right)^{-\epsilon_{\mathrm{M}}^0/E\cos\theta} \frac{\epsilon_{\mathrm{M}}^0}{E\cos\theta} \\ \int_0^X \mathrm{d}X' \frac{\eta(X')\Lambda_{\mathrm{M}}}{X'} \left(\frac{X'}{\Lambda_{\mathrm{M}}} \right)^{\epsilon_{\mathrm{M}}^0/E\cos\theta+1} \left\{ \frac{1}{\epsilon_{\mathrm{M}}/E\cos\theta + 1} - \frac{X'/\Lambda'_{\mathrm{M}}}{\epsilon_{\mathrm{M}}/E\cos\theta + 2} \right. \\ \left. + \frac{1}{2!} \frac{(X'/\Lambda'_{\mathrm{M}})^2}{\epsilon_{\mathrm{M}}/E\cos\theta + 3} - \dots \right\}.\end{aligned} \tag{4.24}$$

This may be approximated for the high and for the low energy regime. If $E\cos\theta \ll \epsilon_{\mathrm{M}}^0$, the meson does not penetrate deep into the atmosphere before decaying and the integrand is only large for X' in the neighborhood of X. Thus, $\eta(X')$ can be taken out of the integral and replaced by $\eta(X)$. In the other case, where $E\cos\theta$ is not small compared to the critical energy ϵ_{M}^0, the correction term $\mathcal{M}^1$ is very small compared to $\mathcal{M}^0$ and the second-order error made by taking $\eta(X')$ out of the integral is negligible [175]. In this energy regime, interaction dominates since the time dilation effect allows the mesons to travel large distances before decaying.
With the solution of the meson production spectrum $\mathcal{M}$ for $T = T_{\mathrm{eff}}$ written as $\mathcal{M}^0$ and $\epsilon_{\mathrm{M}} = \epsilon_{\mathrm{M}}^0(1 + \eta)$, $\Delta\mathcal{M} \equiv \mathcal{M} - \mathcal{M}^0$ can be defined and expressed as [178]

$$\begin{aligned}\Delta\mathcal{M} = \frac{Z_{\mathrm{NM}}}{\lambda_{\mathrm{N}}} N_0(E) e^{-X/\Lambda_{\mathrm{M}}} \frac{\epsilon_{\mathrm{M}}^0 \eta X}{E\cos\theta} \times \left[\left\{ \frac{1}{(\epsilon_{\mathrm{M}}(X)/E\cos\theta + 1)^2} \right. \right. \\ \left. - \frac{X/\Lambda'_{\mathrm{M}}}{(\epsilon_{\mathrm{M}}(X)/E\cos\theta + 2)^2} + \frac{1}{2!} \frac{(X/\Lambda'_{\mathrm{M}})^2}{(\epsilon_{\mathrm{M}}(X)/E\cos\theta + 3)^2} - \dots \right\} \\ \left. - \left\{ \frac{1}{(\epsilon_{\mathrm{M}}^0/E\cos\theta + 1)^2} - \frac{X/\Lambda'_{\mathrm{M}}}{(\epsilon_{\mathrm{M}}^0/E\cos\theta + 2)^2} + \frac{1}{2!} \frac{(X/\Lambda'_{\mathrm{M}})^2}{(\epsilon_{\mathrm{M}}^0/E\cos\theta + 3)^2} - \dots \right\} \right].\end{aligned} \tag{4.25}$$

Writing this expression to first order in η yields

$$\Delta\mathcal{M} = \frac{Z_{\rm NM}}{\lambda_{\rm N}} N_0(E) e^{-X/\Lambda_{\rm M}} \frac{\epsilon^0_{\rm M}\eta X}{E\cos\theta} \times \left\{ \frac{1}{(\epsilon^0_{\rm M}/E\cos\theta+1)^2} - \frac{2X/\Lambda'_{\rm M}}{(\epsilon^0_{\rm M}/E\cos\theta+2)^2} + \frac{1}{2!}\frac{3(X/\Lambda'_{\rm M})^2}{(\epsilon^0_{\rm M}/E\cos\theta+3)^2} - \dots \right\}. \tag{4.26}$$

Considering equations 4.12 and 4.14, the variation of the meson production spectrum can be translated into an expression for the change in differential muon intensity:

$$\Delta\frac{{\rm d}I_\mu}{{\rm d}E_\mu} = \int_0^\infty {\rm d}X \frac{\epsilon^0_{\rm M}}{X\cos\theta(1-r_{\rm M})} \int_{E_\mu}^{E_\mu/r_{\rm M}} \frac{{\rm d}E}{E^2} \frac{Z_{\rm NM}}{\lambda_{\rm N}} N_0(E) e^{-X/\Lambda_{\rm M}} \frac{\epsilon^0_{\rm M}\eta X}{E\cos\theta} \times \left\{ \frac{1}{(\epsilon_{\rm M}/E\cos\theta+1)^2} - \frac{2X/\Lambda'_{\rm M}}{(\epsilon_{\rm M}/E\cos\theta+2)^2} + \frac{1}{2!}\frac{3(X/\Lambda'_{\rm M})^2}{(\epsilon_{\rm M}/E\cos\theta+3)^2} - \dots \right\}. \tag{4.27}$$

This can be written as [178]:

$$\Delta\frac{{\rm d}I_\mu}{{\rm d}E_\mu} = \frac{Z_{\rm NM}}{\lambda_{\rm N}} \left(\frac{\epsilon^0_{\rm M}}{E_\mu\cos\theta}\right)^2 \frac{E_\mu^{-(\gamma+1)}}{(1-r_{\rm M})} \int_0^\infty {\rm d}X e^{-X/\Lambda_{\rm M}} \eta I_{\rm M}(z), \tag{4.28}$$

where

$$I_{\rm M}(Z) = \int_1^{1/r_{\rm M}} \frac{{\rm d}z}{z^{-(\gamma+2)}} \times \left\{ \frac{1}{(\epsilon^0_{\rm M}/E\cos\theta+z)^2} - \frac{2X/\Lambda'_{\rm M}}{(\epsilon^0_{\rm M}/E\cos\theta+2z)^2} + \frac{1}{2!}\frac{3(X/\Lambda'_{\rm M})^2}{(\epsilon_{\rm M}/E\cos\theta+3z)^2} - \dots \right\}. \tag{4.29}$$

Solutions of this integral can be derived for $E_\mu \gg \epsilon_\pi$, described as $I^{\rm H}_\mu$, and for $E_\mu \ll \epsilon_\pi$, described as $I^{\rm L}_\mu$. These may be found as [178]

$$\begin{aligned} I^{\rm H}_\mu(E_\mu) &= \frac{1}{\gamma+3}\left[1-(r_{\rm M})^{\gamma+3}\right]\left\{1 - \frac{2X/\Lambda'_{\rm M}}{2^2} + \frac{1}{2!}\frac{3(X/\Lambda'_{\rm M})^2}{3^2} - \dots\right\} \\ &= \frac{1}{\gamma+3}\left[1-(r_{\rm M})^{\gamma+3}\right]\sum_{\rm n=0}^{\infty}\frac{(-X/\Lambda'_{\rm M})^{\rm n}}{{\rm n!(n+1)}} \\ &= \frac{1}{\gamma+3}\left[1-(r_{\rm M})^{\gamma+3}\right](1-e^{-X/\Lambda'_{\rm M}})\frac{\Lambda'_{\rm M}}{X} \end{aligned} \tag{4.30}$$

and

$$
\begin{aligned}
I_{\mu}^{\mathrm{L}}(E_{\mu}) &= \frac{1}{\gamma+1}\left[1-(r_{\mathrm{M}})^{\gamma+1}\right]\left(\frac{E_{\mu}\cos\theta}{\epsilon_{\mathrm{M}}}\right)^{2}\left\{1-2X/\Lambda'_{\mathrm{M}}+\frac{1}{2!}3(X/\Lambda'_{\mathrm{M}})^{2}-\dots\right\} \\
&= \frac{1}{\gamma+1}\left[1-(r_{\mathrm{M}})^{\gamma+1}\right]\left(\frac{E_{\mu}\cos\theta}{\epsilon_{\mathrm{M}}}\right)^{2}\sum_{\mathrm{n}=0}^{\infty}\frac{(-X/\Lambda'_{\mathrm{M}})^{\mathrm{n}}(\mathrm{n}+1)}{\mathrm{n}!} \\
&= \frac{1}{\gamma+1}\left[1-(r_{\mathrm{M}})^{\gamma+1}\right]\left(\frac{E_{\mu}\cos\theta}{\epsilon_{\mathrm{M}}}\right)^{2}(1-X/\Lambda'_{\mathrm{M}})e^{-X/\Lambda'_{\mathrm{M}}}.
\end{aligned}
\tag{4.31}
$$

The two solutions can be combined to get an expression valid for all energies and the change in the differential muon intensity can be approximated as [178]

$$
\Delta\frac{\mathrm{d}I_{\mu}}{\mathrm{d}E_{\mu}} \simeq \frac{E_{\mu}^{-(\gamma+1)}}{1-Z_{\mathrm{NM}}}\int_{0}^{\infty}\mathrm{d}X(1-X/\Lambda'_{\mathrm{M}})^{2}e^{-X/\Lambda'_{\mathrm{M}}}\eta(X)\frac{A_{\mathrm{M}}^{1}}{1+B_{\mathrm{M}}^{1}K(X)(E_{\mu}\cos\theta/\epsilon_{\mathrm{M}}^{0})^{2}}. \tag{4.32}
$$

In this expression,

$$
A_{\mathrm{M}}^{1} \equiv \frac{Z_{\mathrm{N},\mathcal{M}}}{(1-r_{\pi})}\frac{1-(r_{\mathrm{M}})^{\gamma+1}}{\gamma+1},
$$

$$
B_{\mathrm{M}}^{1} \equiv \frac{(\gamma+3)}{(\gamma+1)}\frac{1-(r_{\mathrm{M}})^{\gamma+1}}{1-(r_{\mathrm{M}})^{\gamma+3}},
$$

and

$$
K(X) \equiv \frac{(1-X/\Lambda'_{\mathrm{M}})^{2}}{(1-e^{-X/\Lambda'_{\mathrm{M}}})\Lambda'_{\mathrm{M}}/X}.
$$

In equation 4.32, the solution at low meson energies has been replaced with an approximation preserving the physical behavior of the system at low energies as outlined in the following. Low energy mesons are relatively insensitive to temperature changes since their path length before the decay is very small due to the short lifetime and the missing effect of time dilation. Hence, the passage of these mesons is not affected relevantly by the small changes in density caused by small temperature fluctuations. The expected behavior that low energy mesons produced in the interactions of primary cosmic rays with the atmosphere decay at large heights is accounted for in equation 4.32. However, the decays of these mesons do not contribute to the muons reaching detectors as deep as Borexino since the energies of the produced muons are well below the required threshold energy [178].
As X approaches Λ'_{M}, a slight dip in the distribution occurs that arises due to combining the high and low energy solutions of equation 4.28 in the approximated equation 4.32. The solution derived for low energy muons goes to zero for $X = \Lambda'_{\mathrm{M}}$ and falls below zero if $E_{\mu} \ll \epsilon_{\mathrm{M}}$. This is caused by the effect that very

low-energetic muons decay in flight into electrons and cause a deficit in muons correlated to positive temperature changes. The so-called negative temperature coefficient quantifying this correlation has been investigated in [175, 181] but it cannot be measured at detectors deeper than 44 m we [175] due to the absorption of the relevant low-energetic muons. The dip and subsequent rise in the spectrum for $X > 480\,\mathrm{g/cm^2}$ do not affect the analysis for deep detectors since the weights used to calculate the effective temperature consider that interactions in the lower atmosphere only play a minor role in the production of high-energetic muons [178]. These weights, which will be derived later in this section, are integrated over the entire atmosphere in discrete steps of $\mathrm{d}X$ and properly normalized such that this effect will not influence the analysis performed at a detector like Borexino.
With inserting $\eta(X) \equiv (T(X) - T_{\mathrm{eff}})/T_{\mathrm{eff}}$ in equation 4.32, the relation between atmospheric temperature fluctuations and the modulation of the cosmic muon flux can be expressed as

$$\Delta I_\mu \equiv \int_{E_{\mathrm{thr}}}^{\infty} \Delta \frac{\mathrm{d}I_\mu}{\mathrm{d}E_\mu} \mathrm{d}E_\mu = \int_0^{\infty} \mathrm{d}X \alpha(X) \frac{\Delta T(X)}{T_{\mathrm{eff}}} e^{X/\Lambda_{\mathrm{M}}} \tag{4.33}$$

with the temperature coefficient $\alpha(X)$ defined as

$$\alpha(X) = \int_{E_{\mathrm{thr}}}^{\infty} \mathrm{d}E_\mu \frac{A^1_{\mathrm{M}} E_\mu^{-(\gamma+1)}}{1 + B^1_{\mathrm{M}}(E_\mu \cos\theta/\epsilon_{\mathrm{M}})^2}. \tag{4.34}$$

Since cosmic muons originate from the decays of kaons and pions, for which M applies independently, the total muon intensity is the sum of the two contributions as in equation 4.22. The variation of the muon flux caused by temperature fluctuations can be written as

$$\Delta I_\mu \equiv \int_0^{\infty} \mathrm{d}X \alpha^\pi(X) \frac{\Delta T(X)}{T_{\mathrm{eff}}} e^{X/\Lambda_\pi} + \int_0^{\infty} \mathrm{d}X \alpha^{\mathrm{K}}(X) \frac{\Delta T(X)}{T_{\mathrm{eff}}} e^{X/\Lambda_{\mathrm{K}}}. \tag{4.35}$$

Up to this point, T_{eff} has been treated as an arbitrary temperature. However, T_{eff} needs to be determined by weights of the atmospheric levels such that the isothermal atmosphere approximation can be made. From $\eta(X) = (T(X) - T_{\mathrm{eff}})/T_{\mathrm{eff}}$, T_{eff} is defined as the temperature for which $\epsilon_{\mathrm{M}} = \epsilon^0_{\mathrm{M}}$ and, thus, $\Delta I_\mu = 0$. This leads to [178]

$$T_{\mathrm{eff}} = \frac{\int_0^{\infty} \mathrm{d}X\, T(X) \alpha^\pi(X) + \int_0^{\infty} \mathrm{d}X\, T(X) \alpha^{\mathrm{K}}(X)}{\int_0^{\infty} \mathrm{d}X\, \alpha^\pi(X) + \int_0^{\infty} \mathrm{d}X\, \alpha^{\mathrm{K}}(X)}. \tag{4.36}$$

Since, in practice, the temperature is measured at discrete levels, the integral is translated into a sum leading to

$$T_{\mathrm{eff}} \simeq \frac{\sum_{\mathrm{n}=0}^{N} \Delta X_{\mathrm{n}}\, T(X_{\mathrm{n}}) (W^\pi_{\mathrm{n}}(X_{\mathrm{n}}) + W^{\mathrm{K}}_{\mathrm{n}}(X_{\mathrm{n}}))}{\sum_{\mathrm{n}=0}^{N} \Delta X_{\mathrm{n}}\, (W^\pi_{\mathrm{n}}(X_{\mathrm{n}}) + W^{\mathrm{K}}_{\mathrm{n}}(X_{\mathrm{n}}))} \tag{4.37}$$

with the weight functions defined as [178]

$$W_{\mathrm{n}}^{\pi}(X_{\mathrm{n}}) \equiv \frac{A_{\pi}^{1} e^{-X_{\mathrm{n}}/\Lambda_{\pi}} (1 - X_{\mathrm{n}}/\Lambda_{\pi}')^2}{\gamma + (\gamma+1) B_{\pi}^{1} K(X_{\mathrm{n}}) (E_{\mathrm{thr}} \cos\theta/\epsilon_{\pi})^2},$$
$$W_{\mathrm{n}}^{\mathrm{K}}(X_{\mathrm{n}}) \equiv \frac{A_{\mathrm{K}}^{1} e^{-X_{\mathrm{n}}/\Lambda_{\mathrm{K}}} (1 - X_{\mathrm{n}}/\Lambda_{\mathrm{K}}')^2}{\gamma + (\gamma+1) B_{\mathrm{K}}^{1} K(X_{\mathrm{n}}) (E_{\mathrm{thr}} \cos\theta/\epsilon_{\mathrm{K}})^2},$$
$$K(X_{\mathrm{n}}) \equiv \frac{(1 - X_{\mathrm{n}}/\Lambda_{\mathrm{M}}')^2}{(1 - e^{-X_{\mathrm{n}}/\Lambda_{\mathrm{M}}'})\Lambda_{\mathrm{M}}'} / X_{\mathrm{n}}$$

and $1/\Lambda_{\mathrm{M}}' \equiv 1/\Lambda_{\mathrm{N}} - 1/\Lambda_{\mathrm{M}}$. By using appropriate values for the constants, a numerical value of the effective temperature can be found. The relevant values are $A_{\pi}^{1} = 1$, $A_{\mathrm{K}}^{1} = 0.38 \times r_{\mathrm{K}/\pi} = 0.054$ with the atmospheric kaon to pion production ratio $r_{\mathrm{K}/\pi}$, $B_{\pi}^{1} = 1.47$, and $B_{\mathrm{K}}^{1} = 1.74$. Further, $\Lambda_{\mathrm{N}} = 120\,\mathrm{g/cm^2}$, $\Lambda_{\pi} = 160\,\mathrm{g/cm^2}$, and $\Lambda_{\mathrm{K}} = 180\,\mathrm{g/cm^2}$ [79, 176]. The expected value for the threshold energy folded with the zenith angle distribution of muons arriving at a detector $\langle E_{\mathrm{thr}} \cos\theta \rangle$ is site dependent. Using a Monte Carlo simulation that includes the shape of the rock overburden of the LNGS, a value of $\langle E_{\mathrm{thr}} \cos\theta \rangle = (1.34 \pm 0.18)\,\mathrm{TeV}$ was found for the location of the Borexino experiment as described in section 5.2.1.
In the pion scaling limit, i.e. ignoring any kaon contribution, the expression for T_{eff} reduces to

$$T_{\mathrm{eff}} \simeq \frac{\sum_{\mathrm{n}=0}^{N} \Delta X_{\mathrm{n}}\, T(X_{\mathrm{n}}) 1/X_{\mathrm{n}} (e^{-X_{\mathrm{n}}/\Lambda_{\pi}} - e^{-X_{\mathrm{n}}/\Lambda_{\mathrm{N}}})}{\sum_{\mathrm{n}=0}^{N} \Delta X_{\mathrm{n}}\, 1/X_{\mathrm{n}} (e^{-X_{\mathrm{n}}/\Lambda_{\pi}} - e^{-X_{\mathrm{n}}/\Lambda_{\mathrm{N}}})}, \tag{4.38}$$

which recovers the calculation for the effective temperature published by the MACRO collaboration [182].
After the definition of the effective atmospheric temperature, a so-called effective temperature coefficient can be determined that relates changes in the effective temperature to fluctuations of the muon flux. This effective temperature coefficient is defined as [178, 182]

$$\alpha_{\mathrm{T}} \equiv \frac{1}{I_{\mu}^{0}} \int_{0}^{\infty} \mathrm{d}X \int_{E_{\mathrm{thr}}}^{\infty} \mathrm{d}E_{\mu} \frac{A_{\mathrm{M}}^{1} E_{\mu}^{-(\gamma+1)}}{1 + B_{\mathrm{M}}^{1} (E_{\mu} \cos\theta/\epsilon_{\mathrm{M}})^2} \tag{4.39}$$

with I_{μ}^{0} the intensity for a given temperature T. Using this, the dependence between atmospheric temperature fluctuations and the muon intensity can be expressed as

$$\frac{\Delta I_{\mu}}{I_{\mu}^{0}} = \int_{0}^{\infty} \mathrm{d}X\, \alpha(X) \frac{\Delta T(X)}{T_{\mathrm{eff}}} = \alpha_{\mathrm{T}} \frac{\Delta T_{\mathrm{eff}}}{T_{\mathrm{eff}}}. \tag{4.40}$$

For a properly weighted atmospheric temperature distribution, α_{T} is theoretically predicted to be [182]

$$\alpha_{\mathrm{T}} = \frac{T}{I_{\mu}^{0}} \frac{\partial I_{\mu}}{\partial T}. \tag{4.41}$$

Considering the muon spectrum as described by equation 4.14, this expression can be translated into [175]

$$\alpha_{\mathrm{T}} = -\frac{E_{\mathrm{thr}}}{I_\mu^0}\frac{\partial I_\mu}{\partial E_{\mathrm{thr}}} - \gamma. \tag{4.42}$$

With the intensity from equation 4.22, this leads to the effective temperature coefficient being predicted as

$$\alpha_{\mathrm{T}} = \frac{1}{D_\pi}\frac{1/\epsilon_{\mathrm{K}} + A_{\mathrm{K}}(D_\pi/D_{\mathrm{K}})^2/\epsilon_\pi}{1/\epsilon_{\mathrm{K}} + A_{\mathrm{K}}(D_\pi/D_{\mathrm{K}})/\epsilon_\pi}, \tag{4.43}$$

where

$$D_\pi \equiv \frac{\gamma}{\gamma+1}\frac{\epsilon_\pi}{1.1E_{\mathrm{thr}}\cos\theta} + 1$$

$$D_{\mathrm{K}} \equiv \frac{\gamma}{\gamma+1}\frac{\epsilon_{\mathrm{K}}}{1.1E_{\mathrm{thr}}\cos\theta} + 1$$

and $A_{\mathrm{K}} = 0.38 \times r_{\mathrm{K}/\pi} = 0.054$ as above [79, 176]. Neglecting the kaon contribution and setting $A_{\mathrm{K}} = 0$, this can be reduced to MACRO's expression for $\langle\alpha_{\mathrm{T}}\rangle_\pi$ [182]. Qualitatively summarizing the above evaluations, the atmosphere is composed of many different levels that vary continuously in temperature and pressure, which makes it extremely difficult to record the entire temperature distribution of the atmosphere and determine where exactly a muon and the corresponding meson have been produced. Hence, to study the effect of variations of the atmospheric temperature on the cosmic muon flux, the atmosphere is modeled as an isothermal meson-producing entity. However, since the atmosphere clearly is not an isothermal body, the weighting of the atmospheric levels must be done in a way that the essential hadron interaction physics are included to allow the description of the atmosphere with a characteristic temperature T_{eff} [175, 182]. The weights approximately increase exponentially with height since high energy muons are mostly produced in the upper atmosphere. Both the atmospheric temperature and the weights used to determine T_{eff} for the location of the LNGS are shown in figure 4.2.

The red line shows the ten year average of the temperature measured at several altitude layers at the location of the LNGS as provided by the European Center for Medium-range Weather Forecast (ECMWF) [183]. The temperature first falls with increasing height since the Earth's surface typically is the warmest spot in the troposphere. After the tropopause at $\sim 12\,\mathrm{km}$ height, the temperature decrease slows down before changing into a temperature increase. This increase is caused by the absorption of ultraviolet radiation from the Sun in the ozone layer, which is part of the stratosphere.

The weights calculated accordingly to equation 4.37 are shown by the black line. They reflect the main atmospheric features that determine the production of muons

reaching a detector under the rock shielding of the LNGS of $\sim 3,800$ mwe. Most probably, the cosmic ray protons interact at the very top of the atmosphere where, consequently, also most of the mesons decaying into high-energetic muons are produced. High energy mesons that are produced lower in the atmosphere have, due to the increased density, a higher probability to interact before decaying and, thus, to produce muons below the necessary energy to reach the Borexino detector. Additionally, the critical energies of the involved mesons are of decisive relevance for the computation of the weights since the ratio between the actual meson energy and the critical energy determines the probability of the meson to interact or to decay. A meson with higher energy than the critical energy is more likely to interact before it decays and this probability increases with increasing meson energy. These effects are considered in the determination of the weights for the various atmospheric temperature levels to enable the isothermal approximation, which results in an approximated $e^{-X/\Lambda_N}\mathrm{d}X$ trend of the weights.
For experiments aiming to explore the relation between fluctuations of the atmospheric temperature and the cosmic muon flux, the measured muon count rate needs to be related to the observed temperature fluctuations. This count rate is given by:

$$R_\mu = \int I_\mu(\Omega)\epsilon(\Omega)A_{\mathrm{tot}}(\Omega)\,\mathrm{d}\Omega, \tag{4.44}$$

where $R_\mu = N_\mu/t$ describes the number of muons observed over a certain time period t. A_{tot} is the effective area of the detector, ϵ is the efficiency of muon detection, and the expression needs to be integrated over the solid angle Ω. Since the geometry of the Borexino detector has not been changed during the time of the data acquisition, A_{tot} is constant for the present analysis. Further, due to the sphericity of the Inner Detector (ID), the acceptance is not dependent on the incident angle of a muon and a measurement with minimum systematics can be performed.
The absence of any non-constant background and the extremely high muon identification efficiency guaranty a stable experimental acceptance of the Borexino detector over time. Hence, equation 4.44 leads to

$$\frac{\Delta I_\mu}{I_\mu} = \frac{\Delta R_\mu/\epsilon(\Omega)A_{\mathrm{tot}}(\Omega)}{\langle R_\mu\rangle/\epsilon(\Omega)A_{\mathrm{tot}}(\Omega)} = \frac{\Delta R_\mu}{\langle R_\mu\rangle} \tag{4.45}$$

and variations of the rate of cosmic muons measured with the Borexino detector directly correspond to variations of the intensity of cosmic muons. Thus, the correlation between the measured signal and temperature fluctuations can be described as in equation 4.40 and

$$\int_0^\infty \mathrm{d}X\,\alpha(X)\frac{\Delta T(X)}{T(X)} = \alpha_{\mathrm{T}}\frac{\Delta T_{\mathrm{eff}}}{\langle T_{\mathrm{eff}}\rangle} = \frac{\Delta R_\mu}{\langle R_\mu\rangle}, \tag{4.46}$$

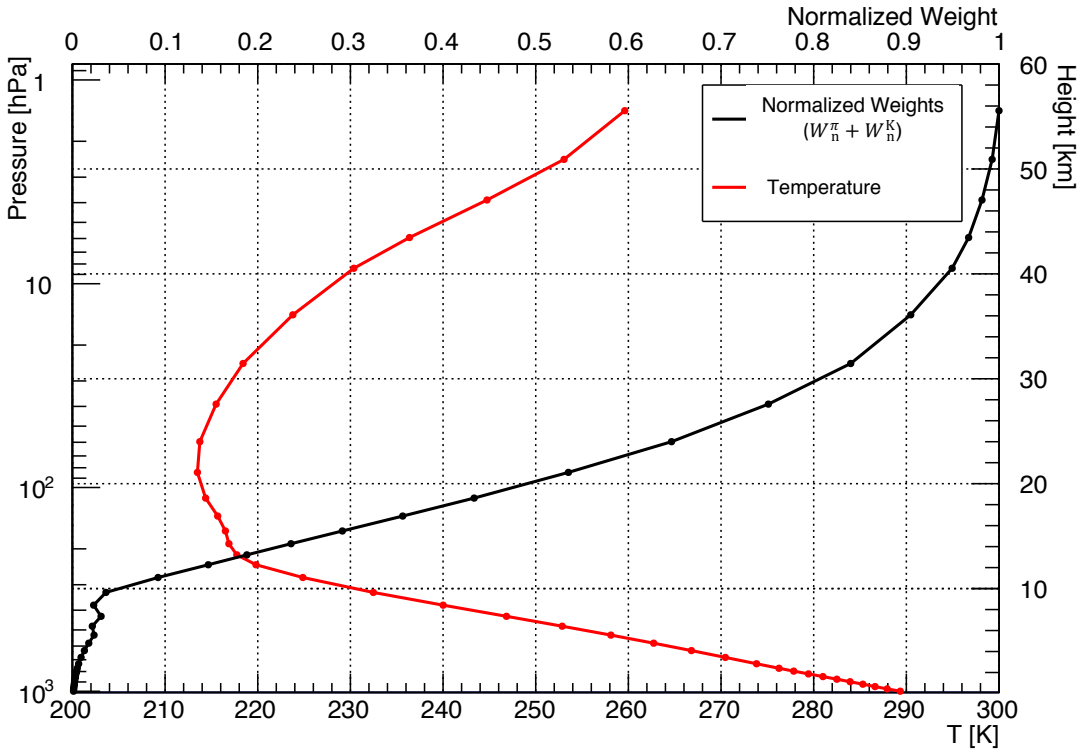

Figure 4.2: Atmospheric temperature and assigned weights to compute T_{eff}. The ten year average of the temperature at several atmospheric depths as provided by the ECMWF [183] for the location of the LNGS is shown by the red line. The black line shows the weights that determine the effective temperature in the isothermal atmosphere approximation computed accordingly to equation 4.37. The application of these weights allows to model the clearly non-isothermal atmosphere as an isothermal meson-producing entity with the effective temperature T_{eff}.

which allows to determine the effective temperature coefficient α_{T}.
With increasing muon energy, the intensity becomes proportional to the meson critical energy that depends linearly on the atmospheric temperature. Hence, the effective temperature coefficient approaches a value of $\alpha_{\text{T}} = 1$ for muons of highest energies or measurements carried out extremely deep underground. Thus, the dimensionless parameter α_{T} qualitatively determines the fraction of mesons that contribute to the observed cosmic muon flux and are sensitive to temperature variations of the atmosphere [178].

4.2 Measurement of the Seasonal Modulation of the Muon Flux at Borexino

In Borexino, muons are identified by two different approaches using data from the OD muon veto and one additional algorithm based on ID data. First, muons are flagged by the hardware trigger of the OD, the Muon Trigger Board (MTB). This custom 6U VME unit developed for Borexino at the Massachussets Institute of Technology issues a trigger if at least six PMT hits are recognized within 150 ns in the OD. This threshold efficiently avoids dark noise triggers, however, light entering the water tank through leaks may cause the trigger to be issued [80].
While the MTB is a pure hardware tag, the Muon Clustering algorithm (MCR) complementarily provides a software based muon identification method using OD data. The algorithm searches for clusters of PMT hits in two subsets of OD PMTs, the PMTs on the SSS surface and the PMTs on the floor of the water tank. The flag is set if an event causes at minimum four PMTs to give a signal in at least one of the PMT subsets within 150 ns [108].
The Inner Detector Flag (IDF) uses the large light output caused by a muon passing the ID and the different pulse shape of muons compared to point-like neutrino events to identify cosmic muons. Thus, the peak time of an event, i.e. the time between the onset of the pulse and the peak, the meantime, i.e. the average time difference of a hit to the onset of the pulse, and the Gatti parameter [117] that is described in section 7.6 are utilized to identify muon events [108].
Due to the complexity of the IDF condition and the special care that must be taken not to mistakenly identify neutrino signal events as muons, the efficiency of the OD tags is higher than for the IDF, which provides an efficiency of $\epsilon_{\mathrm{IDF}} \geq (98.90 \pm 0.02)\%$ [108]. Further, the MCR has been found to provide a slightly higher muon identification efficiency of $\epsilon_{\mathrm{MCR}} \geq (99.28 \pm 0.02)\%$ than the MTB with $\epsilon_{\mathrm{MTB}} \geq (99.25 \pm 0.02)\%$ [108] and it features a higher operational time since the MTB was only installed four weeks after the start of data taking. However, since the OD data was read out nevertheless, the MCR could be used to identify cosmic muons right from the beginning. Based on these considerations, muons are defined as events that are identified by the MCR and also trigger the ID in the present analysis. The sphericity of the ID guarantees a measurement with minimum systematics and an acceptance independent of the muon's incident angle.
Data taken in ten years from May 16th, 2007 to May 15th, 2017 are used. A day-wide binning is applied on the measured muon flux. To prevent statistical instabilities in the data sample, only data acquired on $3,218$ days at which a minimum detector livetime of eight hours was provided are considered. With the cross section for muon interactions of $146\,\mathrm{m}^2$ defined by the radius of the SSS, the resulting effective exposure of the dataset is $\sim 4.2 \times 10^5\,\mathrm{m}^2\mathrm{d}$, in which $\sim$

1.2×10^7 muons were recorded. Besides the phase of the purification campaign in 2010 and 2011 prior to the second phase of the Borexino solar neutrino program, no prolonged downtime of the detector affects the dataset.
In section 4.2.1, the efficiency of the applied muon definition is investigated in more detail. After describing how events related to the CERN Neutrino to Gran Sasso (CNGS) beam can be removed from the data sample in section 4.2.2, the results of the measurement of the seasonal modulation of the cosmic muon flux are presented in section 4.2.3. In section 4.2.4, a study of the correlation between the flux of cosmic muons measured by Borexino and the atmospheric temperature is performed.

4.2.1 Efficiency of the Muon Identification

With the definition of muons as events that are tagged by the MCR and also produce a trigger in the ID, the efficiency of the muon identification is determined by the MCR since the low energy threshold of the ID absolutely guarantees a light registration and the associated trigger generation if a muon crosses this subdetector.
To estimate the efficiency of the MCR, a pure sample of muons is needed to test if these events are identified by the MCR. Due to the correlation between the MCR and the MTB, the sample needs to be based solely on ID data since this subdetector is completely independent from the OD in terms of light propagation. Such a pure muon sample can be provided by events tagged as muons by the IDF. This software tag based on pulse shape discrimination techniques reliably identifies muons in the ID and provides huge statistics for the efficiency estimation. Only very small contaminations caused by, e.g., fast neutrons or atmospheric neutrino NC and CC interactions as explored in chapter 7 are expected in this reference sample.
Further, the MCR may be tested based on a sample of high-energetic events that generate more than $5,000$ PMT hits in the ID. Since this threshold equals an energy deposition of $(20-30)$ MeV for point-like events, it lies well above the endpoints of the solar neutrino spectra and the kinetic energies of the decay products of the ^{238}U and ^{232}Th chains. Also this sample is expected to contain extremely small contaminations from atmospheric neutrino interactions and fast neutrons. However, a slightly higher level of contamination compared to the IDF tagged sample is expected since no pulse shape discrimination is applied and the IDF is tuned to not misidentify neutrino signal events as muons. Thus, its overefficiency is kept at a minimum.
Since all muons entering the ID have to cross several meters of water independent of their energy deposition in the ID, the estimated efficiency based on these tests is expected to be valid for all muon energies and tracks through the ID [108]. The

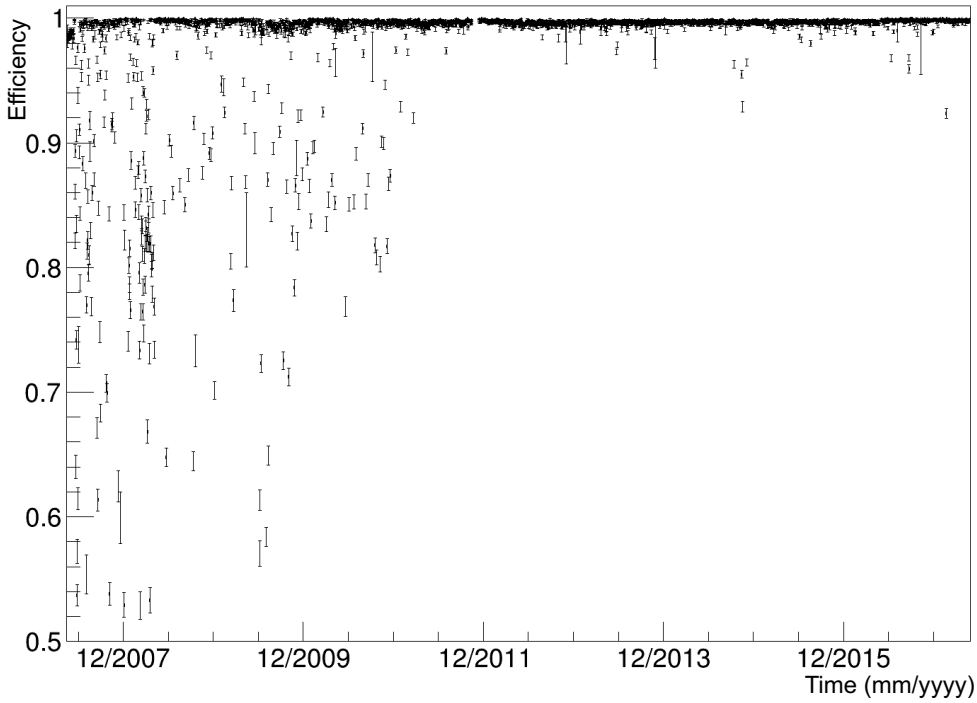

Figure 4.3: Efficiency of the MCR computed via a sample of IDF tagged events.

independence of the two subdetectors in terms of light propagation further ensures this assumption. Due to the small contaminations of the reference samples, the calculated values constitute lower limits of the actual muon identification efficiency.
In principle, muons originating from the CNGS beam [184] as described in section 4.2.2 could also be used as a reference sample for the MCR. However, the OD is tuned to identify cosmic muons that arrive mainly from directions close to vertical such that an efficiency determination using the horizontally arriving CNGS muons would strongly underestimate the efficiency of the MCR for cosmic muon identification.
Figure 4.3 shows the efficiency of the MCR as calculated based on a sample of events tagged by the IDF. The MCR shows some inefficiencies for the years from 2007 to 2010 that are caused by runs for which the OD data acquisition failed and the MCR could not be performed. For data taken later and especially for the second phase of Borexino after the purification campaign in 2010 and 2011, the MCR is found to work reliably and identify muons at a very high and stable efficiency. However, some days with a lower efficiency are still observed. The effect of the small efficiency variations is taken into account by correcting the measured muon rate on a daily basis with the computed efficiency. The small gap in the data belongs to a period of water extractions during the calibration campaign in 2011

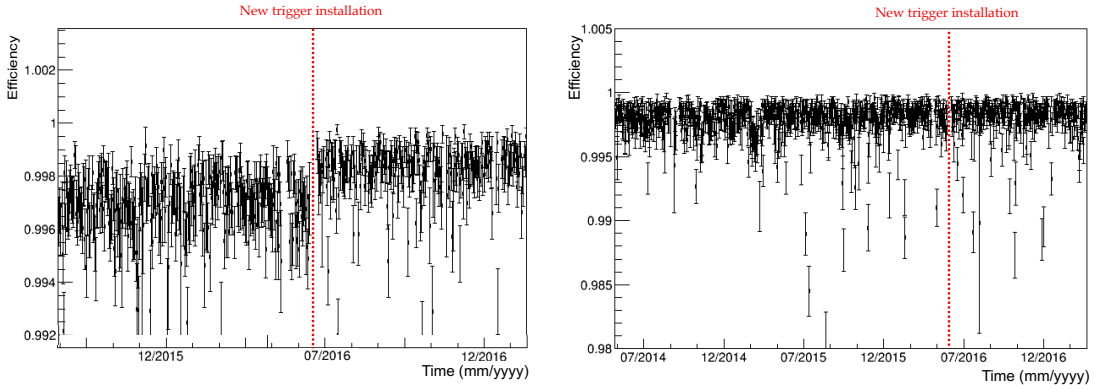

Figure 4.4: Efficiency of the MCR around the installation of the new trigger system. On the *left* side, the efficiency including all possible values of the BTB input are shown, the *right* side shows the constant efficiency when events featuring BTB input values provided for service triggers are excluded.

that was excluded from the analysis.
Further, a significant increase of the muon identification efficiency in May 2016 may be guessed in figure 4.3 and becomes evident on the left side of figure 4.4 that shows a zoom in the relevant time region. This increase is caused by the installation of a new trigger system that was assembled to mitigate the aging process of the trigger system and enhance its flexibility and ability to detect physical events. The time when the new setup was installed is marked by the red line in figure 4.4 and the efficiency increase afterwards is clearly visible on the left side. As detailed in the following, the MCR efficiency was mainly affected by a change of the way service triggers are issued. First, the general trigger handling in Borexino is described after which emphasis to the service trigger generation in the two systems is given.
Every signal occurring in the detector is registered at the Borexino Trigger Board (BTB), a custom double 6U VME device that potentially issues a trigger. Eight ID PMT outputs are collected in one digital Laben board in which all hits registered at the PMTs together with the corresponding time are stored for $\sim 6.5\,\mu$s [185]. These digital boards were developed in collaboration with the Laben S.p.A. company [186]. Whenever the collective sum of hits registered at all Laben boards exceeds a threshold of twenty PMT hits within 100 ns, a comparator signal is sent to the BTB that registers this input and, consequently, opens a gate of $16\,\mu$s for the data acquisition. With the opening of the gate, the hits in the storage of the Laben boards are read until the gate is closed. Besides the comparator, the BTB may receive several further inputs causing it to issue a trigger as summarized in table 4.1. Different priorities are assigned to the respective inputs reflecting the importance of a trigger signal. Depending on the type of the event, a trigger type

Trigger	Trigger Type	BTB Input	Priority
Neutrino	1	0	1
Muon MTB	2	4	2
Neutron Gate	128	8	3
Laser355	4	16	4
Laser266	16	32	5
Laser394	8	64	7
Calibration	32	64	6
Random	64	64	8

Table 4.1: Trigger types and corresponding BTB inputs used in Borexino. For OD triggers, the MTB sends an input value of 4 to the BTB that issues the trigger. Service triggers are issued with a BTB input value of 64, neutrino type events by a comparator signal with a BTB input value of 0. The associated trigger types of the respective event classes and the priority at which a certain BTB input is handled are listed additionally.

(TT) is assigned in the data acquisition process.
While the comparator firing is registered at an input value of 0 and is treated with the highest priority, the MTB can cause the generation of a trigger with the BTB input value of 4. However, the arrival of the MTB information is artificially delayed and for an ID muon, the comparator will cause the trigger generation. After its initialization, the MTB remains set for $\sim 6\,\mu$s and the BTB inputs are read 850 ns after the comparator firing was recognized. The event still gets flagged with a BTB input value of 4 but with a trigger type of 1 due to the comparator issuing the trigger. In case the muon only passes the OD and the MTB causes the trigger generation, the trigger type 2 is assigned to the event. After each event with triggers in both subdetectors, i.e. events with a comparator and an MTB input registered by the BTB, a gate of 1.6 ms is opened to collect cosmogenic neutrons. This special gate is started with a BTB input value of 8 and a trigger type of 128 is assigned to the events collected within the gate.
Besides the physical inputs, several service triggers may be issued. Thus, calibration triggers may be used to distribute calibration pulses to all ID channels, random triggers that are only artificial without any light generation may be used to study PMT dark noise, and laser triggers may be issued at which the ID PMTs are illuminated with a laser and the OD PMTs with an LED to study the timing of the PMTs. These are generated via an external clock setting up a BTB input value of 64. Different trigger types are assigned to distinguish the service trigger classes. The BTB inputs 16 and 32 may be run as special run modes [186].
The increase of the MCR efficiency was found to be caused by a different generation of the service triggers in the old and the new trigger system. The service

trigger generation and the associated reason for the tiny MCR inefficiency in the old setup are depicted qualitatively in figure 4.5. On the top, the behavior of the trigger for the interference of a muon with a service trigger generation is depicted. In the middle and on the bottom, qualitative illustrations of the pulses acquired in the ID and in the OD for such an event are shown, respectively.
In the old trigger system, a $\sim 230\,\mathrm{Hz}$ clock initiated the BTB input value of 64 that remained set for $27\,\mu\mathrm{s}$. This time window is depicted in green in the top part of figure 4.5. A prescale factor of 100 was applied and only at a rate of $\sim 0.5\,\mathrm{Hz}$, the service trigger was actually issued. However, the execution of the routine resulted in a blindness towards any inputs or comparator information of the BTB for $\sim 18\,\mu\mathrm{s}$ marked in black. If a muon arrived during this time, the MTB was set but did not generate a trigger and the initial increase of the comparator sum also passed unrecognized by the BTB. After the routine to create a service trigger was finished, a muon could eventually still produce a comparator trigger on its afterpulse, in which case the event was written. Potentially, depending on the actual arrival time of the muon relative to the end of the blind window caused by the service trigger generation routine, also the BTB input value of 4 might still have been set when the BTB inputs were read. In this case, the present BTB input values of 64 and 4 were summed and the event was tagged with a BTB input value of 68. If the BTB input value of 4 was not set anymore when the inputs were read, only the registered BTB input value of 64 was assigned.
For such an overlap of a muon with a service trigger generation and a registration of the muon on its afterpulse, the entire pulse could still be acquired in the ID. Since information on the hits on the ID PMTs is stored for $6.5\,\mu\mathrm{s}$ in the Laben boards, this information may be accessed even though the gate for the acquisition was opened late with respect to the onset of the pulse as depicted in the middle of figure 4.5. Thus, the IDF, potentially, still obtained enough information to identify the muon and the event enters in the reference sample.
However, in the OD, no hits are stored and only PMT hits registered after the start of the gate may be read. Thus, the first hits in the OD were lost and only information on the tail of the pulse in the OD was available. This is depicted on the bottom of figure 4.5. The information of the OD pulse in the colored area was lost caused by the delayed opening of the gate with respect to the muon passage. Due to this, the MCR could not work reliably for these events since most of the OD PMT hits and clusters are produced around the peak of the hit time spectrum shortly after the onset of the pulse. Thus, a tiny inefficiency of the MCR was introduced by the service trigger generation in the old setup that could be observed in the test with the IDF tagged muon sample.
In the new trigger system, the BTB 64 input is set with a precise 200 Hz clock. It remains set for only 330 ns and no dead time is observed. Thus, the probability

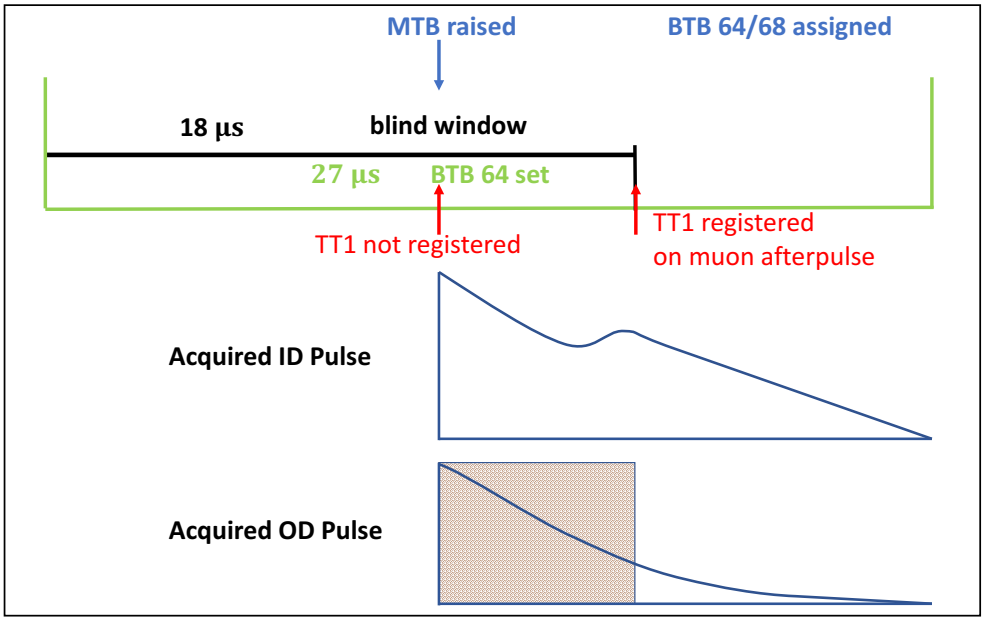

Figure 4.5: Service trigger generation and associated MCR inefficiency in the old trigger setup. On the *top*, the behavior of the trigger setup for the interference of a muon with a service trigger is shown. A $\sim 230\,\mathrm{Hz}$ clock initiated the BTB input value of 64 that remained set for $27\,\mu\mathrm{s}$ marked in green. The routine to set the input value resulted in a blind window of $\sim 18\,\mu\mathrm{s}$ towards any BTB inputs marked in black. If a muon arrives within this blind window and issues the MTB, neither the MTB nor the initial rise of the comparator (TT1) are registered. After the blind window, the muon may still issue a comparator trigger on the afterpulse and the gate for the data acquisition is opened. Depending on whether the MTB is still set when the inputs are read, the event is flagged with a BTB input value of 64 or 68. In the *middle*, the acquired ID pulse is shown qualitatively. Due to the storage of hits in the Laben boards, the entire pulse may be read and the IDF can still identify the muon. On the *bottom*, the acquired OD pulse is shown qualitatively. The actual passage of the muon occurred significantly before the gate for the data acquisition was opened and the OD PMT hits occurring during the blind window, marked by the colored area, are lost. Only the minority of hits registered in the tail of the OD pulse are available and the MCR fails to find a cluster of PMT hits.

for a muon to interfere with a set BTB 64 input value is strongly reduced. Since, further, all OD PMT hits are registered also in these cases due to the absence of any deadtime, the MCR works reliably even for the rare interferences. This overcome deadtime of the service trigger generation explains the observed slight but significant increase of the MCR efficiency after the new trigger system was

installed.
Figure 4.4 shows on the right side the efficiency of the MCR in the time region of the installation of the new trigger system computed based on a test with a sample of events tagged by the IDF. The time of the installation of the new trigger is marked by the red line. In the tested dataset, any event correlated to the generation of a service trigger, i.e. any event with a BTB input value of 64 or 68, was discarded from the analysis. For this dataset, the efficiency is constant in both trigger systems proving that the increase of the MCR efficiency is related to the different approach for the service trigger initialization.
However, it is difficult to precisely calculate or measure the temporal overlap between a service trigger and a cosmic muon for which the MCR fails to identify clusters in the old trigger setup due to, e.g., jitters of the deadtime window, of the comparator firing on a muon afterpulse, or of the start of the data acquisition gate after the comparator signal was registered. Further, it strongly depends on the distinct muon pulse shape for how long after the muon passage the MCR may still register clusters in the OD PMT subsets. Thus, events with a BTB input value of 64 or 68 were excluded from the analysis resulting in a deadtime of $\sim 0.6\%$ for the period in which the old trigger setup was operated and a very small deadtime for the new trigger setup. Besides its influence on the measurement of the mean cosmic muon flux, these different deadtimes need to be considered when combining the data acquired with the two trigger setups to guaranty a stable measurement of the seasonal modulation of the cosmic muon flux and its correlation to the atmospheric temperature without introducing any systematic effects.
The computation of the efficiency tested with a sample of high-energetic events was found to yield consistent results. For the analysis of the cosmic muon flux, the efficiency based on the IDF tagged sample as presented here was used since less contaminations are expected in this reference sample.

4.2.2 Removing of CNGS Events from the Sample

The CERN Neutrino to Gran Sasso (CNGS) facility has been designed to send a ν_μ beam with a mean neutrino energy of 17 GeV from CERN to the LNGS. It was operational in several cycles from 2008 to 2012 with the main purpose of studying neutrino oscillations in appearance mode via the transition of ν_μ into ν_τ. The first evidence of such a transition using atmospheric ν_μ was found in the Super-Kamiokande experiment based on an unbinned maximum likelihood fit [187]. After having been exposed to the CNGS beam for five years from 2008 to 2012, the OPERA experiment at the LNGS reported the observation of three ν_τ candidates originating from the beam. Due to the high signal to noise level, the absence of $\nu_\mu \rightarrow \nu_\tau$ oscillations could be excluded at 3.4σ [188].
The CNGS beam was further used to study the speed of ν_μ at 17 GeV energy.

Firstly, the OPERA collaboration reported an unexpected measurement of a neutrino velocity higher than the speed of light in September 2011 [189]. This result, however, was withdrawn later [190, 191] and also other experiments at the LNGS including Borexino reported neutrino velocities consistent with the expectation of neutrinos traveling almost at but slower than the speed of light [192, 193].
At the CNGS facility, a 400 GeV proton beam is fast extracted from the CERN SPS accelerator. During a cycle of 6 s, two extractions of 10.5 μs separated by 50 ms and a nominal intensity of $2.4 \cdot 10^{13}$ protons on the carbon target (pot) per extraction are realized. The positively charged part of the emerging kaons and pions is guided towards Gran Sasso and decays in a 1,000 m long vacuum tube into muons and ν_μ. All remaining hadronic contaminations of the beam are absorbed in a hadron stopper [184]. Due to the distance between CERN and Gran Sasso of ~ 730 km [192], all the muons produced in the interactions of the proton beam are absorbed and do not reach the LNGS.
In CC interactions of ν_μ from the CNGS beam, however, muons are produced close to or inside the Borexino detector. Such muons can potentially obtain sufficient energy to enter or cross the detector and, thus, disturb the analysis of modulations of the cosmic muon flux. Hence, these events need to be identified and removed from the dataset. This was done by measuring the difference between the time of a proton extraction at CERN and the time of events in the Borexino detector. Figure 4.6 shows this time difference for data taken in 2011 and 2012 while the CNGS beam was operational. The first peak of time differences corresponds to events that are directly correlated to the CNGS beam, i.e. muons produced in CC interactions of the ν_μ from the beam. Every event with a time difference to a proton extraction of $\Delta t \in [2.4\,\text{ms}, 2.416\,\text{ms}]$ was tagged as a CNGS related event and discarded in the analysis. This interval is chosen conservatively to securely remove all muons that are correlated to the CNGS beam. The second peak in figure 4.6 consists of events that were acquired during the neutron gate that is opened after every event that was identified as a muon by the MTB and triggers the ID. Since most of the CNGS related muons cause a trigger signal in the OD, these gates are also found in correlation with the CNGS beam. However, the corresponding events are not rejected since they do not include CNGS related muons.
To check the stability of the CNGS event tagging, the number of CNGS tagged events was compared to the CNGS beam intensity. Figure 4.7 shows on the top and in blue the intensity of the CNGS beam in 10^{16} pot per day over the time during which the beam was operational, in the middle and red the corresponding number of CNGS tagged events in Borexino per day, and on the bottom in green the ratio between the number of CNGS tagged events and the CNGS beam intensity per 10^{16} pot per day. The CNGS intensity is mirrored well by the number of coincidences and a mean value of $\sim 150 - 200$ coincidences per day is found during

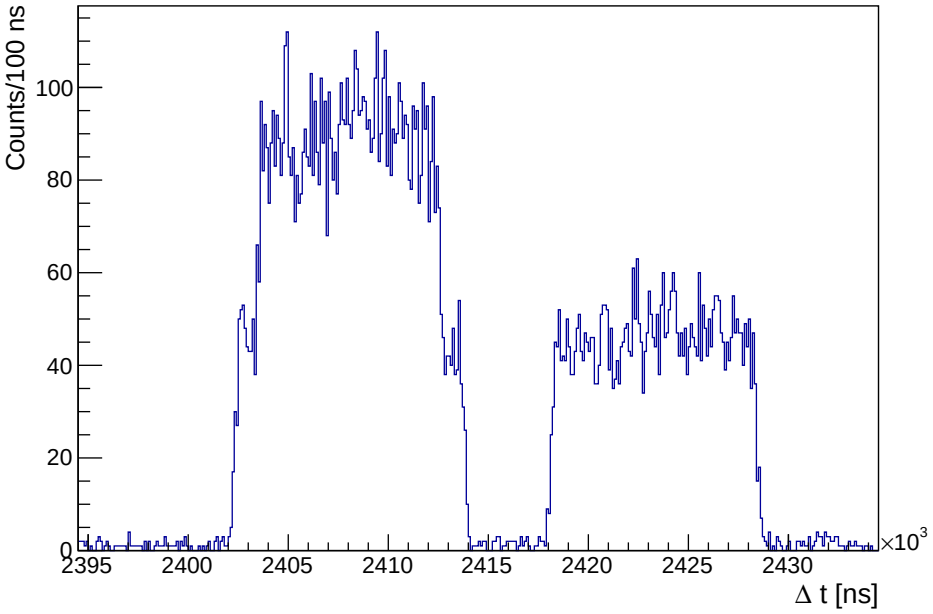

Figure 4.6: Time difference between CNGS proton extractions and Borexino events. The first peak corresponds to events directly correlated to the CNGS beam, the second peak consists of events observed in the neutron gate that is opened after each muon that crosses the ID. Events with $\Delta t \in [2.4\,\text{ms}, 2.416\,\text{ms}]$ were tagged as CNGS related events and discarded in the analysis.

the operation of the CNGS beam. The ratio between the number of coincidences and the CNGS intensity, shown on the bottom, is found to be very stable over the whole operational time of the CNGS beam. Only a few spikes or days with a low ratio occur. These are, however, related to days when the CNGS intensity was rather low and should be attributed to the small statistics.
To further ensure that all CNGS events are removed from the dataset, the azimuth angle distribution of muons after the CNGS cut has been applied may be studied. While the azimuth angle distribution of cosmic muons is determined by the shape of the rock overburden with an increased flux from directions where the shielding is comparably small, CNGS related muons point back straight towards their origin at CERN.
In Borexino, three tracking algorithms are available. The Inner Detector Tracking algorithm uses only data from the ID to compute the entry and exit point of a muon on the inner part of the SSS and determines the track by a linear fit through these two points. The second tracking algorithm uses only information from the OD to also compute entry and exit point on the SSS for muons crossing

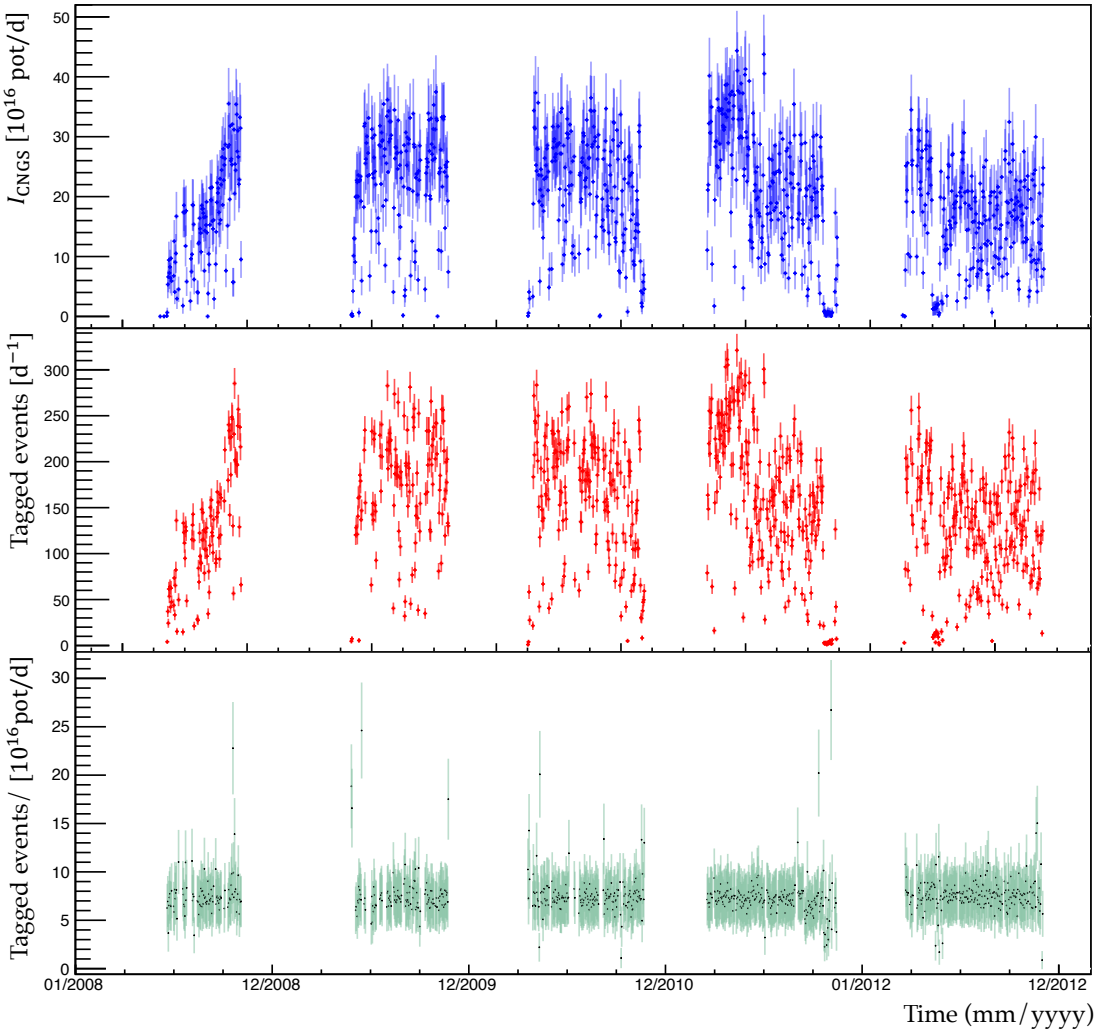

Figure 4.7: CNGS intensity, number of CNGS tagged events, and ratio between tagged events and CNGS intensity. *Top:* The intensity of the CNGS beam in 10^{16} pot per day is shown in blue. *Middle:* The number of CNGS tagged events per day is shown in red. The beam intensity is mirrored well and a mean value of $\sim 150-200$ coincidences per day is found. *Bottom*: The ratio between the number of CNGS tagged events and the CNGS beam intensity per 10^{16} pot per day is shown in green. The CNGS identification method works stably and reliably with only a few deviations due to low statistics on the respective days.

the ID. The track is equally obtained by a linear fit through the two points. The so-called Global Tracking algorithm combines the information from both tracking algorithms and determines the track by a fit through the available entry and exit

points, i.e. at maximum through four points [80, 62, 108]. For the analysis of CNGS related events, the Inner Detector Tracking is expected to work best since the OD PMT distribution is optimized for vetoing cosmic muons. Thus, the PMT coverage is smaller for large zenith angles, which lowers the tracking accuracy for the horizontally arriving CNGS related muons. This affects also the Global Tracking since it includes OD data. The uniform PMT coverage of the ID guarantees an efficient track reconstruction also for CNGS related muons.
Figure 4.8 shows the azimuth angle distribution of muons that have been tracked using the Inner Detector Tracking algorithm on a logarithmic scale. On the left side, the azimuth angle distribution for events that are tagged as CNGS events is shown. The peak towards low azimuth angles indicates the origin of these events at CERN that is located at $\phi = 6.2°$ in the Borexino coordinate system. The small bump of the distribution at $\sim 180°$ results from events for which the real entry and exit points of the track were mistakenly interchanged by the tracking algorithm, such that the muon was registered as arriving from the opposite direction. On the right side, the azimuth angle distribution of muons that were tracked after the CNGS beam has been switched off and for which the cosmic origin is guaranteed is shown in red. The distribution mirrors the topology of the mountain ridge that constitutes the rock overburden of the detector. More cosmic muons arrive from the South and North since the mountain flanks fall deeper in these directions and the rock coverage is smaller compared to other directions [80]. In blue, the azimuth angle distribution of muons that were identified while the CNGS beam was operational but after the removal of CNGS tagged events is shown. The exact accordance of both distributions ensures that the described method reliably identifies all CNGS related events, such that no background for cosmic muon studies correlated to the CNGS beam is left after the application of the cut.

4.2.3 Seasonal Modulation of the Muon Flux at Borexino

After the determination of the muon identification efficiency and the removal of the background related to the CNGS beam, a measurement of the cosmic muon flux with the Borexino detector may be performed. Data taken in ten years from May 16th, 2007 to May 15th, 2017 are used and a daily binning is applied to the measured muon flux. Muons are defined as events that are identified by the MCR since this muon identification method was found to provide the highest efficiency and maximum operational time. The measured daily muon rate is corrected by the estimated MCR efficiency of the corresponding day as presented in section 4.2.1. Events not triggering the ID are discarded to select tracks passing through both the OD and ID volumes. The relevant detector cross section is $146\,\mathrm{m}^2$ determined by the radius of the SSS. Due to the spherical geometry of the ID, the acceptance is independent of the incident angle of the muon, which guarantees a measurement

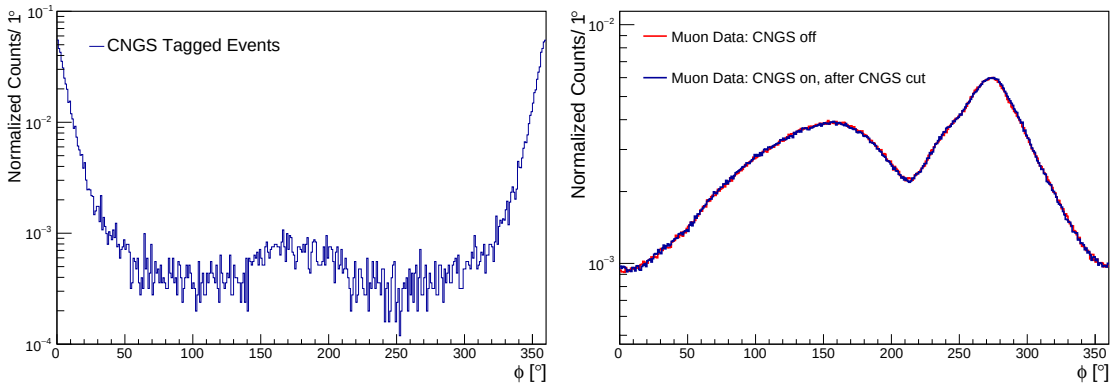

Figure 4.8: Azimuth angle distributions of CNGS muons and cosmic muons. *Left:* Azimuth angle distribution for CNGS tagged events. The distribution peaks at low values pointing back towards CERN at $\phi = 6.2°$. *Right:* The azimuth angle distribution for muons that were registered when the CNGS beam was off is shown in red. The distribution of these muons of guaranteed cosmic origin mirrors the topology of the detector's rock overburden. The azimuth angle distribution for muons that occurred during the operational time of the CNGS beam but after the CNGS cut was applied is shown in blue. The accordance of both distributions ensures that all CNGS events have been removed and only cosmic muons remain in the sample.

with minimum systematics. To prevent statistical instabilities in the data sample, only data acquired on $3,218$ days at which a minimum detector livetime of eight hours was provided were considered. The resulting effective exposure of the dataset is $\sim 4.2 \times 10^5\,\mathrm{m^2 d}$, in which $\sim 1.2 \times 10^7$ muons were recorded.
As detailed in section 4.1.2, the muon flux observed underground is expected to be modulated due to changes of the atmospheric temperature. In the stratosphere, where muons receiving sufficient energy to reach the Borexino detector are mainly produced, temperature modulations mostly occur on the scale of seasons. Since the higher temperature in summer lowers the average density of the atmosphere, the probability that the muon-producing mesons decay in flight before their first interaction is increased due to their longer mean free path. Only muons produced in these decays obtain sufficient energy to pass through the rock coverage and reach the Borexino detector. As a consequence, the cosmic muon flux as measured by Borexino is expected to follow the modulation of the atmospheric temperature. This modulation is seasonal at leading order and the cosmic muon flux $I_\mu(t)$ at

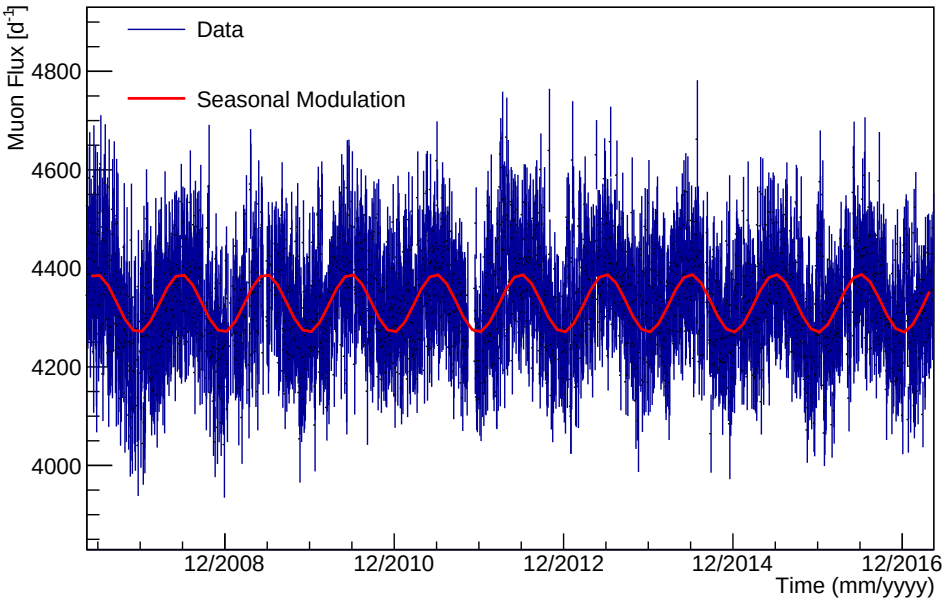

Figure 4.9: Measurement of the cosmic muon flux at the Borexino detector. The red line represents a fit of the clearly discernible seasonal modulation according to equation 4.47. The fit returns $I_\mu^0 = (4,329.1 \pm 1.3)\,\mathrm{d}^{-1}$, $\delta I_\mu = (58.9 \pm 1.9)\,\mathrm{d}^{-1} \mathrel{\widehat{=}} (1.36 \pm 0.04)\%$, $T = (366.3 \pm 0.6)\,\mathrm{d}$, and $t_0 = (174.8 \pm 3.8)\,\mathrm{d}$ at a $\chi^2/\mathrm{NDF} = 3921/3214$.

the Borexino detector can be parametrized in first approximation as [174]

$$I_\mu(t) = I_\mu^0 + \Delta I_\mu = I_\mu^0 + \delta I_\mu \cos\left(\frac{2\pi}{T}(t - t_0)\right) \tag{4.47}$$

with I_μ^0 being the mean cosmic muon flux, δI_μ the amplitude of the modulation, T the period, and t_0 the phase. However, sudden temperature fluctuations may still appear and short-term variations of the atmospheric temperature are expected to perturb the pure seasonal modulation. Further, maxima and minima of the temperature usually occur at different dates in consecutive years and the assumption of a mere seasonal modulation can only last as a first order approximation.
Figure 4.9 shows the cosmic muon flux as measured by Borexino together with a fit according to equation 4.47. The fit returns a mean cosmic muon flux of $I_\mu^0 = (4,329.1 \pm 1.3)\,\mathrm{d}^{-1}$, an amplitude of $\delta I_\mu = (58.9 \pm 1.9)\,\mathrm{d}^{-1} \mathrel{\widehat{=}} (1.36 \pm 0.04)\%$, a period of $T = (366.3 \pm 0.6)\,\mathrm{d}$, and a phase of $t_0 = (174.8 \pm 3.8)\,\mathrm{d}$. The first maximum of the muon flux, thus, corresponds to June 25th, 2007. With the cross section for muons in this analysis being $\sigma = 146\,\mathrm{m}^2$ as determined by the radius

of the SSS, the measured mean cosmic muon flux translates to a muon rate of

$$R_\mu = (3.432 \pm 0.001) \times 10^{-4}\,\mathrm{m}^{-2}\mathrm{s}^{-1}. \tag{4.48}$$

The observed values agree well with the results of the former Borexino measurement of the cosmic muon flux [174]. However, a slightly higher mean flux is measured in the present analysis compared to the rate of $R_\mu = (3.41 \pm 0.01) \times 10^{-4}\,\mathrm{m}^{-2}\mathrm{s}^{-1}$ reported in the previous Borexino publication. This may be explained by the formerly unknown deadtime introduced by the 230 Hz clock initiating the service trigger generation as described in section 4.2.1. Further, the mean cosmic muon flux is found to vary in different years as detailed below, such that a slightly different flux may be expected for different datasets and measuring times. The period and phase clearly reveal the expected seasonal character of the modulation with a maximum in summer when the atmosphere is less dense. The small gap in the data in 2011 corresponds to a period of water extraction during the purification campaign that was excluded from the analysis.

To estimate the stability of the fit and evaluate systematic uncertainties, the data were fitted in two year moving subsets. Further, the muon definition was changed and the procedure repeated for events with a valid trigger in both subdetectors. The efficiency of this muon definition is determined by the MTB due to the higher threshold and lesser light yield of the OD compared to the ID. It was computed accordingly to the procedure outlined in section 4.2.1 and analogously to the approach for the MCR tagged main analysis sample, the measured muon rate was corrected by the efficiency on a daily basis. Even though the efficiency of the MTB was found to be slightly lower compared to the MCR, it is working absolutely stably without any strong fluctuations. Thus, this sample also allows to investigate if the fluctuations observed in the MCR efficiency caused by some data acquisition failures especially in the first phase up to 2011 affect the stability of the modulation result. Since the MTB and MCR are based on complementary concepts with the first being a pure hardware flag and the latter a software based flag, the MTB flagged sample constitutes a reliable test of any systematic effects in the MCR tagged main analysis sample.

For the sample identified by the MTB, events in coincidence with a service trigger have not been excluded. Thus, the deadtime is different compared to the MCR tagged sample in which events with a BTB input of 64 or 68 have been removed. Since muons passing through the detector during the deadtime caused by the routine generating the service trigger in the old setup may still produce a comparator trigger on the afterpulse, the effective deadtime introduced by this process is reduced for muon events. Instead of the total deadtime of 18 μs per trigger generation, only an approximate deadtime of $\sim 10\,\mu$s at a 230 Hz clock rate was estimated for muons. However, as has been mentioned, this deadtime may not be determined with absolute precision due to jitters of several of the involved parameters and the

Time	Muon Definition	Mean Flux [d^{-1}]	Amplitude [d^{-1}]	Period [d]	Phase [d]
2007-2017	MCR	4329.1 ± 1.3	58.9 ± 1.9	366.3 ± 0.6	174.8 ± 3.8
	MTB	4330.0 ± 1.2	59.3 ± 1.8	364.5 ± 0.6	183.9 ± 3.3
2007-2009	MCR	4309.1 ± 3.4	72.9 ± 4.6	366.0 ± 6.5	182.4 ± 7.1
	MTB	4310.6 ± 3.0	74.2 ± 4.1	354.9 ± 5.6	197.2 ± 5.8
2009-2011	MCR	4338.3 ± 3.3	45.61 ± 4.5	393.3 ± 12.1	153.4 ± 12.6
	MTB	4341.2 ± 2.9	47.2 ± 4.0	398.2 ± 10.9	146.5 ± 11.3
2011-2013	MCR	4331.8 ± 3.1	75.5 ± 4.2	357.0 ± 5.6	172.7 ± 6.5
	MTB	4332.4 ± 2.8	73.8 ± 3.9	358.9 ± 5.3	174.6 ± 6.1
2013-2015	MCR	4344.8 ± 3.0	56.3 ± 4.2	370.6 ± 7.5	175.3 ± 8.1
	MTB	4346.6 ± 2.8	55.0 ± 3.8	375.2 ± 7.3	173.0 ± 8.0
2015-2017	MCR	4324.5 ± 2.9	60.0 ± 4.0	379.9 ± 7.5	175.9 ± 7.8
	MTB	4322.2 ± 3.1	62.1 ± 4.2	368.1 ± 9.8	181.0 ± 7.7

Table 4.2: Fit results of the cosmic muon flux modulation for different statistics and muon definitions.

low statistical basis on which it can be estimated. Thus, this sample contains a slight systematic uncertainty with respect to the mean muon flux. Since this does not affect the parameters of the seasonal modulation especially in the data subsets for which no overlap between the operation of the different trigger setups is included, the sample is still well suited to evaluate systematic uncertainties of the modulation parameters measured for the MCR tagged main analysis dataset. The results of the fits of each subset and for both muon definitions are summarized in table 4.2.
A slight deviation in the measured mean cosmic muon flux between the MTB tagged and the MCR tagged sample is observed with the MTB yielding a higher rate except for the last subset with data from 2015 to 2017. In this period, the mean muon flux is found to be slightly smaller than for the MCR tagged sample. This indicates that the deadtime for muons introduced by the service trigger routine in the old trigger system has been slightly overestimated. Still, the measured mean cosmic muon fluxes of both samples are found to be fully compatible with each other in every subset, such that the uncertainty introduced by the deadtime estimation is found to be negligible.
However, the mean cosmic muon flux varies significantly between the subsets. Since the mean atmospheric temperature is expected to vary for different time periods, a slight deviation of the mean cosmic muon flux for different periods may be expected. Another reason may be the existence of a long-term modulation of the cosmic muon flux as investigated in section 4.3. Additionally, the varying amount of water comprised in the rock of the Gran Sasso mountain massif is expected to

minorly affect the cosmic muon flux observed in the underground laboratory. Since the samples for both muon definitions show a similar behavior, the effect is not supposed to be caused by instabilities of the detector or the muon identification efficiency and a physical origin must be assumed. Thus, the mean muon flux measured based on the MCR tagged sample for the whole dataset is found to be a reliable result.
The modulation amplitude also varies for different subsets while the results for the two muon samples agree within the statistical uncertainties in each subset. The agreement between the two muon samples again indicates a physical origin such as stronger or weaker extrema of the atmospheric temperature in different time periods rather than detector instabilities to cause this behavior.
For both data samples, a period close to the seasonal expectation is found in all subsets with the exception of the period from 2009 to 2011 where both samples indicate a higher period. However, also the statistical uncertainty of this parameter as returned from the fit is higher in this subset than for the other time windows. This is expected to be caused by the reduced sample size in this subset due to the exclusion of data taken during water extraction processes as a part of the detector purification in 2011. Since for both samples consistent periods extremely close to the seasonal expectation are found when using the entire dataset, this effect is found to wash out and to be negligible with respect to the presented result.
Also the measured phase of the modulation is found to vary significantly for both muon samples in the period from 2009 to 2011, for which a smaller phase is measured with relatively high statistical uncertainties. Analogously to the measured modulation period, this is expected to be caused by the reduced sample size for this time period. Apart from this, a higher phase is observed in the MTB tagged sample in the first subset from 2007 to 2009. Since this is the only strong deviation between the two muon samples, it is expected that the increased phase is caused by the delayed installation of the MTB resulting in reduced statistics together with a less stable behavior of the OD trigger in 2007. Thus, only the MTB tagged sample is affected and no systematic effect with respect to the MCR tagged main analysis sample is observed. When data acquired in 2007 is excluded in the MTB tagged sample and the fit performed using nine years of data, a reduced phase of (176.0 ± 3.8) d results. This indicates that the instability of the MTB in the first year slightly affects the phase of the seasonal modulation measured in this muon sample. The better agreement between the phases observed in the two muon samples when the first year is excluded from the MTB sample underlines the stability of the result obtained from the MCR tagged sample.
Since consistent values for all fit parameters are found for both muon definitions in the investigated data subsets, no systematic uncertainties affecting the result of the analysis of the cosmic muon flux modulation measured with Borexino are

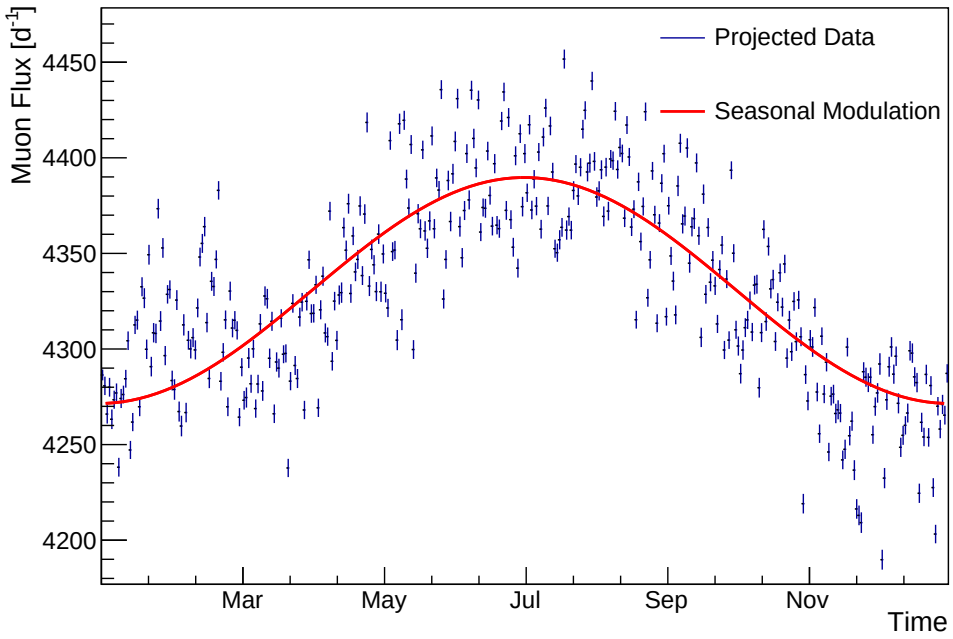

Figure 4.10: Cosmic muon flux data projected to one year and normalized to the flux per day. A fit of the seasonal modulation with a fixed period is depicted in red. The fit returns a mean cosmic muon flux of $I_\mu^0 = (4,330.6 \pm 0.3)\,\mathrm{d}^{-1}$, an amplitude of $\delta I_\mu = (59.1 \pm 0.4)\,\mathrm{d}^{-1} \mathrel{\widehat{=}} (1.365 \pm 0.009)\%$, and a phase of $t_0 = (181.7 \pm 0.4)\,\mathrm{d}$ at a $\chi^2/\mathrm{NDF} = 13703/362$.

observed. Thus, any systematic effects are expected to be strongly overpowered by the statistical uncertainties for the MCR tagged sample.
To further investigate the phase of the cosmic muon flux assuming a purely seasonal modulation and to allow the comparison of this parameter with other experiments, the data were projected to one year and the average muon flux per day was calculated. In turn, the data were fitted accordingly to equation 4.47 but with the period fixed to exactly one year, thus, a priori enforcing the seasonal character of the investigated modulation. The projected data together with the fit result are shown in figure 4.10. The fit returns a mean cosmic muon flux of $I_\mu^0 = (4,330.6 \pm 0.3)\,\mathrm{d}^{-1}$, a modulation amplitude of $\delta I_\mu = (59.1 \pm 0.4)\,\mathrm{d}^{-1} \mathrel{\widehat{=}} (1.365 \pm 0.009)\%$, and a phase of $t_0 = (181.7 \pm 0.4)\,\mathrm{d}$ at a $\chi^2/\mathrm{NDF} = 13703/362$. All values except for the phase agree with the ones obtained by fitting the unprojected dataset accordingly to equation 4.47 with the period left as a free parameter. However, the modulation parameters may be further constrained by the approach of projecting the data to

one year due to the enhanced statistics and reduced uncertainties of each bin. The small difference in the phase is found to originate from fixing the period to exactly one year. When a similar approach is chosen for the fit to the unprojected data, a consistent phase is obtained.
Besides the seasonal modulation, a clear deviation from the sinusoidal behavior of the cosmic muon flux is visible with a second, less pronounced maximum in the first months of the year. This may be explained by a more turbulent and less stable environment in the upper atmosphere during winter leading to stronger fluctuations of temperature and density.
It is known that planetary Rossby waves with horizontal wavelengths of several thousand kilometers propagate from the troposphere upwards to the stratosphere in winter. When these waves break, the temperature of the polar stratosphere increases rapidly and the polar wintertime westerly vortex circulation is weakened or even reversed [194]. Depending on the strength of the temperature and wind shift, these events are classified as major or minor Sudden Stratospheric Warmings (SSWs). While minor SSWs are quite frequent [195] and the temperature increase is less strong and less abrupt, major SSWs may cause temperature increases in the polar stratosphere of more than 50 K in a few days [177]. In a final warming in spring, the stratospheric winter circulation is changed from westerly to easterly without reestablishing the westerly circulation. The circulation, then, remains in this easterly direction until autumn [196]. The MINOS experiment could observe an enhanced cosmic muon flux correlated to a major SSW [177].
Since these effects are centered at the poles, they are strongly weakened at lower latitudes. Nevertheless, the strong temperature disturbances during winter and especially before the final warming that is usually seen in March might explain the deviation of the muon flux from the mere seasonal approximation in winter and spring. Further, these turbulences lead to a less steep increase of the cosmic muon flux from its minimum in winter towards the maximum in summer compared to the rapid decrease from summer to winter. Thus, a bent sinusoidal function considering this effect describes the data better. The assumption of a purely seasonal modulation may only last as a first order approximation of the temporal muon flux evolution, which explains the poor reduced χ^2 of the sinusoidal fit.
In table 4.3, the result of the present analysis is compared to measurements of the cosmic muon flux from several other experiments located at the LNGS. The observed period and phase agree well with results from other experiments, even though there is a slight difference to the phase measured by LVD using their whole dataset [200]. The GERDA experiment reports a later maximum of the flux of cosmic muons [197] than the other experiments. However, deviations are expected for different times of data taking since extrema of the atmospheric temperature occur on different days in different years and the GERDA result is based on only three

Experiment	Borexino (This Work)	Borexino Phase I [174]	GERDA [197]	MACRO [198]	LVD I [199]	LVD II [200]
Location	Hall C	Hall C	Hall A	Hall B	Hall A	Hall A
Time	2007-2017	2007-2011	2010-2013	1991-1997	2001-2008	1992-2016
Rate $[10^{-4}\mathrm{m}^{-2}\mathrm{s}^{-1}]$	3.432 ± 0.001	3.41 ± 0.01	3.47 ± 0.07	3.22 ± 0.08	3.31 ± 0.03	3.3332 ± 0.0005
Amplitude $[10^{-6}\mathrm{m}^{-2}\mathrm{s}^{-1}]$	4.7 ± 0.2	4.4 ± 0.2	4.72 ± 0.33	–	5.0 ± 0.2	5.2 ± 0.3
Period [d]	366.3 ± 0.7	366 ± 3	–	–	367 ± 15	365.1 ± 0.2
Phase [d]	181.7 ± 0.4	179 ± 6	191 ± 4	–	185 ± 15	187 ± 3

Table 4.3: Results of the cosmic muon flux measurement with Borexino from this work compared to further measurements carried out at the LNGS.

years of data.
The measured mean flux of cosmic muons is slightly higher for the present analysis than the result from the former measurement of Borexino [174]. This slight deviation is mainly caused by the now properly treated and formerly unknown small inefficiency of the MCR due to the deadtime resulting from the service trigger generation in the old trigger setup. Additionally, the mean cosmic muon flux observed underground is not constant at all time periods as summarized in table 4.2, which might also add to the slight differences of the obtained results.
While the flux is totally compatible with the result from GERDA, deviations are observed when it is compared to the results from MACRO [182] and the two measurements from LVD [199, 200]. Besides the mentioned effect of measuring at different time periods, this might be caused by the different locations of the experiments in the LNGS resulting in a slightly different rock coverage. The steep mountain flank closer to Hall C might, thus, be the explanation for the reduced cosmic muon flux measured by LVD and MACRO that are located in Hall A and B, respectively. This difference in the rock coverage has formerly been assumed to explain slight deviations of the angular distributions of muons seen by the respective detectors [80]. Unlike Borexino, the other experiments carried out at the LNGS contain a dependence of the acceptance on the muon incident angle, which also might affect the results.
Since this measurement agrees well with the results from other experiments at the LNGS concerning the phase of the modulation of the cosmic muon flux, the possibility to explain the DAMA/LIBRA signal as caused by cosmic muons gets further constrained. The DAMA/LIBRA experiment is a direct dark matter search experiment located at the LNGS utilizing twenty-five scintillating NaI(Tl) crystals of 9.70 kg each as a target material [201]. Using its phase I data corresponding to

an exposure of $\sim 1.04\,\mathrm{kton} \times \mathrm{yr}$, a modulation of events in the lowest energy range with an annual period and the maximum at June 2nd has been observed with a significance of more than 9σ [202].
Due to the rotation of the Earth around the Sun that itself moves with respect to the galactic halo, a seasonal modulation of the relative velocity between the wind of weakly interacting massive particles (WIMPs), which are a favorite dark matter candidate [203], and the Earth is expected [204]. Since, further, the interaction probability between WIMPs and a detector target strongly depends on their relative velocity [205], the modulation of the relative velocity should be mirrored in a variation of the WIMP interaction rate. The maximum of this modulation is supposed to occur at June 2nd in accordance with the DAMA/LIBRA signal. Since the amplitude of the modulation measured by the DAMA/LIBRA experiment also matches the expectations for a WIMP signal, the collaboration interprets the observed modulation as a smoking gun signature and claims the first detection of dark matter interactions [202].
However, the DAMA/LIBRA result is widely doubted since it is in strong tension with measurements of several other direct dark matter experiments that exclude the best fit region of the DAMA/LIBRA experiment in the WIMP parameter space [206]. Due to this, various attempts were made to explain the observed modulation as caused by different particles. Thus, a correlation of the DAMA/LIBRA signal to the modulation of the cosmic muon flux as measured by LVD has been discussed [207]. Further, a combination of a signal generated by cosmogenic neutrons that are produced by cosmic muons in the surroundings of the detector and by solar neutrinos that correct the phase of the neutrons to an earlier maximum has been proposed [208]. However, this solution was objected in [209].
With the present measurement of the seasonal modulation of the cosmic muon flux, the phase difference between the DAMA/LIBRA signal and the cosmic muon flux is confirmed leaving the cosmic muon flux as a sole explanation of the DAMA/LIBRA signal as improbable. Even though some possibilities for a combination of the cosmic muon flux with other modulated signals to generate a modulation as observed by the DAMA/LIBRA experiment might still be thought of, such an explanation seems rather unlikely. A further and substantial test of the DAMA/LIBRA signal is planned with the SABRE experiment [210] that will use the same target material and try to measure the observed annual modulation at the LNGS and at the Stawell Underground Physics Laboratory (SUPL) in Australia. Since all atmospheric effects are expected to reverse their phase from northern to southern hemisphere, a measurement of the same modulation in equal detectors at both hemispheres would strongly strengthen the dark matter hypothesis.

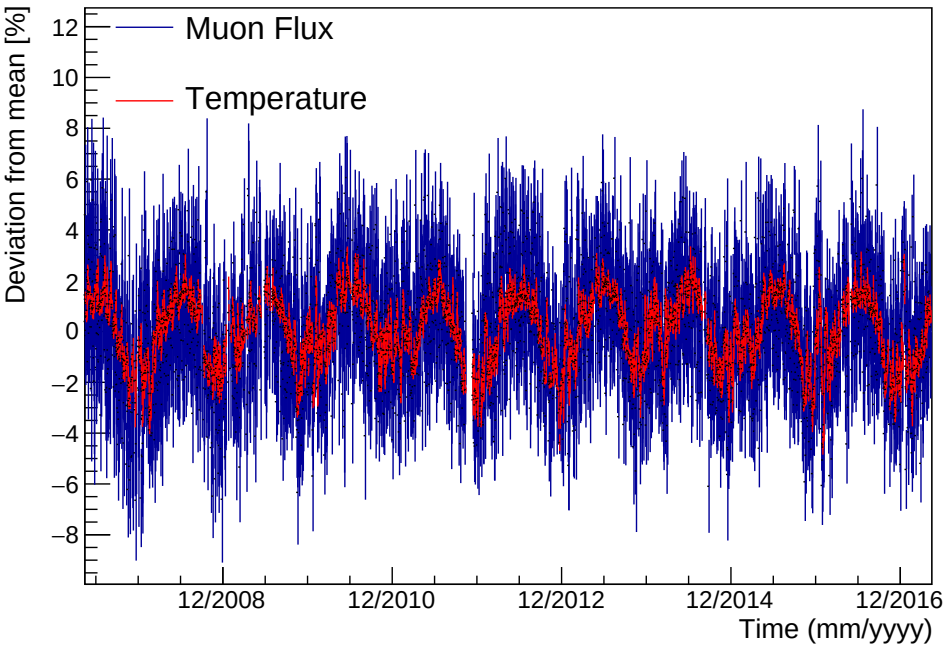

Figure 4.11: Percent deviations of the cosmic muon flux from its mean in blue and of the effective atmospheric temperature in red. A correlation is clearly visible.

4.2.4 Correlation to the Atmospheric Temperature

As motivated in section 4.1.2, the observed seasonal modulation of the flux of high-energetic cosmic muons is expected to be caused by density variations of the atmosphere through which the mean free path of the muon-producing mesons is altered. These density variations are strongly correlated to variations of the temperature in the upper atmosphere that occur mainly on the scale of seasons. Figure 4.11 shows the modulations of the cosmic muon flux in blue and of the effective atmospheric temperature T_{eff} in red, both scaled to percent deviations. As detailed in section 4.1.2, the effective atmospheric temperature is introduced to model the atmosphere as an isothermal meson-producing entity. T_{eff} is chosen such that in an isothermal atmosphere with this temperature, the same meson intensity is generated as in the actual atmosphere with its slant depth dependent temperature distribution $T(X)$. To allow this approximation, properly chosen weights that account for the physics determining the meson and muon production at different atmospheric depths are included in the calculation of the effective temperature.
The temperature data were obtained from the European Center for Medium-range Weather Forecasts (ECMWF) [183] that provides measurements of the temper-

Parameter	Cosmic muon flux	Effective atmospheric temperature
Amplitude	$(1.380 \pm 0.009)\%$	$(1.54 \pm 0.01)\%$
Period	$(366.3 \pm 0.6)\,\mathrm{d}$	$(365.42 \pm 0.04)\,\mathrm{d}$
Phase	$(181.7 \pm 0.4)\,\mathrm{d}$	$(182.8 \pm 0.2)\,\mathrm{d}$

Table 4.4: Modulation parameters of the cosmic muon flux and of the effective atmospheric temperature. The amplitudes and phases reveal the seasonal modulation of the two observables and the accordance of the parameters indicates the correlation. The slightly enhanced amplitude of the temperature modulation compared to the cosmic muon flux hints that not all mesons relevant for the production of cosmic muons measured at Borexino are affected by variations of the atmospheric temperature.

ature at 37 pressure levels between 1 hPa and 1,000 hPa four times a day. For the closest grid point to the LNGS available, the effective temperature has been computed for each of these measurements accordingly to equation 4.37. Since the threshold energy for the muons to arrive at a specific underground detector enters in the weights to calculate T_{eff}, not only the temperature measurements but also the calculation of T_{eff} is site dependent. The mean of the four calculated values was assigned as the effective temperature to the corresponding day and the uncertainty was determined by the variation of the estimations.
For both observables, the seasonal modulation is clearly visible. A fit of a sinusoidal to the temperature data with similar parameters as in equation 4.47 for the muon modulation yields a relative amplitude of $\delta T \mathrel{\widehat{=}} (1.54 \pm 0.01)\%$ at a mean temperature of $T = (220.89 \pm 0.01)\,\mathrm{K}$. The resulting period and phase are $\tau = (365.42 \pm 0.04)\,\mathrm{d}$ and $t_0 = (182.8 \pm 0.2)\,\mathrm{d}$, respectively. However, the $\chi^2/\mathrm{NDF} = 106392/3214$ of the fit clearly reveals that a sinusoidal is only a poor reproduction of the fine-grained temperature data.
Table 4.4 summarizes the observed modulation parameters of the cosmic muon flux and of the effective atmospheric temperature. The observed periods clearly reveal the seasonal character of the modulations and the accordance of the phases indicates the correlation of both observables. The slightly enhanced amplitude of the temperature modulation compared to the cosmic muon flux modulation hints that not all mesons relevant for the production of high-energetic cosmic muons penetrating the LNGS rock coverage and arriving at the detector are affected by variations of the atmospheric temperature. Since kaons and pions have different decay properties, the observed strength of the correlation between the effective atmospheric temperature and the cosmic muon flux may be used to determine the atmospheric kaon to pion production ratio as presented in chapter 5.
Figure 4.12 exemplarily shows the variation of the cosmic muon flux in blue and the variation of the effective atmospheric temperature in red for data acquired from

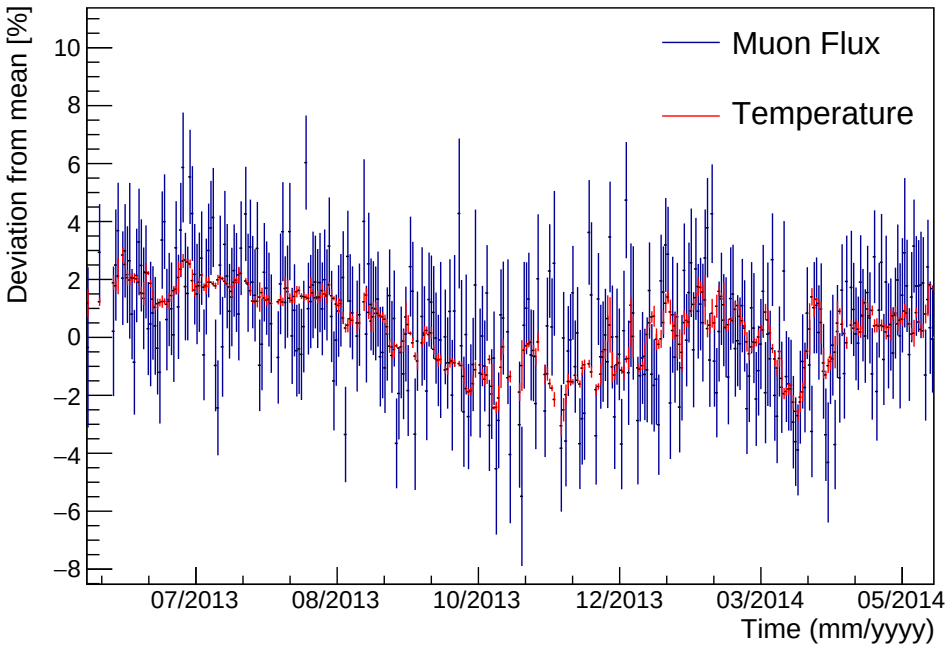

Figure 4.12: Percent deviations of the cosmic muon flux from its mean in blue and of the effective atmospheric temperature in red. Data of one year from May 2013 to May 2014 are shown. A deviation from the seasonal behavior occurs in spring and short-term variations of the temperature are promptly mirrored in the muon flux.

May 2013 until May 2014, again scaled to percent deviations from the respective mean. A clear deviation from the sinusoidal behavior is observed in spring of 2014 resulting in a secondary maximum of both the temperature and the muon flux. Further, shortly after this secondary maximum, an abrupt increase in temperature is observed that is immediately mirrored by an increased muon flux. Thus, the correlation between the cosmic muon flux and the effective atmospheric temperature may not only be observed on a seasonal scale but short-term temperature fluctuations are found to promptly affect the cosmic muon flux.
To quantify the correlation between the cosmic muon flux and the effective atmospheric temperature, the effective temperature coefficient α_{T} as derived in section 4.1.2 is commonly used. As detailed there, for a measurement of the cosmic muon flux and the effective atmospheric temperature, the effective temperature coefficient is defined via

$$\frac{\Delta I_\mu}{\langle I_\mu \rangle} = \alpha_{\mathrm{T}} \frac{\Delta T_{\mathrm{eff}}}{\langle T_{\mathrm{eff}} \rangle}. \tag{4.49}$$

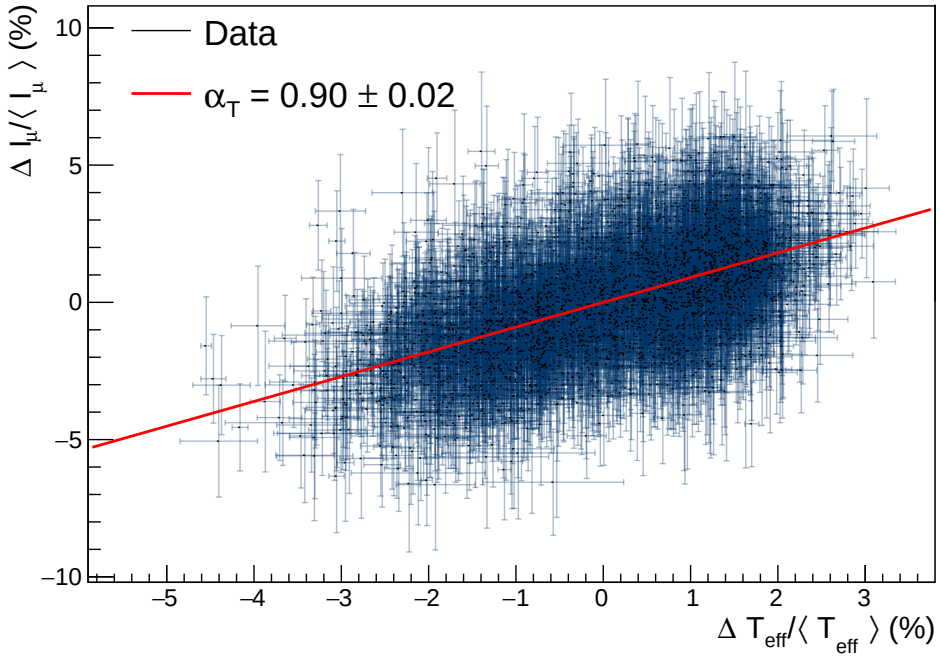

Figure 4.13: Deviations from the mean cosmic muon flux versus deviations from the mean effective atmospheric temperature, both scaled to percent deviations. Each data point corresponds to one day. The correlation factor between the two datasets is 0.55, indicating a positive correlation. A fit according to equation 4.49 yields $\alpha_T = 0.90 \pm 0.02$.

Figure 4.13 shows the percent deviation of the cosmic muon flux versus the percent deviation of the effective atmospheric temperature. Each data point corresponds to one day. The correlation factor (R-value) [211] between both datasets is found to be 0.55, indicating a positive correlation. The slope of a fit to the data according to equation 4.49 yields

$$\alpha_T = 0.90 \pm 0.02, \tag{4.50}$$

which agrees with the former Borexino result [174].
Similar to the approach for the measurement of the seasonal modulation of the cosmic muon flux, the data were split into subsets of two years and α_T was computed for each subset to examine possible systematic effects of the measurement. Further, the muon sample based on a MTB identification was used additionally to determine α_T in each subset and for the whole dataset. Table 4.5 summarizes the results.
The MTB and MCR tagged samples agree well in every time bin. However, the

Time period	Muon Definition	α_{T}
2007-2017	MCR	0.90 ± 0.02
	MTB	0.92 ± 0.02
2007-2009	MCR	0.99 ± 0.06
	MTB	1.04 ± 0.05
2009-2011	MCR	0.85 ± 0.06
	MTB	0.87 ± 0.05
2011-2013	MCR	0.92 ± 0.05
	MTB	0.92 ± 0.05
2013-2015	MCR	0.94 ± 0.05
	MTB	0.93 ± 0.05
2015-2017	MCR	0.81 ± 0.04
	MTB	0.81 ± 0.04
2007-2016	MCR	0.93 ± 0.02
	MTB	0.94 ± 0.02
2008-2017	MCR	0.89 ± 0.02
	MTB	0.90 ± 0.02
2008-2016	MCR	0.91 ± 0.03
	MTB	0.92 ± 0.02

Table 4.5: Determination of α_{T} for different time periods and muon definitions. Some deviations are observed but the exclusion of the corresponding data does not alter the result significantly. Both muon definitions agree well.

values in the time periods from 2007 to 2009 and from 2015 to 2017 deviate more than 1σ from the result using the entire dataset. The discrepancy in the first time period is expected to be caused by an unstable behavior of the detector during the first year of data taking, especially for the MTB tagged sample that shows a higher tension. For the last period, a residual effect of the installation of the new trigger might affect the measurement. However, some measurements not agreeing within the 1σ range are statistically expected and the deviations are not huge considering the statistical uncertainties of the values obtained in the subsets.
To estimate the impact of the in- or exclusion of these periods, α_{T} was determined for the time from 2007 to 2016, from 2008 to 2017, and from 2008 to 2016. In this way, data taken during the two years expected to cause the deviations were excluded singly and jointly for both years to check if the inclusion of these data affects the result of the entire dataset. The results agree well with the measurement using the whole statistics, such that the inclusion of the deviating periods was not found to affect the presented result. Thus, systematic effects caused by instabilities of the detector are expected to be overpowered by the statistical uncertainty

Experiment	Time period	α_{T}
Borexino (This work)	2007-2017	0.90 ± 0.02
Borexino Phase I [174]	2007-2011	0.93 ± 0.04
GERDA [197]	2010-2013	0.96 ± 0.05 0.91 ± 0.05
MACRO [198]	1991-1997	0.91 ± 0.07
LVD II [200]	1992-2016	0.93 ± 0.02

Table 4.6: Comparison of measurements of the effective temperature coefficient at the LNGS. The result obtained in the present work agrees with the other measurements.

returned by the fit.
Additionally, the computations of the mean of the cosmic muon flux and of the mean of the effective atmospheric temperature were altered to check if the way they are computed affects the measurement of the effective temperature coefficient. For the presented results, a sinusoidal modulation was fitted to the data to determine the mean muon flux and the mean effective atmospheric temperature. Alternatively, a constant function was fitted to the data. Both methods yield consistent results and the measurement was not found to be affected by the way the mean is computed.
The effective temperature coefficient has been measured by several experiments at the LNGS and at other underground laboratories. The values reported by LNGS based experiments are listed in table 4.6. The result presented in this analysis agrees with the other measurements carried out at the LNGS. The GERDA experiment published two values for the same muon sample based on two different temperature datasets [197].
Depending on the depth of the underground laboratory, the minimum energy a muon has to possess in order to reach a detector changes. Thus, α_{T} is expected to increase with rising depth since the threshold energy increases and a higher fraction of the muon-producing mesons is affected by temperature fluctuations of the atmosphere. Figure 4.14 shows several measurements of α_{T} performed at different depths. The depth is parametrized by the average of the product of the threshold energy and the cosine of the zenith angle $\langle E_{\mathrm{thr}} \cos\theta \rangle$ as in equation 4.43. Due to the distinct shape of the rock overburden, the actual value of $\langle E_{\mathrm{thr}} \cos\theta \rangle$ is difficult to predict and needs in principle to be calculated by Monte Carlo simulations for each underground experimental site. For the LNGS, formerly several values were reported.
In [179], $\langle E_{\mathrm{thr}} \cos\theta \rangle = 1.833\,\mathrm{TeV}$ was predicted. However, a flat rock coverage was assumed in this estimation while the shape of the mountain ridge results in a lowered threshold energy for muons arriving from comparably large zenith angles at

the LNGS. Thus, $\langle E_{\mathrm{thr}} \cos\theta \rangle$ differs compared to a location at a similar vertical depth but with a flat overburden and is expected to be significantly smaller for the LNGS. The MACRO [182] and LVD [199] experiments assumed a threshold energy of $E_{\mathrm{thr}} > 1.3\,\mathrm{TeV}$. In the scope of this thesis, a Monte Carlo simulation considering the shape of the LNGS rock overburden was performed as presented in section 5.2.1 and a value of $\langle E_{\mathrm{thr}} \cos\theta \rangle = (1.34 \pm 0.18)\,\mathrm{TeV}$ was estimated. Thus, this value is used for the LNGS based experiments in the following evaluations.
In figure 4.14, the weighted mean of the measurements carried out at the LNGS is shown and compared to values obtained at other experimental sites. The results of the LNGS based measurements from MACRO [198], LVD [200], GERDA [197], and Borexino [174] as listed in table 4.6 are compared to the result from this work for Borexino in the insert of figure 4.14. Concerning the other measurements, the Double Chooz [212], the MINOS [176], and the Daya Bay [213] experiments explicitly calculated the value of $\langle E_{\mathrm{thr}} \cos\theta \rangle$. The measured values are, thus, drawn accordingly. For the other experiments that are shown, namely IceCube [214], AMANDA [215], and Barrett [175], the measured values of α_{T} are drawn at the threshold energy corresponding to their mean depth. Thus, uncertainties of the actual value of $\langle E_{\mathrm{thr}} \cos\theta \rangle$ are expected but not drawn since no estimation is made. Besides the measurements, the theoretical expectation of α_{T} in dependence on $\langle E_{\mathrm{thr}} \cos\theta \rangle$ for the central value of the atmospheric kaon to pion production ratio $r_{\mathrm{K}/\pi} = 0.149 \pm 0.06$ [197] is represented by the red line. The expected value of α_{T} for the assumption that only pion decays contribute to the cosmic muon flux underground is depicted by the upper black dashed line, the expected value of α_{T} for the assumption that only kaon decays contribute by the lower black dotted line. The measurements favor a muon flux originating from a composition of kaon and pion decays.
The combination of the measurements can be used to determine the atmospheric kaon to pion production ratio $r_{\mathrm{K}/\pi}$ by fitting the data points accordingly to equation 4.43 with $r_{\mathrm{K}/\pi}$ left as a free parameter. Such a fit is represented by the green line and the data points match best for

$$r_{\mathrm{K}/\pi} = 0.08 \pm 0.02. \tag{4.51}$$

This agrees with the theoretical prediction and with the result obtained in [197] of $r_{\mathrm{K}/\pi} = 0.10 \pm 0.03$ using a similar approach but including a different set of measurements. However, systematic uncertainties like the exact value of $\langle E_{\mathrm{thr}} \cos\theta \rangle$ for the respective experimental sites have not been considered and the result may only last as an indication. Further, the measured values of α_{T} depend on the assumed kaon to pion production ratio since this quantity is included in the computation of T_{eff}. This inter-value dependency is not taken into account here. A more stringent measurement of the atmospheric kaon to pion production ratio using Borexino data alone is presented in chapter 5.

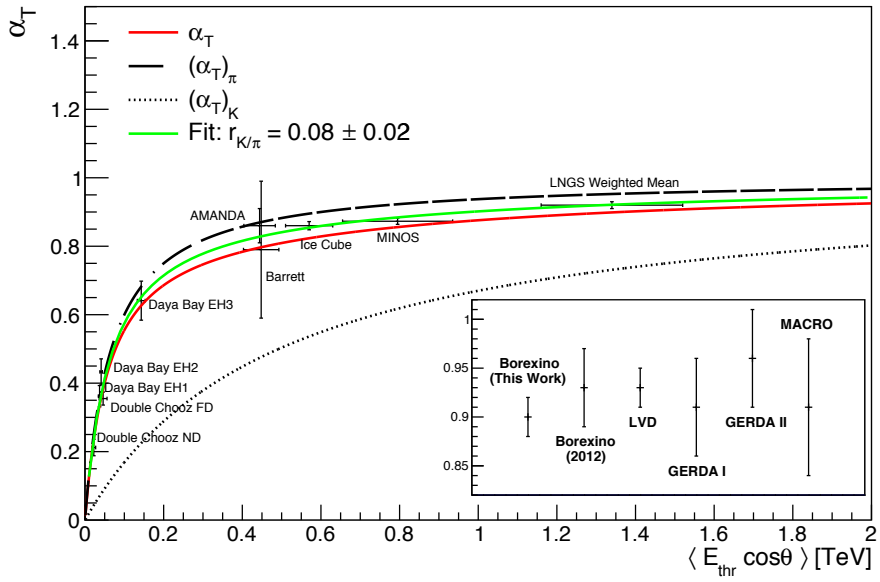

Figure 4.14: The effective temperature coefficient α_T is shown in dependence on the threshold energy $\langle E_{\text{thr}} \cos\theta \rangle$ with measurements from various experiments. The red line shows the expected α_T for the predicted atmospheric kaon to pion production ratio of $r_{K/\pi} = 0.149$ [197]. The upper dashed black line shows the expected α_T assuming only a pion contribution to the cosmic muon flux, the lower dotted black line the expectation for only a kaon contribution. Measurements from Double Chooz [212], Barrett [175], AMANDA [215], IceCube [214], MINOS [176], Daya Bay [213], and the weighted mean of measurements performed at the LNGS are shown. The LNGS based measurements from GERDA [197], MACRO [182], LVD [200], and Borexino [174] are shown together with the Borexino measurement from this work in the insert. The green line shows a fit of the data points returning an atmospheric kaon to pion production ratio of $r_{K/\pi} = 0.08 \pm 0.02$.

4.3 Long-Term Modulation of the Cosmic Muon Flux

Besides the well explored and well understood seasonal modulation of the cosmic muon flux, the existence of a subleading, longer-term modulation has been investigated and noticed by various authors as in [207] for the LVD data. In [216], data from Borexino [174], LVD [217], and MACRO [218] were combined to analyze the cosmic muon flux for a time period of over 20 years and a modulation with a period between 10 and 11 years was found to be significant. This period was not observed in the atmospheric temperature data but a correlation in period and phase with the solar activity was reported.

In principle, the cosmic ray intensity at the Earth is found to be in anticorrelation with the solar activity. Due to the enhanced solar magnetic field at high solar activities, lower-energetic cosmic rays are prevented from hitting the atmosphere and producing particle showers due to their small gyroradius [219]. Since the energy spectrum of cosmic rays follows a power law as described in section 4.1.1, low-energetic particles strongly dominate the cosmic ray flux and an overall anticorrelation between the solar activity and the cosmic ray intensity at the Earth results. As a possibility to explore the cosmic ray intensity at Earth, the flux of cosmic ray neutrons is monitored at various sites. The mentioned anticorrelation is even as distinct that neutron monitors may be used to measure the solar activity. Thus, minima in the neutron flux are found to clearly correspond to maxima in the solar activity [220].
However, the flux of cosmic muons observed underground is expected to be unaffected by changes of the solar activity. For the production of these muons, cosmic ray particles of very high energies are required and the passage of high-energetic primary cosmic ray particles is not expected to be influenced by the solar magnetic field [216]. Thus, in principle, neither a correlation nor an anticorrelation between the cosmic muon flux underground and the solar activity is anticipated.
As a possible source of a correlation between the solar activity and the intensity of high-energetic cosmic rays at the Earth, the Tibet Air Shower Array reported a modification of the Sun's shadow for 10 TeV cosmic ray particles in anticorrelation with the solar activity [221]. The Sun with an optical diameter of 0.5° as viewed from the Earth blocks cosmic rays arriving from its location in the sky. In [221], it was shown that the size of the shadow the Sun casts on 10 TeV cosmic rays is affected by the solar magnetic field with the shadow being smaller at high solar activities by up to 50%. This effect could be a physical explanation of a possible correlation between the solar activity and the flux of cosmic muons measured underground since this primary cosmic ray energy is very close to the energies necessary to produce muons arriving at Borexino.
To investigate the existence of a long-term modulation of the cosmic muon flux at Borexino, equation 4.47 is rewritten to account for a second, subleading, and potentially long-term modulation as

$$I_\mu(t) = I_\mu^0 + \Delta I_\mu = I_\mu^0 + \delta I_\mu \cos\left(\frac{2\pi}{T}(t - t_0)\right) + \delta I_\mu^{\text{long}} \cos\left(\frac{2\pi}{T^{\text{long}}}(t - t_0^{\text{long}})\right). \tag{4.52}$$

The measured cosmic muon flux was fitted accordingly as shown in figure 4.15 by the green line. For comparison, also the fit of a single sinusoidal described by equation 4.47 is shown by the red line. The fit including two sinusoidals returns parameters of the seasonal modulation that are consistent with the ones obtained in section 4.2. Additionally to the seasonal modulation, a long-term modulation of the cosmic

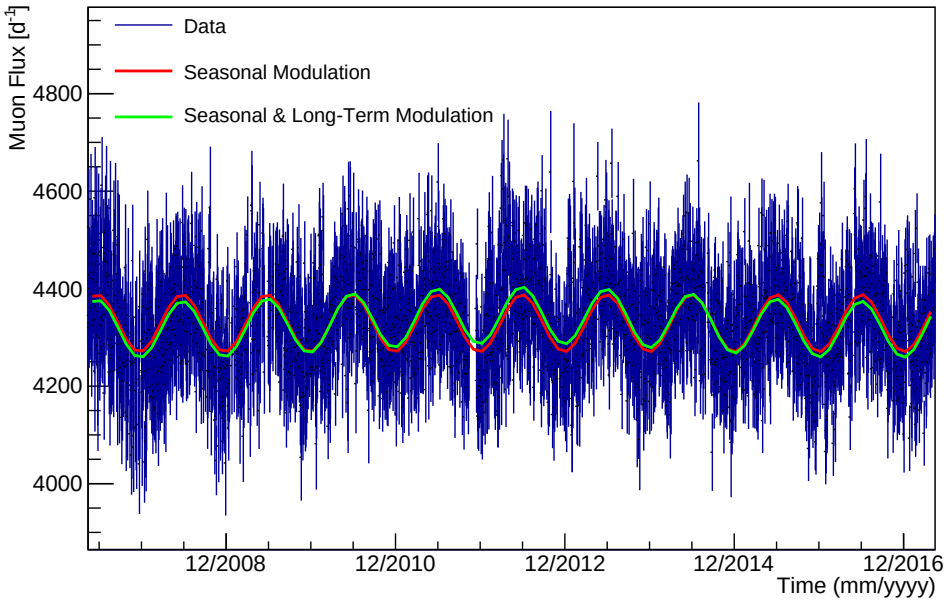

Figure 4.15: The cosmic muon flux observed in Borexino is fitted accordingly to equation 4.52 represented by the green line. For comparison, also the fit of the seasonal modulation explored in section 4.2 is shown by the red line. Besides the parameters of the seasonal modulation, the fit returns a long-term period of $T^{\text{long}} = (3,010 \pm 299)\,\text{d} = (8.25 \pm 0.82)\,\text{yr}$ with an amplitude of $\delta I_\mu^{\text{long}} = (14.7 \pm 1.8)\,\text{d}^{-1} \mathrel{\widehat{=}} (0.34 \pm 0.04)\%$ and a phase of $t_0^{\text{long}} = (1,993 \pm 271)\,\text{d}$ at a $\chi^2/\text{NDF} = 3855/3211$.

muon flux with a period of $T^{\text{long}} = (3,010 \pm 299)\,\text{d} = (8.25 \pm 0.82)\,\text{yr}$, an amplitude of $\delta I_\mu^{\text{long}} = (14.7 \pm 1.8)\,\text{d}^{-1} \mathrel{\widehat{=}} (0.34 \pm 0.04)\%$, and a phase of $t_0^{\text{long}} = (1,993 \pm 271)\,\text{d}$ is observed. Thus, the maximum of the long-term modulation is expected in June 2012. The χ^2/NDF of the fit reduces from 3921/3214 when only a single modulation according to equation 4.47 is fitted to the data to 3855/3211 for the inclusion of the second sinusoidal.
To check the significance of this long-term modulation, a Lomb-Scargle analysis [222, 223] was performed for the measured cosmic muon flux as well as for the atmospheric temperature as presented in the following section. In case the possibly significant long-term modulation was caused by variations of the atmospheric temperature, a similar modulation of the temperature data must be expected. In section 4.3.2, the modulation of the solar activity and its correlation to the cosmic muon flux are investigated.

4.3.1 Lomb-Scargle Analysis

Lomb-Scargle periodograms [222, 223] are a common method to analyze a binned dataset of n measured values $\{X(t_\mathrm{i})\}$ with $\mathrm{i} \in [1, n]$ for the presence of modulations described by [174]

$$N(t) = N_0 \cdot \left(1 + A \cdot \sin(\frac{2\pi t}{T} + \phi)\right), \tag{4.53}$$

where $N(t)$ is the expected value of the observable X at the time t, N_0 the mean value of the dataset, A the relative amplitude of the modulation, T its period, and ϕ its phase.
To perform a spectral analysis of the dataset $\{X(t_\mathrm{j})\}$, classically, the discrete Fourier transform can be defined as [223]

$$FT_X(T) = \sum_{\mathrm{j}=1}^{n} X(t_\mathrm{j}) e^{-i\frac{2\pi}{T}\cdot t_\mathrm{j}}. \tag{4.54}$$

Based on this, the periodogram is conventionally defined as

$$\begin{aligned} P_X(T) &= \frac{1}{n}|FT_X(T)|^2 \\ &= \frac{1}{n}\left|\sum_{\mathrm{j}=1}^{n} X(t_\mathrm{j}) e^{-i\frac{2\pi}{T}\cdot t_\mathrm{j}}\right|^2 \\ &= \frac{1}{n}\left[\left(\sum_{\mathrm{j}=1}^{n} X_\mathrm{j} \cos\left(\frac{2\pi}{T} t_\mathrm{j}\right)\right)^2 + \left(\sum_{\mathrm{j}=1}^{n} X_\mathrm{j} \sin\left(\frac{2\pi}{T} t_\mathrm{j}\right)\right)^2\right]. \end{aligned} \tag{4.55}$$

In case that a modulation with a period T is present in the dataset $\{X(t_\mathrm{i})\}$, the factors $X(t_\mathrm{j})$ and $e^{-i\frac{2\pi}{T}\cdot t_\mathrm{j}}$ are in phase resulting in a large contribution to the sum in equation 4.55. For other values of T, the terms in the sum are randomly positive or negative and a small value is obtained due to the cancellation of the terms [223]. However, this classical periodogram is very noisy [224] and suffers from spectral leakage especially for unevenly sampled datasets. Thus, a modulation with a period T that is actually present in the dataset does not only produce a high power at this period but also at, in particular higher, harmonics of this modulation [225]. Nevertheless, slightly modified or smoothed periodograms are found to be a good tool to detect and quantify sinusoidal modulations in a given dataset. The Lomb-Scargle analysis is based on a modified periodogram defined by [223]

$$P_X(T) = \frac{1}{2}\left\{\frac{\left[\sum_{\mathrm{j}=1}^{n} X_\mathrm{j} \cos\left(\frac{2\pi}{T}(t_\mathrm{j} - \tau)\right)\right]^2}{\sum_{=1\mathrm{j}}^{n} \cos^2\left(\frac{2\pi}{T}(t_\mathrm{j} - \tau)\right)} + \frac{\left[\sum_{\mathrm{j}=1}^{n} X_\mathrm{j} \sin\left(\frac{2\pi}{T}(t_\mathrm{j} - \tau)\right)\right]^2}{\sum_{\mathrm{j}=1}^{n} \sin^2\left(\frac{2\pi}{T}(t_\mathrm{j} - \tau)\right)}\right\}, \tag{4.56}$$

with the phase factor τ satisfying

$$\tan\left(\frac{4\pi}{T}\cdot\tau\right)=\frac{\sum_{\mathrm{j}=1}^{n}\sin(\frac{4\pi}{T}\cdot t_{\mathrm{j}})}{\sum_{\mathrm{j}=1}^{n}\cos(\frac{4\pi}{T}\cdot t_{\mathrm{j}})}. \tag{4.57}$$

This periodogram features a simple statistical behavior and essentially equals the minimization of the sum of squares in a least squares fitting of sinusoidal functions to the data [223]. Due to the quadratic sums of the cosine and sine being used, the power calculated with this periodogram for a certain modulation period T is independent of the phase of the modulation as long as the overall time in which the data was acquired is large with respect to the tested period [226].
For a measurement of n independent data points, each data point is further weighted by the ratio of its inverse variance to the average value of the inverse variance of the dataset to account for the statistics of individual bins. Thus, weights of [161]

$$w_{\mathrm{j}}=\frac{1}{\sigma_{\mathrm{j}}^2}/\langle\frac{1}{\sigma_{\mathrm{j}}^2}\rangle \tag{4.58}$$

are defined and the Lomb-Scargle power for a certain period T is modified as

$$\begin{aligned}P_X(T)=\frac{1}{2\sigma^2}\Bigg\{&\frac{\left[\sum_{\mathrm{j}=1}^{n}w_{\mathrm{j}}(X(t_{\mathrm{j}})-\bar{X})\cos\left(\frac{2\pi}{T}(t_{\mathrm{j}}-\tau)\right)\right]^2}{\sum_{\mathrm{j}=1}^{n}\cos^2\left(\frac{2\pi}{T}(t_{\mathrm{j}}-\tau)\right)}\\&+\frac{\left[\sum_{\mathrm{j}=1}^{n}w_{\mathrm{j}}(X(t_{\mathrm{j}})-\bar{X})\sin\left(\frac{2\pi}{T}(t_{\mathrm{j}}-\tau)\right)\right]^2}{\sum_{\mathrm{j}=1}^{n}\sin^2\left(\frac{2\pi}{T}(t_{\mathrm{j}}-\tau)\right)}\Bigg\}\end{aligned} \tag{4.59}$$

with σ and $\bar{X}$ being the weighted variance and weighted mean of the dataset, respectively. Also in the estimation of the phase factor τ, the weights are included and τ is defined via

$$\tan\left(\frac{4\pi}{T}\cdot\tau\right)=\frac{\sum_{\mathrm{j}=1}^{n}w_{\mathrm{j}}\sin(\frac{4\pi}{T}\cdot t_{\mathrm{j}})}{\sum_{\mathrm{j}=1}^{n}w_{\mathrm{j}}\cos(\frac{4\pi}{T}\cdot t_{\mathrm{j}})}. \tag{4.60}$$

Figure 4.16 shows on the left side in blue the result of a Lomb-Scargle analysis for the ten year cosmic muon data acquired in Borexino. The red line represents the 99.5% confidence level for statistical fluctuations. This level has been obtained by generating 10^4 white noise samples. To generate these samples, the distributions of the measured cosmic muon flux and the detector livetime per day in the data sample were fitted with Gaussians. From the distribution of the livetime, a value was randomly drawn and the standard deviation of the muon flux distribution was

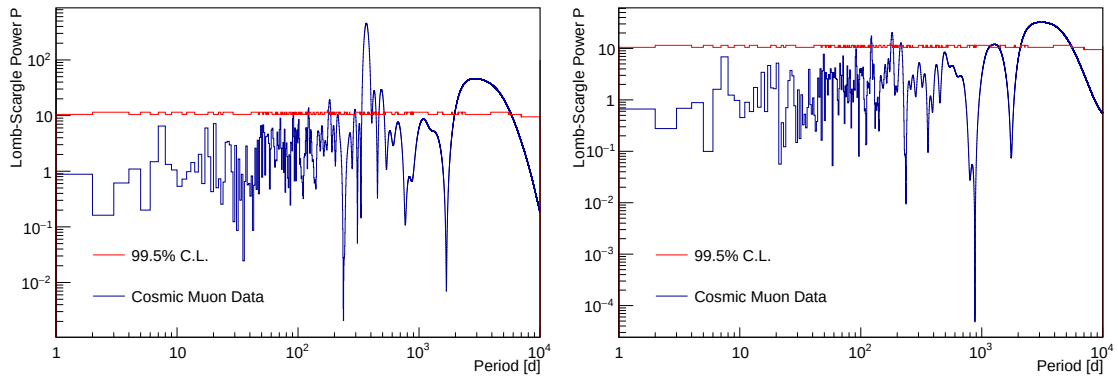

Figure 4.16: Lomb-Scargle periodograms of the cosmic muon flux at Borexino shown in blue. On the *left* side, the periodogram is drawn for the original data. On the *right* side, the seasonal modulation has been subtracted statistically to confirm the significance of the long-term modulation. The red lines depict the 99.5% confidence level of statistical fluctuations.

scaled by the ratio of one day to the drawn livetime to account for fluctuations caused by a lesser livetime at certain days in the original muon sample. In turn, a muon flux was drawn from the Gaussian with this adjusted standard deviation. For every day at which a muon flux has been measured, a white noise data point was created to provide an equal spacing as in the original dataset. The 99.5% confidence level for a certain period T to be present in the dataset was then defined as the Lomb-Scargle power P_{thr} that is higher than the Lomb-Scargle power of $9,950$ white noise samples for this period.

The seasonal modulation of the cosmic muon flux produces a clear and narrow peak in the Lomb-Scargle periodogram. Further, additional peaks on the verge of significance are present at periods slightly larger than seasonal. These might be attributed to a residual noisiness of the periodogram that still finds harmonics of the actually present period to be significant. One slightly significant Lomb-Scargle power is found for a period of $\sim 180\,\text{d}$. This period is expected to represent the deviations from the sinusoidal assumption with a secondary maximum in winter as shown in figure 4.10. Due to this maximum, a bent sinusoidal accounting for a less steep increase of the flux from winter to summer describes the data better, which manifests as a significant subleading peak at $\sim 180\,\text{d}$ in the Lomb-Scargle periodogram.

Besides these periods around the seasonal modulation, the second-most significant peak is found at a period of $\sim 3,000\,\text{d}$ in the Lomb-Scargle periodogram. This period agrees well with the long-term modulation found by the fit to the cosmic muon data according to equation 4.52.

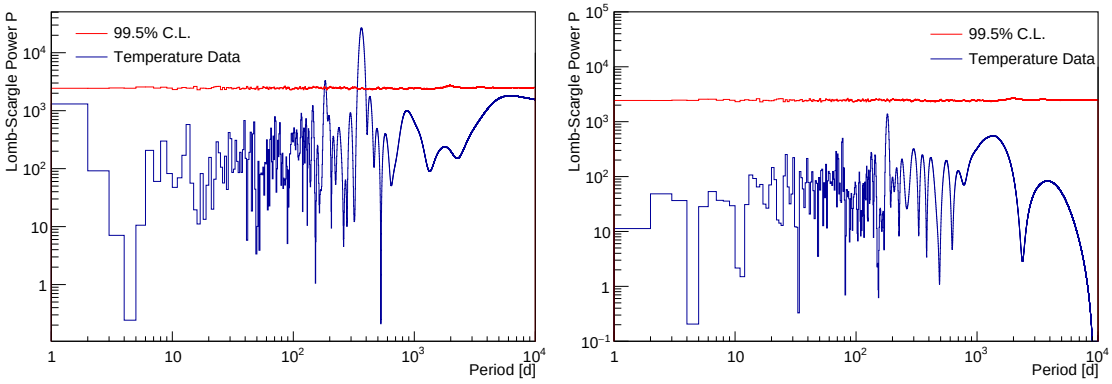

Figure 4.17: Lomb-Scargle periodograms of the effective atmospheric temperature shown in blue. On the *left* side, the periodogram is drawn for the original data. On the *right* side, the seasonal modulation has been subtracted statistically. The red lines depict the 99.5% confidence level of statistical fluctuations.

However, since it is only possible to derive a statistically rigorous conclusion for the dominant peak in a Lomb-Scargle periodogram [216], a Lomb-Scargle periodogram was generated for the cosmic muon data with the seasonal modulation statistically subtracted. This was done by evaluating equation 4.47 with the parameters obtained in the analysis of the seasonal modulation at a given time and subtracting the obtained value from the actual data point. On the right side of figure 4.16, the resulting periodogram together with the 99.5% confidence level calculated in the same way as described above is presented. The long-term modulation is found to generate the highest power in this Lomb-Scargle periodogram and clearly remains above the significance level. Thus, the presence of the long-term modulation found by fitting the cosmic muon flux accordingly to equation 4.52 is confirmed by the Lomb-Scargle analysis. Further, the statistical subtraction of the seasonal modulation presses the corresponding peak and the peaks for slightly higher periods under the significance level. This reveals these peaks to be correlated to the seasonal modulation as harmonics. The peak of the $\sim 180\,\mathrm{d}$ modulation, however, remains above the significance level, which indicates its physical origin.
To check whether this long-term modulation is correlated to the temperature of the atmosphere, the Lomb-Scargle analysis was also performed for the effective atmospheric temperature data shown by the blue line in figure 4.17. As can be seen on the left side, the seasonal modulation of the effective atmospheric temperature produces a clearly significant peak at a period of $\sim 365\,\mathrm{d}$. Also the second order modulation with a period of 180 d observed in the muon flux is found to be significantly present in the temperature data. The red line again represents the 99.5% confidence level as calculated by performing the Lomb-Scargle analysis for

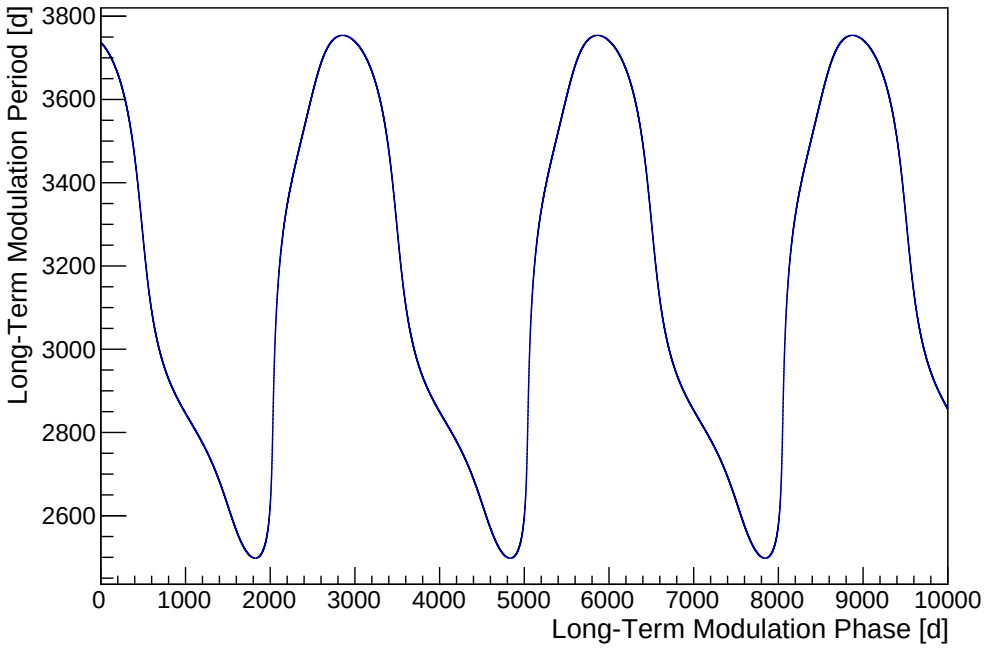

Figure 4.18: Impact of the phase of the long-term modulation on the reconstructed long-term modulation period. The actually inserted long-term modulation with a period of $3,010\,\mathrm{d}$ is reconstructed between $\sim 2,550\,\mathrm{d}$ and $\sim 3,750\,\mathrm{d}$ depending on its phase.

10^4 white noise samples. For the temperature, these white noise samples have been produced by drawing a temperature and an uncertainty from the distributions of the effective atmospheric temperature and its uncertainties for each day for which data was acquired. Besides these peaks, no further peaks and especially no significant long-term modulations are found.
To guaranty that no significant long-term modulation can be introduced by the subtraction of the seasonal modulation as performed for the muon flux data, this procedure was also applied to the effective atmospheric temperature data. As shown on the right side of figure 4.17, after the subtraction of the seasonal modulation, no significant peak is obtained. This proves that the long-term modulation observed in the cosmic muon flux is not correlated to the atmospheric temperature and that the Lomb-Scargle analysis is not biased by the procedure of subtracting the seasonal modulation.
Since the observed period of the long-term modulation of the cosmic muon flux with $\sim 8.25\,\mathrm{yr}$ is close to the measurement time of $10\,\mathrm{yr}$, the actual phase of this long-term modulation is expected to influence the position at which it will generate

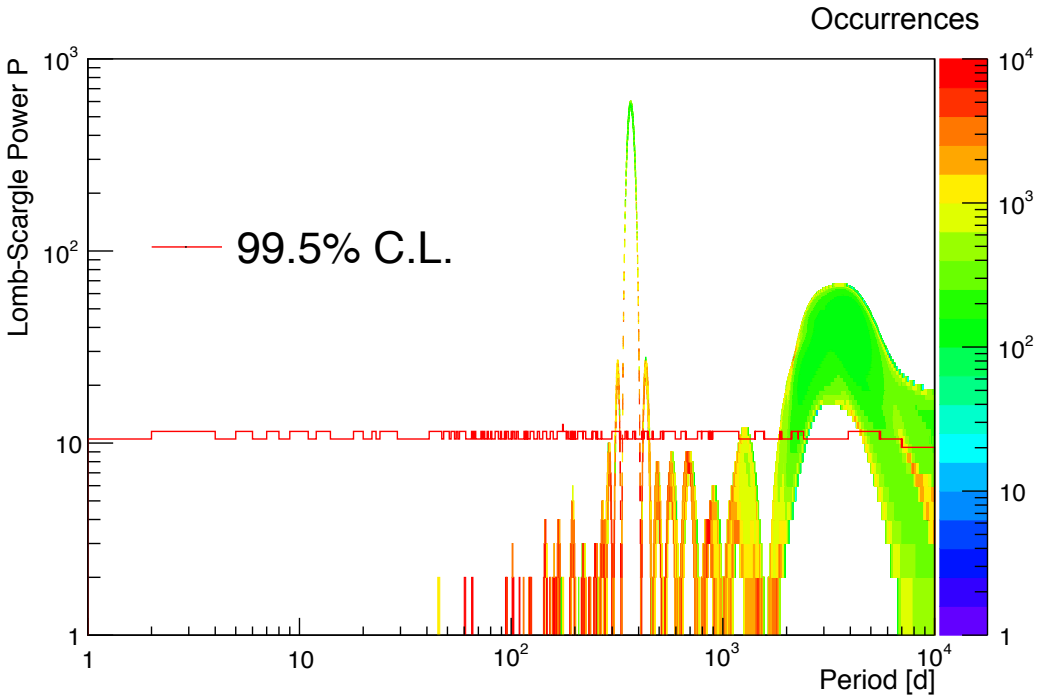

Figure 4.19: Superposition of Lomb-Scargle periodograms for artificially generated muon samples with altered phases of the observed long-term modulation. The red line shows the 99.5% confidence level of statistical fluctuations. The location and maximum Lomb-Scargle power of the peak of the long-term modulation depend on the phase. Independent of the phase, the long-term modulation is found to be significant.

a peak in the Lomb-Scargle periodogram. This influence was analyzed by artificially generating data samples that are modulated as described by equation 4.52 with the parameters given by the fit result. However, the phase of the long-term modulation was altered from 0 d to 10,000 d in steps of one day and the location of the peak of the long-term modulation in the Lomb-Scargle periodogram was analyzed. Figure 4.18 shows the result. Depending on the phase of the long-term modulation, the inserted period of 3,010 d generates a maximum in the Lomb-Scargle periodogram between $\sim 2,550$ d and $\sim 3,750$ d, which indicates the absolute uncertainty of the measured long-term period in the Lomb-Scargle periodogram. The location of the peak in the Lomb-Scargle periodogram depending on the phase shows a periodic behavior with the maxima being separated by the actually inserted period of the long-term modulation of 3,010 d, as can be expected.
To check the impact of the phase of the long-term modulation on the significance of this modulation, a Lomb-Scargle periodogram was produced for each artificially

generated sample of the seasonally and long-term modulated datasets with altered phases of the long-term modulation. Figure 4.19 shows the superposition of these Lomb-Scargle periodograms. Independent of the inserted phase, a significant peak for a long-term modulation is found in the Lomb-Scargle periodogram. However, the location of the peak and its maximum Lomb-Scargle power are affected by the inserted phase. The narrow peak located at $\sim 365\,\mathrm{d}$ shows that the observation of the seasonal modulation is clearly not affected by the phase of the long-term modulation.
In summary, a long-term modulation with a period of $T = (3,010 \pm 299)\,\mathrm{d}$ and a phase of $t_0 = (1,993 \pm 271)\,\mathrm{d}$ is found in the cosmic muon flux measured with Borexino and its significance is confirmed by a Lomb-Scargle analysis of the data. The actual phase of the long-term modulation is found to affect the location of the reconstructed period in the Lomb-Scargle periodogram but not the significance of the long-term modulation. Thus, the width of the peak above the significance level in the Lomb-Scargle periodogram indicates the uncertainty of the significant period. A similar modulation is not observed in the effective atmospheric temperature, such that a different origin than density variations of the upper atmosphere must be expected to cause the long-term modulation of the cosmic muon flux.

4.3.2 Correlation to the Solar Activity

The solar activity has been suspected to cause a long-term modulation of the cosmic muon flux by various authors and a positive correlation between the two observables was found in [216]. The solar activity is often measured by the number of sunspots, i.e. dark spots on the Sun's surface optically observable by telescopes [227]. These sunspots indicate areas where intense magnetic fields loop up and huge amounts of particles are erupted in solar flares. Since the modulation of the solar activity causes changes of the magnetic field, the sunspot number is strongly correlated to the activity of the Sun and used as the key indicator of the solar activity [227].
Since individual solar cycles are known to vary significantly in their period [227], it is not sensible to use a dataset containing sunspot data earlier than the start of data taking of the Borexino experiment when investigating the correlation of the cosmic muon flux to the solar activity. To investigate such a correlation, a Lomb-Scargle analysis of the daily sunspot data (see figure 4.21) provided by the World Data Center SILSO, the Royal Observatory of Belgium in Brussels [228], for the time frame corresponding to the cosmic muon data acquired by Borexino was performed. In figure 4.20, the most significant peak in the Lomb-Scargle periodogram is registered at a period of $\sim 3,050\,\mathrm{d}$, in coincidence with the long-term modulation of the cosmic muon flux. The 99.5% confidence level was computed as described above by generating 10^4 white noise samples with randomly drawn val-

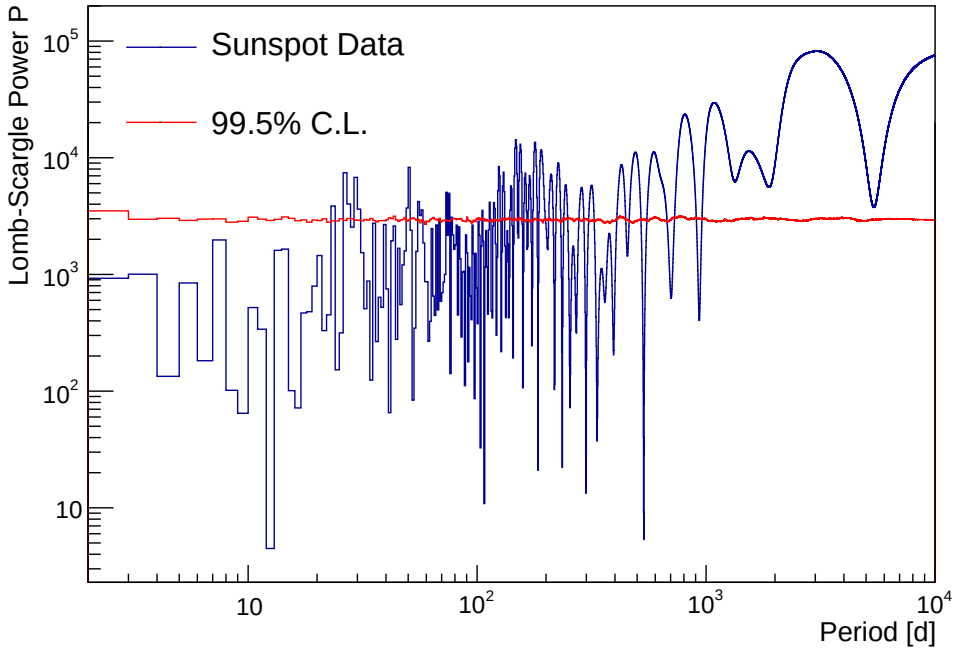

Figure 4.20: Lomb-Scargle periodogram of the sunspot number from May 2007 to May 2017 with data taken from [228]. The most significant peak is found at a period of $\sim 3,050$ d, in coincidence with the cosmic muon flux.

ues and errors from the corresponding distributions of the sunspot data. Based on this limit, further significant subleading modulations of smaller periods are found to be present in the sunspot data.
Besides the modulation of the solar cycle, several authors observed a 154 d periodic signal in the solar activity [229, 230, 231]. In the sunspot data, this periodicity usually occurs around sunspot cycle maxima [232]. Further, a period of about 2 yr has been found to be present [233, 234]. In particular, these periods are found around the maxima of solar cycles in form of double peaks and the so-called Gneyshev-Gap between those peaks [235]. These double peaks are thought to be caused by the solar cycle being characterized by two waves of activity [236, 237]. Such a structure can be observed in the solar cycle corresponding to the Borexino data taking period as shown in figure 4.21. Thus, the peaks in the Lomb-Scarle periodogram for smaller periods than the solar cycle may be attributed to these observations and harmonics of these periods.
A further significant peak is indicated at very high periods in the Lomb-Scargle periodogram. This peak might be associated to longer-term modulations of the solar cycle like the Even-Odd effect describing that odd numbered cycles usually

feature higher maxima than even numbered cycles resulting in a modulation with a period of about two solar cycles in the sunspot data [238].
To estimate the maximum of the solar activity and its agreement to the phase of the observed long-term modulation of the cosmic muon flux, a fit to the sunspot data was performed. Following [239], the solar activity $F(t)$ in an individual solar cycle may be described by a cubic power law and a Gaussian decline as

$$F(t) = A\left(\frac{t-t_\mathrm{s}}{b}\right)^3\left[\exp\left(\frac{t-t_\mathrm{s}}{b}\right)^2 - c\right]^{-1} \tag{4.61}$$

with A being the amplitude of the solar cycle, t_s the starting time, b the rise time, and c an asymmetry parameter. This function considers the effect that solar cycles are found to be asymmetric with a faster rise from minimum to maximum and a slower decay [240].
Since the minimum of the solar cycle corresponding to the Borexino data acquisition time is found around March 2009, the sunspot data is fitted from this month to May 2017 as presented in figure 4.21. The fit returns an amplitude of $A = (168.1 \pm 0.4)$ sunspots per day, a starting time of $t_\mathrm{s} = (-434 \pm 3)\,\mathrm{d}$ prior the minimum set at March 1st, 2009, a rise time of $b = (1,578 \pm 3)\,\mathrm{d}$, and an asymmetry parameter of $c = 0.000 \pm 0.001$ at a poor $\chi^2/\mathrm{NDF} = 143145/2672$. Nevertheless, these values are in a sensible range compared to the average values of solar cycles that are found as $A = 195$ sunspots per day, $b = 56\,\mathrm{months}$, $t_\mathrm{s} = -4\,\mathrm{months}$ prior the minimum, and $c = 0.8$ [227]. Based on the fit, the maximum of the solar cycle corresponding to the Borexino data taking campaign occurs around April 8th, 2013.
To further probe the agreement between the long-term modulation of the cosmic muon flux and the solar activity, the measured cosmic muon flux was fitted similarly to equation 4.61 after statistically subtracting the seasonal modulation. An amplitude of $A = (45.4 \pm 8.1)$ muons per day, a starting time of $t_\mathrm{s} = (-34 \pm 111)\,\mathrm{d}$ prior the minimum set at March 1st, 2009, a rise time of $b = (1,207 \pm 116)\,\mathrm{d}$, and an asymmetry parameter of $c = 1.00 \pm 0.02$ at a $\chi^2/\mathrm{NDF} = 3301/2665$ were obtained. These parameters indicate a maximum in March 2012.
Table 4.7 summarizes the observed parameters of the long-term modulation of the cosmic muon flux for both fits and the observed parameters of the modulation of the solar activity. While the periods of the modulations are found to agree well, the maxima are found to be consistent without observing a distinct accordance. Further, the large uncertainties of the parameters of the long-term modulation of the cosmic muon flux for both fits as well as the large reduced χ^2 of the fit to the sunspot data indicate that the results need to be treated with care. A correlation between the solar activity and the flux of high-energetic cosmic muons can neither be ruled out nor clearly be proven by the observations. However, especially the

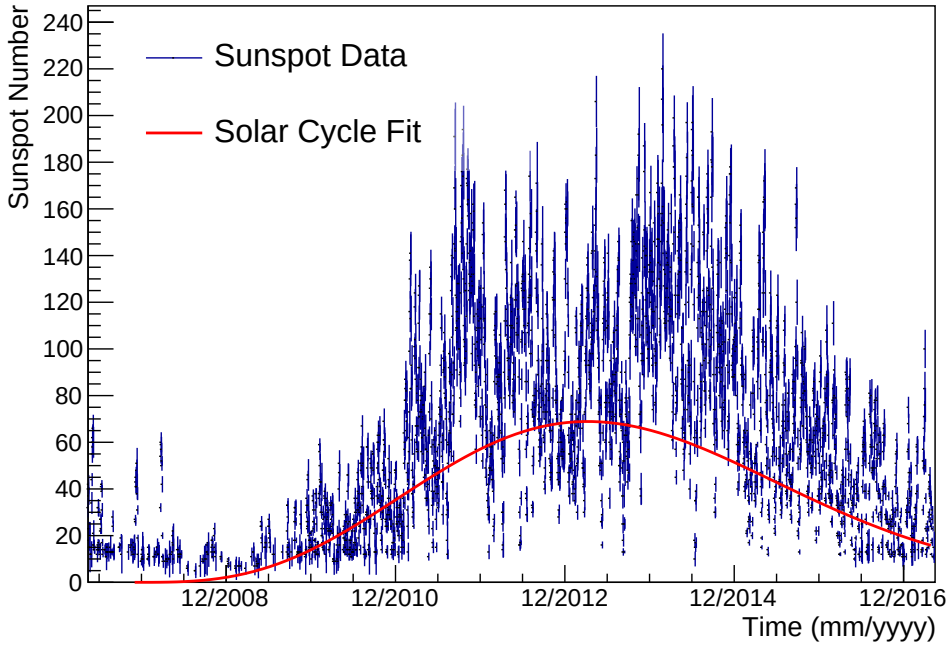

Figure 4.21: Fit to the solar cycle corresponding to the Borexino data taking period based on equation 4.61. The fit returns an amplitude of $A = (168.1 \pm 0.4)$ sunspots per day, a starting time of $t_s = (-434 \pm 3)$ d prior the minimum set at March 1st, 2009, a rise time of $b = (1,578 \pm 3)$ d, and an asymmetry parameter of $c = 0.000 \pm 0.001$ at a $\chi^2/\text{NDF} = 143145/2672$. The sunspot data was obtained from the World Data Center SILSO, the Royal Observatory of Belgium in Brussels [228].

striking agreement between the modulation periods observed in the Lomb-Scargle analysis motivates to investigate this phenomenon more deeply. Further, when fitting the cosmic muon flux measured by Borexino in two year moving subsets of the data as summarized in table 4.2, the highest mean cosmic muon flux is observed in the subset from May 2013 to May 2015 and, thus, later than the maximum of the long-term modulation as obtained from the fits. Additionally, a higher mean cosmic muon flux was observed in the subset from 2009 to 2011 compared to the subset from 2011 to 2013 resembling the two peak structure observed in the solar activity. Even though the assumption that this behavior might be caused by an influence of the solar activity on the cosmic muon flux is highly speculative, a further investigation of the correlation between the solar activity and the cosmic muon flux can be encouraged by these observations.
To clarify the observed phenomena, especially a measurement of the cosmic muon

	Half Period/ Rise Time [d]	Maximum
Muon Flux (Sinusoidal Fit)	$1,505 \pm 150$	June 16th, 2012 $\pm$ 271 d
Muon Flux (Gaussian Fit)	$1,207 \pm 116$	March 4th, 2012 $\pm$ 227 d
Solar Activity (Gaussian Fit)	$1,578 \pm 3$	April 8th, 2013 $\pm$ 6 d

Table 4.7: Parameters of the long-term modulation of the cosmic muon flux and the solar activity.

flux over a longer time period would be beneficial to confirm or deny the presence of a long-term modulation in agreement with the solar activity for several solar cycles. Further, a broader understanding of the dynamical processes inside the Sun and the way they affect high-energetic cosmic ray particles traveling towards the Earth might predict or strictly contradict a correlation between the cosmic muon flux and the solar activity.

Chapter 5

Measurement of the Atmospheric Kaon to Pion Production Ratio

As has been shown in the preceding chapter, the residual flux of cosmic muons arriving at the Borexino detector is found to be seasonally modulated in leading order. This modulation is related to seasonal temperature and density variations of the upper atmosphere that alter the mean free path of the parent mesons and affect the probability for them to decay in flight. However, only if the parent kaons and pions decay in flight without any interaction with the nuclei of the atmosphere before the decay, the produced cosmic muons receive sufficient energy to pass through the rock coverage of the LNGS. Thus, the effect that temperature variations of the upper atmosphere alter the mean free path of the mesons is transmitted to the flux of cosmic muons observed underground.
Due to the different properties of kaons and pions concerning their propagation and decay, the probability for kaons and pions to decay in flight is differently sensitive to temperature variations of the upper atmosphere. Since kaons have a higher rest mass than pions, they decay quicker into muons and feature a shorter decay length. Thus, they are less sensitive to temperature variations in the atmosphere and feature a principally higher probability to decay in flight than pions. This is described by a relatively high critical kaon energy $\epsilon_{\mathrm{K}} = (851 \pm 14)\,\mathrm{GeV}$ [176] that separates the decay from the interaction regime for those mesons in the upper atmosphere. Kaons up to the energy of ϵ_{K} are more likely to decay while kaons of higher energies most probably interact before decaying. Since pions are lighter, their decay length is longer and the probability for them to decay in flight is stronger dependent on the atmospheric temperature and the mean free path. For pions, the critical energy $\epsilon_{\pi} = (114 \pm 3)\,\mathrm{GeV}$ [176] is, accordingly, lower than for kaons.
Due to these effects, the strength of the correlation between the atmospheric temperature and the cosmic muon flux underground depends on the ratio at which

kaons and pions are produced in the upper atmosphere. For an increased kaon fraction, less parent mesons are affected by temperature variations and the correlation between the atmospheric temperature and the cosmic muon flux underground gets weaker.
As presented in section 4.1.2, fluctuations of the measured cosmic muon flux in an underground experiment may be related to fluctuations in the atmospheric temperature by the so-called effective temperature coefficient α_{T}. Thus, α_{T} can be determined via

$$\frac{\Delta I_{\mu}}{I_{\mu}^{0}} = \alpha_{\mathrm{T}} \frac{\Delta T_{\mathrm{eff}}}{T_{\mathrm{eff}}}, \tag{5.1}$$

where ΔI_{μ} is the variation of the cosmic muon flux from its mean I_{μ}^{0} and ΔT_{eff} the variation of the effective atmospheric temperature from its mean T_{eff}. To allow the study of the correlation between the cosmic muon flux and fluctuations of the temperature in the atmosphere, the effective atmospheric temperature T_{eff} needs to be introduced to model the atmosphere as an isothermal meson-producing entity. T_{eff} is defined as the temperature of an isothermal atmosphere in which the same meson intensities are generated as observed in the actual atmosphere with its slant depth dependent temperature distribution $T(X)$.
The effective temperature coefficient α_{T} parametrizes the strength of the correlation between the cosmic muon flux observed underground and the atmospheric temperature. It can be qualitatively understood as the fraction of mesons that contribute to the measured muon flux and that are affected by temperature variations in the upper atmosphere with respect to their in-flight decay probability. Considering the different sensitivity of kaon and pion decays towards temperature variations in the upper atmosphere, α_{T} can be interpreted as an indirect measurement of the atmospheric kaon to pion production ratio $r_{\mathrm{K}/\pi}$.
Since the atmospheric kaon to pion production ratio enters in the calculation of the effective atmospheric temperature, the measurement of α_{T} based on equation 5.1 contains a weak dependence on $r_{\mathrm{K}/\pi}$. By comparing the measured value of α_{T} for different input values of $r_{\mathrm{K}/\pi}$ with a theoretical estimation of α_{T} at the LNGS for the respective kaon to pion production ratio, an estimate of this quantity can be obtained.
In current cosmic ray models, the atmospheric kaon to pion production ratio can only be predicted with an uncertainty of the order of 40% [241]. Previous measurements have been performed at accelerators for p + p collisions [242, 243], Au + Au collisions [244], p + $\bar{\mathrm{p}}$ collisions [245], and Pb + Pb collisions [246], while the MINOS [176, 178] and the IceCube [214] collaborations reported a measurement of the atmospheric kaon to pion ratio inferred indirectly via a measurement of the effective temperature coefficient. Results of many older measurements using various reactions are summarized and referred to in [247]. Additionally, the

atmospheric kaon to pion production ratio may be estimated by combining the measurements of the effective temperature coefficient from experiments at various depths as shown in section 4.2.4. However, this approach is affected by strong uncertainties that are difficult to quantify, such that the inferred value may only last as an indication of the kaon to pion production ratio.
In the following, a measurement of the atmospheric kaon to pion production ratio through the modulation of the cosmic muon flux observed with Borexino is presented. In this case, no further experimental data has to be included. In section 5.1, the dependence of the measured value of α_{T} on $r_{\mathrm{K}/\pi}$ is investigated. To calculate the predicted value of α_{T} at the LNGS in dependence on $r_{\mathrm{K}/\pi}$, a Monte Carlo simulation was performed as presented in section 5.2. In section 5.3, the experimental and theoretical results are combined in a χ^2 fit to obtain a measurement of the atmospheric kaon to pion production ratio. In section 5.4, a second approach to determine $r_{\mathrm{K}/\pi}$ via the ratio of observed muons that were produced by kaons to muons that were produced by pions is followed. The chapter is concluded with a comparison of the two results to each other and to measurements from other experiments in section 5.5.

5.1 Experimental Determination of α_{T} Depending on the Kaon to Pion Production Ratio

The effective atmospheric temperature allows to describe the atmosphere as an isothermal meson-producing entity and is approximated for measurements of the temperature at discrete atmospheric depths X_{n} as (see equation 4.37 in section 4.1.2)

$$T_{\mathrm{eff}} \simeq \frac{\sum_{\mathrm{n}=0}^{N} \Delta X_{\mathrm{n}}\, T(X_{\mathrm{n}})(W_{\mathrm{n}}^{\pi}(X_{\mathrm{n}}) + W_{\mathrm{n}}^{\mathrm{K}}(X_{\mathrm{n}}))}{\sum_{\mathrm{n}=0}^{N} \Delta X_{\mathrm{n}}\, (W_{\mathrm{n}}^{\pi}(X_{\mathrm{n}}) + W_{\mathrm{n}}^{\mathrm{K}}(X_{\mathrm{n}}))}. \tag{5.2}$$

The weight function accounting for the kaon contribution to the cosmic muon production $W_{\mathrm{n}}^{\mathrm{K}}(X_{\mathrm{n}})$ is given by [178]

$$W_{\mathrm{n}}^{\mathrm{K}}(X_{\mathrm{n}}) \equiv \frac{A_{\mathrm{K}}^{1} e^{-X_{\mathrm{n}}/\Lambda_{\mathrm{K}}} (1 - X_{\mathrm{n}}/\Lambda_{\mathrm{K}}')^2}{\gamma + (\gamma+1) B_{\pi}^{1} K(X_{\mathrm{n}}) (E_{\mathrm{thr}} \cos\theta/\epsilon_{\pi})^2}. \tag{5.3}$$

A_{K}^{1} describes the strength of the kaon contribution and is connected to the atmospheric kaon to pion production ratio $r_{\mathrm{K}/\pi}$ via [176]

$$A_{\mathrm{K}}^{1} = 0.38 \times r_{\mathrm{K}/\pi}. \tag{5.4}$$

Thus, the calculated value of the effective atmospheric temperature depends on the inserted value of $r_{\mathrm{K}/\pi}$ and this dependence is propagated to the measurement

of the effective temperature coefficient α_{T}. Since α_{T} is determined through a fit of the correlation between the cosmic muon flux and the effective temperature as defined by equation 5.1, the measured value is weakly affected by the applied kaon to pion production ratio in the calculation of T_{eff}.
As described in section 4.2.4, the temperature data provided by the European Center for Medium-range Weather Forecasts (ECMWF) [183] was used to determine T_{eff}. Based on four measurements of the temperature in the atmosphere at 37 pressure levels between 1 hPa and 1,000 hPa, the effective atmospheric temperature was calculated four times a day and the mean of the four estimations was assigned as the effective atmospheric temperature of the corresponding day. Then, α_{T} was determined via the correlation between the effective temperature and the measured cosmic muon flux as described by equation 5.1.
To determine the dependence of the measured value of α_{T} on the kaon to pion production ratio, the effective temperature was calculated for each day at which the cosmic muon flux has been measured with the inserted value of $r_{\mathrm{K}/\pi}$ altered between 0 and 0.3 in steps of 10^{-3}. Subsequently, α_{T} was determined for each set of T_{eff} via the correlation to the cosmic muon flux.
The results of these measurements of α_{T} in dependence of the atmospheric kaon to pion production ratio are shown in figure 5.3 depicted in blue. The very weak dependence of α_{T} on $r_{\mathrm{K}/\pi}$ is strongly exceeded by the statistical uncertainties of the measurements. As described in section 4.2.4, statistical uncertainties were found to strongly overpower any systematic effects caused by detector instabilities with respect to the measured value of α_{T}. Thus, no systematic effects are expected to influence the measurements of α_{T} and only statistical uncertainties are considered.

5.2 Determination of the Theoretical Expectation of α_{T}

As shown in section 4.1.1, the differential muon energy spectrum is given by [79]

$$\frac{\mathrm{d}I_\mu}{\mathrm{d}E_\mu} \simeq A \times E_\mu^{-(\gamma+1)} \left(\frac{1}{1 + 1.1 E_\mu \cos\theta/\epsilon_\pi} + \frac{\eta}{1 + 1.1 E_\mu \cos\theta/\epsilon_{\mathrm{K}}} \right), \tag{5.5}$$

where

$$\eta \equiv 0.635 \frac{Z_{\mathrm{NK}}}{Z_{\mathrm{N}\pi}} \frac{1 - r_\pi}{1 - r_{\mathrm{K}}} \frac{1 - r_{\mathrm{K}}^{\gamma+1}}{1 - r_\pi^{\gamma+1}}, \tag{5.6}$$

$r_{\mathrm{M}} = m_\mu^2/m_{\mathrm{M}}^2$ for the meson species M, ϵ_{M} the critical energy of the meson species M, θ the zenith angle of the muon, and $\gamma = 1.78 \pm 0.05$ the muon spectral index as measured by the LVD experiment [131]. Z_{NK} and $Z_{\mathrm{N}\pi}$ are the spectrum weighted inclusive cross sections for kaon and pion production from primary cosmic rays,

respectively. Starting from this expression, an approximation of the total muon flux in an underground laboratory can be made as [175]

$$I_\mu \simeq B \times E_{\mathrm{thr}}^{-\gamma} \left(\frac{1}{\gamma + (\gamma+1)1.1E_{\mathrm{thr}}\cos\theta/\epsilon_\pi} + \frac{\eta}{\gamma + (\gamma+1)1.1E_{\mathrm{thr}}\cos\theta/\epsilon_{\mathrm{K}}} \right). \tag{5.7}$$

Here, $E_{\mathrm{thr}}(\theta,\phi)$ describes the minimum energy a muon arriving from a zenith angle θ and an azimuth angle ϕ with respect to the position of the LNGS has to possess in order to penetrate through the rock coverage and reach the detector. As shown in section 4.1.1, this threshold energy can be calculated as [79]

$$E_{\mathrm{thr}} = \epsilon(e^{bD(\theta,\phi)} - 1) \tag{5.8}$$

with $\epsilon = a/b \simeq 500\,\mathrm{GeV}$ the critical energy below which the energy loss of muons is dominated by ionization instead of radiative processes, $D(\theta,\phi)$ the angle dependent distance the muon has to traverse through the rock in order to reach the detector, and $a \approx 2\,\mathrm{MeV}/(\mathrm{g\,cm^{-2}})$ [79] and $b \approx 4.0 \times 10^{-6}\,\mathrm{g^{-1}cm^2}$ [180] the parameters describing the energy loss of the muon through ionization and radiation, respectively.
As detailed in section 4.1.2, α_{T} is theoretically predicted as

$$\alpha_{\mathrm{T}} = \frac{T}{I_\mu^0}\frac{\partial I_\mu}{\partial T} \tag{5.9}$$

for a properly weighted atmospheric temperature distribution. This expression can be translated into [175]

$$\alpha_{\mathrm{T}} = -\frac{E_{\mathrm{thr}}}{I_\mu^0}\frac{\partial I_\mu}{\partial E_{\mathrm{thr}}} - \gamma \tag{5.10}$$

for the muon spectrum described by equation 5.5. Using the expression given by equation 5.7, the effective temperature coefficient is calculated to be

$$\alpha_{\mathrm{T}} = \frac{1}{D_\pi}\frac{1/\epsilon_{\mathrm{K}} + A_{\mathrm{K}}(D_\pi/D_{\mathrm{K}})^2/\epsilon_\pi}{1/\epsilon_{\mathrm{K}} + A_{\mathrm{K}}(D_\pi/D_{\mathrm{K}})/\epsilon_\pi}, \tag{5.11}$$

where

$$D_\pi \equiv \frac{\gamma}{\gamma+1}\ \frac{\epsilon_\pi}{1.1E_{\mathrm{thr}}\cos\theta} + 1$$

$$D_{\mathrm{K}} \equiv \frac{\gamma}{\gamma+1}\ \frac{\epsilon_{\mathrm{K}}}{1.1E_{\mathrm{thr}}\cos\theta} + 1$$

and $A_{\mathrm{K}} = 0.38 \times r_{\mathrm{K}/\pi}$ [176].
To determine the theoretical expectation of α_{T} at the LNGS dependent on the atmospheric kaon to pion production ratio, a Monte Carlo simulation was developed.

In this simulation, first, a zenith angle is drawn randomly from the zenith angle distribution of cosmic muons at the surface. This distribution in general is $\propto \cos^2(\theta)$ since it is strongly dominated by the most abundant low-energetic muons. However, it shifts towards $\propto \sec(\theta)$ for muons with $E_\mu \gg \epsilon_\pi$ and $\theta < 70°$ [7]. The chosen zenith angle is inserted into equation 5.5 and a muon energy is drawn from the spectrum. An azimuth angle ϕ is assigned randomly from a uniform distribution in the interval $\phi \in [0, 2\pi]$. Then, the threshold energy E_{thr} necessary for a muon arriving from the zenith angle θ and the azimuth angle ϕ is calculated based on equation 5.8 and an altitude profile of the Gran Sasso mountain massif obtained using the Google Maps Elevation API [248]. If the chosen muon energy exceeds the necessary threshold energy, α_{T} is calculated accordingly to equation 5.11 for the chosen zenith angle θ and the calculated threshold energy E_{thr}. For every value of $r_{\text{K}/\pi}$ between 0 and 0.3 in steps of 10^{-3}, 10^4 muons reaching the detector were simulated and the mean value of α_{T} was assigned as the theoretical expectation for the respective $r_{\text{K}/\pi}$ value.
In the following two sections, this Monte Carlo simulation and its performance are presented and the systematic uncertainties of the determination of the theoretically expected α_{T} are analyzed.

5.2.1 Monte Carlo Simulation for the Prediction of α_{T}

Figure 5.1 shows a track of a simulated cosmic muon in red and the altitude profile of the Gran Sasso mountain massif obtained using the Google Maps Elevation API [248] on the left side. The Google Maps excerpt for which the altitude profile was generated is shown on the right. The black circle in the altitude profile indicates the position of the LNGS at 42.456500°N and 13.570444°E at an altitude of 963 m [186] and the yellow star marks the point where the muon enters the rock. To calculate the threshold energy for a muon arriving from a given direction, the distance between its entry point into the rock and the LNGS is determined. The calculated distance is multiplied with the average rock density at Gran Sasso $\rho = 2.71 \pm 0.05\,\text{g/cm}^3$ [249] to obtain the slant depth in meters water equivalent (m we). In the rare cases in which a muon arriving at a huge zenith angle passes through one of the adjacent mountain tops of Monte Aquila, then continues its track through the air again before finally entering the rock and traveling to the LNGS, all the distances the muon passes through the rock are summed.
The zenith angle distribution used for the simulation is based on the information mentioned above and composed of $I_\mu \propto \sec\theta$ for $\theta < 70°$ and $I_\mu \propto \cos^2\theta$ for $\theta \geq 70°$. Both parts of the function were adjusted to match at $\theta = 70°$, the function was normalized, and the zenith angles are randomly drawn from this distribution. This description of the zenith angle distribution was compared to a simulation based on the MCEq software [250] that is used to simulate the propagation of

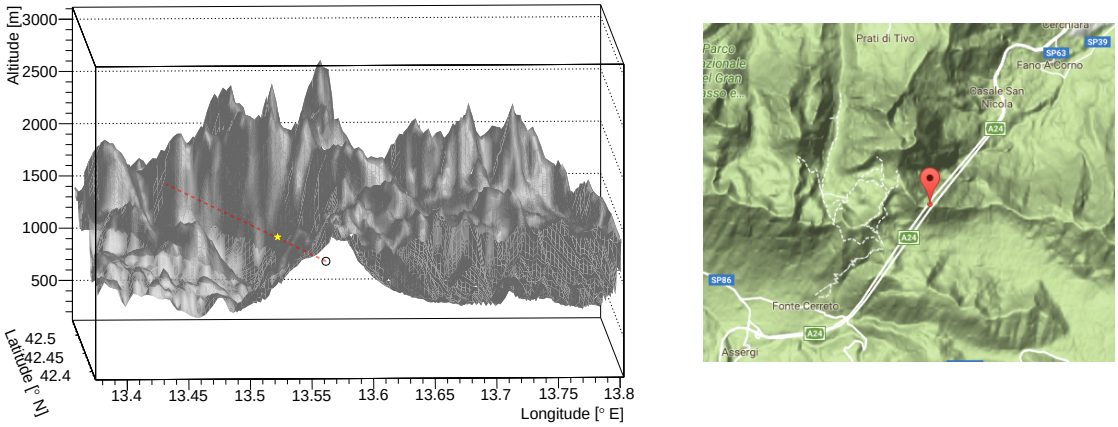

Figure 5.1: Muon track and altitude profile together with the corresponding Google Maps excerpt. *Left:* A muon track for $\theta = 1.5\,\text{rad}$ and $\phi = 3.8\,\text{rad}$ is depicted by the dotted red line. The circle shows the position of the LNGS and the star the entry point of the muon into the rock. The altitude profile as obtained using the Google Maps Elevation API [248] is shown in gray. *Right:* Google Maps excerpt from which the altitude profile was extracted.

showers through the atmosphere by solving the applying cascade equations and a good agreement was found [251].
To save computation time, the rock coverage a muon arriving from the direction (θ, ϕ) has to pass through to reach the LNGS was first calculated for pairs of (θ, ϕ) in steps of $0.5°$ each and the calculated depth was saved in a two dimensional histogram. After randomly drawing θ from the zenith angle distribution and ϕ from a uniform distribution, the precalculated depth profile was used to estimate the threshold energy E_{thr} for a muon to reach the LNGS from the drawn direction accordingly to equation 5.8.
Figure 5.2 shows the zenith and azimuth angle distributions of muons reaching the LNGS as obtained from the simulation in blue compared to the distributions measured with Borexino in red. The main features of the angular distributions are reflected in the simulation. The zenith angle distribution of simulated muons mirrors the shift of the distribution caused by the shape of the rock coverage from its maximum at the surface at low zenith angles towards higher values of θ. Considering that no detector resolution effects enter in the simulation and that the angular resolution of the Borexino tracking algorithms has been estimated to be $\sim (3-5)°$ [108], the simulated and measured distributions are found to agree comparably well. Further, the Borexino tracking has been found to show a widening of the $\cos\theta$ distribution compared to the distribution measured by MACRO, which

was attributed to an inferior performance of the Borexino tracking [80]. Thus, the differences between the simulated and measured zenith angle distributions might be caused to a significant extent by inaccuracies of the experimental tracking capabilities.
Also the two peak structure in the azimuth angle distribution is reproduced in the simulation. This structure emerges due to the shape of the rock coverage. The Gran Sasso massif is a mountain ridge with deeper falling flanks at the South and the North resulting in a reduced rock coverage for muons arriving from those directions [80]. Thus, the flux of muons arriving from these directions is increased and two peaks in the azimuth angle distribution arise.
However, even though the main features of the angular distributions are reconstructed in the simulation and the agreement to the measurements is quite good, no absolute agreement is achieved. This indicates that uncertainties of the rock map, the position of the LNGS, and the zenith angle distribution need to be considered. Further, especially in the simulated azimuth angle distribution, some steps are visible that are caused by the binning of θ and ϕ in 0.5° wide bins to calculate the direction dependent threshold energy.
Besides the prediction of α_T, the simulation allows to infer the expected value of the direction dependent threshold energy folded with the cosine of the zenith angle distribution $\langle E_\mathrm{thr} \cos\theta \rangle$. This quantity enters in the computation of the atmospheric temperature and determines the predicted value of α_T at a certain underground site for a given atmospheric kaon to pion production ratio. Thus, it is used as a parametrization of the respective depths to compare the measurements of α_T from experiments located at different underground laboratories in figure 4.14. By calculating the mean value of this product for 10^4 muons reaching the underground laboratory using the simulation, a value of $\langle E_\mathrm{thr} \cos\theta \rangle = (1.34 \pm 0.18)\,\mathrm{TeV}$ was obtained. The uncertainty was calculated by altering the input parameters of the simulation as detailed in the following section and recalculate $\langle E_\mathrm{thr} \cos\theta \rangle$. In former publications, the zenith angle distribution and the impact of the profile of the rock coverage of the LNGS were mostly neglected and values of $E_\mathrm{thr} \simeq 1.3\,\mathrm{TeV}$ [182, 199] and $E_\mathrm{thr} = 1.833\,\mathrm{TeV}$ [179] were reported for the LNGS. However, due to the impact of a reduced coverage of the laboratory for muons arriving from the flanks of the mountain ridge compared to a laboratory with a flat overburden, the zenith angle distribution of incoming muons must be considered to derive a comparable parametrization of the depth. Thus, $\langle E_\mathrm{thr} \cos\theta \rangle$ needs to be used to compare measurements carried out at different experimental sites since the effect of the shape of the respective rock overburden for different underground laboratories is considered in the computation of this value.
To further probe the accuracy of the simulation, its result was compared to a simulation using the MUSUN (MUon Simulations UNderground) code [133]. This

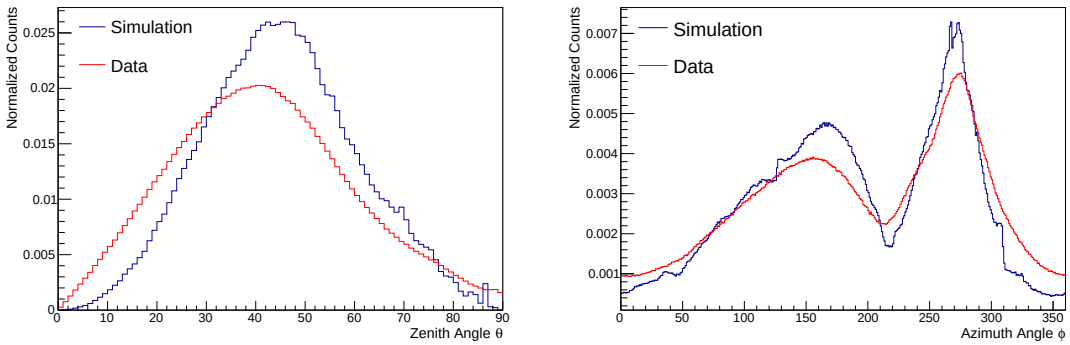

Figure 5.2: Comparison of the angular distributions obtained from the Monte Carlo simulation in blue and the measured distributions in red. The zenith angle is shown on the *left*, the azimuth angle on the *right* side. A good agreement between the measured and simulated distributions is observed.

simulation is tuned for the location of the LVD experiment and has been found to accurately reproduce the measurement of the azimuth angle distribution at their experimental site [252] in Hall A and the mean muon energy at the LNGS of $E_\mu = (270 \pm 3_{\text{stat}} \pm 18_{\text{syst}})\,\text{GeV}$ as measured by the MACRO experiment [134].
MUSUN is established on the output of the MUSIC (MUon SImulation Code) [133] simulation tool. MUSIC allows to simulate the propagation of muons through large stretches of matter taking into account energy losses of the muons through ionization, bremsstrahlung, pair production, and muon-nucleus inelastic scattering. To determine the energy and angular distributions of muons at the location of the LVD experiment, first, muons of various initial energies are propagated through matter using MUSIC and their energy distribution in dependence on the depth is stored. Then, MUSUN considers the slant depth distribution as seen from the LVD experiment. By folding this slant depth distribution with the energy and angular distribution of muons at the surface and using the MUSIC output, MUSUN allows to directly investigate the cosmic muon flux and its properties at the location of the LVD experiment [133, 252].
To calculate α_T based on the MUSUN code, 10^8 muons were simulated at the location of the LVD experiment and their zenith and azimuth angles as well as the corresponding threshold energies were stored. Then, for each $r_{\text{K}/\pi}$ value, 10^5 of these muons were picked randomly and α_T was calculated. The mean difference between the effective temperature coefficient based on the Google Maps altitude profile and the MUSUN simulation is $\Delta\alpha_\text{T} = \alpha_{\text{T, Google}} - \alpha_{\text{T, MUSUN}} = 5 \cdot 10^{-5}$ and, hence, very small. This further ensures that the simulation developed using the Google Maps Elevation API altitude profile and the inferred prediction of α_T are reliable since MUSUN has been found to provide very accurate estimations of the

cosmic muon flux underground.
Figure 5.3 shows the result of the effective temperature coefficient in dependence on $r_{\mathrm{K}/\pi}$ as predicted by the simulation in red. With increasing kaon to pion production ratio, the value of α_{T} decreases since the probability for kaons to decay in flight is less sensitive to temperature variations of the upper atmosphere than the probability for pion decays in flight. Thus, the correlation between the atmospheric temperature and the cosmic muon flux gets weaker for a higher kaon contribution to the flux and α_{T} decreases. Several systematic uncertainties of the predicted value of α_{T} need to be considered that are introduced by uncertainties of the input parameters of the simulation. These uncertainties are presented and estimated in the following section.

5.2.2 Systematic Uncertainties of the Calculation of α_{T}

Since several of the input parameters of the simulation contain an uncertainty, also the resulting value of α_{T} is affected by these uncertainties. Consequently, these effects must be considered when comparing the predicted values to the measurement in order to infer $r_{\mathrm{K}/\pi}$.
To estimate the systematic uncertainty of the determination of the effective temperature coefficient, the values of the considered uncertainty sources were successively set to the border of their uncertainty margin and the simulation was repeated with the altered input value. The contribution of the respective uncertainty source to the systematic uncertainty of the α_{T} calculation was then estimated as the difference between the altered and the original result of the simulation. For every uncertainty source, the simulation was run for the highest and the lowest value within the error margin to make sure that no nonlinear effects are missed. However, the contributions of the uncertainty sources were found to be very symmetric. Thus, the higher uncertainty obtained was, conservatively, assigned as the upper and lower uncertainty margin of the calculated value of α_{T}. Further, a possible dependence of the uncertainty of α_{T} on $r_{\mathrm{K}/\pi}$ was taken into account by running the simulation with the altered input parameter for all considered values of $r_{\mathrm{K}/\pi}$.
Table 5.1 gives an overview of the considered uncertainty sources and their contributions to the systematic uncertainty of the α_{T} calculation. The uncertainties are given at the best fit value of $r_{\mathrm{K}/\pi}$ inferred by the combined χ^2 fit presented in section 5.3.
The most important uncertainty is introduced by the altitude profile and, thus, the depth profile used in the simulation. Since the accuracy of the altitude profile is not given, a 5% uncertainty was assumed. This is expected to well cover the actual uncertainty since in the comparison with exactly known altitudes like the mountain tops of the Gran Sasso massif, the obtained profile was found to be very accurate. The contribution of this uncertainty at the best fit value is $\Delta\alpha_{\mathrm{T}} = \pm 0.0066$ but has

Uncertainty source	$\Delta\alpha_{\mathrm{T}}$
Altitude profile $\Delta D(\theta, \phi) = 5\%$	0.0066
Gran Sasso rock density $\rho = 2.71 \pm 0.05\,\mathrm{g/cm^3}$ [249]	0.0029
Critical kaon energy $\epsilon_{\mathrm{K}} = 851 \pm 14\,\mathrm{GeV}$ [176]	0.0011
Critical pion energy $\epsilon_{\pi} = 114 \pm 3\,\mathrm{GeV}$ [176]	0.0002
Muon spectral index $\gamma = 1.78 \pm 0.05$ [131]	0.0007
Zenith angle $\Delta\theta = 10\%$	0.0038
Comparison to MUSUN	0.0005
$\sum$	0.0151

Table 5.1: Sources of systematic uncertainties of the theoretical prediction of α_{T}. The uncertainties of α_{T} were estimated by setting the values of the input parameters to the border of their error margin and rerunning the simulation. Uncertainties are given at the best fit value of $r_{\mathrm{K}/\pi}$ based on the combined χ^2 fit shown in figure 5.3.

a dependence on $r_{\mathrm{K}/\pi}$. For an altered depth, i.e. if the simulation is run with 95% or 105% of the depth calculated from the altitude profile, the uncertainty increases with an increasing kaon to pion ratio. This can be explained since for lower depths, also less energetic muons may penetrate through the reduced rock coverage such that the factor $\langle E_{\mathrm{thr}} \cos\theta \rangle$ is reduced. This smaller $\langle E_{\mathrm{thr}} \cos\theta \rangle$ steepens the slope of the expected α_{T} in dependence of $r_{\mathrm{K}/\pi}$ as obtained from equation 5.11. Hence, the slope for the lowered depth is steeper than for the original depth while the slope for the increased depth is less steep. In both cases, the difference between the original simulation and the simulation for the altered input value increases with $r_{\mathrm{K}/\pi}$.
Qualitatively, this effect may be understood since for higher threshold energies, the fraction of kaons that are affected by temperature variations is increased. In principle, kaons decay relatively quickly and the probability for them to decay in flight is less sensitive to small temperature variations of the atmosphere than for pions. Thus, the effective temperature coefficient decreases with increasing kaon to pion production ratio. However, the parent mesons must possess higher kinetic energies to produce muons of higher energies. Due to this, a higher threshold energy for muons implies higher kinetic energies and increased decay lengths of the parent mesons, which increases the fraction of kaon decays that are affected by temperature variations. At larger depths with higher threshold energies, the effective temperature coefficient, thus, decreases slower with increasing kaon to pion production ratio. For a lowered depth, the threshold energy is decreased and a lesser fraction or, in an extreme picture, no kaons are affected by temperature variations. Hence, the effective temperature coefficient falls quickly with increasing $r_{\mathrm{K}/\pi}$ for lower depths and the difference of α_{T} to the original value increases

with $r_{\mathrm{K}/\pi}$ for a lowered as well as for an increased depth.
Closely connected to the uncertainty of the depth profile is the uncertainty of the density of the rock since this quantity effectively also affects the depths and, thus, the threshold energy. Nevertheless, it is treated as a separate and unique uncertainty source. The measured value of the density of the Gran Sasso rock is $\rho = 2.71 \pm 0.05\,\mathrm{g/cm^3}$ [249]. By altering this observable within its error margin, an uncertainty of $\Delta\alpha_{\mathrm{T}} = \pm 0.0029$ at the best fit value is obained. Again, the systematic uncertainty of the α_{T} calculation introduced by the density of the rock coverage increases with increasing $r_{\mathrm{K}/\pi}$ due to the effects described above.
Another systematic uncertainty evolves through the uncertainties of the critical meson energies that are given by $\epsilon_\pi = (114 \pm 3)\,\mathrm{GeV}$ and $\epsilon_{\mathrm{K}} = (851 \pm 14)\,\mathrm{GeV}$ [176] for pions and kaons, respectively. At the best fit value, the systematic uncertainty related to the pion critical energy is $\Delta\alpha_{\mathrm{T}} = \pm 0.0002$ and the one related to the kaon critical energy $\Delta\alpha_{\mathrm{T}} = \pm 0.0011$. Both contributions are altered with increasing $r_{\mathrm{K}/\pi}$. With increasing kaon to pion ratio, the uncertainty of α_{T} introduced by the critical kaon energy increases while the uncertainty caused by the critical pion energy decreases. Due to the larger absolute uncertainty of the critical kaon energy, the increase of the systematic uncertainty of the α_{T} calculation with $r_{\mathrm{K}/\pi}$ caused by the critical kaon energy strongly overpowers the decrease of the critical pion energy contribution. Thus, the overall contribution of the uncertainties of the critical meson energies increases with $r_{\mathrm{K}/\pi}$.
The muon spectral index is measured as $\gamma = 1.78 \pm 0.05$ [131] and also introduces a systematic uncertainty in the Monte Carlo simulation to calculate α_{T}. At the best fit value of $r_{\mathrm{K}/\pi}$, its contribution is $\Delta\alpha_{\mathrm{T}} = \pm 0.0007$. Also this uncertainty contribution slightly rises with increasing kaon to pion production ratio since the muon spectral index affects the slope of the predicted effective temperature coefficient depending on $r_{\mathrm{K}/\pi}$ as given by equation 5.11. The muon spectral index defines the decrease of the muon energy spectrum described by equation 5.5. With an increased muon spectral index, the spectrum decreases faster and the high-energetic tail of the spectrum is depopulated. Thus, less muons of highest energies that are strongly affected by the temperature variations are produced and the correlation gets weaker. Hence, for higher values of γ, the expected temperature coefficient decreases. For a higher kaon contribution, this effect is further enhanced due to the higher critical energy of kaons compared to pions.
As can be seen in figure 5.2, the measured zenith angle distribution for muons arriving at the LNGS is not reproduced absolutely accurately by the simulation. The small discrepancy between the measured and predicted distributions is expected to arise mainly due to the omission of the resolution of the muon track reconstruction of the Borexino detector in the simulation. However, also a combination of uncertainties of the altitude profile, the position of the LNGS, and the zenith angle

distribution of muons at the surface is expected to affect the result. To estimate the effect of an inaccurate knowledge of the surface zenith angle distribution on the calculation of α_{T}, an uncertainty of the drawn zenith angle of $\Delta\theta = 10\%$ is assumed. Also this uncertainty is treated conservatively since the good agreement between the assumed zenith angle distribution at the surface with the result of the MCEq simulation [251] and between the simulated angular distributions at the LNGS and the measured distributions indicate a rather low inaccuracy. Nevertheless, since the zenith angle distribution strongly affects the prediction of α_{T} through its influence on the effective rock coverage and since it directly enters in the calculation of α_{T} via the factor $E_{\mathrm{thr}} \cos\theta$, it is important not to underestimate its uncertainty.

At the best fit value of $r_{\mathrm{K}/\pi}$, the systematic uncertainty introduced by the zenith angle is found to be $\Delta\alpha = \pm 0.0038$. The contribution to the systematic uncertainty of α_{T} is found to vary with $r_{\mathrm{K}/\pi}$ since it alters $\langle E_{\mathrm{thr}} \cos\theta \rangle$ in equation 5.11 and, thus, affects the slope of the predicted α_{T} in dependence on $r_{\mathrm{K}/\pi}$ as detailed above. However, the relation between an altered value of θ and the predicted α_{T} is complex due to the shape of the rock overburden. In the simulation, a tendency towards an increasing contribution to the systematic uncertainty with increasing $r_{\mathrm{K}/\pi}$ is found.

Finally, the comparison of the result of the simulation to the result based on the MUSUN simulation code may be used to evaluate the systematics of the simulation procedure. Since the result of the MUSUN code was optimized for the LVD location in Hall A of the LNGS, the difference between the two simulations can further be used to estimate the systematic uncertainty introduced due to the inaccurate knowledge of the position of the Borexino experiment in the Google Maps Elevation API altitude profile.

The difference at the best fit value is $\Delta\alpha_{\mathrm{T}} = \pm 0.0005$ and it varies around its mean value of $\langle \Delta\alpha_{\mathrm{T}} \rangle = 5 \times 10^{-5}$ for different values of $r_{\mathrm{K}/\pi}$. The difference to the MUSUN result is assigned as a symmetric uncertainty to the estimated effective temperature coefficient for each $r_{\mathrm{K}/\pi}$ value. Since no huge difference to the result using the MUSUN code is found, no further estimation of the contribution of an inaccuracy of the position of the LNGS to the systematic uncertainty of the α_{T} estimation is necessary since any inaccuracy of this quantity would manifest in the comparison of the results of the two simulation codes. Thus, the position of the LNGS in the altitude profile can be assumed to be chosen very accurately such that no strong uncertainty of the predicted value of α_{T} is introduced. Considering all uncertainty sources and summing the contributions linearly, an overall uncertainty of the predicted effective temperature coefficient of $\Delta\alpha_{\mathrm{T}} = 0.0151$ results at the best fit value of $r_{\mathrm{K}/\pi}$.

5.3 Combined χ^2 Fit of the Experimental Measurement and the Theoretical Expectation of α_{T}

The measured value of α_{T} in dependence on $r_{\mathrm{K}/\pi}$ and the theoretical prediction obtained by the Monte Carlo simulation can be combined to indirectly measure the atmospheric kaon to pion production ratio. Thus, both available estimations of α_{T} for each value of $r_{\mathrm{K}/\pi}$, the measurement and the theoretical prediction, are regarded as independent Gaussian random variables distributed around their true values. While the respective true value is supposed to be unknown, the variances of the α_{T} estimations are given by the statistical uncertainty of the measured value and the uncertainties considered in the Monte Carlo simulation to predict α_{T}. Since no systematic shift is expected when the measurement and the Monte Carlo simulation are repeated, the assumption of a Gaussian distribution of the observed values of α_{T} is plausible.
Following the method of least squares, an estimator of the true value of a quantity λ given n independent measurements of this quantity may be found by minimizing the test statistic [253]

$$\chi^2(\lambda) = \sum_{\mathrm{i}=1}^{n} \frac{(y_{\mathrm{i}} - \lambda)^2}{\sigma_{\mathrm{i}}^2}. \tag{5.12}$$

Here, y_{i} represent the measured values with their respective variances σ_{i} and the sum considers the whole available set of n measurements. The 1σ margin for the combination of the measurements may be found by solving [253]

$$\chi^2(\lambda) = \chi^2_{\mathrm{min}} + 1. \tag{5.13}$$

Applying this to the measured and predicted values of α_{T}, the most probable value of α_{T} for a certain kaon to pion production ratio may be estimated by minimizing

$$\chi^2(\alpha_{\mathrm{T}}) = \frac{(\alpha_{\mathrm{T,exp}} - \alpha_{\mathrm{T}})^2}{\sigma^2_{\mathrm{exp}}} + \frac{(\alpha_{\mathrm{T,theo}} - \alpha_{\mathrm{T}})^2}{\sigma^2_{\mathrm{theo}}}. \tag{5.14}$$

$\alpha_{\mathrm{T,exp}}$ represents the measured value of α_{T} with its statistical uncertainty σ_{exp} at a given value of $r_{\mathrm{K}/\pi}$, $\alpha_{\mathrm{T,theo}}$ the theoretical prediction of α_{T} with its uncertainty σ_{theo} at the same $r_{\mathrm{K}/\pi}$ value.
The best fit value of $r_{\mathrm{K}/\pi}$ may be found at the overall minimum of χ^2 for all $r_{\mathrm{K}/\pi}$ values. Since the curves of the experimental and theoretical estimations of α_{T} cross at that value of $r_{\mathrm{K}/\pi}$ as can be seen in figure 5.3, a minimum of $\chi^2_{\mathrm{min}} = 0$ results for this kaon to pion production ratio. Thus, only if a minimum of $\chi^2 \leq 1$ may be found at a certain value of $r_{\mathrm{K}/\pi}$, the best estimate of α_{T} at that kaon to pion

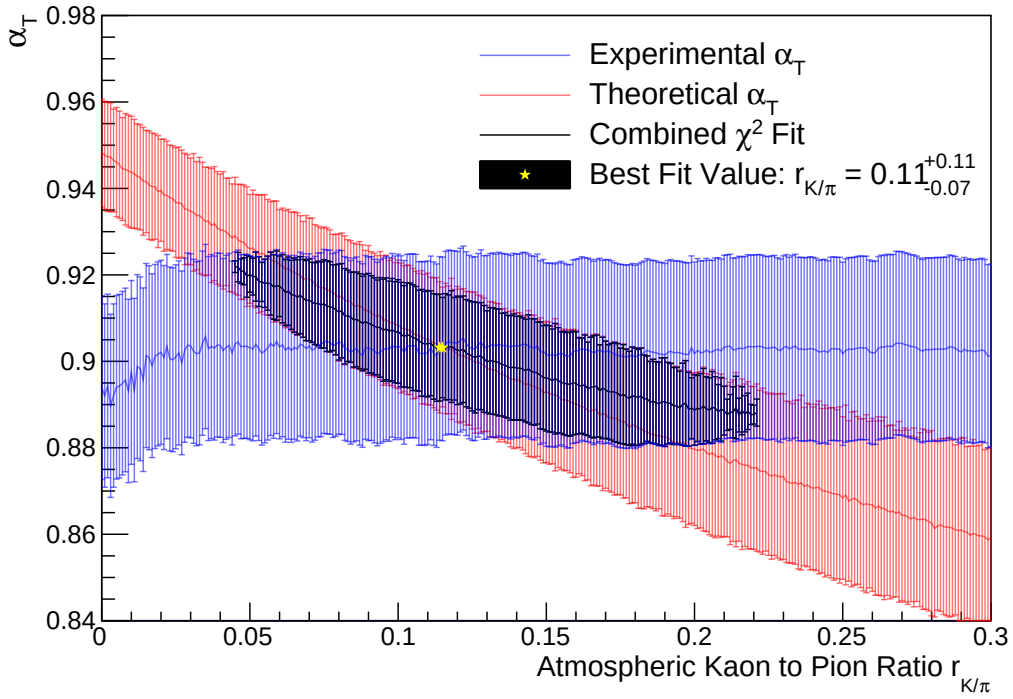

Figure 5.3: Combined χ^2 fit to determine the atmospheric kaon to pion production ratio. The measurement of α_T in dependence on $r_{K/\pi}$ is depicted in blue, the theoretical Monte Carlo prediction of α_T in red. The black curve shows the 1σ region of the combined χ^2 fit of the measured and predicted values. The best fit value at $r_{K/\pi} = 0.11^{+0.11}_{-0.07}$ is marked by the yellow star.

production ratio still agrees within 1σ with the overall best estimate of α_T considering all tested $r_{K/\pi}$ values. Values of $r_{K/\pi}$ for which the minimum of equation 5.14 is found to be larger than one are, thus, disfavored by more than 1σ. In case a minimum below one can be found at a certain $r_{K/\pi}$ value, the 1σ contour is given by the value of α_T for which equation 5.14 equals one.
Figure 5.3 shows the experimental measurement of α_T in dependence on the atmospheric kaon to pion production ratio in blue, the theoretical Monte Carlo prediction in red, and the 1σ contour of the combined χ^2 fit in black. The best fit value that is obtained for $r_{K/\pi} = 0.11^{+0.11}_{-0.07}$ is marked by the yellow star.

5.4 Determination of the Atmospheric Kaon to Pion Production Ratio via the Cosmic Muon Production Ratio

In [179], a generic approach for a measurement of the atmospheric kaon to pion production ratio based on a measurement of the effective temperature coefficient is introduced. In this approach, the ratio of observed muons produced in kaon decays to muons produced in pion decays is calculated and used to infer $r_{\mathrm{K}/\pi}$. In the following, this approach is presented and pursued using the Borexino measurement of α_{T}.
Experimentally, the effective temperature coefficient α_{T} is determined by correlating fluctuations of the measured muon rate $R_\mu = N/t$ to fluctuations of the effective temperature T_{eff} via

$$\frac{\Delta R_\mu}{\langle R_\mu \rangle} = \alpha_{\mathrm{T}} \frac{\Delta T_{\mathrm{eff}}}{T_{\mathrm{eff}}}. \tag{5.15}$$

The overall muon count rate is composed of muons originating from kaon decays and muons originating from pion decays. Thus, equation 5.15 may be split into the two meson components and rewritten as

$$\frac{\Delta R_\mu^\pi + \Delta R_\mu^{\mathrm{K}}}{\langle R_\mu^\pi \rangle + \langle R_\mu^{\mathrm{K}} \rangle} = \alpha_{\mathrm{T}} \frac{\Delta T_{\mathrm{eff}}}{T_{\mathrm{eff}}}. \tag{5.16}$$

Rearranging this equation yields

$$\frac{T_{\mathrm{eff}}}{\alpha_{\mathrm{T}} \Delta T_{\mathrm{eff}}} \left(\frac{\Delta R_\mu^\pi}{\langle R_\mu^\pi \rangle} + \frac{\Delta R_\mu^{\mathrm{K}}}{\langle R_\mu^\pi \rangle} \right) - 1 = \frac{\langle R_\mu^{\mathrm{K}} \rangle}{\langle R_\mu^\pi \rangle} = \frac{N_{\mathrm{K}}}{N_\pi}. \tag{5.17}$$

Here, $\frac{N_{\mathrm{K}}}{N_\pi}$ describes the ratio of muons originating from kaons N_{K} to muons originating from pions N_π. This ratio will be referred to as $r_\mu(\mathrm{K}/\pi)$ in the following. In the pion scaling limit, i.e. under the assumption that only pions are affected by temperature variations in the upper atmosphere, the correlation may be described by

$$\frac{\Delta R_\mu^\pi}{\langle R_\mu^\pi \rangle} = (\alpha_{\mathrm{T}})_\pi \frac{\Delta T_{\mathrm{eff}}}{\langle T_{\mathrm{eff}} \rangle}. \tag{5.18}$$

The effective temperature coefficient for only pion contribution $(\alpha_{\mathrm{T}})_\pi$ can be derived from equation 5.11 by neglecting the kaon contribution, i.e. by setting $A_{\mathrm{K}} = 0$. This yields

$$(\alpha_{\mathrm{T}})_\pi = 1/\left[\frac{\gamma}{\gamma + 1} \frac{\epsilon_\pi}{1.1 E_{\mathrm{thr}} \cos\theta} + 1 \right], \tag{5.19}$$

which recovers the expression formerly published by MACRO [182]. Analogously, the kaon contribution to the correlation can be expressed as

$$\frac{\Delta R_\mu^{\mathrm{K}}}{\langle R_\mu^{\mathrm{K}}\rangle} = (\alpha_{\mathrm{T}})_{\mathrm{K}} \frac{\Delta T_{\mathrm{eff}}}{\langle T_{\mathrm{eff}}\rangle} \tag{5.20}$$

with $(\alpha_{\mathrm{T}})_{\mathrm{K}}$ being the effective temperature coefficient under the assumption that only kaons are affected by temperature variations. This coefficient may be derived from equation 5.9 by setting the pion contribution in equation 5.5 to zero. Thus [178],

$$(\alpha_{\mathrm{T}})_{\mathrm{K}} = 1/\left[\frac{\gamma}{\gamma+1}\frac{\epsilon_{\mathrm{K}}}{1.1E_{\mathrm{thr}}\cos\theta}+1\right]. \tag{5.21}$$

Inserting equations 5.18 and 5.20 into equation 5.17 yields for the ratio of muons originating from kaon decays to muons originating from pion decays

$$r_\mu(\mathrm{K}/\pi) = \frac{1}{\alpha_{\mathrm{T}}}\left((\alpha_{\mathrm{T}})_\pi + (\alpha_{\mathrm{T}})_{\mathrm{K}}\frac{\langle R_\mu^{\mathrm{K}}\rangle}{\langle R_\mu^{\pi}\rangle}\right) - 1. \tag{5.22}$$

Setting $\frac{\langle R_\mu^{\mathrm{K}}\rangle}{\langle R_\mu^{\pi}\rangle} = \frac{N_{\mathrm{K}}}{N_\pi} = r_\mu(\mathrm{K}/\pi)$ and solving for $r_\mu(\mathrm{K}/\pi)$, this can be translated into

$$r_\mu(K/\pi) = \frac{(\alpha_{\mathrm{T}})_\pi/\alpha_{\mathrm{T}} - 1}{1-(\alpha_{\mathrm{T}})_{\mathrm{K}}/\alpha_{\mathrm{T}}}. \tag{5.23}$$

Here, α_{T} denotes the actually measured value of the effective temperature coefficient while $(\alpha_{\mathrm{T}})_{\mathrm{K}}$ and $(\alpha_{\mathrm{T}})_\pi$ need to be determined using the Monte Carlo simulation described in section 5.2.1.
Theoretically, the ratio of muons originating from kaon decays to muons originating from pion decays can be derived by integrating equation 5.5 and

$$r_\mu(K/\pi) = \frac{I_\mu^{\mathrm{K}}}{I_\mu^{\pi}} = 5.73 \times \eta \tag{5.24}$$

with

$$I_\mu^{\mathrm{K}} \sim B \times E_{\mathrm{thr}}^{-\gamma}\left(\frac{\eta}{\gamma+(\gamma+1)1.1\langle E_{\mathrm{thr}}\cos\theta\rangle/\epsilon_{\mathrm{K}}}\right) \tag{5.25}$$

and

$$I_\mu^{\pi} \sim B \times E_{\mathrm{thr}}^{-\gamma}\left(\frac{1}{\gamma+(\gamma+1)1.1\langle E_{\mathrm{thr}}\cos\theta\rangle/\epsilon_{\pi}}\right) \tag{5.26}$$

as in equation 5.7. The expectation value of $\langle E_{\mathrm{thr}}\cos\theta\rangle = (1.34\pm0.18)\,\mathrm{TeV}$ was determined in the Monte Carlo simulation as described in section 5.2.1. With $\frac{Z_{\mathrm{NK}}}{Z_{\mathrm{N}\pi}} = r_{\mathrm{K}/\pi}$ [79, 254], equation 5.6 becomes

$$\eta = 0.635 \times r_{\mathrm{K}/\pi}\frac{1-r_\pi}{1-r_{\mathrm{K}}}\frac{1-r_{\mathrm{K}}^{\gamma+1}}{1-r_\pi^{\gamma+1}} = 0.365 \times r_{\mathrm{K}/\pi}. \tag{5.27}$$

Inserting that expression into equation 5.24, the atmospheric kaon to pion production ratio can be related to the ratio of muons produced in kaon decays to muons produced in pion decays via

$$r_{\mathrm{K}/\pi} = 0.48 \times r_{\mu}(\mathrm{K}/\pi). \tag{5.28}$$

In principle, the measured value depends on the value of the kaon to pion production ratio that is used to determine the effective temperature as described above. However, as can be seen in figure 5.3, this dependence is extremely weak and strongly overpowered by the statistical uncertainty of the measurement. This allows to neglect this weak dependence and use the measured value reported in section 4.2.4 of

$$\alpha_{\mathrm{T}} = 0.90 \pm 0.02 \tag{5.29}$$

in equation 5.23. The values of $(\alpha_{\mathrm{T}})_{\pi}$ and $(\alpha_{\mathrm{T}})_{\mathrm{K}}$ and their uncertainties have been determined via the Monte Carlo simulation described in section 5.2.1 as

$$(\alpha_{\mathrm{T}})_{\pi} = 0.95 \pm 0.01 \tag{5.30}$$

and

$$(\alpha_{\mathrm{T}})_{\mathrm{K}} = 0.75 \pm 0.01, \tag{5.31}$$

respectively. Inserting these values into equation 5.23 yields for the ratio of muons produced by kaons to muons produced by pions

$$r_{\mu}(\mathrm{K}/\pi) = 0.33 \pm 0.19. \tag{5.32}$$

Using this result and equation 5.28, the atmospheric kaon to pion production ratio may be inferred as

$$r_{\mathrm{K}/\pi} = 0.16 \pm 0.09. \tag{5.33}$$

In this approach, only the uncertainties of the measured and estimated values of the effective temperature coefficient entering equation 5.23 are considered. The atmospheric kaon to pion production ratio is assumed as the sole unknown quantity in the theoretical prediction of $r_{\mu}(\mathrm{K}/\pi)$ as given by equation 5.24. However, this expression in principle also contains uncertainties due to $\langle E_{\mathrm{thr}} \cos\theta \rangle$, ϵ_{π}, and ϵ_{K} entering the computation of I_{μ}^{π} and I_{μ}^{K} and, further, equation 5.24 gives only an approximation of the muon production ratio. Thus, the uncertainties following this approach may be assumed to be underestimated and the result based on the combined χ^2 fit presented in section 5.3 is expected to be more reliable. Nevertheless, both values agree within their uncertainty ranges and sensible results may be obtained following both methods.

5.5 Comparison to Other Measurements

In the scope of this thesis, two measurements of the atmospheric kaon to pion production ratio have been performed using Borexino data. Additionally, one estimation based on the combination of the Borexino result with further measurements of the effective temperature coefficient α_{T} from various experiments is presented in section 4.2.4. The values obtained by the two measurement techniques introduced in the present chapter agree well within their statistical uncertainties. These uncertainties are relatively large, mainly due to the statistical uncertainties of the measured effective temperature coefficient α_{T}. Since the statistical uncertainty of the measurement of α_{T} strongly exceeds any systematic effects, a measurement with higher statistics would be needed to further constrain the uncertainties. However, due to the procedure of extracting the effective temperature coefficient via a linear fit to the correlation between the cosmic muon flux and the effective atmospheric temperature according to equation 5.1, major improvements can only be achieved by using larger detectors with higher muon statistics per day. With a higher absolute muon count rate, the uncertainty of the individual bins decreases and the fit results are improved. A longer measurement time for similar count rates, on the other hand, will only shrink the uncertainty slowly and minorly. Further, the method of deriving the kaon to pion production ratio via a combined χ^2 fit as presented in section 5.3 is estimated to yield more reliable results since in the calculation of $r_{\mathrm{K}/\pi}$ via the cosmic muon production ratio as presented in section 5.4, several approximations are included.
The determination of the kaon to pion production ratio via a fit to the measurements of α_{T} from various experiments located at different depths also yields a consistent result. However, as has been mentioned, the statistical uncertainty of this result is expected to be strongly overpowered by systematic effects like the uncertainty of $\langle E_{\mathrm{thr}} \cos\theta \rangle$ for the different experimental sites. The $r_{\mathrm{K}/\pi}$ value assumed by the contributing experiments to determine T_{eff} and to measure α_{T} introduces a further uncertainty that was neglected in this estimation. Thus, the result of the fit may only last as an indication.
The atmospheric kaon to pion production ratio was formerly measured at several accelerator experiments, namely for $\mathrm{p} + \mathrm{p}$ collisions [242, 243], $\mathrm{Au} + \mathrm{Au}$ collisions [244], $\mathrm{p} + \bar{\mathrm{p}}$ collisions [245], and $\mathrm{Pb} + \mathrm{Pb}$ collisions [246]. Additional older measurements are summarized in [247]. Further, $r_{\mathrm{K}/\pi}$ was measured indirectly from cosmic rays via the effective temperature coefficient as presented in this chapter by MINOS [176, 178] and IceCube [214]. The MINOS collaboration performed two measurements and obtained $r_{\mathrm{K}/\pi} = 0.12^{+0.07}_{-0.05}$ [176] based on a combined χ^2 fit of the experimental measurement and a theoretical Monte Carlo prediction of α_{T} and $r_{\mathrm{K}/\pi} = 0.12 \pm 0.05$ [178] for a determination via the muon production ratio. The IceCube collaboration published a preliminary result on the atmospheric kaon to

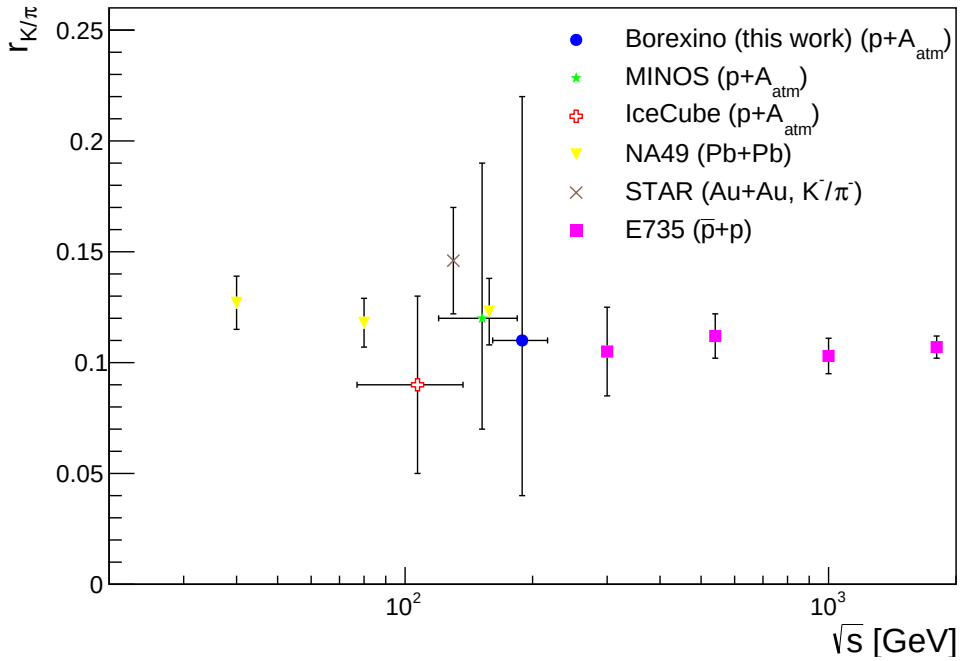

Figure 5.4: Comparison of $r_{\mathrm{K}/\pi}$ as measured by various experiments. The STAR measurement was performed using Au+Au collisions at RHIC [244], the NA49 measurement using Pb+Pb collisions at SPS [246], and the E735 measurement using $\bar{\mathrm{p}} + \mathrm{p}$ collisions at Tevatron [245]. The MINOS [176] and IceCube [214] measurements as well as the Borexino result from this work were obtained indirectly via a measurement of the effective temperature coefficient.

pion production ratio of $r_{\mathrm{K}/\pi} = 0.09 \pm 0.04$ [214] based on a combined χ^2 fit of the experimental and theoretical determinations of α_{T}. The significantly higher muon rate at this experiment compared to the other two experiments that follow a similar approach allows IceCube to perform a more precise measurement.
Figure 5.4 shows a comparison of the value obtained in this work using the Borexino data based on the combined χ^2 fit and values from the STAR measurement obtained via Au+Au collisions at RHIC [244], from the NA49 measurement obtained via Pb+Pb collisions at SPS [246], from the E735 measurement obtained via $\bar{\mathrm{p}} + \mathrm{p}$ collisions at Tevatron [245], and the MINOS [176] and IceCube [214] measurements based on cosmic ray data as mentioned above. Since the muon energy is expected to be on average $\sim$ one tenth of the energy of the primary cosmic ray proton [176], the threshold energy of 1.79 TeV for muons arriving from straight above at the LNGS translates to a primary proton energy of $\sim$ 18 TeV. The center of mass energy for this measurement of $\sqrt{s} = 190\,\mathrm{GeV}$ is, thus, calculated as for

a collision $p + A_{atm}$ of an 18 TeV proton on a fixed target nucleon at the top of the atmosphere. However, due to the broad range of primary energies contributing to the muon flux observed in underground laboratories and the shape of the rock coverage, an uncertainty of the center of mass energy needs to be considered for Borexino as well as for the measurements from IceCube and MINOS.
Due to the indirect approach of measuring $r_{K/\pi}$ via the effective temperature coefficient, the measurements based on cosmic ray data do not compare directly to the measurements performed at accelerators with fixed beam energies. Nevertheless, the values agree within their uncertainties. While the indirect measurements feature larger uncertainties, they encounter this disadvantage by measuring the atmospheric kaon to pion production ratio in situ. The uncertainties are largest for the Borexino measurement due to the highest rock coverage of the three measurements determining $r_{K/\pi}$ indirectly. However, Borexino contributes the data point at the highest center of mass energy for indirect as well as fixed target measurements at the present date.

Chapter 6

Seasonal Modulation of the Cosmogenic Neutron Production Rate

Cosmogenic neutrons are produced in the Borexino detector through spallation processes of cosmic muons on carbon nuclei of the scintillator target. These neutrons are thermalized via scattering interactions off protons and carbon nuclei and eventually, after a mean capture time of $\sim 260\,\mu$s [137], captured on either a hydrogen or a carbon nucleus. Based on the scintillator composition and the neutron capture cross sections, 99% of the captures occur on hydrogen evoking the emission of a 2.2 MeV γ ray in the deuteron deexcitation. In the remaining 1% of the cases, the neutron is captured on carbon. In the deexcitation of ^{13}C, a total γ ray energy of 4.95 MeV is released [137]. Since the thermalization of the neutrons to sub-eV energies proceeds within tens of ns, the proton recoil signal cannot be disentangled from the much stronger light output caused by the muon. Thus, the neutrons are only visible through the deexcitation γ rays.
Due to the origin of cosmogenic neutrons, the cosmogenic neutron production rate is expected to undergo a seasonal modulation with similar parameters as measured for the flux of cosmic muons in section 4.2. Further, cosmogenic neutrons have been discussed as a possible background for direct dark matter searches [255]. In case the modulation phase was found to deviate from the cosmic muon flux, cosmogenic neutrons might mimic the expected modulation of the interaction rate of dark matter particles due to the motion of the Earth within the galactic halo [204].
After summarizing the method of cosmogenic neutron detection in Borexino in section 6.1, the modulation of the cosmogenic neutron production rate is analyzed in section 6.2. As described there, a discrepancy between the amplitude of the modulation of the cosmogenic neutron production rate and the amplitude of the cosmic muon flux modulation is registered. In section 6.3, the interpretation of this

discrepancy arising due to a seasonal modulation of the mean energy of muons observed at the LNGS as proposed by the LVD experiment [256] is followed and the implied energy change is calculated. In section 6.4, the implications of a modulation of the mean muon energy are discussed and found to strongly contradict this hypothesis.

6.1 Cosmogenic Neutron Detection in Borexino

An efficient detection of cosmogenic neutrons is of decisive relevance especially for the identification of decays of cosmogenic radio-isotopes through the Threefold Coincidence technique [138] as described in section 2.3.3. To guaranty a high neutron identification efficiency and enable the background suppression necessary for the analyses of rare neutrino events, the Borexino data acquisition was modified in December 2007 [80]. Since this modification, a special acquisition gate is opened immediately after each event that triggers both the OD and the ID, a signature most probably caused by a muon crossing the ID. The length of this gate is set to 1.6 ms, the maximum provided by the electronics. This ensures the registration of most of the neutron captures within this acquisition gate. Based on the neutron capture time of $\sim 260\,\mu$s [137], $\sim 6\%$ of the neutron captures are expected to occur already in the usual $16\,\mu$s data acquisition gate in which the muon is registered. In the subsequent neutron gate of 1.6 ms, 93.8% of the captures are expected. The remaining 0.2% of the capture γ rays are emitted after the neutron gate is closed. Even though the two acquisition gates are meant to be consecutive, a short deadtime of (150 ± 50) ns arises between the two gates due to electronic delays in the trigger formation [108].
Neutrons are identified as clusters in the neutron trigger gate, i.e. as time correlated hits of the PMTs above the background noise level. A dedicated clustering algorithm had to be developed for this purpose. The commonly used algorithm that identifies peak structures of correlated hits in the time profile of an event is designed for low energy neutrino events at low background rates. This background is mostly correlated to the PMTs and may be dark noise, late pulses, or PMT afterpulses. However, the immensely large light output of the initial muon that potentially generates a neutron results in a huge amount of noise hits in the neutron gate. The neutron clustering algorithm, thus, considers the local noise level to search for an excess of hits marking a start of a potential neutron capture peak. Then, the shape of the peak following this starting point in the hit time spectrum is used to discriminate physical events from noise events [62].
Since the neutron captures are followed by the emission of γ rays at distinct energies, namely a single 2.2 MeV γ ray for the dominant capture on hydrogen and a total γ ray energy of 4.95 MeV for the capture on carbon, clear peaks around

these energies broadened by the detector resolution constitute the neutron signature. However, the light output and the detection efficiency are expected to decrease near the IV since a part of the emitted γ rays escapes into the buffer where the light output is strongly quenched. Further, muons can generate hadronic and electromagnetic showers consisting of many particles, which results in a huge light output. For such events, the rate of afterpulses caused by residual ionized gas in the vacuum between the dynodes of the PMTs is strongly increased. Thus, the number of hits registered on a Laben VME board at which the output of eight PMTs is collected can exceed the available storage of this board. In this case, additional PMT hits in the remaining muon and subsequent neutron gate cannot be registered and the effective optical coverage in the neutron gate as well as the visible energy for following interactions are reduced [62].
The energy estimator used for the detection of cosmogenic neutrons is the number of hits on the PMTs since the charge information is not reliable in the neutron gate due to instabilities caused by the large muon light output [62]. The effect of saturated Laben boards on the visible energy is taken into account by a correction factor of $N_\mathrm{b}/(N_\mathrm{b} - N_\mathrm{eb})$. In this factor, $N_\mathrm{b} = 280$ is the total number of Laben boards and N_eb the number of saturated boards. These saturated boards are commonly labeled as empty boards describing the fact that no hits can be registered on these boards, which explains the subscript. For events occurring during the neutron gate, the observed number of PMT hits is multiplied by this correction factor to obtain a stable energy estimation [80].
The efficiency of the neutron detection in the neutron gate has been evaluated with the help of a parallel single channel data acquisition system that is based on the analog output of all ID PMTs. Thus, it is not affected by the saturation of the Laben boards. However, the baseline of the front-end electronics needs 30 μs to stabilize after the passage of a muon and the first part of the hit time spectrum acquired after a muon is highly populated by noise events. Due to this, the active time window for the efficiency analysis had to be chosen to start after the baseline stabilization 30 μs after the muon passage to enable an efficient neutron detection in the reference system [137].
Based on the secondary acquisition system, electronic noise contaminating the neutron captures in the neutron gate has been found to be efficiently removed by the application of a 1.3 MeV energy threshold on the candidate clusters. This energy threshold was, consequently, chosen as the criterion for the identification of neutron candidate clusters to evaluate the neutron identification efficiency using the main electronics. The resulting detection efficiency for neutron captures after the stabilization of the baseline was measured to be [137]

$$\epsilon_\mathrm{det} = (91.7 \pm 1.7_\mathrm{stat} \pm 0.9_\mathrm{syst})\%. \tag{6.1}$$

The fraction of neutron captures occurring at least 30 μs after the passage of the initial muon is $\epsilon_{\mathrm{t}} = (89.1 \pm 0.8)\%$ based on the measured value for the neutron capture time of $\tau = (259.7 \pm 1.3_{\mathrm{stat}} \pm 2.0_{\mathrm{syst}})\,\mu\mathrm{s}$ [137].
Considering these efficiencies that determine the neutron identification, the cosmogenic neutron capture rate in Borexino was measured to be [137]

$$R_{\mathrm{n}} = (90.2 \pm 2.0_{\mathrm{stat}} \pm 2.4_{\mathrm{syst}})\,(\mathrm{d100\,t})^{-1}. \tag{6.2}$$

Additionally, the rate of muons generating at least one neutron that is captured in the IV was found to be [137]

$$R_{\mu_{\mathrm{n}}} = (67.5 \pm 0.4_{\mathrm{stat}} \pm 0.2_{\mathrm{syst}})\,\mathrm{d}^{-1}. \tag{6.3}$$

These values correspond to an average neutron multiplicity of $M = 3.61 \pm 0.08_{\mathrm{stat}} \pm 0.07_{\mathrm{syst}}$ for neutron-producing muons. However, the distribution of the neutron multiplicity reaches up to $\sim 10^3$ neutrons for extremely strong showers [137].

6.2 Measurement of the Modulation of the Cosmogenic Neutron Production Rate

To investigate the modulation of the cosmogenic neutron production rate, a similar approach as for the cosmic muon flux presented in section 4.2 was followed. With the cosmic muon flux being modulated seasonally at leading order, the cosmogenic neutron production rate is expected to undergo a similar seasonal modulation. Thus, it may be described by

$$R_{\mathrm{n}}(t) = R_{\mathrm{n}}^0 + \delta R_{\mathrm{n}} \cos\left(\frac{2\pi}{T}(t - t_0)\right), \tag{6.4}$$

where R_{n}^0 is the average cosmogenic neutron production rate, δR_{n} the amplitude of the modulation, T the period, and t_0 the phase. Due to the origin of cosmogenic neutrons, parameter values similar to those obtained in the analysis of the seasonal modulation of the cosmic muon flux as presented in section 4.2.3 can be expected. The cosmogenic neutron production rate was investigated by searching for clusters in the 1.6 ms neutron gate that is opened after each event that triggers both subdetectors. Thus, cosmogenic neutrons were analyzed starting in January 2008 after the implementation of the neutron gate. Similarly to the analysis of the cosmic muon flux, data acquired until May 15th, 2017 were used, such that approximately 9.5 years of accumulated data were analyzed. Since the number of cosmogenic neutrons produced per day is relatively small, the number of detected neutron captures in the neutron gate was binned in a month-wide binning with a month defined as

the twelfth part of 365 days. Further, only the innermost 3.8 m of the IV were used to minimize the rate of capture γ rays that escape into the buffer and are not detected.
Since the neutron gates are opened after every muon that crosses the ID and that was identified by the Muon Trigger Board (MTB), the hardware trigger of the OD, the stable identification of cosmogenic neutrons relies on the stability of the muon identification efficiency of the MTB. Analogously to the approach detailed in section 4.2.1, the MTB efficiency was tested with a pure muon sample selected by the Inner Detector Flag (IDF). Despite the MTB efficiency being slightly lower than the efficiency of the Muon Clustering algorithm (MCR) that was used in the muon flux analyses, the MTB was found to work extremely stably in the analyzed time period. This ensures a stable opening of the neutron gates, which is the first prerequisite for a stable neutron identification. Since, further, no major detector operations that might strongly affect the energy reconstruction in the ID were performed, a stable neutron identification within the neutron gate with only a very small efficiency decrease due to the PMT loss is expected. Thus, the modulation of the cosmogenic neutron production rate may be investigated without efficiency corrections since the stable efficiency only implies a constant shift of the uncorrected rate without affecting the modulation parameters.
However, no seasonal modulation may be observed in the acquired neutron data by applying a fit according to equation 6.4. A possible explanation may be the occurrance of extremely strong showers generated by cosmic muons with neutron multiplicities up to $\sim 10^3$ neutrons. These events are assumed to follow a non-Poissonian probability distribution and, thus, to strongly dilute the expected seasonal modulation of the cosmogenic neutron production rate, especially considering the comparably small mean neutron production rate of $\sim 90\,(\mathrm{d100\,t})^{-1}$ [137].
To overcome this effect and check if high multiplicity events are indeed precluding the observation of a seasonal modulation in the cosmogenic neutron production rate, two different approaches were followed. First, the number of neutron-producing muons was analyzed. In a Lomb-Scargle analysis, it was investigated if a significant peak for the seasonal modulation appears in the periodogram when the actual number of neutrons produced by a muon is neglected. Figure 6.1 shows on the left side in blue the Lomb-Scargle periodogram for the measured number of neutron-producing muons per day in a month-wide binning together with the 95% confidence level of statistical fluctuations. The 95% confidence level was calculated similar to the procedure described in section 4.3.1 for the cosmic muon flux. 10^4 white noise samples were generated by randomly drawing a number of neutron-producing muons with its error for each month from the measured distribution and a Lomb-Scargle analysis of these artificial datasets was perfomed. The confidence level was defined as the Lomb-Scargle power that contains $9,500$ of the white noise

samples.
For the number of neutron-producing muons, a significant peak in the Lomb-Scargle periodogram appears at a period of $\sim 365\,\mathrm{d}$. Thus, a seasonal modulation becomes apparent when the multiplicity of cosmogenic neutrons is neglected, which supports the hypothesis that high multiplicity events dilute the expected seasonal modulation in the cosmogenic neutron production rate. Apart from this peak, no further significant modulations are observed in the dataset.
Besides neglecting the neutron multiplicity entirely, a cut on the neutron multiplicity was introduced to discard high multiplicity showers in a second approach to extract the seasonal modulation. Thus, a Lomb-Scargle analysis was performed for datasets excluding neutrons that were produced by muons featuring more than a certain maximum number of follow-up neutrons. By gradually increasing the maximum neutron multiplicity, it was found that the seasonal modulation remains significant in the Lomb-Scargle periodogram up to a maximum neutron multiplicity of ten.
Figure 6.1 shows on the right and in blue the Lomb-Scargle periodogram for the cosmogenic neutron production rate including neutrons produced in showers with a maximum neutron multiplicity of ten. The 95% confidence level of statistical fluctuations is depicted by the red line. For this multiplicity, a significant peak is still observed in the Lomb-Scargle periodogram at a period of one year. If cosmogenic neutrons produced in showers featuring higher multiplicities are included, the peak for the seasonal modulation drops below the confidence level and the seasonal modulation may not be observed anymore.
While for a maximum multiplicity of ten, $\sim 40\%$ of the totally produced neutrons are excluded, the fraction of muons that generate more than ten neutrons in a shower is extremely small [80, 137]. Thus, the vast majority of events in which neutrons are produced is included by this cut and only rarely occurring high-multiplicity showers are discarded. This further strongly strengthens the hypothesis that high-multiplicity showers following a non-Poissonian probability distribution are the reason that the expected seasonal modulation may not be observed in the entire cosmogenic neutron production rate.
In conclusion, the presence of a seasonal modulation of the rate of neutron-producing muons and of the cosmogenic neutron production rate excluding neutrons produced in showers featuring more than ten neutrons is confirmed by the Lomb-Scargle analysis. This justifies to infer the modulation parameters by projecting the data to one year and applying a sinusoidal fit with the period fixed to the seasonal assumption. Following this approach, the comparably low statistics and associated large uncertainties in the month-wide bins may be compensated to derive precise measurements of the phase and amplitude of the seasonal modulation. As has been mentioned, the modulation parameters are not affected by the stable

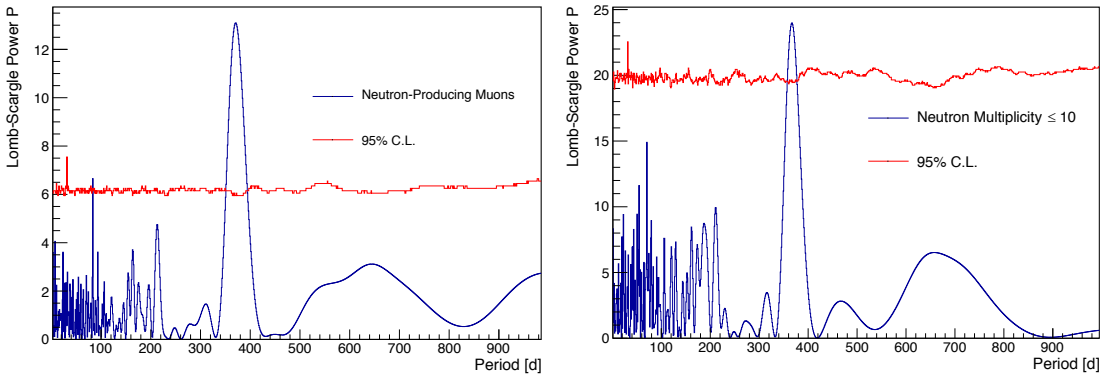

Figure 6.1: Lomb-Scargle periodograms of neutron-producing muons and cosmogenic neutrons detected in Borexino. On the *left* side, the periodogram for the number of neutron-producing muons is shown. A significant peak for a seasonal modulation is observed. On the *right* side, the Lomb-Scargle periodogram for neutrons produced by muons featuring at the maximum ten follow-up neutrons is shown. Up to this multiplicity, the seasonal modulation may still be observed in the data. The red lines depict the 95% confidence level of statistical fluctuations for both datasets.

neutron identification efficiency and no efficiency corrections were applied.
Figure 6.2 shows on the left the data of neutron-producing muons in ~ 9.5 years projected to one year and averaged to the rate per day in a month-wide binning. The red line depicts a fit to the data according to equation 6.4 with the period fixed to twelve months. A mean rate of $R^0_{\mu_\mathrm{n}} = (36.8 \pm 0.1)\,\mathrm{d}^{-1}$, an amplitude of $\delta R_{\mu_\mathrm{n}} = (0.9 \pm 0.2)\,\mathrm{d}^{-1} \mathrel{\widehat{=}} (2.3 \pm 0.5)\%$, and a phase of $t_0 = (6.3 \pm 0.4)\,\mathrm{months}$ are observed. The reduced χ^2 of the fit is $\chi^2/\mathrm{NDF} = 11/9$. For the cosmogenic neutron production rate including neutrons produced in showers featuring up to ten neutrons shown in figure 6.2 on the right, a rate of $R^0_{\mathrm{n}\leq 10} = (61.9 \pm 1.5)\,\mathrm{d}^{-1}$, an amplitude of $\delta R_{\mathrm{n}\leq 10} = (1.6 \pm 0.2)\,\mathrm{d}^{-1} \mathrel{\widehat{=}} (2.6 \pm 0.4)\%$, and a phase of $t_0 = (6.0 \pm 0.3)\,\mathrm{months}$ at a $\chi^2/\mathrm{NDF} = 42/9$ are observed. While the phase is in good agreement with the seasonal modulation of the cosmic muon flux, the amplitude of the modulation is higher with a difference of about $(2-3)\sigma$ to the amplitude of the muon flux modulation of $\delta I_\mu \mathrel{\widehat{=}} (1.365 \pm 0.009)\%$ as inferred in section 4.2.3.
To check if consistent values are found for more stringent cuts on the neutron multiplicity, data for varying cuts on the neutron multiplicity were selected, projected to one year, and fitted with a sinusoidal for a fixed period. Table 6.1 lists the observed phases and amplitudes together with the values measured for the number of neutron-producing muons. The measured parameters of the phase and amplitude of the seasonal modulation agree for all samples. The cosmogenic neutron production rate is found to be modulated in phase with the cosmic muon

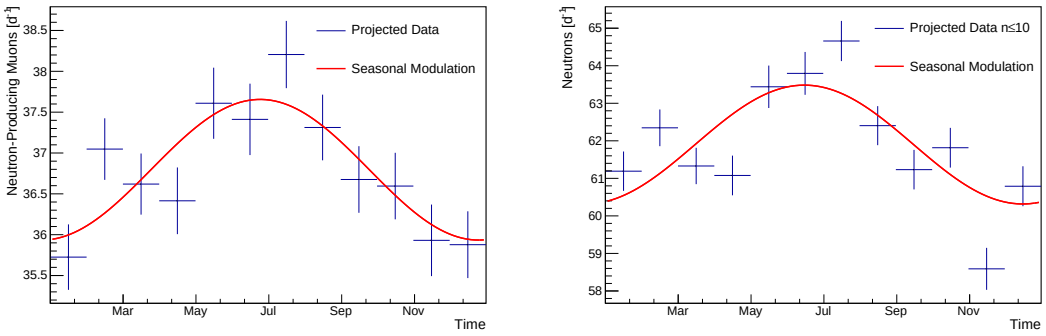

Figure 6.2: Seasonal modulation of the rate of neutron-producing muons on the *left* and the cosmogenic neutron production rate for neutron multiplicities $n \leq 10$ on the *right* projected to one year. The red line shows a sinusoidal fit to the data according to equation 6.4 with the period fixed to twelve months. The fit returns a mean rate of neutron-producing muons of $R^0_{\mu_\mathrm{n}} = (36.8 \pm 0.1)\,\mathrm{d}^{-1}$, an amplitude of $\delta R_{\mu_\mathrm{n}} = (0.9 \pm 0.2)\,\mathrm{d}^{-1} \mathrel{\widehat{=}} (2.3 \pm 0.5)\%$, and a phase of $t_0 = (6.3 \pm 0.4)$ months. The reduced χ^2 is $\chi^2/\mathrm{NDF} = 11/9$. For the cosmogenic neutron production rate for neutron multiplicities $n \leq 10$, a rate of $R^0_{\mathrm{n}\leq 10} = (61.9 \pm 1.5)\,\mathrm{d}^{-1}$, an amplitude of $\delta R_{\mathrm{n}\leq 10} = (1.6 \pm 0.2)\,\mathrm{d}^{-1} \mathrel{\widehat{=}} (2.6 \pm 0.4)\%$, and a phase of $t_0 = (6.0 \pm 0.3)$ months at a $\chi^2/\mathrm{NDF} = 42/9$ are observed.

flux and the maximum to occur accordingly about one month later than expected for dark matter interactions. However, the amplitude of the seasonal modulation of the cosmogenic neutron production rate is measured to be higher than for the cosmic muon flux, independent of the multiplicity cut up to a maximum neutron multiplicity $n \leq 10$.

To further probe this effect, a so-called residual approach was followed. In this approach, the average cosmogenic neutron production rate was computed in three months in summer and three months in winter for each dataset. The amplitude was inferred by assuming a sinusoidal modulation around the mean of the two values. Similarly, the increased amplitude of the rate of neutron-producing muons as observed through the fit was revised. The amplitudes extracted following this approach are listed in the fourth column of table 6.1. The values agree with the amplitudes inferred through the sinusoidal fit for each dataset. This confirms the increased modulation amplitude of the cosmogenic neutron production rate and of the rate of neutron-producing muons compared to the modulation of the cosmic muon flux. Further, consistent values on the relative amplitude are found between the datasets independent of the applied neutron multiplicity cut. The accordance of the amplitudes of the cosmogenic neutron production rate and of the rate of neutron-producing muons shows that the mean neutron multiplicity for neutron-

Neutron Multiplicity	Phase Projected [months]	Amplitude Projected [%]	Amplitude Residual [%]
$n = 1$	6.6 ± 0.5	2.3 ± 0.6	2.6 ± 1.0
$n \leq 2$	6.1 ± 0.3	2.6 ± 0.5	2.8 ± 0.8
$n \leq 3$	5.8 ± 0.4	2.2 ± 0.4	2.5 ± 0.8
$n \leq 4$	6.0 ± 0.3	2.2 ± 0.4	2.3 ± 0.7
$n \leq 5$	6.1 ± 0.3	2.3 ± 0.4	2.4 ± 0.7
$n \leq 10$	6.0 ± 0.3	2.6 ± 0.4	2.7 ± 0.7
Neutron-producing muons	6.3 ± 0.4	2.3 ± 0.5	2.5 ± 0.8

Table 6.1: Parameters of the seasonal modulation observed for different neutron multiplicity cuts and the number of neutron-producing muons. The second and third column show the phase and the amplitude of the seasonal modulation inferred through the fit to the projected data, respectively. The fourth column shows the relative amplitude of the modulation following the residual approach.

producing muons remains constant throughout the year.
The modulation of the cosmogenic neutron production rate at the LNGS has formerly been measured by the LVD experiment [256]. An even higher modulation amplitude of $\delta R_{\mathrm{n}} = (7.7 \pm 0.8)\%$ and a phase of $t_0 = (7.0 \pm 0.4_{\mathrm{stat}} \pm 0.5_{\mathrm{syst}})$ months have been reported. This corresponds to a maximum approximately one month after the maximum of the cosmic muon flux. Both values differ from the present analysis of Borexino data. However, the approach of the LVD experiment was slightly different. In the LVD analysis, the modulation of the cosmogenic neutron production rate relative to the observed number of muons was analyzed. This might be a reason for the discrepancy between the phase of the seasonal modulation of the cosmogenic neutron production rate reported by LVD and the phase measured in the present work. While the phase measured for the modulation of the cosmogenic neutron production rate in Borexino matches the phase of the modulation of the cosmic muon flux as expected, the phase reported by LVD is higher, even though a relatively large error margin is given. However, this effect is not stressed in the LVD publication [256]. The agreement of the phase of the modulation of the cosmogenic neutron production rate to the modulation of the cosmic muon flux measured with Borexino strongly supports the accuracy of the present measurement.
With respect to the discrepancy in the measured amplitudes, two effects might be reflected. Neutron production on heavier elements in the detector construction materials needs to be considered for the LVD experiment. These production processes might, potentially, increase the modulation amplitude of the cosmogenic neutron production rate compared to a pure production in the scintillator liquid of Borexino. Further, the cut on the multiplicity necessary to observe the seasonal

modulation of the cosmogenic neutron production rate in Borexino might affect the observed amplitude. The stability of the relative amplitude of the modulation for a varying cut on the neutron multiplicity as shown in table 6.1, however, indicates that the effect of including higher multiplicities does not significantly affect the result.

6.3 Modulation of the Mean Cosmic Muon Energy

Since the neutron production rate depends on the muon energy, the increased amplitude of the modulation of the cosmogenic neutron production rate compared to the amplitude of the modulation of the cosmic muon flux was interpreted as an indirect measurement of a seasonal modulation of the mean energy of muons at the LNGS by the LVD experiment [256].
Following this interpretation and the formalism outlined in [257], the difference between the modulation amplitudes may be used to determine the change of the mean cosmic muon energy between summer and winter. In this approach, the production of cosmogenic neutrons by cosmic muons is assumed to be fairly approximable by considering all muons to arrive with the applying mean energy $\overline{E}_\mu$. Thus, the number of produced neutrons N_n is expected to follow a dependency [257]

$$N_\mathrm{n} \propto \overline{E}_\mu^{\alpha} \tag{6.5}$$

with $\alpha = 0.78$ for neutron production in liquid scintillator [258]. The relative maximum of the cosmogenic neutron production rate defined as

$$k_\mathrm{n} = \frac{R_\mathrm{n}^\mathrm{max}}{R_\mathrm{n}^0} = 1 + \frac{\delta R_\mathrm{n}}{R_\mathrm{n}^0} \tag{6.6}$$

may be related to the relative maximum of the modulation of the cosmic muon flux defined as

$$k_\mu = \frac{I_\mu^\mathrm{max}}{I_\mu^0} = 1 + \frac{\delta I_\mu}{I_\mu^0} \tag{6.7}$$

via [257]

$$k_\mathrm{n} = k_\mu \cdot k_{E_\mu}. \tag{6.8}$$

The coefficient k_{E_μ} accounts for the energy dependence of the neutron production and relates the maximum change of the cosmogenic neutron production rate to the maximum change of the cosmic muon flux. Consequently, it is connected to the change of the mean muon energy via [257]

$$k_{E_\mu} = \left(\frac{\overline{E}_\mu^\mathrm{max}}{\overline{E}_\mu} \right)^{\alpha}. \tag{6.9}$$

Following these evaluations, the maximum of the mean muon energy may be calculated via

$$\overline{E}_{\mu}^{\max} = k_{E_\mu}^{1/\alpha} \cdot \overline{E}_{\mu} = \left(\frac{k_{\mathrm{n}}}{k_{\mu}}\right)^{1/\alpha} \cdot \overline{E}_{\mu}. \tag{6.10}$$

The mean energy of cosmic muons at the LNGS was measured by the MACRO experiment to be $\overline{E}_{\mu} = (270 \pm 21)\,\mathrm{GeV}$ [134]. Using the measured central values of the cosmogenic neutron production rate for the maximum neutron multiplicity of ten for which the seasonal modulation may still be observed $k_{\mathrm{n}} = 1.026 \pm 0.004$ and of the cosmic muon flux $k_{\mu} = 1.01365 \pm 0.00009$, a maximum mean energy of

$$\overline{E}_{\mu}^{\max} = 274.2\,\mathrm{GeV} \tag{6.11}$$

follows. Based on these considerations, an amplitude of a modulation of the mean energy of cosmic muons at the LNGS of

$$\delta E_{\mu} = 4.2\,\mathrm{GeV} \mathrel{\widehat{=}} 1.6\% \tag{6.12}$$

could explain the observed discrepancy of the amplitudes of the modulations of the cosmic muon flux and the cosmogenic neutron production rate. Due to the significantly higher amplitude of the modulation of the cosmogenic neutron production rate observed by LVD, their measurement also implies a much higher change of the mean muon energy. Thus, a modulation of the mean muon energy with an amplitude of $\sim 10\%$ corresponding to $\sim 28\,\mathrm{GeV}$ was reported [256].

6.4 Discussion

In the LVD measurement and the present analysis of Borexino data, the amplitude of the seasonal modulation of the cosmogenic neutron production rate was found to be higher than the amplitude of the seasonal modulation of the cosmic muon flux. This difference was interpreted as an indirect measurement of a seasonal modulation of the mean muon energy at the LNGS by the LVD collaboration [256]. While the measurement of the LVD experiment would imply a modulation of the mean muon energy by $\sim 28\,\mathrm{GeV}$, the values reported in the present work based on Borexino data could be explained by a significantly smaller change of the mean energy of $\sim 4.2\,\mathrm{GeV}$.
This hypothesis is strongly challenged by the observation of an equally high modulation amplitude of the number of neutron-producing muons. In case of a significant increase of the mean muon energy due to a seasonal modulation, a higher mean neutron multiplicity and, accordingly, also a seasonal modulation of this quantity must be expected. However, the accordance of the amplitude of the number of neutron-producing muons to the cosmogenic neutron production rate proves the

neutron multiplicity to be constant throughout the seasons.
To further probe the interpretation of the higher amplitude of the cosmogenic neutron production rate as an indirect measurement of a seasonal modulation of the mean energy of cosmic muons, several simulations were performed and analyzed in collaboration with V. A. Kudryavtsev. In a first step, the energy spectrum of muons at the surface was approximated by a simple power law with a spectral index of 2.77. Muons were propagated to the LNGS using the MUSIC/MUSUN software code [133] and the expected cosmic muon flux and the mean muon energy underground were analyzed. By altering the spectral index to 2.76, an increase of the mean energy of $\sim 1\,\mathrm{GeV}$ was observed [259]. However, the muon flux was found to be increased by $\sim 14\%$ [259]. Due to the hardened spectrum, much more muons above the threshold energy arrive at the surface of the Earth and reach the LNGS. This is in strong dissent to the measured modulation amplitude of the cosmic muon flux of $(1.365 \pm 0.009)\%$ as detailed in section 4.2.3. Thus, a modulation of the mean cosmic muon energy of several GeV was found to be highly improbable by this simulation.
Additionally, detailed simulations of the muon production in the atmosphere and the muon surface spectrum at the location of the Gran Sasso region based on the MCEq software code [250] were performed. This code allows to predict the high-energetic part of the atmospheric muon and neutrino spectra by solving the applying cascade equations. The simulations were performed by S. Meighen-Berger for several models of the summer and winter atmosphere. The resulting muon surface spectra were used as an input for the MUSIC/MUSUN code to obtain the corresponding underground spectra.
The resulting flux of cosmic muons underground for the simulated input spectra was found to vary by $\sim (2-3)\%$ between summer and winter, which agrees very well with the measured amplitude of the seasonal modulation of the cosmic muon flux of $(1.365 \pm 0.009)\%$. However, only slight deviations of the mean muon energy of less than $\sim 0.1\,\mathrm{GeV}$ were observed [259], again disfavoring the interpretation of a strong modulation of the mean energy of cosmic muons underground.
The performed simulations consistently show that a strong modulation of the mean energy of cosmic muons underground is extremely improbable and would imply a much higher modulation of the flux of cosmic muons than observed by any experiment at the LNGS. Especially the simulation with an altered muon spectral index predicting a strong change of the muon fux underground for a comparably small increase of the mean muon energy shows that the hypothesis of a modulation of the mean muon energy must be withdrawn.
While a modulation of the mean muon energy is excluded by the simulations, small deviations in the muon energy spectrum between summer and winter without affecting the mean muon energy within the accuracy of the simulations are

still possible. Thus, a more complex energy dependence of the cross section for neutron production in a liquid scintillator than the conventionally assumed $\overline{E}_{\mu}^{\alpha}$ law [257] may be hypothesized to explain the observations. However, uncertainties of the atmosphere models on which the simulations of the muon production in the atmosphere are based and of the neutron production processes in the liquid scintillator make it extremely difficult to investigate this percent-level effect with the available simulation tools.
Besides a physical origin of the observed phenomena, unconsidered systematic effects might perturb a precise determination of the parameters of the modulation of the cosmogenic neutron production rate and engender the increased amplitude. However, no systematic effect resulting in a significant overefficiency of the neutron identification as clusters in the neutron gate in summer that could increase the observed modulation amplitude is known. Thus, the observed parameters of the modulation of the cosmogenic neutron production rate are expected to be reliable and a physical origin of the increased amplitude must be supposed.

Chapter 7

Search for Low-Energy Atmospheric Neutrino Interactions in Borexino

Atmospheric neutrinos originate from decays of kaons and pions in the upper atmosphere. When primary cosmic radiation interacts with nuclei of the atmosphere, these mesons are produced in hadronic showers and decay into muons and the corresponding neutrinos or antineutrinos. For muon energies up to $\sim 1\,\mathrm{GeV}$, most of the muons decay into electrons before reaching the Earth's surface and ν_e and $\overline{\nu}_\mathrm{e}$ contributions to the atmospheric neutrino flux are generated.
In the Borexino detector, atmospheric neutrinos may interact via charged current (CC) and neutral current (NC) interactions with the target material. Since CC interactions usually result in very high energy depositions, the signal from these interactions is strongly overpowered by the background from cosmic muons. However, NC interactions generate moderate visible energies and provide a clear signature. Thus, they are a favorable detection channel for atmospheric neutrinos in liquid scintillator experiments.
Since atmospheric neutrinos reach up to energies of $\sim$ TeV, relatively high kinetic energies may be supplied to neutrons in NC interactions between the neutrinos and carbon nuclei of a liquid scintillator target as in Borexino. During their thermalization, the neutrons transfer energy to recoil protons in scattering interactions. Due to the quenching effect, the visible energy generated by the protons is strongly reduced compared to energy depositions of charged leptons as produced in CC interactions of atmospheric neutrinos [111]. Nevertheless, the recoil protons may receive sufficient energy from the high-energetic neutrons that a visible energy deposition results despite the quenching. Due to the broad energy range of the initial atmospheric neutrinos, also the resulting visible energy depositions cover a large energy window.

Since the neutrons thermalize quickly and are captured on, mostly, hydrogen initiating the emission of a characteristic 2.2 MeV γ ray, a signature similar to the inverse β decay (IBD) interaction initialized by an $\overline{\nu}_{\mathrm{e}}$ described in section 2.2.2 arises. Thus, the coincidence between a prompt energy deposition caused by the proton recoils and a delayed 2.2 MeV γ ray emission constitutes a possibility to search for NC interactions of atmospheric neutrinos in a liquid scintillator experiment. Utilizing this signature, the KamLAND experiment observed atmospheric neutrino NC interactions in a visible energy range corresponding to $(7.5-30)$ MeV for electron depositions [260]. Backgrounds for such a search arise mainly due to real IBD interactions of $\overline{\nu}_{\mathrm{e}}$.
A source of terrestrial $\bar{\nu}_{\mathrm{e}}$ are the decays of radioactive isotopes of the ^{238}U and ^{232}Th chains in the Earth's crust producing the so-called geo-neutrinos. These have been measured by the KamLAND [150, 151] and the Borexino [12, 124, 152] experiment and extend up to energies of ~ 3.4 MeV. A man-made $\overline{\nu}_{\mathrm{e}}$ source are reactor plants producing reactor $\bar{\nu}_{\mathrm{e}}$ with energies up to ~ 8 MeV [2, 261]. Naturally produced $\bar{\nu}_{\mathrm{e}}$ of higher energies are expected to be of cosmic origin.
Of special interest and dominating the cosmic $\bar{\nu}_{\mathrm{e}}$ flux between ~ 8 MeV and ~ 15 MeV is the Diffuse Supernova Neutrino Background (DSNB) [66, 260]. The DSNB is a permanent weak flux of neutrinos and antineutrinos from past and distant supernovae (SNe) as described in section 1.4.3. The current best limits on the DSNB neutrino flux are obtained by the Super-Kamiokande experiment [262]. Even though these limits are already close to theoretical predictions, the DSNB so far escapes a detection [66]. However, future experiments like the upcoming JUNO [68] or the gadolinium enhanced Super-Kamiokande [69] experiment will feature the necessary target mass and sensitivity such that a measurable signal of the order of a few events per year can be expected in these detectors. Besides the DSNB, exotic scenarios like conversion of solar neutrinos into antineutrinos [263] or annihilation of dark matter particles into $\nu\bar{\nu}$ pairs [264] could generate IBD events at similar energies.
Even though neutrinos of all flavors are expected to be produced at approximately equal luminosities in core collapse SNe, the main channel through which DSNB neutrinos can be observed is the IBD [68]. Thus, atmospheric neutrino NC interactions constitute a major background for a future detection of the DSNB in liquid scintillator based experiments. As can be seen in figure 2.5 for the representative case of the JUNO experiment, atmospheric neutrino NC interactions are even expected to overpower the DSNB neutrino signal by more than one order of magnitude in the relevant energy region [68]. An identification and suppression of these interactions is, hence, vital for a DSNB detection in liquid scintillator experiments.
While the Borexino detector is too small to detect the weak flux of DSNB neutri-

nos, a small number of atmospheric neutrino NC interactions is expected in the data due to the long operational time of approximately ten years. After summarizing the production of atmospheric neutrinos in the following section 7.1 and illustrating the relevant NC interactions in section 7.2, a search of atmospheric neutrino NC interactions in the Borexino detector is performed. In section 7.3, the selection of candidate events is described, in section 7.4, background contributions to the search of atmospheric neutrino NC interactions are analyzed, and in section 7.5, the selected candidates are evaluated. In section 7.6, a pulse shape analysis of the candidate events is presented. In section 7.7, the chapter is concluded with a discussion of the implications of these analyses for future liquid scintillator experiments aiming for the detection of the DSNB.

7.1 Atmospheric Neutrino Production

As described in section 4.1.1, the production of cosmic muons in the decays of pions

$$\pi^{+/(-)} \rightarrow \mu^{+/(-)} + {}^{(}\overline{\nu}_{\mu}^{)} \tag{7.1}$$

and kaons

$$\mathrm{K}^{+/(-)} \rightarrow \mu^{+/(-)} + {}^{(}\overline{\nu}_{\mu}^{)} \tag{7.2}$$

in the atmosphere is accompanied by the generation of the corresponding ν_{μ} or $\bar{\nu}_{\mu}$ to conserve lepton family number. Regarding atmospheric neutrinos, also the decay of cosmic muons into electrons

$$\mu^{+/(-)} \rightarrow \mathrm{e}^{+/(-)} + {}^{(}\overline{\nu}_{\mu}^{)} + {}^{(}\overline{\nu}_{\mathrm{e}}^{)} \tag{7.3}$$

needs to be considered, through which further neutrinos are generated. In a regime in which all particles decay, a ratio of muon type neutrinos to electron type neutrinos of

$$(\nu_{\mu} + \overline{\nu}_{\mu})/(\nu_{\mathrm{e}} + \overline{\nu}_{\mathrm{e}}) \sim 2 \tag{7.4}$$

is, accordingly, expected. Roughly equal energies are carried on average by the neutrinos of the decay chain due to the kinematics of pion and muon decays [79]. The observation of the ratio of electron neutrinos to muon neutrinos being ~ 1 by the Kamiokande experiment [265] revealed the presence of neutrino oscillations in the atmospheric sector. Due to the time dilation for particles traveling at relativistic velocities, the muon decay length becomes larger than the distance between the muon production point and the Earth's surface of approximately 15 km for energies above ~ 2.5 GeV. Thus, the ratio of electron type neutrinos to muon type neutrinos quickly decreases with increasing energies above 1 GeV. At high energies, the only, albeit small contributions to atmospheric electron neutrinos are the kaon

decays $\mathrm{K}_\mathrm{L}^0 \rightarrow \pi + \mathrm{e} + \nu_\mathrm{e}$ and $\mathrm{K}^\pm \rightarrow \pi^0 + \mathrm{e} + \nu_\mathrm{e}$ [79].
Due to the negligible mass of the neutrino, the rest frame momentum of the meson decays expressed by equations 7.1 and 7.2 is given by $p_\mathrm{r} = (1 - m_\mu^2/m_\mathrm{M}^2) \cdot m_\mathrm{M}/2$ and the differential flux per energy for muons and the corresponding neutrinos can be written as [79]

$$\frac{\mathrm{d}n_\nu}{\mathrm{d}E_\nu} = \frac{\mathrm{d}n_\mu}{\mathrm{d}E_\mu} = \frac{Bm_\mathrm{M}}{2p_\mathrm{r}P_\mathrm{L}}. \tag{7.5}$$

Here, B is the branching ratio of the decay of the meson M into muons and muon neutrinos, m_M the meson's mass, and P_L the momentum of the decaying meson in the laboratory frame. Since the decaying mesons with the energy E in the laboratory frame can be assumed to be relativistic, the kinematic limits on the energies of the produced muons and neutrinos are [79]

$$\frac{m_\mu^2}{m_\mathrm{M}^2} \cdot E \leq E_\mu \leq E \tag{7.6}$$

and

$$0 \leq E_\nu \leq \left(1 - \frac{m_\mu^2}{m_\mathrm{M}^2}\right) \cdot E, \tag{7.7}$$

respectively. Numerically, the numbers

$$\langle E_\mu \rangle / E_\pi = 0.79 \text{ and } \langle E_\nu \rangle / E_\pi = 0.21 \tag{7.8}$$

for pions and

$$\langle E_\mu \rangle / E_\mathrm{K} = 0.52 \text{ and } \langle E_\nu \rangle / E_\mathrm{K} = 0.48 \tag{7.9}$$

for kaons are obtained [79]. Since for pion decays, the mean energy of the produced muons is much higher than the mean energy of the produced neutrinos, the pion contribution to high-energetic ν_μ is suppressed. Thus, kaons become the predominant source of high-energetic atmospheric ν_μ. In their decays, approximately equal energies are transferred to the produced muons and neutrinos on average.
As described in section 4.1.1, the production spectrum of cosmic muons can be expressed as

$$\begin{aligned} \mathcal{P}_\mu(E_\mu, X, \cos\theta) =& \frac{\epsilon_\pi}{X\cos\theta(1 - r_\pi)} \int_{E_\mu}^{E_\mu/r_\pi} \frac{\mathrm{d}E}{E} \frac{\mathcal{M}(E, X, \cos\theta)}{E} \\ &+ \frac{0.635 \cdot \epsilon_\mathrm{K}}{X\cos\theta(1 - r_\mathrm{K})} \int_{E_\mu}^{E_\mu/r_\mathrm{K}} \frac{\mathrm{d}E}{E} \frac{\mathcal{M}(E, X, \cos\theta)}{E} \end{aligned} \tag{7.10}$$

with $\epsilon_\pi = (114 \pm 3)\,\mathrm{GeV}$ [176] the critical energy separating the interaction from the decay regime for pions, $\epsilon_\mathrm{K} = (851 \pm 14)\,\mathrm{GeV}$ [176] the critical energy for kaons,

X the atmospheric slant depth, $r_{\mathrm{M}} \equiv m_\mu^2/m_{\mathrm{M}}^2$ with M denoting the respective meson species kaon and pion, and $\mathcal{M}(E, X, \cos\theta)$ the meson intensity as defined by equation 4.7. Considering equation 7.5, the neutrino production spectrum can be expressed in the same form but the limits of the integration need to be adjusted. These limits define the range of parent energies that allow the production of a muon or muon neutrino of a given energy. Hence, using equations 7.6 and 7.7, the neutrino production spectrum can be expressed as [79]

$$\begin{aligned}\mathcal{P}_\nu(E_\nu, X, \cos\theta) =& \frac{\epsilon_\pi}{X\cos\theta(1-r_\pi)} \int_{E_\nu/(1-r_\pi)}^{\infty} \frac{\mathrm{d}E}{E} \frac{\mathcal{M}(E, X, \cos\theta)}{E} \\ &+ \frac{0.635 \cdot \epsilon_{\mathrm{K}}}{X\cos\theta(1-r_{\mathrm{K}})} \int_{E_\nu/(1-r_{\mathrm{K}})}^{\infty} \frac{\mathrm{d}E}{E} \frac{\mathcal{M}(E, X, \cos\theta)}{E}.\end{aligned} \tag{7.11}$$

Analogously to the procedure for cosmic muons, the differential energy spectrum of atmospheric muon neutrinos can be obtained by integrating the production spectrum over the entire atmosphere:

$$\frac{\mathrm{d}I_\nu}{\mathrm{d}E_\nu} = \int_0^\infty \mathcal{P}_\nu(E_\nu, X)\,\mathrm{d}X. \tag{7.12}$$

An approximate solution of this integral is given by [79]

$$\frac{\mathrm{d}I_\nu}{\mathrm{d}E_\nu} = A \times N_0(E_\nu) \left(\frac{A_{\pi\nu}}{1 + B_{\pi\nu} \cdot E_\nu \cos\theta/\epsilon_\pi} + 0.635 \frac{A_{\mathrm{K}\nu}}{1 + B_{\mathrm{K}\nu} \cdot E_\nu \cos\theta/\epsilon_{\mathrm{K}}} \right), \tag{7.13}$$

where $N_0(E_\nu)$ describes the differential meson production spectrum of the form $E^{-(\gamma+1)}$ with the spectral index γ and

$$A_{\pi\nu} \equiv Z_{\mathrm{N}\pi} \frac{(1-r_\pi)^{-(\gamma+1)}}{(1-r_\pi)(\gamma+1)},$$

$$A_{\mathrm{K}\nu} \equiv Z_{\mathrm{NK}} \frac{1 - r_{\mathrm{K}}^{-(\gamma+1)}}{(1-r_{\mathrm{K}})(\gamma+1)},$$

and

$$B_{\mathrm{M}\nu} \equiv \frac{\gamma+2}{\gamma+1} \frac{1}{1-r_{\mathrm{M}}} \frac{\Lambda_{\mathrm{M}} - \Lambda_{\mathrm{N}}}{\Lambda_{\mathrm{N}} \ln(\Lambda_{\mathrm{M}}/\Lambda_{\mathrm{N}})}.$$

In these factors, Λ_{N} denotes the absorption mean free path of the meson-producing cosmic particle N as in section 4.1.1, Λ_{M} the absorption mean free path of the meson species M, and Z_{NM} the spectrum weighted inclusive cross section. The difference between $A_{\pi\nu}$ and $A_{\mathrm{K}\nu}$ is related to the suppressed contribution of pions to the atmospheric ν_μ flux compared to their contribution to the cosmic muon flux. This is expressed by the factor $(1-r_\pi)^{-(\gamma+1)}$ in the term describing the pion contribution to the atmospheric muon neutrino flux. The factor $1 - r_{\mathrm{M}}^{-(\gamma+1)}$ describes the pion contribution to the cosmic muon flux and the kaon contribution to both neutrino and muon fluxes. For $\gamma = 1.7$, the ratio of the two factors is ~ 0.13 [79].

7.2 Neutral Current Interactions of Atmospheric Neutrinos

Several NC reaction channels of atmospheric neutrinos exist in the liquid scintillator target of the Borexino detector. Due to the scintillator liquid being composed of hydrocarbons, ^{12}C is the most abundant isotope with an isotopic abundance of 98.9% [9]. Thus, it constitutes the major target for NC interactions of atmospheric neutrinos.
Table 7.1 lists possible NC reactions of atmospheric neutrinos on ^{12}C together with their branching ratios. In many reactions and especially the one with the highest branching ratio

$$\nu_{\mathrm{x}} + {}^{12}\mathrm{C} \rightarrow \nu_{\mathrm{x}} + \mathrm{n} + {}^{11}\mathrm{C}, \tag{7.14}$$

a neutron is knocked out of the ^{12}C nucleus. These neutrons together with the other reaction products can generate a visible signal through scattering reactions off protons and carbon nuclei. The neutrons ejected in the NC interactions are thermalized and captured on a proton with a capture time of $\tau_{\mathrm{n}} = (259.7 \pm 1.3_{\mathrm{stat}} \pm 2.0_{\mathrm{syst}})\,\mu\mathrm{s}$ [137]. After the capture, the deuteron binding energy is released in form of a 2.2 MeV γ ray. In about 1% of the cases, the neutron is captured on ^{12}C, which results in the release of a total γ ray energy of 4.95 MeV [62]. With these two energy depositions, the first signal caused by recoiling protons and the subsequent emission of the capture γ ray mimic the IBD signature described in section 2.2.2. Despite the strong quenching of proton recoil signals, similar energies of the prompt candidates may result for atmospheric neutrino NC and DSNB neutrino IBD interactions due to the high energies of up to $\sim$ TeV [85] that are reached by atmospheric neutrinos. Thus, NC interactions of atmospheric neutrinos induce the most challenging background for a potential detection of the DSNB in liquid scintillators as can be seen in figure 2.5 [68].
Atmospheric neutrino NC interactions have been observed by the KamLAND experiment based on a delayed coincidence condition for visible energies of the prompt candidates between 7.5 MeV and 30 MeV [260]. With approximately ten years of acquired data, several of these interactions may also be expected in the Borexino data. Utilizing the delayed coincidence signature generated by atmospheric neutrino NC interactions, a search for these interactions in the Borexino detector was performed as presented in the following sections.

7.3 Event Selection

To search for atmospheric neutrino NC interactions in the Borexino detector, data acquired between December 9th, 2007 and September 2nd, 2017 were used corre-

Reaction channel	Branching ratio
(1) $\nu_x + {}^{12}C \rightarrow \nu_x + n + {}^{11}C$	38.8%
(2) $\nu_x + {}^{12}C \rightarrow \nu_x + p + n + {}^{10}B$	20.4%
(3) $\nu_x + {}^{12}C \rightarrow \nu_x + 2p + n + {}^{9}Be$	15.9%
(4) $\nu_x + {}^{12}C \rightarrow \nu_x + p + d + n + {}^{8}Be$	7.1%
(5) $\nu_x + {}^{12}C \rightarrow \nu_x + \alpha + p + n + {}^{6}Li$	6.6%
(6) $\nu_x + {}^{12}C \rightarrow \nu_x + 2p + d + n + {}^{7}Li$	1.3%
(7) $\nu_x + {}^{12}C \rightarrow \nu_x + 3p + 2n + {}^{7}Li$	1.2%
(8) $\nu_x + {}^{12}C \rightarrow \nu_x + d + n + {}^{9}B$	1.2%
(9) $\nu_x + {}^{12}C \rightarrow \nu_x + 2p + t + n + {}^{6}Li$	1.1%
(10) $\nu_x + {}^{12}C \rightarrow \nu_x + \alpha + n + {}^{7}Be$	1.1%
(11) $\nu_x + {}^{12}C \rightarrow \nu_x + 3p + n + {}^{8}Li$	1.1%
Other reaction channels	4.2%

Table 7.1: Branching ratios of different NC reactions of atmospheric neutrinos on ^{12}C [148].

sponding to a livetime of 2,709 days. Only events occurring inside the Inner Vessel (IV) and with a minimum distance of 25 cm to the vessel border were considered to avoid backgrounds from the vessel surface. The application of this fiducial volume cut constrains the exposure to 1.64 kt $\times$ yr.
The selection cuts for prompt and delayed candidate events were chosen based on the geo-neutrino analysis from Borexino [12] and similar to the cuts of the analysis of atmospheric neutrino NC reactions by the KamLAND experiment [260].
Thus, prompt candidate events were required to deposit a visible energy between 3,750 p.e. and 15,000 p.e. to mirror the energy window of the KamLAND analysis of 7.5 MeV to 30 MeV with the Borexino charge to energy conversion of $\sim$ 500 p.e./MeV [9]. The choice of equal energy windows is appropriate since similar low- and high-energetic backgrounds as for KamLAND exist and have to be suppressed. The low-energetic backgrounds rejected by the lower energy threshold are mainly reactor antineutrinos, geo-neutrinos, and the neutron-unstable, cosmogenically produced radio-isotopes ^{9}Li and ^{8}He. At high energies, backgrounds due to untagged muons and fast neutrons are expected to strongly overpower the signal from atmospheric neutrino NC interactions [260], such that the application of the high energy cut is required. Additionally, direct comparability to the result from KamLAND is guaranteed by restricting the search to an equal energy range.
Potential delayed capture γ ray events were required to deposit a visible energy between 860 p.e. and 1300 p.e. as in the geo-neutrino analysis [12]. This energy range covers the peak around the 2.2 MeV energy deposition of the γ ray emitted after a neutron capture on hydrogen. Additionally, captures on carbon were considered in

a visible energy range between 2,100 p.e. and 2,900 p.e. Delayed candidates were searched for in a time window of 20 μs to 1,000 μs after a prompt candidate. The minimum time difference between prompt and delayed events is determined by the length of the 16 μs gate in which the prompt candidate is acquired plus the time the baseline of the PMTs needs to stabilize after high-energetic events. The maximum time difference reproduces the KamLAND cut and equals approximately four times the neutron capture time in Borexino.
To avoid noise contaminations of the sample, only events for which exactly one cluster of PMT hits was found were considered as prompt or delayed candidates. Clusters correspond to single scintillation light emissions and in principle, multiple clusters may be identified in the acquisition gate of 16 μs during which an event is recorded. However, such events are usually caused by noise, random coincidences, or fast radioactive decays and, thus, commonly removed from the analyses [9].
The maximum distance between a prompt and a delayed event was set to 1.6 m, again reproducing the KamLAND cut to guaranty the comparability of the results. Finally, the Gatti parameter $g_{\alpha\beta}$ was used to avoid background events mistakenly being registered as delayed candidates. Figure 7.1 shows the distribution of the Gatti parameter for 10^4 simulated 2.2 MeV γ rays in the Borexino detector. By requiring $g_{\alpha\beta} < 0.015$ for delayed candidates as in the geo-neutrino analysis [12], the collection of real capture γ ray events is not harmed while several fake delayed candidate events, e.g. due to ^{214}Po, can be avoided. ^{214}Po decays under the emission of an α particle into ^{210}Pb. The α particle is emitted mono-energetically at 7.8 MeV and the visible energy output is, due to the quenching, well below the energy window of the capture γ rays. However, in rare cases, ^{214}Po decays into excited states of ^{210}Pb, which deexcite via the emission of 799.7 keV and 1097.7 keV γ rays. In these cases, the emitted energy is close to the energy window of the capture γ rays but due to the high value of the Gatti parameter of the emitted α particle, these fake delayed candidates may be rejected.
To suppress contributions from fast neutrons generated in spallation processes of cosmic muons either in the rock surrounding the detector or the OD, a 2 ms veto was applied after each muon that was registered in the OD. Further, backgrounds originating from cosmogenically generated radio-isotopes as described in section 7.4.5 were suppressed by a 2 s veto after each muon crossing the ID. These cuts lead to a deadtime of $\sim 10\%$ and an effective exposure after the cuts of 1.48 kt $\times$ yr for a livetime of 2,455 days.

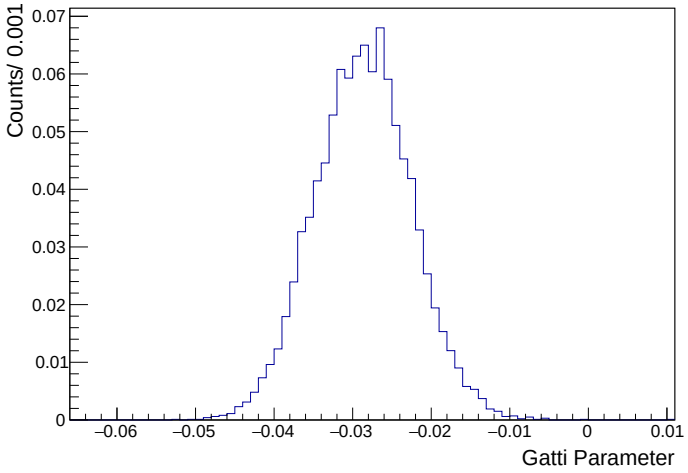

Figure 7.1: Distribution of the Gatti parameter for simulated 2.2 MeV γ rays.

7.4 Expected Backgrounds for a Detection of Atmospheric Neutrino Neutral Current Interactions

Various backgrounds exist for the detection and identification of NC interactions of atmospheric neutrinos in liquid scintillator experiments. These background sources either mimic or initiate the IBD coincidence and, thus, would also constitute a background for a DSNB analysis in future experiments. In the following, possible background sources are described and their abundance in the dataset of the analysis of atmospheric neutrino NC interactions in Borexino is estimated.

7.4.1 Random Coincidences

Physically uncorrelated event pairs may be present in the data within the same energy, time, and spatial separation windows as defined in section 7.3 for the search of atmospheric neutrino NC interactions. To estimate the contribution of such random coincidences, events were selected within the respective prompt and delayed energy windows but in a time window of 1 s to 2 s after the prompt candidate. This enlarged time window guarantees sufficiently high statistics for the estimation of the contribution of random coincidences. Opening the window 1 s after the prompt candidate ensures that no physical correlation between the prompt and delayed candidates needs to be considered. The same cuts after the passage of cosmic muons as for candidates of atmospheric neutrino NC interactions were

applied. In the dataset, 525 random coincidences are found in the shifted time window for a total of 11,285 prompt event candidates. Thus, a contribution of random coincidences in the dataset of 0.52 ± 0.02 events can be expected.

7.4.2 Diffuse Supernova Neutrino Background

NC reactions of atmospheric neutrinos on ^{12}C strongly overpower a DSNB signal in liquid scintillator based detectors due to the extremely weak DSNB neutrino flux. Even though a detection of the DSNB neutrino flux requires much larger detectors than Borexino, a small number of IBD interactions of DSNB neutrinos could still constitute a background for the search of atmospheric neutrino NC interactions.
As described in section 1.4.3, the current understanding of core collapse SNe assumes that all neutrino species are thermally produced at approximately equal luminosities during a core collapse SN [52]. Thus, the total energy released in the form of neutrinos of $L_\nu \sim 3 \times 10^{53}\,\mathrm{erg}$ [266] is equally shared between all neutrino flavors. Neglecting that the respective neutrino species decouple at slightly different temperatures due to a flavor specific opacity of the neutron rich matter in which the neutrinos are thermalized before emerging [52], the mean energies of all species are assumed to be equal. These approximations lead to equal fluxes of DSNB neutrinos for all flavors and neutrino oscillations may be neglected in the following estimations.
The DSNB spectrum measured in a detector on Earth only considering a detection via the IBD is given by

$$\frac{\mathrm{d}R_\nu}{\mathrm{d}E_\nu} = \frac{\mathrm{d}F_\nu}{\mathrm{d}E_\nu} \cdot \sigma_\nu(E_\nu) \cdot N_\mathrm{p} \tag{7.15}$$

with $\frac{\mathrm{d}F_\nu}{\mathrm{d}E_\nu}$ being the differential DSNB $\bar{\nu}_\mathrm{e}$ neutrino flux, $\sigma_\nu(E_\nu)$ the energy dependent IBD cross section, and N_p the number of protons contained in the target volume. With $N_\mathrm{p} \simeq 1.7 \times 10^{31}$ [124] in the Borexino IV, the applied fiducial volume cut of a minimum distance of 25 cm to the vessel border for any candidate event implies $N_\mathrm{p} \simeq 1.4 \times 10^{31}$ for the present analysis.
As described in section 1.4.3, the DSNB spectrum at Earth may be expressed as [56]

$$\frac{\mathrm{d}F_\nu(E_\nu)}{\mathrm{d}E_\nu} = \frac{c}{H_0} \int_0^{z_\mathrm{max}} R_\mathrm{SN}(z) \frac{\mathrm{d}N_\nu(E'_\nu)}{\mathrm{d}E'_\nu} \frac{\mathrm{d}z}{\sqrt{\Omega_\mathrm{m}(1+z)^3 + \Omega_\Lambda}}. \tag{7.16}$$

Here, $H_0 = 70\,\mathrm{km\,s^{-1}\,Mpc^{-1}}$ is the Hubble constant, $\Omega_\mathrm{m} \sim 0.3$ and $\Omega_\Lambda \sim 0.7$ the contribution of matter to the total density of the Universe and the cosmic constant, respectively, c the speed of light, $E' = E(1+z)$ the redshift corrected neutrino energy, and $\frac{\mathrm{d}N_\nu}{\mathrm{d}E_\nu}(E_\nu)$ the average SN neutrino energy spectrum as derived in section 1.4.2. The integral considers all redshifts for which SNe occurred and the first SNe are expected at $z_\mathrm{max} \simeq 5$. The factor $1/H_0\sqrt{\Omega_\mathrm{m}(1+z)^3 + \Omega_\Lambda}$ accounts

for the expansion of the Universe, which results in a reduced neutrino flux from individual SNe at large redshifts.
The neutrino emission spectrum of a SN can be vaguely approximated by a Maxwell-Boltzmann distribution due to the thermal production of the neutrinos [101] and

$$\frac{\mathrm{d}N_\nu(E_\nu)}{\mathrm{d}E_\nu} = \mathcal{C}\frac{L_\nu}{\langle E_\nu\rangle^2}\left(\frac{E}{\langle E_\nu\rangle}\right)^2 e^{-\frac{3E}{\langle E_\nu\rangle}}, \tag{7.17}$$

where $\mathcal{C}$ is a normalization factor and the mean neutrino energy $\langle E_\nu\rangle$ is in the range of 12 MeV to 21 MeV [148]. As detailed in section 1.4.3, the mere thermal spectrum is affected by several processes that slightly change the spectral shape. Thus, neutrino oscillations in and around the proto-neutron star and the finite width of the neutrinosphere from which the neutrinos emerge alter the SN $\overline{\nu}_\mathrm{e}$ spectrum as observed on Earth compared to the Maxwell-Boltzmann assumption [56]. However, these effects are small and do not strongly affect the expected signal, such that they are neglected in the following.
For the energy dependent IBD cross section, an approximation of [267]

$$\sigma_\nu(E_\nu) = p_\mathrm{e}E_\mathrm{e}E_\nu^{-0.07056+0.02018\ln(E_\nu/\mathrm{MeV})-0.001953\ln^3(E_\nu/\mathrm{MeV})} \times 10^{-43}\,\mathrm{cm}^2 \tag{7.18}$$

can be found. In this expression, p_e denotes the positron momentum, $E_\mathrm{e} = E_\nu - 0.782\,\mathrm{MeV}$ is the total energy of the positron, and all energies are expressed in MeV. Depending on the actual SN model that is used, theoretical estimations of the integrated DSNB $\overline{\nu}_\mathrm{e}$ flux range from $\Phi_\nu = 11.7\,\mathrm{cm}^{-2}\mathrm{s}^{-1}$ to $\Phi_\nu = 16.1\,\mathrm{cm}^{-2}\mathrm{s}^{-1}$ [56].
The expected background for the search of NC reactions of atmospheric neutrinos due to DSNB neutrino interactions can be calculated via

$$R_\nu = \int_{E_\mathrm{min}}^{E_\mathrm{max}} \mathrm{d}E_\nu \frac{\mathrm{d}F_\nu(E_\nu)}{\mathrm{d}E_\nu}\sigma(E_\nu)N_\mathrm{p}\Phi_\nu t \tag{7.19}$$

with $E_\mathrm{min} = 8.282\,\mathrm{MeV}$, $E_\mathrm{max} = 30.782\,\mathrm{MeV}$, and $t = 2,455\,\mathrm{d}$ for the present analysis.
Based on a numerical integration of the spectrum described by equation 7.16 in the relevant energy region, the expected background for the search of atmospheric neutrino NC interactions caused by DSNB $\overline{\nu}_\mathrm{e}$ is estimated to be 0.21 ± 0.15 events. The error margin covers the results for combinations of the highest and lowest predicted DSNB flux with mean SN neutrino energies of 12 MeV and 21 MeV.

7.4.3 Charged Current Atmospheric Neutrino Interactions

CC interactions of atmospheric neutrinos on protons or carbon nuclei in the scintillator impose a background to the search for atmospheric neutrino NC reactions

since they can produce or mimic the IBD signature. The KamLAND collaboration reported an expected number of atmospheric $\bar{\nu}_e$ IBD interactions in the energy window from 7.5 MeV to 30 MeV of ~ 0.06 events in 4.53 kt $\times$ yr of accumulated data [260]. These events are dominated by reactions on protons due to the higher cross section compared to reactions on carbon nuclei [268]. The estimation is based on atmospheric neutrino spectra calculated for the location of the KamLAND experiment. The same calculations yield an atmospheric $\bar{\nu}_e$ flux at Gran Sasso that is a factor of 1.60 higher than at the Kamioka mine at a neutrino energy of 100 MeV [269]. Following these considerations and scaling the KamLAND result to the exposure of the present analysis, 0.03 atmospheric $\bar{\nu}_e$ IBD interactions are expected as a background for atmospheric neutrino NC interactions in the Borexino detector.

Besides $\overline{\nu}_e$, atmospheric ν_μ and $\bar{\nu}_\mu$ can interact with protons and carbon nuclei via CC interactions and produce muons and neutrons. The produced muon can generate a prompt signal while the neutron thermalizes and is eventually captured releasing the 2.2 MeV delayed γ ray signal. However, since a major part of the neutrino energy is necessary to produce the muon, the muons only receive small kinetic energies and, thus, are stopped in the scintillator and decay into an electron and two neutrinos. This decay constitutes a possibility to distinguish such events via the triple coincidence between the prompt muon signal, its decay, and the neutron capture. However, due to the lifetime of the muon of $\sim 2.2\,\mu$s, which is not affected significantly in the scintillator [270], most of the decays occur already within the 16 μs gate of the prompt event. Such events are expected to mostly produce two clusters in the PMT hit time spectrum, one due to the energy loss of the muon and one caused by the electron produced in its decay. Thus, the majority of atmospheric ν_μ CC interactions is rejected in the analysis since only events with exactly one cluster of PMT hits were considered.

By simulating muons with 1 MeV kinetic energy in the center of the Borexino detector, it was found that indeed just $(14.4 \pm 1.2)\%$ of the muon decays produce only one cluster. For these events, the thermalization of the electron into which the muon decays is expected to strongly populate the tail of the PMT hit time pulse. Thus, a very high value of the Gatti parameter is expected for atmospheric ν_μ CC interactions only producing one cluster. As shown in the following sections, also this behavior is confirmed by Monte Carlo simulations.

KamLAND estimated a contribution of 4.0 ± 0.9 of such events in their dataset using the cross sections calculated in [271]. The combined flux of atmospheric ν_μ as well as $\bar{\nu}_\mu$ is calculated to be a factor of 1.62 higher at Gran Sasso than at Kamioka for a neutrino energy of 199.5 MeV [269]. By scaling these estimations to the Borexino exposure, an expected number of 2.1 ± 0.5 of such events in the Borexino dataset results. Considering the prediction of the Monte Carlo simulation

that most of these interactions will produce prompt candidates with more than one cluster, the expected background for the search of atmospheric neutrino NC interactions due to atmospheric ν_μ and $\overline{\nu}_\mu$ CC interactions is 0.30 ± 0.07 events.

7.4.4 Reactor Antineutrinos

Reactor $\bar{\nu}_\mathrm{e}$ are produced in the β decays of neutron-rich fission products of the four fuel components of nuclear power plants ^{235}U, ^{238}U, ^{239}Pu, and ^{241}Pu. Due to a general shutdown of nuclear power plants in Italy that was completed in 1990, the weighted mean distance of the Borexino detector to operational nuclear power plants is rather large with $\sim 1,000\,\mathrm{km}$. Thus, the interaction rate of reactor $\bar{\nu}_\mathrm{e}$ is relatively small compared to other experiments. However, reactor $\bar{\nu}_\mathrm{e}$ still dominate the $\bar{\nu}_\mathrm{e}$ flux registered at Borexino for $E_\nu < 7.5\,\mathrm{MeV}$ [12] and since the tail of the reactor $\bar{\nu}_\mathrm{e}$ spectrum extends to even higher energies, reactor $\bar{\nu}_\mathrm{e}$ remain a possible background source for the analysis of atmospheric neutrino NC interactions.
An extensive estimation of the reactor $\bar{\nu}_\mathrm{e}$ flux and interaction rate at Borexino has been performed in an analysis of the DSNB neutrino flux in Borexino independent from this thesis [272]. The following evaluations of the background from reactor $\overline{\nu}_\mathrm{e}$ for the analysis of atmospheric neutrino NC interactions are based on these considerations.
The expected interaction rate of reactor $\overline{\nu}_\mathrm{e}$ in the Borexino detector is in principle given by

$$R_\mathrm{reac} = \sigma(E) \times P_\mathrm{ee}(E) \times \Phi_\mathrm{reac}(E), \tag{7.20}$$

where $\sigma(E)$ is the energy dependent IBD cross section, $P_\mathrm{ee}(E)$ the survival probability for $\bar{\nu}_\mathrm{e}$, and $\Phi_\mathrm{reac}(E)$ the reactor $\bar{\nu}_\mathrm{e}$ flux. For a single reactor, the $\bar{\nu}_\mathrm{e}$ flux may be calculated as [273]

$$\Phi_\mathrm{single}(E) = \sum_\mathrm{k} \alpha_\mathrm{k} \times \Phi_\mathrm{k}(E). \tag{7.21}$$

The index k considers the four relevant fuel components ^{235}U, ^{238}U, ^{239}Pu, and ^{241}Pu. α_k denotes the number of fissions of the isotope k, and $\Phi_\mathrm{k}(E)$ is the $\bar{\nu}_\mathrm{e}$ spectrum of the corresponding isotope. Considering the contributions of a total of N_reac reactor cores, the differential reactor $\bar{\nu}_\mathrm{e}$ spectrum at the Borexino detector can be evaluated via [124]

$$\Phi_\mathrm{reac}(E) = \sum_{\mathrm{r}=1}^{N_\mathrm{reac}} \sum_{\mathrm{m}=1}^{N_\mathrm{months}} \frac{T_\mathrm{rm}}{4\pi L_\mathrm{r}^2} P_\mathrm{rm} \times \sum_\mathrm{k} \frac{f_\mathrm{k}}{E_\mathrm{k}} \Phi_\mathrm{k}(E) P_\mathrm{ee}(E, \hat{\theta}, L_\mathrm{r}). \tag{7.22}$$

The index r sums the contributions from all reactor cores N_reac while the index m considers the spectra of a single reactor core in a month m. Then, the contributions of N_months months for the whole time frame corresponding to the exposure of the

present analysis are summed. In the calculation of the monthly $\bar{\nu}_e$ spectra for a reactor r, T_{rm} is the operational time of the reactor r in the month m, P_{rm} the effective thermal power of the reactor r in the month m, and L_r the distance of the reactor r to the Borexino detector. The index k denotes the four relevant fuel components as above and f_k is the fission fraction of the isotope k, E_k the average $\bar{\nu}_e$ energy released per fission of the isotope k, and $\Phi_k(E)$ the corresponding $\bar{\nu}_e$ spectrum as given in [273]. P_{ee} is the $\bar{\nu}_e$ survival probability for an $\bar{\nu}_e$ with energy E after having traveled the distance L_r considering the oscillation parameters $\hat{\theta} = (\Delta m^2_{12}, \sin^2\theta_{12})$.

The calculation has been performed taking into account all reactor cores in the world for the relevant years from 2007 to 2017 [272]. Inserting the resulting spectrum into equation 7.20, an interaction rate in the Borexino detector of $S_{reac} = 84.70\,\text{TNU}$ has been predicted, where 1 Terrestrial Neutrino Unit corresponds to 1 event per year and 10^{32} protons.

As an uncertainty of the prediction, the bump in the reactor neutrino spectrum around 5 MeV that has been observed by several reactor neutrino experiments [274] and that is in disagreement with the expectations according to equation 7.22 has been considered. This has been done by multiplying the predicted reactor $\bar{\nu}_e$ spectra with an energy dependent factor that accounts for the relative deviation of the measured spectrum by the RENO experiment [275] from the prediction. When this bump is considered in the calculation, an expected reactor $\bar{\nu}_e$ interaction rate in the Borexino detector of 87.04 TNU results [272].

The evaluated reactor $\bar{\nu}_e$ spectrum predicts the fraction of reactor $\bar{\nu}_e$ interactions depositing more than 7.5 MeV visible energy in the Borexino detector to be 1.363×10^{-3} [272]. Thus, the estimated interaction rates correspond to a background contribution to the present analysis due to reactor neutrinos of $R_{reac} = 0.109$ and $R_{reac} = 0.112$, depending on whether the reactor anomaly is considered or not.

In addition to this calculation, the measurement of the reactor neutrino rate in Borexino performed in [12] may be utilized to estimate the background for the analysis of atmospheric neutrino NC interactions. Since the measured interaction rate is affected by the detector performance, especially the uncertainty of the prediction derived above may be assessed in the comparison to the measurement. In an analysis of 1,841.9 days livetime correspoding to an efficiency corrected exposure of $0.907\,\text{kton} \times \text{yr}$ after all cuts, the reactor $\bar{\nu}_e$ flux has been derived in a simultaneous fit as a background component of the performed geo-neutrino spectroscopy. Using an un-binned maximum likelihood fit, a reactor $\bar{\nu}_e$ rate of $S_{reac} = (96.6^{+15.6}_{-14.2}(\text{stat.})^{+4.9}_{-5.0}(\text{syst.}))\,\text{TNU}$ has been inferred from the dataset. Assuming the best fit value and considering the exposure of the present analysis, a reactor $\bar{\nu}_e$ background of $R_{reac} = 0.124$ would be expected. The difference of this

estimation to the prediction indicates the uncertainty of the expected background contribution of reactor neutrinos. Thus, the expected amount of reactor $\bar{\nu}_e$ events in the data sample used for the analysis of atmospheric neutrino NC interactions is estimated as

$$R_{\text{reac}} = 0.112 \pm 0.012. \tag{7.23}$$

The expectation value is the predicted number of events including the reactor anomaly and the uncertainty is chosen such that the measured best fit value of the reactor $\bar{\nu}_e$ interaction rate still agrees with this prediction.

7.4.5 Cosmogenic Radio-Isotopes

From the variety of cosmogenic radio-isotopes formed in spallation processes of cosmic muons in the scintillator, ^{8}He ($\tau = 171.7\,\text{ms}$, $Q = 10.7\,\text{MeV}$) and ^{9}Li ($\tau = 257.2\,\text{ms}$, $Q = 13.6\,\text{MeV}$) feature decay modes with electrons and neutrons in the final state. With a 16% branching ratio, the β decay of ^{8}He populates a neutron-unstable state in ^{8}Li, with a branching ratio of 51%, the β decay of ^{9}Li leads to such a state in ^{9}Be [137]. In case of the population of an excited state, the endpoints of the β decays are reduced to 7.4 MeV and 11.2 MeV for ^{8}He and ^{9}Li, respectively. Due to the neutron emission subsequent to the β decay, the decays of these isotopes can mimic an IBD interaction and possibly constitute a background for the analysis of atmospheric neutrino NC interactions.
This background, however, is significantly reduced by the 2 s veto after ID muons and the relatively high energy threshold of the analysis. Since the endpoint of the ^{8}He β decay is below the applied 7.5 MeV energy threshold, only a background contribution from ^{9}Li needs to be considered.
The ^{9}Li production rate in Borexino is measured to be $R(^9\text{Li}) = (0.083 \pm 0.009_{\text{stat}} \pm 0.001_{\text{syst}})\,(\text{d}100\,\text{t})^{-1}$ [137]. Hence, 509 ± 60 ^{9}Li decays are expected in the dataset not considering the applied muon cuts. Using a Monte Carlo simulation of ^{9}Li decays performed for the geo-neutrino analysis of Borexino [12], the fraction of ^{9}Li decays generating a visible energy of more than 3,750 p.e. as required for this analysis was found to be 7.4%. Taking the lifetime of ^{9}Li into account, only 0.04% of the decays are expected not to be excluded by the applied 2 s veto after an ID muon.
For this analysis, only the OD can be used to identify muons since the neutrons being released in atmospheric neutrino NC interactions could be falsely identified as muons by the ID pulse shape based muon identification algorithm (IDF). The efficiency of the two OD muon identification methods when they are combined was found to be $\epsilon_{\text{OD}} \geq (99.38 \pm 0.03)\%$. This was estimated by testing the two identification methods with a sample of events identified as muons by the IDF similar to the procedure described in section 4.2.1. Thus, for $\sim 0.62\%$ of the muons that are

not tagged by the OD muon identification methods, the 2 s veto cannot be applied. Considering the branching ratio of 51% for the production of a neutron-unstable state, the expected number of ^{9}Li decays in the dataset used for the analysis of atmospheric neutrino NC interactions is 0.13 ± 0.01 events. Most of this contribution arises due to ^{9}Li produced by untagged muons.

7.4.6 Fast Neutrons

Fast neutrons are produced by muons in either the OD or the rock surrounding the detector. These neutrons feature a broad energy spectrum extending well into the GeV range. Since they are electromagnetically uncharged, fast neutrons may travel a huge distance before being absorbed and can potentially enter the scintillator without leaving a signal in the OD. Similarly to the neutrons originating from atmospheric neutrino NC reactions, fast neutrons can mimic an IBD signal. Due to the potentially high energies of the neutrons, a prompt signal may be faked by the recoil protons off which the neutrons scatter while a delayed signal is generated by the 2.2 MeV γ ray emitted after the neutron capture.
99.5% of fast neutrons produced in the OD can be vetoed by the 2 ms cut after OD muons [124]. To estimate the amount of fast neutrons that are generated in the OD and enter the analysis, the data within 5 ms after OD muons were analyzed applying the same coincidence conditions as for the search of atmospheric neutrino NC interactions. Zero events were found in the data and the background contribution from fast neutrons originating in the OD can be assumed to be negligible. However, fast neutrons produced in the rock around the detector obtain an average energy of 90 MeV and can, thus, eventually reach the scintillator [124]. To estimate the background arising from fast neutrons produced in the rock, a Monte Carlo simulation was performed.
First, the Monte Carlo simulation developed for the LENA experiment in [148] was utilized to simulate the energy and momentum spectra of neutrons produced by cosmic muons in the rock around Borexino. In a second step, fast neutrons were generated based on these spectra in layers of rock around and above Borexino and propagated into the detector using the official Borexino Monte Carlo simulation [165]. Modifications of this Monte Carlo code were implemented to enable the initialization of the rock layers and the generation of neutrons in this layer with the energy and momentum drawn from the predicted spectra. The separated simulation of the neutron generation was performed since the propagation of muons in rock is very time consuming and the simulation in two steps is more flexible.
As in [148], the neutron production yield was estimated assuming that all cosmic muons arrive with the same mean muon energy at the depth of the LNGS. Thus, 10^6 muons with an energy of 280 GeV [62] were propagated through 15 m of

limestone rock composed of pure $CaCO_3$ with a density of $\rho = 2.73\,\mathrm{g/cm^3}$. This density is slightly higher than the measured central value of the rock density at Gran Sasso of $\rho_{\mathrm{GS}} = (2.71 \pm 0.05)\,\mathrm{g/cm^3}$ [249] but within statistical uncertainties. Since a higher density in principle increases the neutron yield, this slight difference does not affect the result in a way leading to an underestimation of the background contribution caused by fast neutrons. Since the neutron yield also increases with the mean muon energy, the applied energy was conservatively set to the quoted value rather than to the slightly lower central value measured by MACRO of $\overline{E}_\mu = (270 \pm 3_{\mathrm{stat}} \pm 18_{\mathrm{syst}})\,\mathrm{GeV}$ [134].
Most of the neutrons are produced in hadronic or electromagnetic cascades [148]. Since these cascades need space to develop, only neutrons produced after the muon has been propagated for at least 3 m through the rock were considered for the calculation of the neutron yield as in [148]. Based on the simulation, the neutron production yield per unit path length was found to be

$$Y_{\mathrm{n}} = 4.8 \times 10^{-4}\,(\mu\mathrm{g/cm^2})^{-1}. \tag{7.24}$$

This value is slightly lower than the value calculated for the LENA experiment [148] due to the lower mean muon energy at the depth of the LNGS. The discrepancy between this value and the measured neutron yield in the Borexino scintillator of $Y_{\mathrm{n}} = (3.10 \pm 0.07_{\mathrm{stat}} \pm 0.08_{\mathrm{syst}}) \times 10^{-4}\,(\mu\mathrm{g/cm^2})^{-1}$ [137] arises since the neutron production yield per unit path length depends on the mean atomic weight of the material through which the muons propagate [135], which is higher for limestone rock than for pseudocumene.
Figure 7.2 shows the simulated normalized energy spectrum of fast neutrons produced in the rock around the Borexino detector. The spectrum is very broad ranging from keV to $\mathcal{O}(100\,\mathrm{GeV})$. However, it decreases quickly for energies above $\sim (1 - 10)\,\mathrm{MeV}$. The complex form of the decrease is caused by the variety of processes involved in the neutron production.
Approximately 45% of the neutrons were found to obtain kinetic energies below 10 MeV. Due to the quenching of the recoil protons that could potentially mimic a prompt signal after an interaction with a fast neutron in the scintillator target, this low-energetic part of the spectrum does not have to be considered as a potential background for the analysis of atmospheric neutrino NC reactions. Thus, the relevant neutron yield for this analysis is reduced to

$$Y_{\mathrm{n}}(E_{\mathrm{n}} > 10\,\mathrm{MeV}) = 2.7 \times 10^{-4}\,(\mu\mathrm{g/cm^2})^{-1}. \tag{7.25}$$

To simulate the fast neutron background for the analysis of atmospheric neutrino NC interactions, neutrons with energies and momenta as obtained from the LENA simulation were started in two layers of rock positioned beside the Borexino water tank and one layer of rock above the detector. This geometry reflects the location

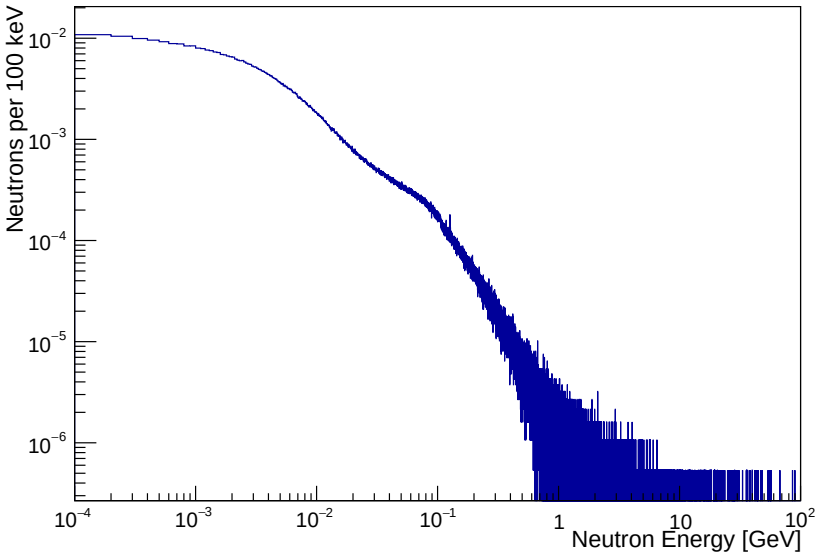

Figure 7.2: Simulated normalized energy spectrum of fast neutrons generated by cosmic muons in the rock around Borexino.

of the Borexino experiment in Hall C of the LNGS with the detector being situated in a tunnel with adjacent rock on two sides. The size of the rock layers was chosen such that the whole length and height of the water tank were covered at two sides. Thus, the layers were built with 18 m length and 18 m height at the sides of the detector and connected above by a $20 \times 20\,\mathrm{m}^2$ rock cuboid.
The attenuation length for neutrons traversing through a material of the density ρ in $\mathrm{g/cm^3}$ reaches a plateau of $\sim (120/\rho)\,\mathrm{g/cm^2}$ for neutron energies above $\sim 200\,\mathrm{MeV}$ [276]. This implies a maximum attenuation length for neutrons in the rock surrounding the Borexino detector of $L \lesssim 45\,\mathrm{cm}$. For neutrons with an energy of 10 MeV, the attenuation length in the rock is $L \sim 10\,\mathrm{cm}$. Thus, the thickness of the rock layers was chosen as 1 m. Since any contributions from neutrons produced in the rock farther away are strongly suppressed, the finite thickness of the rock layers is expected to introduce only a very small uncertainty to the estimation.
Most of the neutrons are produced together with further particles in hadronic or electromagnetic showers. Due to this, it is in principle possible to detect a part of these showers in the OD and veto the correlated neutrons if the shower is produced in the rock close to the detector. However, the conservative assumption was made that these showers are never detected.
The rock layers positioned at the sides of the detector and the cuboid above the detector were treated as two seperate neutron sources. The simulation of the fast

	Sides of detector	Above detector
Muon rate	$0.2\,\mathrm{s}^{-1}$	$0.15\,\mathrm{s}^{-1}$
Mean track length	1.90 m	1.56 m
Produced neutrons ($E \geq 10\,\mathrm{MeV}$)	$6.0 \cdot 10^6$	$3.7 \cdot 10^6$
Muon fraction passing through OD	40%	46%
Neutron tracks towards IV	2.8%	5.5%
Resulting neutron number	$1.0 \cdot 10^5$	$1.1 \cdot 10^5$

Table 7.2: Estimation of the neutrons produced in the rock surrounding the Borexino detector as a potential background for the analysis of atmospheric neutrino NC interactions. For details see text.

neutron background was run individually for each source and the contributions were summed afterwards to increase the flexibility of the simulation. To estimate the number of neutrons that constitute a potential background for the analysis of atmospheric neutrino NC interactions in each source, several calculations and approximations were made. The steps are summarized in table 7.2 and detailed in the following. First, the estimation of the number of neutrons produced in the rock layers at the sides of the detector is described.
Due to the shape of the rock overburden of the LNGS, a significant amount of cosmic muons arrives from non-vertical directions as can be seen in figure 5.2. Thus, the assumption that all muons arrive from vertically above and pass through the entire height of the rock layers of 18 m at the sides of the detector is not reasonable. The rate of muons crossing the rock layers at the sides of the detector as well as their mean path length in the layers were derived using a toy Monte Carlo simulation. Muons were generated randomly in a plane 50 m above the detector with the zenith angle drawn from the measured zenith angle distribution of cosmic muons arriving at Borexino. The dimensions of the plane were increased to the point at which the resulting muon flux through the rock layers was found to converge. With the flux of cosmic muons at the LNGS being $R_\mu = (3.432 \pm 0.001) \times 10^{-4}\,\mathrm{m}^{-2}\mathrm{s}^{-1}$ as analyzed in section 4.2.3, this plane is crossed by $\sim 1.7 \times 10^4$ muons per second. By estimating the fraction of the generated muons that also cross the rock layers beside the detector, it was found that each of the two rock layers is crossed by ~ 0.1 muons per second with a mean muon path length of $\sim 1.90\,\mathrm{m}$. Thus, for the livetime of the present analysis of $2,455\,\mathrm{d}$, $\sim 6.0 \cdot 10^6$ neutrons with kinetic energies above 10 MeV are generated in the two rock layers together.
However, $\sim 40\%$ of the muon tracks through the rock layers were found to also pass through the detector. Since almost all of these muons can be expected to be identified by the highly efficient muon veto, the potentially generated neutrons can be associated to the parent muon and vetoed. This reduces the rate of muons potentially producing fast neutrons as a background for the analysis of atmospheric

neutrino NC interactions to $\sim 6.0 \cdot 10^{-2}$ muons per second.
To save computation time, only neutrons with a track pointing towards the IV were simulated. The contribution of fast neutrons with tracks initially directed outwards is negligibly small [148] and neutrons not crossing the IV do not generate a visible energy output in the relevant energy region due to the additional quenching in the buffer region. Neutrons initially not pointing towards the IV that strongly change their direction due to scattering interactions are expected to lose a high fraction of their energy in these interactions, such that the eventual energy deposition in the IV is below the applied energy threshold. Neutrons that only slightly alter their direction for which the energy loss is expected to be small are still included in this estimation since in the analysis of atmospheric neutrino NC interactions, only events occurring inside the IV and with a minimum distance of 25 cm to the vessel border are considered. Nevertheless, small contributions of neutrons with different tracks cannot be completely excluded and this approximation introduces a small uncertainty.
Based on a second toy Monte Carlo simulation in which starting positions of the neutrons were generated randomly in the two rock layers at the sides of the detector and a direction was assigned from the predicted momentum distribution, the fraction of neutron tracks pointing towards the IV was found to be $\sim 2.8\%$. Taking this into account, the number of fast neutrons generated in the two rock layers at the sides of the detector that could potentially cause a background for the analysis of atmospheric neutrino NC interactions reduces to $\sim 1.0 \cdot 10^5$.
The number of fast neutrons generated above the detector that potentially constitute a background for atmospheric neutrino NC interactions was estimated in a similar way. The rate of muons crossing the cuboid was derived using a toy Monte Carlo simulation with muons started 50 m above the detector and the robustness of the result was tested by varying the dimensions of the plane in which the muons were generated. Based on this simulation, the volume is crossed by ~ 0.15 muons per second with a mean path length of ~ 1.56 m. Thus, $3.7 \cdot 10^6$ neutrons with kinetic energies above 10 MeV are produced in the rock cuboid above the detector in the time corresponding to the exposure of the present analysis.
Of the muons traversing the rock above the detector, $\sim 46\%$ were found to also enter the detector. Thus, fast neutrons eventually created by these muons can be vetoed and do not constitute a potential background for the analysis of atmospheric neutrino NC interactions. The fraction of neutrons directed towards the IV was found to be $\sim 5.5\%$. Performing the same calculations as above, $\sim 1.1 \cdot 10^5$ fast neutrons that may potentially cause a background for the present analysis of atmospheric neutrino NC interactions are expected to be created in the rock cuboid above the detector.
To estimate the amount of fast neutrons that generate a signal passing the cuts

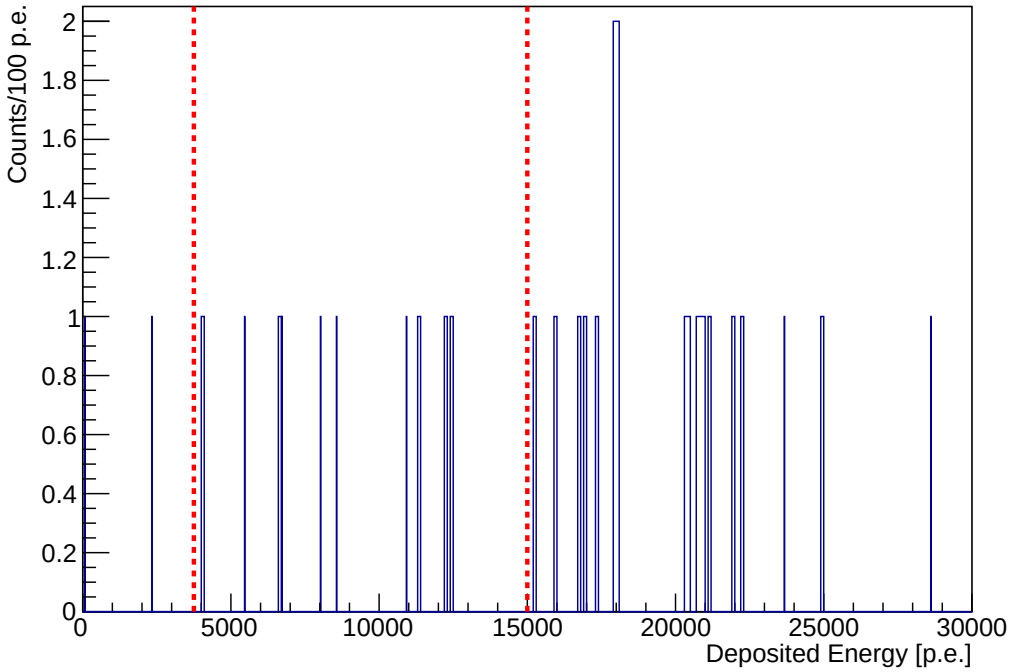

Figure 7.3: Energy distribution of fast neutrons as a background for the analysis of atmospheric neutrino NC interactions. The red dotted lines indicate the energy region in which prompt candidates of atmospheric neutrino NC interactions were considered. In total, a background contribution of 2.0 ± 1.5 fast neutron events is expected.

of the analysis for atmospheric neutrino NC interactions, the full Borexino Monte Carlo simulation chain including the simulation of the electronics and the data processing was executed. For both fast neutron production environments at the sides and above the detector, five times the estimated number of relevant neutrons produced in the time corresponding to the present analysis was simulated.
Figure 7.3 shows the energy distribution of the prompt candidates of the simulated fast neutrons for which a delayed coincidence was observed. For prompt and delayed candidates, all cuts as in the analysis of atmospheric neutrino NC interactions were applied with the exception of the prompt energy cut. The red dotted lines indicate the energy window from $3,750$ p.e. to $15,000$ p.e. in which atmospheric neutrino NC interactions were searched for.
Most of the fast neutron coincidences were found to generate high prompt energy depositions and the background contribution from fast neutrons is significantly reduced by the applied upper energy threshold. Only two events are cut by the lower

energy threshold. In total, ten events passing the cuts implied on candidates for atmospheric neutrino NC interactions with prompt energies in the chosen energy window were found. Of these events, five originated in each production environment. Thus, a background contribution of $2.0^{+0.9}_{-0.6}$ events caused by fast neutrons is expected to be present in the dataset.
However, several approximations were made in the simulation that should be considered in the uncertainties of the evaluation, even though only small effects are expected. Namely, the exclusion of neutrons with tracks not pointing towards the IV and the finite width of the rock layers might result in a slight underestimation of the fast neutron background. This effect is counteracted by the assumption that no shower product accompanying the fast neutron production may be detected in the OD, which would reduce the expected background from fast neutrons produced in the rock. Taking these effects into account, it is appropriate to enlarge the error margins and consider the expected background from fast neutrons produced in the rock around the detector as 2.0 ± 1.5 events.

7.4.7 Untagged Muons

For the present analysis, only the OD could be used to identify muons since the neutrons being released in atmospheric neutrino NC reactions could be falsely identified as muons by the ID pulse shape based muon identification algorithm. However, untagged neutron-producing muons can cause a background for the atmospheric neutrino NC interaction analysis with the muon itself generating a prompt and usually high-energetic signal followed by the delayed 2.2 MeV γ ray after the neutron capture. The efficiency of the two OD muon identification methods combined was found to be $\epsilon_{\mathrm{OD}} \geq (99.38 \pm 0.03)\%$ by testing the two identification methods with a sample of muons identified by the IDF as described in section 4.2.1. Further, the rate of muons that produce neutrons eventually captured in the IV of the Borexino detector has been measured as $(67.5 \pm 0.4_{\mathrm{stat}} \pm 0.1_{\mathrm{syst}})\,\mathrm{d}^{-1}$ [137]. Following these considerations, $1,027 \pm 8$ untagged neutron-producing muons generating neutron captures in the IV are estimated to be present in the dataset.
Only a small number of these muons is expected to actually cause a background for the analysis of atmospheric neutrino NC interactions. Due to the huge energy deposition of 2 MeV/cm, the vast majority of muons that deposit a visible energy in the applied energy window from 3,750 p.e. to 15,000 p.e. only crosses the buffer without entering the scintillator. Unfortunately, the position reconstruction algorithm that is bound to search for point-like events was found to locate a huge fraction of these buffer muons inside the IV due to the immense light output. Nevertheless, the neutrons produced along the track of the muon will mostly be captured in the buffer and the emitted capture γ rays will not satisfy the energy and spatial conditions for delayed candidate events. Further, even if the neutrons

enter the IV, the spatial correlation between the neutron capture point and the wrongly assigned point-like interaction place of the muon will be less clear than for real IBD or atmospheric neutrino NC interactions. Hence, many of these event pairs are expected to be rejected by the spatial correlation condition.
To estimate the background arising from untagged muons for the analysis of atmospheric neutrino NC interactions, the cuts described in section 7.3 were applied to a sample containing muons and the following neutron triggers. In the neutron trigger, all clusters were considered as possible delayed candidates to account for the longer gate length of this trigger compared to normal ID triggers. In the same time period that is used for the atmospheric neutrino NC interaction analysis, 47 event pairs passing all cuts were found in the muon sample. Taking the small inefficiency of the OD into account, an expected contribution from untagged and neutron-producing muons in the dataset of 0.29 ± 0.05 results.
As shown in [137], most of the neutron-producing muons generate showers containing more than one neutron. This allows to reject several of the background events originating from untagged muons by requiring that any prompt event is followed by exactly one delayed event and neglecting events for which two or more delayed candidates are found within the applied time window. Due to inaccuracies of the time determination of events, multiple neutron captures may also manifest as events within the neutron capture energy window preceding prompt candidate events. Thus, also such constellations may be used to identify untagged neutron-producing muons.
Of the 47 candidate events identified in the muon sample, 22 were found to be followed by more than one or preceded by one event in the neutron capture γ ray energy window. Thus, the background arising from untagged muons could be reduced if the requirement that any prompt event is followed by exactly one delayed event is imposed. However, this identification is not unambiguous since also in atmospheric neutrino NC interactions, more than one neutron may be liberated.
Table 7.3 summarizes the considered backgrounds and the estimated contributions. Based on the evaluations above, a total background contribution of 3.6 ± 1.8 events is expected in the dataset.

7.5 Data Analysis

After the application of the cuts described in section 7.3, twelve candidate events were observed in the dataset. Scaling the KamLAND expectation of 16.4 ± 4.7 events [260] to the Borexino dimensions and considering that the overall atmospheric neutrino flux is calculated to be a factor ~ 1.5 higher for neutrino energies above 100 MeV at the Gran Sasso region than at the Kamioka mine [269], 8.0 ± 2.3 atmospheric neutrino NC interactions are expected in the Borexino dataset. This

Source	Events
Random coincidences	0.52 ± 0.02
DSNB $\bar{\nu}_e$	0.21 ± 0.15
Atmospheric ν CC interactions	0.30 ± 0.07 & 0.03
Reactor $\bar{\nu}_e$	0.11 ± 0.01
Cosmogenic radio-isotopes	0.13 ± 0.01
Fast neutrons	2.0 ± 1.5
Untagged muons	0.29 ± 0.05
Signal atmospheric ν NC interactions	8.0 ± 2.3
Sum	11.6 ± 4.1
Observed	12

Table 7.3: Expected backgrounds and signal for the analysis of atmospheric neutrino NC interactions in Borexino. The observed number of events closely matches the expectation.

value is also supported by a Monte Carlo simulation of atmospheric neutrino interactions in Borexino performed independently from this thesis in which 7.8 atmospheric neutrino interactions have been estimated to pass the applied cuts for the exposure of the present analysis [277]. Considering the background contributions evaluated in the preceding section and summarized in table 7.3, a total of 11.6 ± 4.1 events is expected to pass the applied cuts. Thus, the observed number of twelve candidate events agrees very well with the prediction.
Table 7.4 lists the events that were found with the respective energies of the prompt and delayed candidates, their Gatti parameters, and the spatial and temporal separation of prompt and delayed candidate events. The subscript p denotes the prompt, the subscript d the delayed candidates. Additionally, the run and event numbers of the prompt candidates in the Borexino data acquisition system are listed.
As described in section 7.4.7, the background originating from untagged neutron-producing muons can in principle be reduced by requiring that a prompt candidate is not followed by more than one neutron capture γ ray candidate within the applied time window. However, also atmospheric neutrino NC or CC interactions can result in the generation of several neutrons, such that this criterion is not unambiguous. Regarding the candidate events listed in table 7.4, event number 5 is found to be followed by two neutron capture candidates.
Figure 7.4 shows the distribution of the deposited energy of the prompt candidates. The spectrum is found to be rather flat with a possible slight tendency towards higher energy depositions. Such a tendency might be expected since especially the fast neutron background was found to produce rather high-energetic prompt can-

#	Run	Event	$\mathbf{Charge_p}$ [p.e.]	$\mathbf{Gatti_p}$	$\mathbf{Charge_d}$ [p.e.]	$\mathbf{Gatti_d}$	Δt [ms]	ΔR [m]
1	9962	114396	14435	0.03	1104	-0.03	0.287	0.66
2	13853	101676	13680	0.02	1142	-0.03	0.244	0.32
3	15543	5684	3816	-0.04	1136	-0.03	0.301	0.24
4	16059	273434	8181	0.14	1163	-0.03	0.043	0.56
5	16435	218599	4349	0.37	990	-0.01	0.546	1.20
6	18559	46416	7794	-0.005	1069	-0.03	0.640	0.49
7	19044	480873	14587	0.04	1042	-0.03	0.233	0.75
8	21936	657246	13101	0.01	1131	-0.04	0.240	0.20
9	23587	368859	4061	0.10	1177	-0.04	0.150	0.41
10	25065	401176	13730	0.03	1147	-0.03	0.548	0.24
11	25524	117362	9941	0.06	1232	-0.03	0.126	0.13
12	29440	102410	11381	0.05	170	-0.04	0.161	0.26

Table 7.4: Atmospheric neutrino NC interaction candidate events. The subscript p denotes the prompt, the subscript d the corresponding delayed event.

didates. However, the low statistics do not allow to infer any clear derivations. Figure 7.5 shows on the left side the spatial distance of the prompt and delayed candidate events and on the right side their temporal separation. Due to the very limited statistics, the spectra only allow to retrieve tendencies. The spectra do not show any clear deviations from the expected behavior of atmospheric neutrino NC interactions with the main background contribution from fast neutrons.
A suppression or identification of atmospheric neutrino NC interactions is mandatory to enable an observation of the DSNB in future liquid scintillator experiments. As a possible way, simulations for the LENA project have shown that the technique of pulse shape discrimination might constitute a powerful tool to distinguish between atmospheric neutrino NC interactions and actual IBD events caused by the DSNB [148]. In the following section, pulse shape discrimination will be applied to the observed candidate events to prove the observation of atmospheric neutrino NC interactions in the Borexino detector and show the applicability of this technique in future liquid scintillator based experiments aiming for the first observation of the DSNB.

7.6 Pulse Shape Discrimination

A sophisticated technique to distinguish energy depositions of different particles is the Gatti method [117] that is commonly used to discriminate energy depositions of α particles from energy depositions of β particles. First, weighting factors P_i are

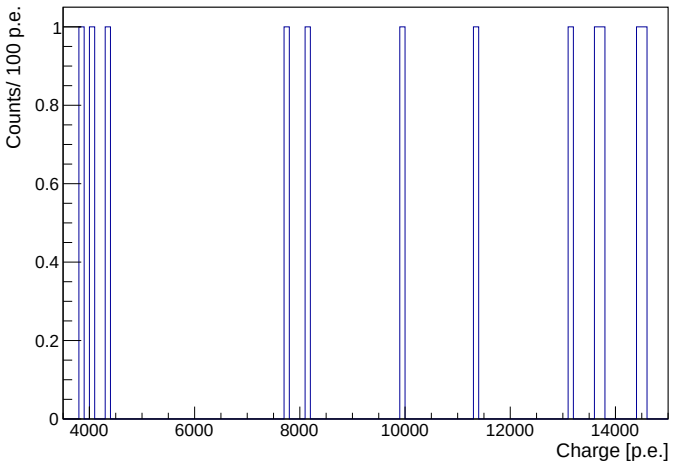

Figure 7.4: Energy spectrum of prompt candidates for atmospheric neutrino NC interactions. The Borexino charge to energy conversion is 500 p.e./MeV [9].

calculated based on average pulses of α and β interactions as

$$P_{\mathrm{i}} = \frac{\alpha_{\mathrm{i}} - \beta_{\mathrm{i}}}{\alpha_{\mathrm{i}} + \beta_{\mathrm{i}}}, \tag{7.26}$$

where α_{i} and β_{i} denote the normalized number of photons arriving in bin i of the respective average pulse. For an actually acquired event, the Gatti parameter is calculated as

$$g_{\alpha,\beta} = \sum_{\mathrm{i}} = P_{\mathrm{i}} S_{\mathrm{i}} \tag{7.27}$$

with S_{i} being the number of photons registered in bin i of the collected event pulse. In Borexino, the Gatti parameter is tuned for the discrimination of interactions from α and β particles. As detailed in section 2.1.2, energy depositions of heavier ionizing particles like α particles at usual energies result in a stronger population of excited triplet states of the scintillator solvent. These triplet states decay significantly slower into the ground state than the excited singlet states that are favorably populated for β like energy depositions. Thus, a slower decay of the registered pulses for energy depositions of heavier particles and a stronger population of the tail of the pulse results. For atmospheric neutrino NC interactions, the prompt signal is generated by recoiling protons. Since these recoil protons similarly to α particles produce higher ionization densities compared to β like events, the Gatti parameter is expected to be an applicable tool to distinguish atmospheric neutrino NC interactions from real IBD events with a positron generating the prompt signal.

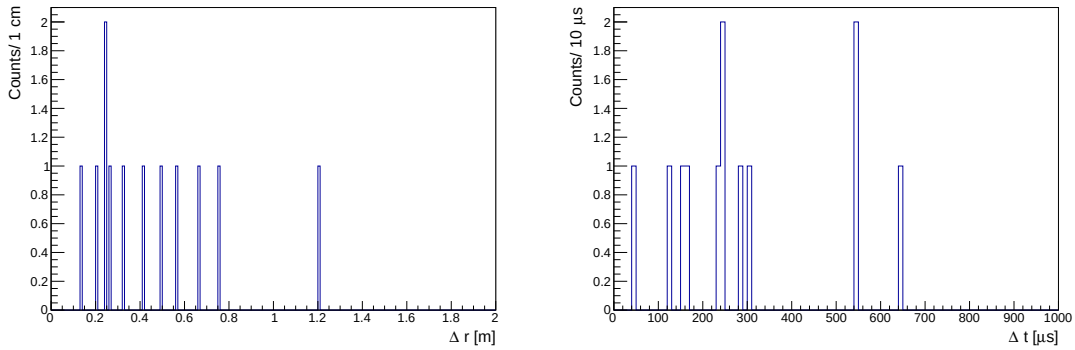

Figure 7.5: Spatial (*left*) and temporal (*right*) separation of prompt and delayed candidate events for atmospheric neutrino NC interactions.

Figure 7.6 shows the distribution of the Gatti parameter for the prompt candidates listed in table 7.4 in blue together with the expected distributions for real IBD prompt events in brown, neutrons as liberated in atmospheric neutrino NC interactions in red, and atmospheric ν_μ CC interactions in green. The expected distributions were generated using the Borexino Monte Carlo simulation [165]. Equal energy and radial cuts as in the data analysis were applied on the simulated events and only events producing one cluster were considered. To generate the distribution for ν_μ CC interactions, low-energetic muons were simulated and their energy loss as well as the decay into an electron was recorded.
The expected distributions of the Gatti parameter clearly differ and show that a huge amount of the observed delayed coincidences in the data is not caused by real IBD events with a positron generating the prompt signal. Positrons are centered around a negative Gatti parameter value around -0.003. High-energetic neutrons feature significantly larger Gatti parameter values due to the differing ionization densities generated in the energy deposition. The distribution of the Gatti parameter for neutrons is further found to be broader than for positrons. This is expected to be caused by the variety of modes through which the neutron may thermalize and generate the prompt signal. Thus, it is expected that, e.g., the reconstructed pulse for an event in which the neutron thermalizes via numerous scattering interactions off several protons that receive sufficient energy to create a visible signal in the detector differs from the reconstructed pulse if the neutron loses most of its energy in a single scattering interaction. However, the heavier ionizing protons preserve the property of creating higher ionization densities and predominantly populating the slower decaying excited triplet states of the scintillator solvent.
Atmospheric ν_μ CC like interactions are found to generate a very broad range of Gatti parameter values. This is expected since the actual time of the muon decay strongly affects the light emission and, thus, the reconstructed pulse. For a

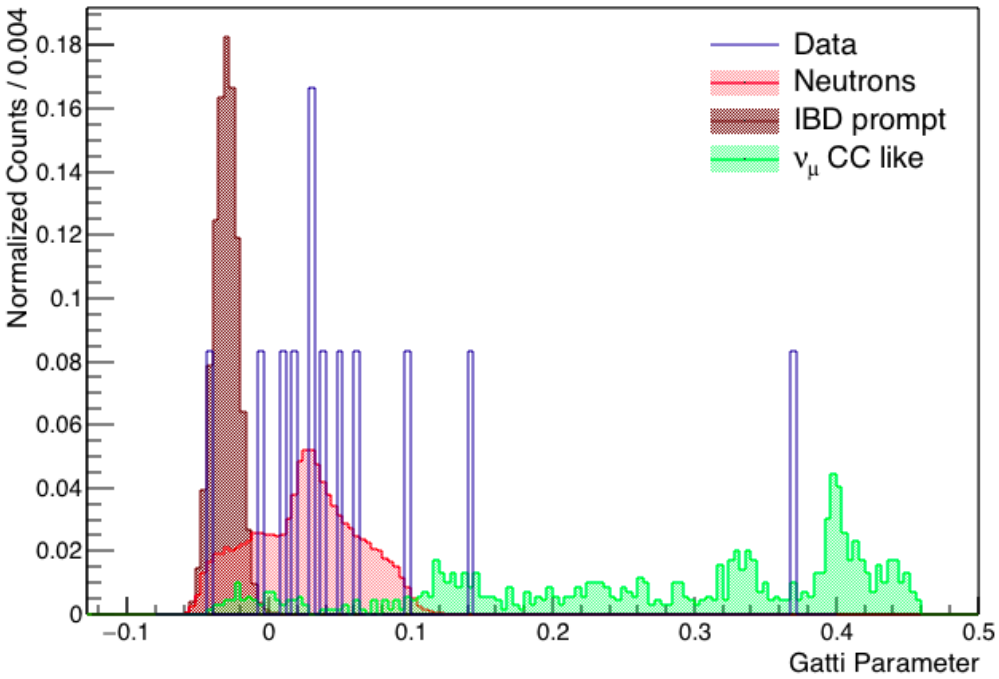

Figure 7.6: Distribution of the Gatti parameter for atmospheric neutrino NC candidate events depicted in blue. The expected distributions of real IBD prompt signals, high-energetic neutrons as liberated in atmospheric neutrino NC interactions, and atmospheric ν_μ CC interactions based on the Borexino Monte Carlo simulation are shown in brown, red, and green, respectively.

later decay, the tail of the pulse is stronger populated and a higher value of the Gatti parameter results. Due to this, the distribution of the Gatti parameter for atmospheric ν_μ CC like interactions extends to even very high Gatti parameter values significantly above the endpoint of the Gatti parameter spectrum for high-energetic neutrons. In case that also events with several clusters of PMT hits are considered, the Gatti parameter distribution of atmospheric ν_μ CC like interactions shows an additional peak at low Gatti values. For these events, the pulse of the first cluster is generated solely by the energy deposition of the low-energetic muon. The effect of the population of the tail of the pulse due to the electron produced in the muon decay does not appear since its energy deposition is registered in a separate cluster. However, as has been mentioned, these events are discarded in this analysis.

Of the twelve prompt candidate events, ten events can be excluded to be real IBD coincidences based on the pulse shape discrimination. These events are re-

constructed at Gatti parameter values larger than the endpoint of the distribution for positrons at corresponding visible energies. Based on the simulated probability density function of the Gatti parameter for real IBD events, the probabilities to obtain a value of the Gatti parameter as high or higher than the observed ones are 0.003 and 0.86 for the remaining two candidates, respectively. Thus, the observation of non-IBD delayed coincidences in the energy region from 7.5 MeV to 30 MeV is clearly confirmed by the pulse shape discrimination.
The observed number of these coincidences with high Gatti parameter values of the prompt candidate accurately matches the expectations for NC interactions of atmospheric neutrinos with a background contribution from fast neutrons. Further, even though the statistics are limited, the Gatti parameter distribution of the observed candidate events closely resembles the predicted distribution for high-energetic neutrons as liberated in NC interactions of atmospheric neutrinos. With this accordance of the distributions and the agreement of the observed and expected rates, the observation of atmospheric neutrino NC interactions in the Borexino detector becomes evident.
The very high value of the Gatti parameter of event number 5 as listed in table 7.4 allows to identify this event as likely being caused by an atmospheric ν_μ CC interaction and underlines the observation of these interactions in the Borexino detector. Within this analysis, pulse shape discrimination techniques could be used for the first time at comparably high visible energies to distinguish between various particle interactions in liquid scintillator detectors.
Conclusively, the data clearly shows that the pulses of atmospheric neutrino NC interactions differ from pulses of real IBD interactions at similar energies. Pulse shape discrimination techniques, thus, constitute an applicable tool to suppress the background from atmospheric neutrino NC interactions when aiming for the detection of the DSNB using liquid scintillator based experiments. While the Borexino liquid scintillator mixture offers an excellent pulse shape discrimination performance, the detector does not provide the necessary target mass to collect a significant number of DSNB neutrino interactions. However, this first identification of atmospheric neutrino NC interactions based on their pulse shape in a running liquid scintillator experiment marks a proof of principle corroborating that sufficiently large future liquid scintillator experiments might be able to achieve the required background reduction to detect the DSNB.

7.7 Implications for Future Liquid Scintillator Experiments

As can be seen in figure 2.5, a detection of the DSNB in future liquid scintillator experiments vitally depends on the suppression of the background originating from atmospheric neutrino NC interactions. With the identification of these interactions in the Borexino detector based on pulse shape discrimination, this technique is shown to be a principally applicable tool to enhance the prospects of a future DSNB detection. Besides the reconstructed pulses, also the spatial separation between the prompt and delayed event is expected to differ for IBD interactions of DSNB neutrinos and atmospheric neutrino NC interactions [278]. While for DSNB interactions, the positron receives almost the entire kinetic energy and is stopped after relatively short distances, the high-energetic neutrons generating the prompt and delayed signal in case of atmospheric neutrino NC interactions may potentially travel large distances before being captured. Thus, this observable might offer a further possibility to suppress a part of this background, even though small kinetic energies of the neutrons must also be considered at the relatively high DSNB neutrino energies [279].
Figure 7.7 shows in brown the normalized distribution of the spatial separation between the prompt and delayed events of simulated DSNB neutrino IBD interactions, in red the normalized distribution of simulated high-energetic neutrons as liberated in atmospheric neutrino NC interactions, and in blue the normalized distribution of the candidate events observed in the Borexino data as listed in table 7.4 on a logarithmic scale. While both simulated distributions peak at similar distances, the distribution for high-energetic neutrons is found to decrease slower towards larger spatial separations and to extend to higher separations. However, the low statistics of the acquired candidate events in the Borexino data make it difficult to clearly prove this effect. This is especially the case since the highest separation found in the data is evidently neither caused by atmospheric neutrino NC interactions nor by a real IBD interaction due to the high Gatti parameter value of 0.37 belonging to the specific candidate. As can be seen in figure 7.6, such high values of the Gatti parameter can be excluded to be caused by any of the mentioned interactions. Thus, this event is not supposed to follow any of the two distributions for atmospheric neutrino NC or DSNB neutrino IBD interactions and must be discarded when estimating the agreement of the data with the two models. To do this, a likelihood analysis was performed and the test statistic

$$L = \prod_{\mathrm{i}} f(x|\lambda) \tag{7.28}$$

was built. Here, $f(x|\lambda)$ is the Poissonian probability to find x events in bin i given an expected mean value λ. The expected mean value λ is given by the product of

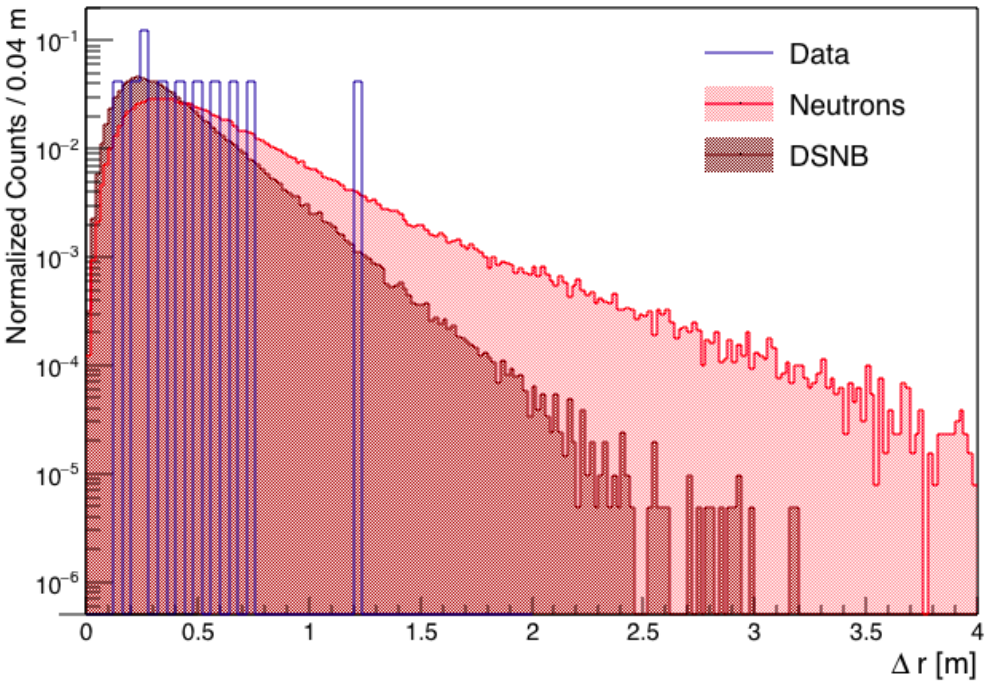

Figure 7.7: Spatial separation of the prompt and delayed candidates for atmospheric neutrino NC interactions shown in blue. The expected distribution for real IBD coincidences at DSNB energies is depicted in brown, the distribution of high-energetic neutrons in red.

the respective probability density function (PDF) evaluated in bin i and the total number of observed candidate events in the dataset. The PDFs are given by the normalized spatial separation distributions of the prompt and delayed events for the considered interaction types. The product considers all bins of the PDF. Then, the log-likelihood function is calculated as

$$\mathcal{L} = -2\ln(L). \tag{7.29}$$

Due to the logarithm, a good agreement between a dataset and the tested model is indicated by a small value of the log-likelihood function. To estimate the agreement of the data with the model for atmospheric neutrino NC interactions and the model for DSNB neutrino IBD interactions, the value of the respective log-likelihood function obtained for the candidate events listed in table 7.4 excluding event number 5 due to its high Gatti parameter was calculated. The result was then compared to 10^4 data samples of similar size that were randomly drawn from the applying PDF. The P-value that quantifies the agreement of the observed

data with the two models may be computed as the fraction of randomly generated datasets resulting in a value of the log-likelihood function as high as or higher than the value obtained for the data. Thus, P-values of 0.70 and 0.97 result for the hypothesis of the data following the PDF for DSNB neutrino IBD coincidences and for the hypothesis of the data following the PDF for high-energetic neutrons, respectively. Even though the P-value for the second hypothesis is larger, the observed candidate events are fully compatible with both distributions and no clear distinction between the two hypotheses is possible. Nevertheless, the agreement of the data to the Monte Carlo estimation for high-energetic neutrons as liberated in atmospheric neutrino NC interactions still indicates that also this observable might be used to separate signal and background contributions in future experiments. However, the distinction of the two event classes via the spatial separation of prompt and delayed event is less obvious and powerful than a distinction via the Gatti parameter since the majority of events is expected to be reconstructed around the peaks of the distributions that only differ slightly.
Besides these two observables, DSNB neutrino IBD and atmospheric neutrino NC interactions feature a different shape of the respective energy spectra as can be seen in figure 2.5. Thus, a multivariate fit of the data including the deposited energy of the observed events, a pulse shape discrimination parameter, and the spatial separation between the prompt and the delayed candidates might be a promising approach in future liquid scintillator based experiments aiming for the first detection of the DSNB.
To estimate the prospects of such an approach, a very basic Monte Carlo driven study was performed. In this estimation, only the DSNB signal and the background from atmospheric neutrino NC interactions were considered while the other backgrounds such as reactor $\overline{\nu}_{\mathrm{e}}$, cosmogenic radio-isotopes, untagged muons, fast neutrons, and atmospheric neutrino CC interactions were neglected. Thus, these background contributions were assumed to be controllable by low and high energy cuts and the definition of a fiducial volume to reject fast neutrons.
The DSNB was simulated as a redshift corrected Maxwell-Boltzmann distribution with a mean neutrino energy of 12 MeV as described by equation 7.16. Small amounts of kinetic energy were also assigned to the neutrons as predicted in [279]. Atmospheric neutrino NC interactions were approximated by uniformly distributed high-energetic neutrons. In principle, also a specific simulation of atmospheric neutrino NC interactions is possible in the Borexino Monte Carlo framework. However, since the detector specifics of the respective future experiment will strongly influence its actual sensitivity and since the flux and the energy distribution of atmospheric neutrinos depend on the geographical location of the experimental site, a basic and simplified description of this component without the claim of completeness seems preferable for the present evaluations.

For the JUNO experiment, 600 atmospheric neutrino NC interactions and 13 to 39 DSNB neutrino IBD interactions are expected in ten years for a visible neutrino energy between 11 MeV and 30 MeV and a fiducial volume of 17 kt [68]. The expected number of DSNB events mainly depends on the mean SN $\overline{\nu}_e$ energy and the rate has been calculated for mean energies in the range of 12 MeV to 21 MeV. Exemplarily, these numbers were considered to probe the potential of the proposed multivariate fit assuming the least optimistic scenario of only 13 DSNB events.
To estimate the detection potential, 3,000 possible signal and background realizations were generated using a toy Monte Carlo simulation. In this simulation, the signal and background distributions of the charge, the Gatti parameter of the prompt candidate, and the spatial distance between prompt and delayed event as obtained from the Borexino Monte Carlo simulation were considered. Poissonian fluctuations of the inserted signal and background components were enabled. To reproduce the detection energy window considered for JUNO, events producing a charge signal between 5,500 p.e. and 15,000 p.e. were included with the Borexino charge to energy conversion of $\sim$ 500 p.e./MeV [9]. Each of the realizations was fitted accordingly to the PDFs of the three included variables using the m-stats tool [280]. The fit results for signal and background components were stored.
Figure 7.8 shows the result of the fit for one Monte Carlo realization projected to the distribution of the charge on the left, to the distribution of the Gatti parameter in the middle, and to the distribution of the spatial separation between prompt and delayed events on the right. For a better illustration of the fit and the PDFs, the expected signal and background rates for ten years of JUNO data were scaled by a factor 1,000 in the presented realization. The black dots show the generated data sample and the green line depicts the fit result as the sum of the contributions from atmospheric neutrino NC and DSNB neutrino IBD interactions. For this specific Monte Carlo realization, the fit returns a DSNB signal of 12.8 ± 0.1 counts and a background due to atmospheric neutrino NC interactions of 600.3 ± 0.8 counts in ten years.
The violet lines represent the distributions of the DSNB events for the respective parameter projections. A distinct shoulder in the fit projected on the Gatti parameter at low values may be observed caused by the DSNB signal, where the red line representing the distribution of atmospheric neutrino NC interactions may be discerned. The other two parameters are much stronger dominated by the background distribution since the separation in these parameters is less pronounced. Thus, the distribution of the atmospheric neutrino NC interactions is covered by the fit result and the generated data points represented by the green line and the black dots, respectively, for these parameters. Nevertheless, the fit was found to strongly benefit from the inclusion of the parameters. Especially the steeper slope of the charge distribution of DSNB events improves the accuracy of the fit.

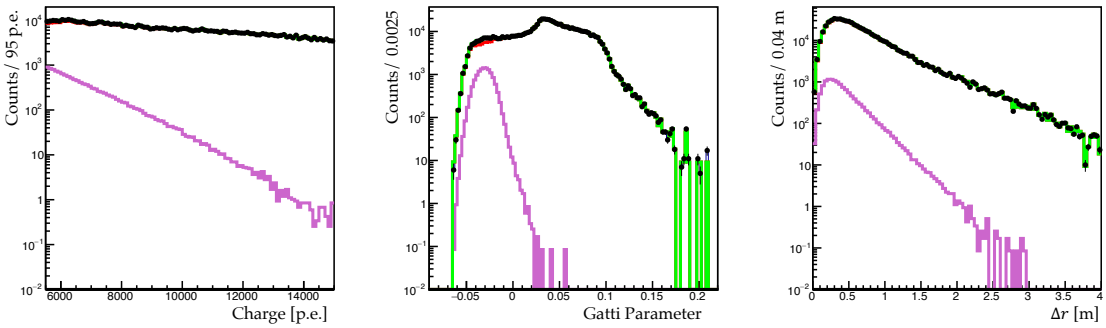

Figure 7.8: Multivariate fit of the DSNB signal and atmospheric neutrino NC interaction background for one Monte Carlo realization of the data. For a better illustration, the expected ten year rates in JUNO were scaled by a factor $1,000$ in the presented realization. On the *left*, the projection on the charge variable, in the *middle*, the projection on the Gatti parameter, and on the *right*, the projection on the spatial separation of prompt and delayed candidates are shown. The black dots represent the generated data. The violet distributions show the contribution of the DSNB signal, the green line the fit result as the sum of the two contributions. The red line representing the contribution of the atmospheric neutrino NC interactions may be discerned in the projection on the Gatti parameter at low values where a shoulder is generated by the DSNB events. For the other projections, the fit is strongly dominated by the atmospheric neutrino NC interactions, such that the fit result and the data points cover the distribution of the atmospheric neutrino NC interactions. For this specific realization, the fit returns a DSNB signal of 12.8 ± 0.1 counts and a background due to atmospheric neutrino NC interactions of 600.3 ± 0.8 counts in ten years.

Also the inclusion of the spatial distance between prompt and delayed events adds some discrimination capabilities even though only a few events are generated at very high Δr that allow a clear assignment to atmospheric neutrino NC interactions in the fit.
Figure 7.9 shows the distribution of the best fit values of the atmospheric neutrino NC interaction background component on the left side and of the best fit values of the DSNB signal on the right side for $3,000$ Monte Carlo realizations assuming the expected event numbers in ten years of JUNO data. The red lines depict Gaussian fits of the distributions. For the atmospheric neutrino NC background, the distribution of the fit results is found with a mean value of 600.0 events and a standard deviation of 24.7 events. For the DSNB signal, a mean value of the distribution of 12.9 events with a standard deviation of 4.3 events is observed. Thus, the expected sensitivity of a liquid scintillator based experiment with a size similar to the JUNO detector assuming this simplified model and following the

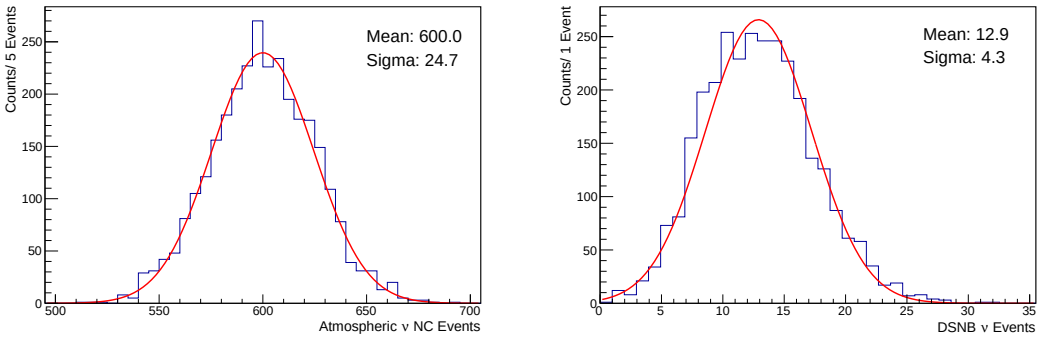

Figure 7.9: The distributions of the multivariate fit results for atmospheric neutrino NC (*left*) and DSNB neutrino IBD interactions (*right*) for 3,000 Monte Carlo realizations assuming the expected rates in ten years of JUNO data are shown in blue. The red lines depict Gaussian fits to the distributions.

approach of a multivariate fit to detect the DSNB is estimated as $\sim 3\sigma$ after ten years of data taking.
However, the actual performance of future experiments strongly and mainly depends on the technical details of the detector. The specific reconstructed signal and background distributions of the three parameters entering the fit determine the actual result. Thus, the estimations inferred here based on Borexino data and on the predictions of the Borexino Monte Carlo simulation may only indicate the potential of future experiments. Detailed and specific sensitivity studies must be performed considering all aspects of the respective detector to derive predictions for the detection prospects of distinct experiments. Especially the application of pulse shape discrimination techniques relies on a good performance of the scintillator as well as the timing of the PMTs.
For the specific case of the JUNO experiment, LAB is planned to be used as a scintillator solvent with the two solutes PPO and bis-MSB added at small concentrations as described in section 2.4. The pulse shape discrimination performance of this solvent for varying concentrations of the two solutes has been investigated in [111] using a neutron beam with energies between $\sim 4.7\,\text{MeV}$ and $\sim 11.2\,\text{MeV}$. It was found to be comparable to the performance of the Borexino scintillator mixture, which has also been probed. Thus, a similar pulse shape discrimination performance of the JUNO scintillator may be expected even though effects due to the higher energies relevant for a DSNB detection might have to be considered.
Further, the JUNO experiment might benefit from the expected unprecedentedly high light yield and energy resolution. This high light yield would in principle provide a higher number of photon hits in the hit time pulses used to determine pulse shape variables, which might improve their accuracy and the discriminability of

signal and background events. Further, a better reconstruction of the deposited energy and the interaction point may increase the differences in the energy and spatial separation distributions of signal and background contributions. However, to realize this high light yield, the aimed at very large attenuation length of $\geq 20\,\mathrm{m}$ must be achieved and also the expected PMT performance has to be accomplished. Besides the Gatti parameter, several other pulse shape variables might offer further and potentially better possibilities to discriminate between the DSNB signal and atmospheric neutrino NC interactions. As a common example, the so-called tail-to-total parameter is used for pulse shape discrimination between lighter and heavier ionizing particles. To compute this parameter, the number of hits occurring after a certain time threshold is compared to the total number of hits in a pulse. The discrimination capabilities rely on the higher population of the tail of a pulse for heavier ionizing particles due to the increased fraction of generated excited triplet states of the scintillator molecules that decay comparably slow. Further, neural networks could be utilized to generate a parameter that features a good distinction between signal and background events and that may be used as an input for the multivariate fit. In Borexino, a neural network in form of a Multi-Layer Perceptron (MLP) algorithm has been developed with the purpose of $\alpha - \beta$ discrimination based on thirteen input parameters and a very good distinction between the event classes could be obtained [160]. Thus, such a technique might also be a favorable choice for a future detection of the DSNB in liquid scintillator based experiments.

With the identification of atmospheric neutrino NC interactions in the Borexino detector based on their pulse shape, a proof of principle could be obtained showing that these techniques offer a possibility to disentangle this major background from the signal in future liquid scintillator based experiments aiming for the first detection of the DSNB. A multivariate fit including a pulse shape parameter, the spatial separation of prompt and delayed candidate events, and the deposited energy of the prompt candidates was found to provide a possibility to make use of the differences in these parameters and combine their discrimination capabilities. Nevertheless, major experimental challenges remain to be overcome to actually enable a detection of the DSNB in future experiments and the prospects vitally depend on the actual detector and scintillator performances.

Chapter 8

Conclusions and Outlook

In the last decades, liquid scintillator based experiments have strongly contributed to the understanding of the neutrino as a particle and of the sources in which neutrinos are generated. Due to the small cross sections for interactions of the only weakly interacting neutrinos, huge target masses of the detectors are required and neutrino experiments are usually built in underground laboratories to shield them against backgrounds from cosmic radiation.
Since May 2007, the Borexino experiment located at the Laboratori Nazionali del Gran Sasso (LNGS) has been accumulating data with the main purpose of the real-time spectroscopy of low-energetic solar neutrinos. Due to the unprecedentedly high radio-purity of the liquid scintillator target and an energy resolution of $\sim$ 5% at 1 MeV visible energy, a rich physics program could be accomplished. As milestones in the solar neutrino spectroscopy, precision measurements of all solar neutrino branches from the pp-chain except for the extremely faint hep neutrinos and the currently best upper limit on the flux of solar CNO neutrinos could be published.
In the first part of the present work, an analysis of the cosmic muon flux and its modulations using ten years of data from the Borexino experiment is presented. Additionally, the seasonal modulation of the cosmogenic neutron production rate was analyzed. These analyses are summarized and concluded in section 8.1. In the second part of the thesis, neutral current (NC) interactions of atmospheric neutrinos were identified in the Borexino data by performing a pulse shape analysis of the observed candidate events. This analysis is summarized and concluded in section 8.2. Closing the thesis, an outlook with respect to the investigated topics and the physics program of the Borexino experiment is given in section 8.3.

8.1 Modulations of the Cosmic Muon Flux and Muon-Induced Neutrons with Ten Years of Borexino Data

Despite the rock overburden of the LNGS of $\sim 3,800\,\mathrm{m\,we}$ for cosmic radiation arriving from straight above, a residual flux of cosmic muons still reaches the Borexino detector. Cosmic muons are produced mainly in the decays of kaons and pions in the upper atmosphere. Since low-energetic muons are absorbed in the rock coverage, a minimum energy is required for cosmic muons to reach the LNGS. These muons are bound to be produced by parent mesons that decay in flight without any interaction before the decay. As a consequence, the cosmic muon flux underground is affected by temperature and density variations of the upper atmosphere that alter the mean free path of the decaying mesons. Since these variations occur mainly on the scale of seasons, a seasonal modulation of the flux of cosmic muons at the LNGS is expected in leading order.
In the scope of this thesis, the cosmic muon flux and its modulations were explored using ten years of Borexino data acquired between May 16th, 2007 and May 15th, 2017. For Borexino, several methods to identify cosmic muons are provided. It was chosen to define muons as events flagged by the so-called Muon Clustering algorithm (MCR) due to its high muon identification efficiency and long operational time. The MCR is a software based muon identification method using data of the Outer Detector (OD) active Water Čerenkov muon veto. Further, the events were required to pass through the Inner Detector (ID) with a cross section for muon interactions of $146\,\mathrm{m}^2$. The resulting effective exposure of the dataset is $\sim 4.2 \times 10^5\,\mathrm{m}^2\mathrm{d}$, in which $\sim 1.2 \times 10^7$ muons were recorded.
The efficiency of this muon definition is determined by the MCR due to the low energy threshold of the ID. The MCR was found to work reliably and stably with some days of lower efficiency in the first years of data taking. A tiny but significant increase of the muon identification efficiency was registered after the installation of a new trigger setup in May 2016. This was found to be caused by a differing generation of service triggers resulting in a small and formerly unknown detector deadtime of $\sim 0.6\%$ in the old setup. To consider slight variations of the muon identification efficiency, the measured muon rate was corrected by the estimated efficiency on a daily basis. The background for the analysis of the cosmic muon flux at Borexino related to the CERN Neutrino to Gran Sasso (CNGS) beam was carefully removed on an event-by-event basis.
For the investigated dataset, a mean cosmic muon flux of $R_\mu = (3.432 \pm 0.001) \times 10^{-4}\,\mathrm{m}^{-2}\mathrm{s}^{-1}$ was measured and a modulation with a period of $T = (366.3 \pm 0.6)\,\mathrm{d}$, a relative amplitude of $\delta I_\mu = (1.36 \pm 0.04)\%$, and a phase of $t_0 = (174.8 \pm 3.8)\,\mathrm{d}$ was observed based on a sinusoidal fit of the data. The parameter values clearly reveal

the leading seasonal character of the muon flux modulation with a first maximum around June 25th, 2007.
To test the stability of the result, the data were analyzed in two year moving subsets and compared to a muon sample identified by the Muon Trigger Board (MTB), the OD hardware trigger. The results between the two muon samples were found to agree well in each subset. However, the mean cosmic muon flux was found to vary significantly for different time periods. This may be explained especially by a long-term modulation that was observed in the cosmic muon flux as summarized below.
To determine the phase assuming a pure seasonal modulation of the cosmic muon flux, the dataset was projected to one year and fitted with a sinusoidal with a fixed period of exactly one year. Consistent values to the results of the fit of the unprojected dataset were found for the mean flux and the modulation amplitude. The phase was altered to $t_0 = (181.7 \pm 0.4)\,\mathrm{d}$ due to the fixing of the period. This corresponds to a first maximum of the strictly seasonal modulation at July 1st, 2007. Deviations from the seasonal approximation were observed with secondary maxima of the flux in the first months of the year. These may be explained by a more turbulent stratosphere in winter and result in a less steep increase of the cosmic muon flux from winter to summer compared to the rapid decrease after its maximum.
The results of the analysis of the seasonal modulation of the cosmic muon flux measured by Borexino were compared to former measurements of LNGS based experiments and found to agree well. With the maximum of the muon flux occurring around the beginning of July, an explanation of the DAMA/LIBRA signal as caused by cosmic muons is confirmed to be very improbable.
To study the correlation of the cosmic muon flux at Borexino to fluctuations of the atmospheric temperature, the atmosphere was modeled as an isothermal meson-producing entity. An effective atmospheric temperature T_{eff} was calculated for each day based on temperature data provided by the European Center for Medium-range Weather Forecasts (ECMWF) [183] for the location of the LNGS. In the computation of T_{eff}, the measured temperature at a certain height was weighted with a factor accounting for the contribution of this atmospheric level to the production of high-energetic cosmic muons.
Based on a sinusoidal fit of the data, the effective atmospheric temperature was found to show a seasonal modulation at leading order with a period $\tau = (365.42 \pm 0.04)\,\mathrm{d}$, a phase $t_0 = (182.8 \pm 0.2)\,\mathrm{d}$, and a relative amplitude $\delta T_{\mathrm{eff}} = (1.54 \pm 0.01)\%$. The agreement of the values for period and phase with the modulation parameters observed in the cosmic muon flux indicates the correlation of the two observables. The higher modulation amplitude of the effective atmospheric temperature hints that not all mesons contributing to the muon flux at Borexino are affected by

temperature fluctuations of the upper atmosphere.
To quantify the correlation between the effective atmospheric temperature and the cosmic muon flux, the so-called effective temperature coefficient α_{T} is commonly used. For the ten year muon sample, $\alpha_{\mathrm{T}} = 0.90 \pm 0.02$ was measured. This result agrees with a former Borexino measurement and with measurements from other LNGS based experiments.
Since the decays of kaons and pions are affected differently by temperature fluctuations in the upper atmosphere, the strength of the correlation between the cosmic muon flux at Borexino and the atmospheric temperature depends on the atmospheric kaon to pion production ratio $r_{\mathrm{K}/\pi}$. Thus, the measured effective temperature coefficient α_{T} may be interpreted as an indirect measurement of $r_{\mathrm{K}/\pi}$ by comparing the measurement to the predicted α_{T} in dependence on the atmospheric kaon to pion production ratio.
Since the value of $r_{\mathrm{K}/\pi}$ enters in the calculation of the effective atmospheric temperature, the measured value of α_{T} contains a weak dependence on the atmospheric kaon to pion production ratio. To explore this dependence, the measurement of α_{T} was repeated using gradually increasing values of $r_{\mathrm{K}/\pi}$ in the calculation of T_{eff}.
To compute the expected atmospheric temperature coefficient, a Monte Carlo simulation was developed. Muons were randomly generated based on the muon energy and angular distributions at the surface and the direction dependent threshold energy was calculated. For gradually increasing values of $r_{\mathrm{K}/\pi}$, α_{T} was estimated for muons above the threshold energy.
By summing the χ^2 profiles of the predicted and measured values of α_{T}, the intersection region was found for $r_{\mathrm{K}/\pi} = 0.11^{+0.11}_{-0.07}$.
Besides the estimation of α_{T}, the Monte Carlo simulation was used to estimate $\langle E_{\mathrm{thr}} \cos\theta \rangle = (1.34 \pm 0.18)\,\mathrm{TeV}$ for the LNGS. This quantity mainly determines the expected value of α_{T} at a certain underground experimental site for a given kaon to pion production ratio. Further, it allows to compare measurements of experiments situated at different underground laboratories since the distinct shape of the rock coverage is included in its estimation.
Following a second approach, the atmospheric kaon to pion production ratio was determined based on an estimation of the ratio of muons produced in kaon decays to muons produced in pion decays. An atmospheric kaon to pion production ratio of $r_{\mathrm{K}/\pi} = 0.16 \pm 0.09$ was obtained.
Both measurements agree well with former measurements of the kaon to pion production ratio. Due to the relatively high rock coverage, Borexino contributes the data point at the highest center of mass energy for indirect as well as fixed target measurements.
Besides the seasonal modulation of the cosmic muon flux, several authors reported the observation of a subleading, long-term modulation and hints of a correlation

between this modulation and the solar activity. By fitting the acquired cosmic muon flux data with the sum of two sinusoidals, a long-term modulation with a period of $T^{\text{long}} = (3,010 \pm 299)\,\text{d}$ and a relative amplitude of $\delta I_{\mu}^{\text{long}} = (0.34 \pm 0.04)\%$ was observed. The measured phase of $t_0^{\text{long}} = (1,993 \pm 271)\,\text{d}$ corresponds to a maximum of this modulation in June 2012.
To evaluate the significance of this modulation, a Lomb-Scargle analysis of the dataset was performed. Based on this analysis, the observed long-term modulation was confirmed to be significantly present in the cosmic muon flux data measured with Borexino. Since a Lomb-Scargle analysis of the atmospheric temperature data revealed that no corresponding modulation exists for this observable, a different physical explanation than density variations of the upper atmosphere must be assumed to cause the observed long-term modulation of the cosmic muon flux.
To investigate a possible correlation between the cosmic muon flux and the solar activity, a Lomb-Scargle analysis of the daily sunspot data as provided by the World Data Center SILSO, the Royal Observatory of Belgium in Brussel [228], was performed. Strikingly, the solar cycle corresponding to the Borexino data taking campaign was found to feature a period of $\sim 3,050\,\text{d}$, in coincidence with the observed long-term modulation of the cosmic muon flux. Based on a fit of the sunspot data, the maxima of the solar activity and the long-term modulation of the cosmic muon flux were found to be consistent without the observation of a distinct accordance. However, the large uncertainties of the parameters of the long-term modulation of the cosmic muon flux and the relatively poor description of the sunspot data by the applied fit function indicate that the result must be treated with care. Hence, a correlation between the solar activity and the cosmic muon flux can neither be proven nor ruled out by the observations. To clarify this phenomenon, especially a longer measurement of the cosmic muon flux across several solar cycles would be beneficial.
In the cosmogenic neutron production rate, a seasonal modulation was found to be significant in the Lomb-Scargle periodogram as long as neutrons produced in showers featuring a neutron multiplicity above ten are excluded from the analysis. While the modulation of the cosmogenic neutron production rate was observed in phase with the cosmic muon flux, a higher amplitude with a difference of about $(2-3)\sigma$ was registered. Similar modulation parameters were found for the rate of neutron-producing muons. The interpretation of this discrepancy arising due to a seasonal modulation of the mean energy of cosmic muons was refuted by Monte Carlo simulations. However, uncertainties of the available atmosphere models and of the neutron production processes precluded to find a clear explanation of this phenomenon using the available simulation tools. Thus, further investigation and a better understanding of the neutron production cross sections, potentially based on dedicated measurements, are needed to clarify these observations.

8.2 Atmospheric Neutrino Neutral Current Interactions

Accompanying the production of cosmic muons, atmospheric muon neutrinos are generated in the decays of pions and kaons in the upper atmosphere. For muon energies up to $\sim 1\,\mathrm{GeV}$, the muons decay before reaching the Earth's surface and further muon and electron neutrinos and antineutrinos are produced.
Atmospheric neutrinos may be observed by NC interactions on carbon nuclei contained in the liquid scintillator. In these interactions, high-energetic neutrons are liberated. A distinct signature of a delayed coincidence between a prompt signal caused by recoil protons and a delayed signal due to a neutron capture γ ray of 2.2 MeV arises. However, this signature is also characteristic for the inverse β decay (IBD) $\overline{\nu}_\mathrm{e} + \mathrm{p} \rightarrow \mathrm{e}^+ + \mathrm{n}$ via which $\overline{\nu}_\mathrm{e}$ may be detected in liquid scintillators. Thus, $\overline{\nu}_\mathrm{e}$ IBD interactions impose a background for the detection of atmospheric neutrino NC interactions.
Conversely, atmospheric neutrino NC interactions constitute the major background for a detection of $\overline{\nu}_\mathrm{e}$ from the Diffuse Supernova Neutrino Background (DSNB) in liquid scintillator based experiments. An analysis of these NC interactions in a running liquid scintillator experiment, thus, allows to study this background for future experiments aiming for the first observation of the DSNB and evaluate suppression possibilities.
While the Borexino detector does not offer the required target mass to aim for an observation of the DSNB, several atmospheric neutrino NC interactions can be expected due to the long operational time of approximately ten years.
To search for such interactions, a delayed coincidence condition was applied on data acquired between December 9th, 2007 and September 2nd, 2017. Prompt candidates were searched for in a visible energy window from 7.5 MeV to 30 MeV as in the analysis of the KamLAND experiment, in which the first observation of atmospheric neutrino NC interactions in a liquid scintillator experiment was reported [260]. The restriction to a fiducial volume defined by a minimum distance of 25 cm to the Inner Vessel border and vetos introduced after the passage of a cosmic muon lead to a deadtime of $\sim 10\%$ and a resulting effective exposure after the cuts of $1.48\,\mathrm{kt} \times \mathrm{yr}$.
Several background sources for the search of atmospheric neutrino NC interactions were considered. Namely, the contributions to the dataset due to random coincidences, reactor $\overline{\nu}_\mathrm{e}$, the DSNB, CC interactions of atmospheric neutrinos, cosmogenic radio-isotopes, fast neutrons produced by muons in the OD or the rock surrounding the detector, and untagged neutron-producing muons were evaluated. The total number of background events passing the cuts applied for atmospheric neutrino NC candidate events was estimated as 3.6 ± 1.8 events. The expected

number of atmospheric neutrino NC interactions was evaluated by scaling the expectation for the analysis of these interactions performed by KamLAND to the exposure and atmospheric neutrino flux of the Borexino detector. Thus, 8.0 ± 2.3 atmospheric neutrino NC interactions are expected in the dataset, such that a total of 11.6 ± 4.1 events is estimated to pass the cuts.
In the data, twelve candidates for atmospheric neutrino NC interactions were observed, which very closely matches the expectation.
To further investigate the origin of the observed candidates, a pulse shape analysis based on the Gatti parameter was performed. The Gatti parameter values of the prompt candidate events were compared to the simulated distributions of prompt events generated in IBD interactions, neutrons as liberated in atmospheric neutrino NC interactions, and atmospheric ν_μ CC like interactions. Equal visible energy cuts as in the data analysis were applied on the simulated events. Ten of the twelve candidate events were identified as evidently not caused by IBD interactions since their Gatti parameters were registered with values above the endpoint of the distribution for IBD interactions. Of the remaining two events, one was found at a P-value of 0.003 to be caused by IBD interactions while the remaining event is fully compatible with an IBD origin.
The observation of delayed coincidences not caused by IBD interactions for prompt energies between 7.5 MeV and 30 MeV in the Borexino detector was clearly confirmed by the pulse shape analysis. Further, the number of observed candidate events matches the expectation extremely well and the distribution of the Gatti parameter of the prompt candidates closely resembles the predicted distribution for high-energetic neutrons as liberated in atmospheric neutrino NC interactions. Thus, the observation of atmospheric neutrino NC interactions in the Borexino detector became evident, which constitutes the second observation of these interactions in a liquid scintillator based experiment. Further, one of the candidate events was found to feature an extremely high Gatti parameter value, which allows its identification as most probably being caused by an atmospheric ν_μ or $\overline{\nu}_\mu$ CC interaction.
In this analysis, pulse shape discrimination techniques could be applied for the first time at comparably high visible energies to separate between different particle interactions. The possibility to discriminate atmospheric neutrino NC interactions from IBD interactions at similar energies could be demonstrated based on data of a running liquid scintillator based experiment. With this proof of principle, it was shown that pulse shape discrimination techniques constitute an applicable and promising tool to suppress the overwhelming background from atmospheric neutrino NC interactions in future experiments aiming for the first observation of the DSNB.
It could be pointed out that also the distribution of the distance between prompt

and delayed candidates differs for DSNB neutrino IBD and atmospheric neutrino NC interactions based on a Monte Carlo simulation of the two event classes. Even though the statistics of the acquired data in Borexino are not sufficient to prove this effect, the data were found to be compatible with the simulated distribution of the spatial separation between prompt and delayed events for high-energetic neutrons that generate the signal for atmospheric neutrino NC interactions. This parameter might be a further possibility to disentangle signal and background contributions in a future experiment aiming for the first detection of the DSNB.
Combining the evaluated discrimination techniques, a multivariate fit based on a pulse shape discrimination parameter, the spatial distance between prompt and delayed events, and the deposited energy of the prompt event was proposed as a possibility to identify a DSNB neutrino signal. To test this approach, a very basic Monte Carlo driven analysis was performed in which only the DSNB signal and a background contribution from atmospheric neutrino NC interactions were considered.
For the JUNO experiment, 600 atmospheric neutrino NC interactions and 13-39 DSNB neutrino interactions are expected in ten years of data for a fiducial volume of 17 kt and prompt energies between 11 MeV and 30 MeV. Considering these numbers for the least optimistic case of 13 signal events, $3,000$ Monte Carlo realizations of the expected data were created and fitted in a multivariate approach. The Gatti parameter, the registered charge, and the spatial distance between prompt and delayed event as predicted by the Borexino Monte Carlo simulation were used as input parameters for the fit. Based on these simplified evaluations, a sensitivity of $\sim 3\sigma$ for the detection of the DSNB was estimated for such a scenario. However, these results may only indicate the potential of future experiments since the respective detector specifics will strongly dominate the actual sensitivity.

8.3 Outlook

In the scope of this thesis, the correlation between the flux of cosmic muons at the LNGS and fluctuations of the atmospheric temperature was analyzed and quantified with the effective temperature coefficient. Despite the long measurement time, the uncertainty of this coefficient is still dominated by the statistics. However, since the accuracy of the measurement of the effective temperature coefficient strongly depends on the statistic uncertainty of the daily measured cosmic muon flux, mainly larger detectors providing an increased number of detected muons per day are required to improve the accuracy.
Similarly, also the measurement of the atmospheric kaon to pion production ratio, which may be inferred from the effective temperature coefficient, relies on the

statistics of the daily muon flux. Since this quantity is currently only known with a $\sim 40\%$ uncertainty, further direct and indirect measurements contributing to a better determination can be valuable.
Besides the seasonal modulation, an evidence for a long-term modulation that is not observed in the atmospheric temperature was found in the cosmic muon flux data. As a possible origin of this modulation, hints for a correlation to the solar activity were observed. The physical reason for a potential influence of the solar activity on the flux of high-energetic cosmic ray particles is currently unknown. However, a small effect was measured by the Tibet Air Shower Array [221] that observed a modulation of the shade the Sun casts on 10 TeV cosmic rays in anti-correlation with the solar activity. Even though this effect seems too small to explain the observed amplitude of the long-term modulation of the cosmic muon flux, it shows that even the flux of high-energetic cosmic rays at the Earth is affected by magnetic effects inside the Sun. This encourages to further investigate the possible correlation between the cosmic muon flux and the solar activity.
To clarify the observed indications, longer measurements of the cosmic muon flux underground spanning several solar cycles would be most beneficial. Such a measurement would allow to confirm or refute the correlation for various solar cycles. Further, a better understanding of the physics processes inside the Sun is required to either explain or exclude a physical correlation between the solar activity and the flux of high-energetic cosmic muons.

With the observation and identification of atmospheric neutrino NC interactions using pulse shape discrimination techniques, Borexino became the second experiment to observe these interactions. Further, a proof of principle could be accomplished that pulse shape discrimination can be a valuable tool to suppress the background from atmospheric neutrino NC interactions in future experiments aiming for the first observation of the DSNB.
The upcoming liquid scintillator based JUNO experiment will feature the necessary target mass to accumulate a detectable number of DSNB neutrino interactions. Since the chosen scintillator mixture is expected to provide a pulse shape discrimination performance comparable to the Borexino scintillator, a sufficient background reduction to receive a significant signal using these techniques might be feasible. However, major experimental challenges still have to be overcome. This includes the realization of an attenuation length $L \gtrsim 20\,\mathrm{m}$ and of the high PMT quantum efficiency of $\sim 30\%$. In case the aimed at unprecedented energy resolution of 3% at 1 MeV can be achieved, the prospects for a DSNB detection by this experiment seem promising.
As a possible analysis technique, a multivariate fit including a pulse shape parameter, the spatial separation of prompt and delayed candidates, and an energy estimator was presented in this thesis. The performance of such an approach was

found to be encouraging, such that it might be a favorable analysis strategy in a future experiment. However, very basic signal and background models were used and non-considered effects might affect the analyses of future experiments. Further, the respective detector specifics will strongly determine its sensitivity. Thus, detailed sensitivity studies for distinct experiments must be performed including detailed modeling of the detector as well as of the signal and background contributions.

In this thesis, the Gatti parameter was used to analyze the pulse shape of the candidate events and prove their discriminability from IBD interactions. While a good performance of this parameter was observed, several other pulse shape parameters are available that might, potentially, be even better suited for a discrimination between atmospheric neutrino NC and DSNB neutrino IBD interactions. The tail-to-total parameter offers another common method to distinguish between energy depositions of different particles in the liquid scintillator. A further possibility is supplied by neural networks that might be used to create an input parameter for the fit providing a high discrimination power. In detailed sensitivity studies for experiments aiming for the observation of the DSNB, different parameters or combinations of parameters need to be tested to ensure that the best possible background suppression is achieved.

Besides the JUNO experiment, the gadolinium enhanced Water Čerenkov Super-Kamiokande experiment will aim for the detection of the DSNB. In Super-Kamiokande, an observation of the DSNB was hindered by the overwhelming background rates so far. These backgrounds may be strongly reduced with the insertion of gadolinium since this allows to access the delayed coincidence generated by IBD interactions of DSNB $\overline{\nu}_{\mathrm{e}}$.

However, major experimental challenges need to be overcome for that experiment as well. These are currently investigated in an extensive R&D project [281]. Namely, a high transparency of the gadolinium enhanced water must be ensured, the water purification system needs to be modified since the original Super-Kamiokande system removes ions, the effect of gadolinium on the detector materials has to be studied, and a uniform distribution of the gadolinium in the water must be achieved. Further, the background from non-IBD neutrons as well as the neutron capture efficiency have to be investigated.

With the upcoming JUNO and gadolinium enhanced Super-Kamiokande experiments, two detectors based on different techniques will be available featuring the necessary target mass and sensitivity to aim for the first observation of the DSNB. While for both experiments, major challenges concerning the detector construction and background suppression need to be solved, the prospects for an observation of the DSNB in the near future are promising. The detection would constitute a milestone in the understanding of core collapse SNe, their rate throughout the history

of the universe, and the neutrino as a particle itself. Further, the first observation might encourage the development of detectors that feature a target mass allowing for precision measurements of the DSNB spectrum. These could give deep insights into the processes involved in core collapse SNe and, especially, investigate the rate at which SNe collapse into neutron stars and black holes.

The Borexino experiment led the way in the spectroscopy of solar neutrinos in the last decade. Most precise measurements of all neutrinos produced in the solar pp-chain could be accomplished except for the least abundant hep neutrinos. Spectroscopic measurements of geo-neutrinos could be performed and the best limit on the solar CNO neutrino flux at the moment of writing was obtained.

In the future, the Borexino collaboration will center its efforts around the observation of solar neutrinos produced in the CNO-cycle. Since the CNO neutrino signal may not be disentangled from the major ^{210}Bi background in a spectral fit due to the similarity of the spectra, the focus is currently set on an independent measurement of the ^{210}Bi rate to constrain this component and allow the observation of the CNO neutrino signal. In case the ^{210}Bi rate may be measured with $\sim 20\%$ precision or better, the first observation of solar CNO neutrinos might be within reach. A successful measurement of the CNO neutrino flux would constitute a further milestone of experimental solar neutrino physics especially allowing to probe the Sun's metallicity and bestow the final climax of the rich Borexino physics program.

List of Figures

List of Tables

Bibliography

[1] P. Gombás. Collected scientific papers by Wolfgang Pauli. *Acta Physica Academiae Scientiarum Hungaricae*, 23(2):251–251, 1967.

[2] C.L. Cowan et al. Detection of the free neutrino: A confirmation. *Science*, 124(3212):103–104, 1956.

[3] R. Davis. A review of the Homestake solar neutrino experiment. *Progress in Particle and Nuclear Physics*, 32(0):13 – 32, 1994.

[4] Q.R. Ahmad et al. Direct evidence for neutrino flavor transformation from neutral current interactions in the Sudbury Neutrino Observatory. *Phys. Rev. Lett.*, 89:011301, 2002, nucl-ex/0204008.

[5] K. Eguchi et al. First results from KamLAND: Evidence for reactor anti-neutrino disappearance. *Phys.Rev.Lett.*, 90:021802, 2003, hep-ex/0212021.

[6] Y. Fukuda et al. Evidence for oscillation of atmospheric neutrinos. *Phys. Rev. Lett.*, 81:1562–1567, 1998.

[7] C. Patrignani et al. (Particle Data Group). Review of Particle Physics. *Chin. Phys.*, C40(10):100001, 2016.

[8] S.M. Bilenky. Majorana neutrino mixing. *J. Phys.*, G32:R127, 2006, hep-ph/0511227.

[9] G. Bellini et al. Final results of Borexino phase-I on low-energy solar neutrino spectroscopy. *Phys. Rev. D*, 89:112007, 2014.

[10] G. Bellini et al. Neutrinos from the primary proton-proton fusion process in the Sun. *Nature*, 512(7515):383–386, 2014.

[11] G. Bellini et al. First evidence of pep solar neutrinos by direct detection in Borexino. *Phys. Rev. Lett.*, 108:051302, 2012.

[12] M. Agostini et al. Spectroscopy of geoneutrinos from 2056 days of Borexino data. *Phys. Rev.*, D92(3):031101, 2015, hep-ex/1506.04610.

[13] S. Weinberg. A model of leptons. *Physical Review Letters*, 19(21):1264–1266, 1967.

[14] J.F. Donoghue. The effective field theory treatment of quantum gravity. *AIP Conf.Proc.*, 1483:73–94, 2012, gr-qc/1209.3511.

[15] L. Landau. On the conservation laws for weak interactions. *Nuclear Physics*, 3(1):127 – 131, 1957.

[16] T.D. Lee and C.N. Yang. Parity nonconservation and a two-component theory of the neutrino. *Phys. Rev.*, 105:1671–1675, 1957.

[17] A. Salam. On parity conservation and neutrino mass. *Il Nuovo Cimento*, 5(1):299–301, 1957.

[18] S.M. Bilenky. Neutrino. History of a unique particle. *Eur.Phys.J. H38*, pages 345–404, 2013, hep-ph/1210.3065.

[19] B. Aharmim et al. Electron energy spectra, fluxes, and day-night asymmetries of ^{8}B solar neutrinos from measurements with NaCl dissolved in the heavy-water detector at the Sudbury Neutrino Observatory. *Phys.Rev.*, C72:055502, 2005, nucl-ex/0502021.

[20] B. Pontecorvo. Mesonium and antimesonium. *J. Exptl. Theoret. Phys.*, 33:549–551, 1957.

[21] Z. Maki, M. Nakagawa, and S. Sakata. Remarks on the unified model of elementary particles. *Progress of Theoretical Physics*, 28(5):870–880, 1962.

[22] S.M. Bilenky et al. Phenomenology of neutrino oscillations. *Prog. Part. Nucl. Phys.*, 43:1–86, 1999, hep-ph/9812360.

[23] M. Kobayashi and T. Maskawa. CP violation in the renormalizable theory of weak interaction. *Prog.Theor.Phys.*, 49:652–657, 1973.

[24] N. Cabibbo. Unitary symmetry and leptonic decays. *Phys. Rev. Lett.*, 10:531–533, 1963.

[25] S.M. Bilenky. On the phenomenology of neutrino oscillations in vacuum. 2012, hep-ph/1208.2497.

[26] S.M. Bilenky et al. On the oscillations of neutrinos with Dirac and Majorana masses. *Physics Letters B*, 94(4):495 – 498, 1980.

[27] J. Haser. Light sterile neutrino searches. In *29th Rencontres de Blois on Particle Physics and Cosmology Blois, France, May 28-June 2, 2017*, 2017, hep-ex/1710.06330.

[28] M. Zralek. From kaons to neutrinos: Quantum mechanics of particle oscillations. *Acta Phys.Polon.*, B29:3925–3956, 1998, hep-ph/9810543.

[29] B. Kayser. Neutrino oscillation phenomenology. In *Neutrinos in particle physics, astrophysics and cosmology. Proceedings, 61st Scottish Universities Summer School in Physics, SUSSP61, St. Andrews, UK, August 8-23, 2006*, pages 51–64, 2008, hep-ph/0804.1121.

[30] N. Schmitz. *Neutrinophysik*. Teubner Studienbücher, Stuttgart, 1997.

[31] F. Capozzi et al. Neutrino masses and mixings: Status of known and unknown 3ν parameters. *Nucl. Phys.*, B908:218–234, 2016, hep-ph/1601.07777.

[32] J. Hosaka et al. Solar neutrino measurements in Super-Kamiokande-I. *Phys.Rev.*, D73:112001, 2006, hep-ex/0508053.

[33] E.K. Akhmedov et al. A simple analytic three flavor description of the day night effect in the solar neutrino flux. *JHEP*, 05:057, 2004, hep-ph/0404083.

[34] P.C. de Holanda et al. Toward precision measurements in solar neutrinos. *Nucl. Phys.*, B702:307–332, 2004, hep-ph/0404042.

[35] J.N. Bahcall et al. New solar opacities, abundances, helioseismology, and neutrino fluxes. *Astrophys. J.*, 621:L85–L88, 2005, astro-ph/0412440.

[36] M. Agostini et al. First simultaneous precision spectroscopy of pp, ^{7}Be, and pep solar neutrinos with Borexino phase-II. 2017, hep-ex/1707.09279.

[37] K. Eguchi et al. First results from KamLAND: Evidence for reactor antineutrino disappearance. *Phys. Rev. Lett.*, 90:021802, 2003, hep-ex/0212021.

[38] G. Bellini et al. Measurement of the solar ^{8}B neutrino rate with a liquid scintillator target and 3 MeV energy threshold in the Borexino detector. *Phys. Rev. D*, 82:033006, 2010.

[39] H. Minakata and C. Pena-Garay. Solar neutrino observables sensitive to matter effects. *Adv. High Energy Phys.*, 2012:349686, 2012, hep-ph/1009.4869.

[40] P.C. de Holanda et al. Solar neutrino spectrum, sterile neutrinos and additional radiation in the Universe. *Phys. Rev.*, D83:113011, 2011, hep-ph/1012.5627.

[41] S. Hannestad et al. Cosmological constraints on neutrino plus axion hot dark matter. *Journal of Cosmology and Astroparticle Physics*, 2007(08):015, 2007.

[42] J. Hofestädt. Prospects for measuring the neutrino mass hierarchy with KM3NeT/ORCA. In *25th European Cosmic Ray Symposium (ECRS 2016) Turin, Italy, September 04-09, 2016*, 2017, physics.ins-det/1701.04078.

[43] E.G. Adelberger et al. Solar fusion cross sections. II. The pp chain and CNO cycles. *Rev. Mod. Phys.*, 83:195–245, 2011.

[44] R. Saldanha. *Precision measurement of the ^{7}Be solar neutrino interaction rate in Borexino.* PhD thesis, Princeton University, 2012.

[45] H.A. Bethe. Energy production in stars. *Phys. Rev.*, 55:434–456, 1939.

[46] J.N. Bahcall et al. Does the Sun shine by pp or CNO fusion reactions? *Phys. Rev. Lett.*, 90:131301, 2003.

[47] J.N. Bahcall et al. What do we (not) know theoretically about solar neutrino fluxes? *Phys. Rev. Lett.*, 92:121301, 2004.

[48] V. Barger et al. Imprint of SNO neutral current data on the solar neutrino problem. *Physics Letters B*, 537(3–4):179 – 186, 2002.

[49] S.J. Smartt. Progenitors of core-collapse supernovae. *ARAA*, 47:63–106, 2009, astro-ph.SR/0908.0700.

[50] K. Kotake et al. Explosion mechanism, neutrino burst, and gravitational wave in core-collapse supernovae. *Rept. Prog. Phys.*, 69:971–1144, 2006, astro-ph/0509456.

[51] H.T. Janka. Neutrino-driven explosions. 2017, astro-ph.HE/1702.08825.

[52] L. Cadonati et al. Supernova neutrino detection in Borexino. *Astropart. Phys.*, 16:361–372, 2002, hep-ph/0012082.

[53] K. Langanke et al. Signal for supernova ν_μ and ν_τ neutrinos in Water Čerenkov detectors. *Phys. Rev. Lett.*, 76:2629–2632, 1996.

[54] T.A. Thompson et al. Shock breakout in core-collapse supernovae and its neutrino signature. *Astrophys. J.*, 592:434, 2003, astro-ph/0211194.

[55] M.T. Keil et al. Monte Carlo study of supernova neutrino spectra formation. *Astrophys. J.*, 590:971–991, 2003, astro-ph/0208035.

[56] S. Ando and K. Sato. Relic neutrino background from cosmological supernovae. *New J. Phys.*, 6:170, 2004, astro-ph/0410061.

[57] T. Totani et al. Future detection of supernova neutrino burst and explosion mechanism. *Astrophys. J.*, 496:216–225, 1998, astro-ph/9710203.

[58] S. Ando and K. Sato. Supernova relic neutrinos and observational implications for neutrino oscillation. *Physics Letters B*, 559(3):113 – 120, 2003.

[59] A.S. Dighe and A.Yu. Smirnov. Identifying the neutrino mass spectrum from the neutrino burst from a supernova. *Phys. Rev.*, D62:033007, 2000, hep-ph/9907423.

[60] R.M. Bionta et al. Observation of a neutrino burst in coincidence with supernova 1987A in the Large Magellanic Cloud. *Phys. Rev. Lett.*, 58:1494–1496, 1987.

[61] K. Hirata et al. Observation of a neutrino burst from the supernova SN1987A. *Phys. Rev. Lett.*, 58:1490–1493, 1987.

[62] J.Q. Meindl. *Reconstruction and measurement of cosmogenic signals in the neutrino experiment Borexino.* PhD thesis, Technische Universität München, 2013.

[63] M. Ikeda et al. Search for supernova neutrino bursts at Super-Kamiokande. *The Astrophysical Journal*, 669(1):519, 2007.

[64] N.Yu. Agafonova et al. On-Line recognition of supernova neutrino bursts in the LVD. *Astroparticle Physics*, 28(6):516 – 522, 2008.

[65] R. Abbasi et al. IceCube sensitivity for low-energy neutrinos from nearby supernovae. *A&A*, 535:A109, 2011.

[66] J.F. Beacom. The diffuse supernova neutrino background. *Ann. Rev. Nucl. Part. Sci.*, 60:439–462, 2010, astro-ph.HE/1004.3311.

[67] M. Malek et al. Search for supernova relic neutrinos at Super-Kamiokande. *Phys. Rev. Lett.*, 90:061101, 2003, hep-ex/0209028.

[68] F. An et al. Neutrino physics with JUNO. *J. Phys.*, G43(3):030401, 2016, physics.ins-det/1507.05613.

[69] S. Horiuchi et al. The diffuse supernova neutrino background is detectable in Super-Kamiokande. *Phys. Rev.*, D79:083013, 2009, astro-ph/0812.3157.

[70] E.E. Salpeter. The luminosity function and stellar evolution. *Astrophys. J.j*, 121:161, 1955.

[71] C. Lunardini. The diffuse supernova neutrino flux, supernova rate and SN1987A. *Astropart. Phys.*, 26:190–201, 2006, astro-ph/0509233.

[72] A.M. Hopkins and J.F. Beacom. On the normalisation of the cosmic star formation history. *Astrophys. J.*, 651:142–154, 2006, astro-ph/0601463.

[73] C. Porciani and P. Madau. On the association of gamma-ray bursts with massive stars: Implications for number counts and lensing statistics. *Astrophys. J.*, 548:522–531, 2001, astro-ph/0008294.

[74] S. Ando. Cosmic star formation history and the future observation of supernova relic neutrinos. *Astrophys. J.*, 607:20–31, 2004, astro-ph/0401531.

[75] T.K. Gaisser et al. Cosmic-ray neutrinos in the atmosphere. *Phys. Rev. D*, 38:85–95, 1988.

[76] G. Barr et al. Flux of atmospheric neutrinos. *Phys. Rev. D*, 39:3532–3534, 1989.

[77] C. Lunardini. Diffuse neutrino flux from failed supernovae. *Phys. Rev. Lett.*, 102:231101, 2009.

[78] Alankrita P. and Cecilia L. Diffuse neutrinos from luminous and dark supernovae: Prospects for upcoming detectors at the $\mathcal{O}(10)$ kt scale. *Journal of Cosmology and Astroparticle Physics*, 2017(11):031, 2017.

[79] T.K. Gaisser et al. *Cosmic rays and particle physics*. Cambridge University Press, 2016.

[80] M. Wurm. *Cosmic background discrimination for the rare neutrino event search in Borexino and LENA*. PhD thesis, Technische Universität München, 2009.

[81] M.M. Winn et al. The cosmic-ray energy spectrum above 10^{17} eV. *Journal of Physics G: Nuclear Physics*, 12(7):653, 1986.

[82] J. Abraham et al. Measurement of the energy spectrum of cosmic rays above 10^{18} eV using the Pierre Auger Observatory. *Phys. Lett.*, B685:239–246, 2010, astro-ph.HE/1002.1975.

[83] K. Greisen. End to the cosmic-ray spectrum? *Phys. Rev. Lett.*, 16:748–750, 1966.

[84] G.T. Zatsepin et al. Upper limit of the spectrum of cosmic rays. *JETP Lett.*, 4:78–80, 1966. Pisma Zh. Eksp. Teor. Fiz. 4 (1966) 114.

[85] T.K. Gaisser. Atmospheric neutrinos. *AIP Conf. Proc.*, 944:140–142, 2007, astro-ph/0612274.

[86] T.K. Gaisser. Fluxes of atmospheric neutrinos and related cosmic rays. *Nucl. Phys. Proc. Suppl.*, 77:133–139, 1999, hep-ph/9811315.

[87] K.S. Hirata et al. Observation of a small atmospheric ν_μ/ν_e ratio in Kamiokande. *Physics Letters B*, 280(1):146 – 152, 1992.

[88] R. Becker-Szendy et al. Electron- and muon-neutrino content of the atmospheric flux. *Phys. Rev. D*, 46:3720–3724, 1992.

[89] W.W.M. Allison et al. Measurement of the atmospheric neutrino flavor composition in Soudan-2. *Phys. Lett.*, B391:491–500, 1997, hep-ex/9611007.

[90] S. Fukuda et al. Tau neutrinos favored over sterile neutrinos in atmospheric muon neutrino oscillations. *Phys. Rev. Lett.*, 85:3999–4003, 2000.

[91] K. Abe et al. Atmospheric neutrino oscillation analysis with external constraints in Super-Kamiokande I-IV. 2017, hep-ex/1710.09126.

[92] R. Davis et al. Search for Neutrinos from the Sun. *Phys. Rev. Lett.*, 20:1205–1209, 1968.

[93] W. Hampel et al. GALLEX solar neutrino observations: Results for GALLEX III. *Physics Letters B*, 388(2):384 – 396, 1996.

[94] V.N. Gavrin. Measurement of the solar neutrino capture rate in SAGE and the value of the pp–neutrino flux at the Earth. *Nuclear Physics B - Proceedings Supplements*, 138(Supplement C):87 – 90, 2005. Proceedings of the Eighth International Workshop on Topics in Astroparticle and Underground Physics.

[95] M. Altmann et al. Complete results for five years of GNO solar neutrino observations. *Phys. Lett.*, B616:174–190, 2005, hep-ex/0504037.

[96] F.P. An et al. The detector system of the Daya Bay reactor neutrino experiment. *Nucl. Instrum. Meth.*, A811:133–161, 2016, physics.ins-det/1508.03943.

[97] Y. Abe et al. Reactor electron antineutrino disappearance in the Double Chooz experiment. *Phys. Rev.*, D86:052008, 2012, hep-ex/1207.6632.

[98] S.H. Seo et al. Spectral measurement of the electron antineutrino oscillation amplitude and frequency using 500 live days of RENO data. 2016, hep-ex/1610.04326.

[99] M.G. Aartsen et al. The IceCube Neutrino Observatory: Instrumentation and online systems. *JINST*, 12(03):P03012, 2017, astro-ph.IM/1612.05093.

[100] A. Albert et al. All-flavor search for a diffuse flux of cosmic neutrinos with nine years of ANTARES data. *Astrophys. J.*, 853(1):L7, 2018, astro-ph.HE/1711.07212.

[101] M. Wurm et. al. The next-generation liquid-scintillator neutrino observatory LENA. *Astroparticle Physics*, 35(11):685 – 732, 2012.

[102] J. Migenda. Astroparticle physics in Hyper-Kamiokande. In *2017 European Physical Society Conference on High Energy Physics (EPS-HEP 2017) Venice, Italy, July 5-12, 2017*, 2017, physics.ins-det/1710.08345.

[103] E.L. Lomon. Classical electrodynamics. John David Jackson. Wiley, New York, 1962. *Science*, 136(3521):1046–1047, 1962.

[104] G.M. Hale and M.R. Querry. Optical constants of water in the 200-nm to 200-μm wavelength region. *Appl. Opt.*, 12(3):555–563, 1973.

[105] K. Abe et al. Letter of intent: The Hyper-Kamiokande experiment — Detector design and physics potential —. 2011, hep-ex/1109.3262.

[106] R. Laha and J.F. Beacom. Gadolinium in Water Cherenkov detectors improves detection of supernova ν_e. *Phys. Rev.*, D89:063007, 2014, astro-ph.HE/1311.6407.

[107] S. Fukuda et al. Solar ^{8}B and hep neutrino measurements from 1258 days of Super-Kamiokande data. *Phys. Rev. Lett.*, 86:5651–5655, 2001, hep-ex/0103032.

[108] G. Bellini et al. Muon and cosmogenic neutron detection in Borexino. *Journal of Instrumentation*, 6(05):P05005, 2011.

[109] G. Alimonti et al. The Borexino detector at the Laboratori Nazionali del Gran Sasso. *Nuclear Instruments and Methods in Physics Research A*, 600:568–593, 2009, physics.ins-det/0806.2400.

[110] J.B. Birks. *The theory and practice of scintillation counting.* Pergamon Press, 1 edition, 1964.

[111] V.F.M. Zimmer. *Studies of proton recoils in organic liquid scintillators used in present and future neutrino experiments*. Dissertation, Technische Universität München, München, 2015.

[112] J. Franck and E.G. Dymond. Elementary processes of photochemical reactions. *Trans. Faraday Soc.*, 21:536–542, 1926.

[113] E. Condon. A theory of intensity distribution in band systems. *Phys. Rev.*, 28:1182–1201, 1926.

[114] J. Benziger et al. A scintillator purification system for the Borexino solar neutrino detector. *Nuclear Instruments and Methods in Physics Research Section A: Accelerators, Spectrometers, Detectors and Associated Equipment*, 587(2):277 – 291, 2008.

[115] T. Marrodan Undagoitia. *Measurement of light emission in organic liquid scintillators and studies towards the search for proton decay in the future large-scale detector LENA*. PhD thesis, Technische Universiät München, 2007.

[116] P. Lombardi et al. Decay time and pulse shape discrimination of liquid scintillators based on novel solvents. *Nuclear Instruments and Methods in Physics Research Section A: Accelerators, Spectrometers, Detectors and Associated Equipment*, 701(Supplement C):133 – 144, 2013.

[117] E. Gatti et al. Particle identification by pulse shape discrimination. *Energ. Nucl.-Milan*, 17(34), 1970.

[118] M. Schwarz et al. Measurements of the Lifetime of Orthopositronium in the LAB-Based Liquid Scintillator of JUNO. 2018, physics.ins-det/1804.09456.

[119] M. Fukugita et al. Reaction cross sections for $\nu + {}^{13}\mathrm{C} \rightarrow e^- + {}^{13}\mathrm{N}$ and $\nu + {}^{13}\mathrm{C} \rightarrow \nu' + {}^{13}\mathrm{C}^*$ for low energy neutrinos. *Phys. Rev. C*, 41:1359–1364, 1990.

[120] M. Fukugita and T. Yanagida. *Physics of neutrinos and applications to astrophysics*. Berlin New York Springer, 2003.

[121] J.F. Beacom et al. Detection of supernova neutrinos by neutrino proton elastic scattering. *Phys. Rev.*, D66:033001, 2002, hep-ph/0205220.

[122] A. Ianni et al. How to observe ^{8}B solar neutrinos in liquid scintillator detectors. *Phys. Lett.*, B627:38–48, 2005, physics.ins-det/0506171.

[123] A. Strumia and F. Vissani. Precise quasielastic neutrino/nucleon cross-section. *Phys. Lett.*, B564:42–54, 2003, astro-ph/0302055.

[124] G. Bellini et al. Observation of geo-neutrinos. *Physics Letters B*, 687:299 – 304, 2010.

[125] J.F. Beacom and M.R. Vagins. GADZOOKS! Anti-neutrino spectroscopy with large Water Cherenkov detectors. *Phys. Rev. Lett.*, 93:171101, 2004, hep-ph/0309300.

[126] S. Dazeley et al. Observation of neutrons with a gadolinium doped Water Cherenkov detector. *Nuclear Instruments and Methods in Physics Research Section A: Accelerators, Spectrometers, Detectors and Associated Equipment*, 607(3):616 – 619, 2009.

[127] F. Ardellier et al. Letter of intent for Double-CHOOZ: A search for the mixing angle θ_{13}. 2004, hep-ex/0405032.

[128] Y. Abe et al. Measurement of θ_{13} in Double Chooz using neutron captures on hydrogen with novel background rejection techniques. *JHEP*, 01:163, 2016, hep-ex/1510.08937.

[129] R.B. Firestone et al. *Table of isotopes*. Number Bd. 4. Wiley, 1999.

[130] T. Enqvist et al. Measurements of muon flux in the Pyhäsalmi Underground Laboratory. *Nucl.Instrum.Meth.*, A554:286–290, 2005, hep-ex/0506032.

[131] M. Aglietta et al. Muon 'depth intensity' relation measured by LVD underground experiment and cosmic ray muon spectrum at sea level. *Phys. Rev.*, D58:092005, 1998, hep-ex/9806001.

[132] W.R. Leo. *Techniques for nuclear and particle physics experiments: A how-to approach*. Springer Berlin Heidelberg, 2012.

[133] V.A. Kudryavtsev. Muon simulation codes MUSIC and MUSUN for underground physics. *Comput. Phys. Commun.*, 180:339–346, 2009, physics.comp-ph/0810.4635.

[134] M. Ambrosio et al. Measurement of the residual energy of muons in the Gran Sasso underground laboratories. *Astroparticle Physics*, 19(3):313 – 328, 2003.

[135] V.A. Kudryavtsev et al. Simulations of muon induced neutron flux at large depths underground. *Nucl. Instrum. Meth.*, A505:688–698, 2003, hep-ex/0303007.

[136] T. Hagner et al. Muon-induced production of radioactive isotopes in scintillation detectors. *Astroparticle Physics*, 14(1):33 – 47, 2000.

[137] G. Bellini et al. Cosmogenic backgrounds in Borexino at 3800 m water-equivalent depth. *JCAP*, 1308:049, 2013, physics.ins-det/1304.7381.

[138] C. Galbiati et al. Cosmogenic ^{11}C production and sensitivity of organic scintillator detectors to pep and CNO neutrinos. *Phys. Rev.*, C71:055805, 2005, hep-ph/0411002.

[139] Y.-F. Li et al. Unambiguous determination of the neutrino mass hierarchy using reactor neutrinos. *Phys. Rev.*, D88:013008, 2013, hep-ex/1303.6733.

[140] V. Antonelli and L. Miramonti. Status and potentialities of the JUNO experiment. In *17th International Workshop on Neutrino Telescopes (Neutel 2017) Venice, Italy, March 13-17, 2017*, 2017, hep-ph/1710.07401.

[141] T. Adam et al. The OPERA experiment target tracker. *Nuclear Instruments and Methods in Physics Research Section A: Accelerators, Spectrometers, Detectors and Associated Equipment*, 577(3):523 – 539, 2007.

[142] J. Sawatzki. Sensitivity study of the neutrino mass hierarchy determination in JUNO using reactor antineutrinos. Master's thesis, Technische Universiät München, Germany, 2014.

[143] F. Capozzi et al. PINGU and the neutrino mass hierarchy: Statistical and systematic aspects. *Phys. Rev.*, D91:073011, 2015, 1503.01999.

[144] M. He. Future reactor experiments. In *15th International Workshop on Neutrino Factories, Super Beams and Beta Beams (NuFact2013) Beijing, China, August 19-24, 2013*, 2013, physics.ins-det/1310.7343.

[145] S. Antusch et al. Unitarity of the leptonic mixing matrix. *JHEP*, 10:084, 2006, hep-ph/0607020.

[146] X. Qian and P. Vogel. Neutrino mass hierarchy. *Prog. Part. Nucl. Phys.*, 83:1–30, 2015, hep-ex/1505.01891.

[147] A. Gando et al. ^{7}Be solar neutrino measurement with KamLAND. *Phys. Rev.*, C92(5):055808, 2015, hep-ex/1405.6190.

[148] R. Möllenberg. *Monte Carlo study of solar* ^{8}B *neutrinos and the diffuse supernova neutrino background in LENA*. Dissertation, Technische Universität München, München, 2013.

[149] M. Wurm et al. Detection potential for the diffuse supernova neutrino background in the large liquid-scintillator detector LENA. *Phys. Rev.*, D75:023007, 2007, astro-ph/0701305.

[150] T. Araki et al. Experimental investigation of geologically produced antineutrinos with KamLAND. *Nature*, 436(7050):499–503, 2005.

[151] A. Gando et al. Partial radiogenic heat model for Earth revealed by geoneutrino measurements. *Nature Geosci*, 4(9):647–651, 2011.

[152] G. Bellini et al. Measurement of geo-neutrinos from 1353 days of Borexino. *Phys. Lett.*, B722:295–300, 2013, hep-ex/1303.2571.

[153] R.S. Raghavan et al. New tools for solving the solar-neutrino problem. *Phys. Rev. Lett.*, 57:1801–1804, 1986.

[154] C. Arpesella et al. First real time detection of ^{7}Be solar neutrinos by Borexino. *Physics Letters B*, 658(4):101 – 108, 2008.

[155] G. Bellini et al. Precision measurement of the ^{7}Be solar neutrino interaction rate in Borexino. *Phys. Rev. Lett.*, 107:141302, 2011.

[156] G. Bellini et al. Absence of a day-night asymmetry in the ^{7}Be solar neutrino rate in Borexino. *Physics Letters B*, 707(1):22 – 26, 2012.

[157] M. Agostini et al. Improved measurement of ^{8}B solar neutrinos with 1.5 kt y of Borexino exposure. 2017, hep-ex/1709.00756.

[158] G. Bonfini. personal communication.

[159] D. Bravo-Berguño et al. The Borexino thermal monitoring and management system. 2017, physics.ins-det/1705.09078.

[160] M. Agostini et al. Seasonal modulation of the ^{7}Be solar neutrino rate in Borexino. *Astroparticle Physics*, 92(Supplement C):21 – 29, 2017.

[161] B. Aharmim et al. A search for periodicities in the ^{8}B solar neutrino flux measured by the Sudbury Neutrino Observatory. *Phys. Rev. D*, 72:052010, 2005.

[162] B. Aharmim et al. Low-energy-threshold analysis of the phase I and phase II data sets of the Sudbury Neutrino Observatory. *Phys. Rev. C*, 81:055504, 2010.

[163] J.P. Cravens et al. Solar neutrino measurements in Super-Kamiokande-II. *Phys. Rev. D*, 78:032002, 2008.

[164] S. Abe et al. Production of radioactive isotopes through cosmic muon spallation in KamLAND. *Phys. Rev. C*, 81:025807, 2010.

[165] M. Agostini et al. The Monte Carlo simulation of the Borexino detector. *Astropart. Phys.*, 97:136–159, 2018, physics.ins-det/1704.02291.

[166] S. Appel. personal communication.

[167] A.M. Serenelli et al. Solar models with accretion. I. Application to the solar abundance problem. *apj*, 743:24, 2011, astro-ph.SR/1104.1639.

[168] W.C. Haxton et al. Solar neutrinos: Status and prospects. *Annual Review of Astronomy and Astrophysics*, 51(1):21–61, 2013.

[169] N. Vinyoles et al. A new generation of standard solar models. *The Astrophysical Journal*, 835(2):202, 2017.

[170] O. Šrámek et al. Geophysical and geochemical constraints on geoneutrino fluxes from Earth's mantle. *Earth and Planetary Science Letters*, 361(Supplement C):356 – 366, 2013.

[171] J.H. Davies and D.R. Davies. Earth's surface heat flux. *Solid Earth*, 1(1):5–24, 2010.

[172] G. Bellini et al. Geo-neutrinos. *Progress in Particle and Nuclear Physics*, 73(Supplement C):1 – 34, 2013.

[173] F.L. Villante et al. A method to extract the CNO solar neutrino signal in ultrapure liquid scintillator detectors. *Journal of Physics: Conference Series*, 375(4):042035, 2012.

[174] G. Bellini et al. Cosmic-muon flux and annual modulation in Borexino at 3800 m water-equivalent depth. *JCAP*, 1205:015, 2012, hep-ex/1202.6403.

[175] P.H. Barrett et al. Interpretation of cosmic-ray measurements far underground. *Reviews of Modern Physics*, 24:133–178, 1952.

[176] P. Adamson et al. Observation of muon intensity variations by season with the MINOS far detector. *Phys. Rev.*, D81:012001, 2010, hep-ex/0909.4012.

[177] S. Osprey et al. Sudden stratospheric warmings seen in MINOS deep underground muon data. *Geophysical Research Letters*, 36(5):n/a–n/a, 2009. L05809.

[178] E.W. Grashorn. *Astroparticle Physics with the MINOS Far Detector*. PhD thesis, University of Minnesota, 2008.

[179] E.W. Grashorn et al. The atmospheric charged kaon/pion ratio using seasonal variation methods. *Astropart. Phys.*, 33:140–145, 2010, hep-ex/0909.5382.

[180] P.J. Hayman et al. The rate of energy loss of high-energy cosmic ray muons. *Proceedings of the Royal Society of London A: Mathematical, Physical and Engineering Sciences*, 275(1362):391–410, 1963.

[181] G.C. Castagnoli and M.A. Dodero. Temperature effect of the muon component underground and pion attenuation length. *Il Nuovo Cimento B (1965-1970)*, 51(2):525–534, 1967.

[182] M. Ambrosio et al. Seasonal variations in the underground muon intensity as seen by MACRO. *Astroparticle Physics*, 7(1):109 – 124, 1997.

[183] D.P. Dee et al. The ERA-Interim reanalysis: Configuration and performance of the data assimilation system. *Quarterly Journal of the Royal Meteorological Society*, 137(656):553–597, 2011.

[184] E. Gschwendtner et al. Performance and operational experience of the CNGS facility. *Conf. Proc.*, C100523:THPEC046, 2010.

[185] G. Korga. personal communication.

[186] D. D'Angelo. *Towards the detection of low energy solar neutrinos in Borexino: Data readout, data reconstruction and background identification.* PhD thesis, Technische Universität München, 2006.

[187] K. Abe et al. Evidence for the appearance of atmospheric tau neutrinos in Super-Kamiokande. *Phys. Rev. Lett.*, 110:181802, 2013.

[188] N.Yu. Agafonova et al. Evidence for $\nu_\mu \to \nu_\tau$ appearance in the CNGS neutrino beam with the OPERA experiment. *Phys. Rev. D*, 89:051102, 2014.

[189] T. Adam et al. Measurement of the neutrino velocity with the OPERA detector in the CNGS beam. *JHEP*, 10:093, 2012, hep-ex/1109.4897v2.

[190] T. Adam et al. Measurement of the neutrino velocity with the OPERA detector in the CNGS beam. *JHEP*, 10:093, 2012, hep-ex/1109.4897v4.

[191] T. Adam et al. Measurement of the neutrino velocity with the OPERA detector in the CNGS beam using the 2012 dedicated data. *JHEP*, 01:153, 2013, hep-ex/1212.1276.

[192] P. Alvarez Sanchez et al. Measurement of CNGS muon neutrino speed with Borexino. *Phys. Lett.*, B716:401–405, 2012, hep-ex/1207.6860.

[193] M. Antonello et al. Precision measurement of the neutrino velocity with the ICARUS detector in the CNGS beam. *JHEP*, 11:049, 2012, hep-ex/1208.2629.

[194] D.G. Andrews et al. *Middle atmosphere dynamics.* Academic Press, 1987.

[195] G. Manney et al. A minor sudden stratospheric warming with a major impact: Transport and polar processing in the 2014/2015 arctic winter. *Geophysical Research Letters*, 42(18):7808–7816, 2015. 2015GL065864.

[196] G.L. Manney and Z.D. Lawrence. The major stratospheric final warming in 2016: Dispersal of vortex air and termination of arctic chemical ozone loss. *Atmospheric Chemistry and Physics*, 16(23):15371–15396, 2016.

[197] M. Agostini et al. Flux modulations seen by the muon veto of the GERDA experiment. *Astropart. Phys.*, 84:29–35, 2016, physics.ins-det/1601.06007.

[198] M. Ambrosio et al. Search for the sidereal and solar diurnal modulations in the total MACRO muon data set. *Phys. Rev. D*, 67:042002, 2003.

[199] N.Yu. Agafonova et al. Analysis of seasonal variations of the cosmic ray muon flux and neutrons produced by muons in the LVD detector. *Bulletin of the Russian Academy of Sciences: Physics*, 75(3):427–430, 2011.

[200] C. Vigorito et al. Underground flux of atmospheric muons and its variations with 25 years of data of the LVD experiment. In *Proceedings of the 35th International Cosmic Ray Conference (ICRC)*, 2017.

[201] R. Bernabei et al. The DAMA/LIBRA apparatus. *Nuclear Instruments and Methods in Physics Research Section A: Accelerators, Spectrometers, Detectors and Associated Equipment*, 592(3):297 – 315, 2008.

[202] R. Bernabei et al. Final model independent result of DAMA/LIBRA phase 1. *The European Physical Journal C*, 73(12), 2013.

[203] G. Jungman et al. Supersymmetric dark matter. *Physics Reports*, 267(56):195 – 373, 1996.

[204] K. Freese et al. Signal modulation in cold-dark-matter detection. *Phys. Rev. D*, 37:3388–3405, 1988.

[205] A.K. Drukier et al. Detecting cold dark-matter candidates. *Phys. Rev. D*, 33:3495–3508, 1986.

[206] X. Xiao et al. Low-mass dark matter search results from full exposure of PandaX-I experiment. 2015, hep-ex/1505.00771.

[207] K. Blum. DAMA vs. the annually modulated muon background. *ArXiv e-prints*, 2011, astro-ph.HE/1110.0857.

[208] J.H. Davis. Fitting the annual modulation in DAMA with neutrons from muons and neutrinos. *Phys.Rev.Lett.*, 113:081302, 2014, hep-ph/1407.1052.

[209] R. Bernabei et al. No role for neutrons, muons and solar neutrinos in the DAMA annual modulation results. *Eur.Phys.J.*, C74(12):3196, 2014, hep-ph/1409.3516.

[210] F. Froborg. SABRE: WIMP modulation detection in the northern and southern hemisphere. *J. Phys. Conf. Ser.*, 718(4):042021, 2016, physics.ins-det/1601.05307.

[211] K. Pearson. VII. Note on regression and inheritance in the case of two parents. *Proceedings of the Royal Society of London*, 58(347-352):240–242, 1895.

[212] T. Abrahão et al. Cosmic-muon characterization and annual modulation measurement with Double Chooz detectors. *JCAP*, 1702(02):017, 2017, hep-ex/1611.07845.

[213] F. P. An et al. Seasonal variation of the underground cosmic muon flux observed at Daya Bay. *JCAP*, 1801(01):001, 2018, 1708.01265.

[214] P. Desiati. Seasonal variations of high energy cosmic ray muons observed by the IceCube Observatory as a probe of kaon/pion ratio. *International Cosmic Ray Conference*, 1:78, 2011.

[215] A. Bouchta. Seasonal variation of the muon flux seen by AMANDA. *International Cosmic Ray Conference*, 2:108, 1999.

[216] E. Fernandez-Martinez and R. Mahbubani. The Gran Sasso muon puzzle. *JCAP*, 1207:029, 2012, astro-ph.HE/1204.5180.

[217] M. Selvi et al. Analysis of the seasonal modulation of the cosmic muon flux in the LVD detector during 2001-2008. In *Proceedings of the 31st International Cosmic Ray Conference (ICRC)*, 2009.

[218] A. Moussa. *Recherche de correlations temporelles des muons cosmiques avec MACRO et perte d'energie des nuclearites*. PhD thesis, PhD Thesis, 2009, 2009.

[219] S.E. Forbush. Cosmic-ray intensity variations during two solar cycles. *Journal of Geophysical Research*, 63(4):651–669, 1958.

[220] I.G. Usoskin et al. Correlative study of solar activity and cosmic ray intensity. *Journal of Geophysical Research: Space Physics*, 103(A5):9567–9574, 1998.

[221] M. Amenomori et al. Probe of the solar magnetic field using the "cosmic-ray shadow" of the Sun. *Phys. Rev. Lett.*, 111(1):011101, 2013, astro-ph.SR/1306.3009.

[222] N.R. Lomb. Least-squares frequency analysis of unequally spaced data. *Astrophysics and Space Science*, 39(2):447–462, 1976.

[223] J.D. Scargle. Studies in astronomical time series analysis. II - Statistical aspects of spectral analysis of unevenly spaced data. *Astrophysical Journal*, 263:835–853, 1982.

[224] P.I. Richards. Computing reliable power spectra. *IEEE Spectrum*, 4(1):83–90, 1967.

[225] E. Masry and M.-C.C. Lui. A consistent estimate of the spectrum by random sampling of the time series. *SIAM Journal on Applied Mathematics*, 28(4):793–810, 1975, https://doi.org/10.1137/0128065.

[226] M. Wurm et al. Search for modulations of the solar ^{7}Be flux in the next-generation neutrino observatory LENA. 83, 2010.

[227] D.H. Hathaway. The solar cycle. *Living Reviews in Solar Physics*, 12:4, 2015, astro-ph.SR/1502.07020.

[228] SILSO World Data Center. The international sunspot number. *International Sunspot Number Monthly Bulletin and online catalogue*, 1997-2017.

[229] E. Rieger et al. A 154-day periodicity in the occurrence of hard solar flares? *Nature*, 312:623 EP, 1984.

[230] T. Bai and E.W. Cliver. A 154 day periodicity in the occurrence rate of proton flares. *The Astrophysical Journal*, 363:299–309, 1990.

[231] J.L. Ballester et al. The near 160 day periodicity in the photospheric magnetic flux. *The Astrophysical Journal*, 566(1):505, 2002.

[232] J. Lean. Evolution of the 155 day periodicity in sunspot areas during solar cycles 12 to 21. *The Astrophysical Journal*, 363:718–727, 1990.

[233] E.E. Benevolenskaya. Double magnetic cycle of solar activity. *Solar Physics*, 161(1):1–8, 1995.

[234] K. Mursula et al. Mid-term quasi-periodicities in geomagnetic activity during the last 15 solar cycles: Connection to solar dynamo strength – To the memory of Karolen I. Paularena (1957-2001). *Solar Physics*, 212(1):201–207, 2003.

[235] M.N. Gnevyshev. The corona and the 11-year cycle of solar activity. *Soviet Astronomy*, 7:311, 1963.

[236] M.N. Gnevyshev. On the 11-years cycle of solar activity. *Solar Physics*, 1:107–120, 1967.

[237] M.N. Gnevyshev. Essential features of the 11-year solar cycle. *Solar Physics*, 51:175–183, 1977.

[238] J.J. Love and E.J. Rigler. Sunspot random walk and 22-year variation. *Geophysical Research Letters*, 39(10), 2012. L10103.

[239] D.H. Hathaway et al. The shape of the sunspot cycle. *Solar Physics*, 151:177–190, 1994.

[240] M. Waldmeier. Neue Eigenschaften der Sonnenfleckenkurve. *Astronomische Mitteilungen der Eidgenössischen Sternwarte Zürich*, 14:105–136, 1935.

[241] G.D. Barr et al. Uncertainties in atmospheric neutrino fluxes. *Phys. Rev.*, D74:094009, 2006, astro-ph/0611266.

[242] A.M. Rossi et al. Experimental study of the energy dependence in proton-proton inclusive reactions. *Nuclear Physics B*, 84(2):269 – 305, 1975.

[243] C. Alt et al. Inclusive production of charged pions in p+p collisions at 158-GeV/c beam momentum. *Eur. Phys. J.*, C45:343–381, 2006, hep-ex/0510009.

[244] C. Adler et al. Kaon production and kaon to pion ratio in Au+Au collisions at $\sqrt{s_{\mathrm{NN}}} = 130\,\mathrm{GeV}$. *Phys. Lett.*, B595:143–150, 2004, nucl-ex/0206008.

[245] T. Alexopoulos et al. Mass-identified particle production in proton-antiproton collisions at $\sqrt{s} = 300$, 540, 1000, and $1800\,\mathrm{GeV}$. *Phys. Rev. D*, 48:984–997, 1993.

[246] S.V. Afanasiev et al. Energy dependence of pion and kaon production in central Pb + Pb collisions. *Phys. Rev.*, C66:054902, 2002, nucl-ex/0205002.

[247] M. Gaździcki and D. Röhrich. Pion multiplicity in nuclear collisions. *Zeitschrift für Physik C Particles and Fields*, 65(2):215–223, 1995.

[248] Google. Google Maps Elevation API. https://developers.google.com/maps/documentation/elevation/intro, 2017. [Online; accessed 13-June-2017].

[249] H. Wulandari et al. Neutron flux underground revisited. *Astropart. Phys.*, 22:313–322, 2004, hep-ex/0312050.

[250] A. Fedynitch et al. Calculation of conventional and prompt lepton fluxes at very high energy. *EPJ Web Conf.*, 99:08001, 2015, hep-ph/1503.00544.

[251] S. Meighen-Berger. personal communication.

[252] V.A. Kudryavtsev et al. Neutron- and muon-induced background in underground physics experiments. *Eur. Phys. J.*, A36:171–180, 2008, astro-ph/0802.3566.

[253] G. Cowan. *Statistical data analysis*. Oxford Science Publications, 1998.

[254] E.W. Grashorn et al. The atmospheric charged kaon/pion ratio using seasonal variation methods. *Astropart. Phys.*, 33:140–145, 2010, hep-ex/0909.5382.

[255] J. Klinger and V.A. Kudryavtsev. Muon-induced neutrons do not explain the DAMA data. *Phys. Rev. Lett.*, 114(15):151301, 2015, hep-ph/1503.07225.

[256] N.Yu. Agafonova. Measurement of the muon-induced neutron seasonal modulation with LVD. In *25th European Cosmic Ray Symposium (ECRS 2016) Turin, Italy, September 04-09, 2016*, 2017, astro-ph.HE/1701.04620.

[257] A.S. Malgin. Seasonal modulations of the underground cosmic-ray muon energy. *Journal of Experimental and Theoretical Physics*, 121(2):212–216, 2015.

[258] N.Yu. Agafonova and A.S. Malgin. Analysis of experimental data on the neutron yield from muons. 76, 2013.

[259] V.A. Kudryavtsev. personal communication.

[260] A. Gando et al. A study of extraterrestrial antineutrino sources with the KamLAND detector. *Astrophys. J.*, 745:193, 2012, astro-ph.HE/1105.3516.

[261] P. Vogel et al. Reactor antineutrino spectra and their application to antineutrino-induced reactions. II. *Phys. Rev. C*, 24:1543–1553, 1981.

[262] M. Malek et al. Search for supernova relic neutrinos at Super-Kamiokande. *Phys. Rev. Lett.*, 90:061101, 2003.

[263] E.K. Akhmedov and J. Pulido. Solar neutrino oscillations and bounds on neutrino magnetic moment and solar magnetic field. *Physics Letters B*, 553(1):7 – 17, 2003.

[264] S. Palomares-Ruiz and S. Pascoli. Testing MeV dark matter with neutrino detectors. *Phys. Rev. D*, 77:025025, 2008.

[265] Y. Fukuda et al. Atmospheric ν_μ/ν_e ratio in the multi-GeV energy range. *Physics Letters B*, 335(2):237 – 245, 1994.

[266] T. Yoshida et al. Neutrino-nucleus reaction cross sections for light element synthesis in supernova explosions. *Astrophys. J.*, 686:448–466, 2008, astro-ph/0807.2723.

[267] A. Strumia and F. Vissani. Precise quasielastic neutrino/nucleon cross-section. *Phys. Lett.*, B564:42–54, 2003, astro-ph/0302055.

[268] K.S. Kim and M.-K. Cheoun. Roles of one-step process on neutrino scattering off ^{12}C. *Physics Letters B*, 679(4):330 – 333, 2009.

[269] M. Honda et al. Calculation of atmospheric neutrino flux using the interaction model calibrated with atmospheric muon data. *Phys. Rev.*, D75:043006, 2007, astro-ph/0611418.

[270] Y. Hu et al. A simple setup to measure muon lifetime and electron energy spectrum of muon decay and its Monte Carlo simulation. 2016, physics.ins-det/1608.06936.

[271] M.S. Athar et al. Charged current anti-neutrino reactions from ^{12}C at MiniBooNE energies. *Phys. Rev.*, D75:093003, 2007, nucl-th/0703015.

[272] B. Ricci. personal communication.

[273] T.A. Mueller et al. Improved predictions of reactor antineutrino spectra. *Phys. Rev.*, C83:054615, 2011, hep-ex/1101.2663.

[274] G. Mention et al. The reactor antineutrino anomaly. *Phys.Rev.*, D83:073006, 2011, hep-ex/1101.2755.

[275] E. Kwon et al. Precise measurement of reactor antineutrino spectrum flux and spectrum at RENO. *Journal of Physics: Conference Series*, 888(1):012137, 2017.

[276] R.H. Thomas and G.R. Stevenson. *Radiological safety aspects of the operation of proton accelerators*. IAEA, 1988.

[277] V. Atroshchenko. personal communication.

[278] J.F. Beacom and L. Oberauer. personal communication.

[279] P. Vogel and J.F. Beacom. Angular distribution of neutron inverse beta decay, $\overline{\nu}_{\mathrm{e}} + \mathrm{p} \rightarrow \mathrm{e}^{+} + \mathrm{n}$. *Phys. Rev. D*, 60:053003, 1999.

[280] M. Agostini. m-stats. https://github.com/mmatteo/m-stats, 2018. [Online; accessed 09-February-2018].

[281] T. Mori. Status of the Super-Kamiokande gadolinium project. *Nuclear Instruments and Methods in Physics Research Section A: Accelerators, Spectrometers, Detectors and Associated Equipment*, 732:316 – 319, 2013. Vienna Conference on Instrumentation 2013.

Acknowledgements

The analyses of the cosmic muon flux were performed in close and extensive collaboration with Michael Wurm (Johannes Gutenberg-Universität Mainz) and Davide D'Angelo (INFN Milano). Additionally, the simulations concerning the cosmogenic neutron production rate were conducted by Vitaly A. Kudryavtsev (University of Sheffield) and Stephan Meighen-Berger (TUM) and the implications were jointly discussed and derived with the four mentioned collaborators. The estimation of the muon identification effiency was strongly supported by Giuseppe Bonfini (LNGS) and George Korga (University of Houston). In the analysis of atmospheric neutrino NC interactions in Borexino, an extensive exchange of ideas with the DSNB working group of the Borexino experiment led by Sandra Zavatarelli (INFN Genova) proceeded. The simulations contributing to this analysis were performed at the Kurchatov computation cluster and the possibility to use these resources is very gratefully acknowledged. The usage was made possible by Igor Machulin, Victor Atroshchenko, and Evgeny Litvinovich (Kurchatov Institute, MEPhI) and assistance in the setup of the simulations as well as helpful discussions on the realization of the analysis were exchanged.

Danksagung

An dieser Stelle möchte ich mich bei all denjenigen bedanken, die mich bei der Entstehung dieser Arbeit unterstützt haben.
Zunächst möchte ich Prof. Stefan Schönert für die freundliche Aufnahme und die Möglichkeit der Promotion am Lehrstuhl E15 herzlich danken.
Bei Prof. Lothar Oberauer als meinem Doktorvater möchte ich mich für die hervorragende Betreuung der Arbeit und die vielen äußerst motivierenden Gespräche und Diskussionen bedanken, für die er sich immer Zeit genommen hat und aus denen sich stets neue Ideen und Möglichkeiten entwickelten. Neben der fachlichen Unterstützung und Betreuung möchte ich mich auch besonders für die vielen und bereichernden Gespräche jenseits der Physik und die immer angenehme Atmosphäre bei der Arbeit bedanken.
Bedanken möchte ich mich auch bei Matteo Agostini, der als Mentor während der Promotion stets bereit war, über verschiedenste Problemstellungen zu diskutieren, sich in diese hineinzudenken und mit hilfreichen Anregungen neue Lösungen zu entwickeln.
Auch bei den Mitgliedern der Borexino Kollaboration möchte ich mich für die freundliche Aufnahme und die gute Zusammenarbeit während der Meetings, am Gran Sasso oder in den Working Groups bedanken.
Ein weiterer, großer Dank gilt Prof. Michael Wurm und Davide D'Angelo, die mir als große Freunde kosmischer Myonen sowie Korrelationsplots jeglicher Art bei den Analysen mit Rat und Tat zur Seite standen. Zahlreiche Ergebnisse dieser Arbeit wären ohne den intensiven Austausch sicherlich nicht möglich gewesen und ohne die humorvollen Diskussionen hätte die Arbeit auch höchstens halb so viel Spaß gemacht.
Ein besonderer Dank gilt natürlich allen, die Teile dieser Arbeit gelesen, korrigiert und damit weiter verbessert haben. Vielen Dank dafür an Birgit Neumair, Julia Sawatzki, Andrea Münster, Sabrina Franke, Simon Appel, Konstantin Schweizer und Walter Potzel.
Für die angenehme Arbeitsatmosphäre am Lehrstuhl E15 möchte ich mich bei allen Mitgliedern des Lehrstuhls und besonders bei meinen Bürokollegen bedanken. Bei Julia Sawatzki, die immer um das Sportprogramm im Büro bemüht ist, bei Simon Appel, den man nicht nur bei der Arbeit als Diskussionspartner, sondern auch am Seil gebrauchen kann, und bei Konstantin Schweizer, der mich mit guten Gesprächen aus so manchem Motivationsloch und Müdigkeitsanfall befreit hat.
Ein herzlicher Dank gilt auch unserer ehemaligen Sekretärin Sabine Kaps und deren Nachfolgerin Paola Mucciarelli, die bei allen verwaltungstechnischen Fragen immer geduldig weiterhelfen. Und dafür, dass man mit Sabine Geburtstagskuchen in schwindelnder Höhe genießen kann.

Ein großer Dank gilt meinen Kommilitonen und guten Freunden Georg Stockinger und Franz Haslbeck, mit deren Zusammenarbeit und Unterstützung jeder Skisprung-Wettkampf und auch alle sonstigen Herausforderungen, die während des Studiums auftreten können, erfolgreich bewältigt werden konnten.
Abschließend möchte ich meinen Eltern Ilona und Thomas und meiner Schwester Rebekka danken, die mich in allen Lagen unterstützen und für mich da sind. Mein ganz besonderer Dank gilt meiner Freundin Jana, auf deren Hilfe ich mich immer verlassen kann und die mir in jeder Situation geduldig mit Rat und Tat zur Seite steht.
Vielen Dank!